Scuola Internazionale Superiore di Studi Avanzati

MICROVESICLES:

NEUROGLIAL UNCONVENTIONAL SIGNALING TO CORTICAL BRAIN CELLS

CANDIDATE

Mattia Musto

SUPERVISORS

Loredana Casalis

Laura Ballerini

Index

ABSTRACT

Extracellular vesicles (EVs) represent an alternative and recently discovered way by which diverse cell phenotype can deliver complex messages through released vesicles and their cargoes to neighbor or distant targets. EVs mediate fundamental physiological and pathological processes in biological systems.

In particular, we focused on neuron-glia communication mediated by microvesicles (MVs), a subpopulation of EVs that directly originate by outward budding of cellular plasma membrane, which are mostly released under specific stimuli. Given the nanosized dimension and origin of MVs, we tested the ability of carbon-based nanomaterial (small graphene oxide nanoflakes, s-GO), which are demonstrated to interface cells and interact with their physiology at the level of their plasma membrane, to affect the mechanisms governing vesicles release. We first investigated whether s-GO affected the ability of astrocytes to release synaptic-like MVs in pure glial cultures. Our results describe the potential of GO nanosheets to alter different modes of interneuronal communication systems in the central nervous system (CNS). We further tested the reactivity of microglia, a sub-population of neuroglia that acts as the first active immune response, when challenged by chronic s-GO delivery at high doses. We investigated the tissue reactivity in 3D tissue models by using organotypic spinal cord cultures, ideally suited for studying long-term interference with cues delivered at controlled times and concentrations and in isolated neuroglia cultures. In the latter condition, we further tested the role of microglial micro-vesicle release in mediating cell responses to s-GO. Finally, starting from the observation that small graphene oxide flakes (s-GO) are able to boost MVs basal release in cortical glial cells of rodents after a sub-chronic treatment of 6-8 days, we compared through the use of highly sensitive and resolutive nanotechnological tools, MVs obtained under s-GO exposure with MVs obtained by stimulation with the purinergic agonist bzATP, known to induce such release in glial cells. The structural and macromolecular similarities found, suggested a comparable nature of s-GO-derived MVs with the bzATP-derived ones, despite the unusual induction of release. We finally investigated the acute effects of those populations of vesicles exerted on single cortical neurons by focusing on their synaptic activity. We found that both the MVs types

induced an increase in spontaneous post synaptic currents (PSCs) on neurons, after 15 minutes from MVs administration.

INTRODUCTION

1. EXTRACELLULAR VESICLES (EVs)

Communication among cells is an imperative and basic task of any multicellular organisms and it is accomplished by adopting diverse strategies. Traditionally, the known pathways of intercellular communication included the expression of signaling molecules on the cellular plasma membrane and the secretion of soluble ligands (the so called secretome) (Gundacker et al., 2009; Makridakis and Vlahou, 2010), and various cell-cell contact interactions, like gap junctions or tunneling nanotubes that allow metabolic and electrical pairing (Mendoza-Naranjo et al., 2011; Valiunas et al., 2005). However, recent studies enlarged this scenario with an additional signaling modality, once restricted only to specialized blood cells, that involves the release of small membrane vesicles in the extracellular environment able to affect target cells (Hess et al., 1999; Holme et al., 1994; Maas et al., 2017; Raposo and Stoorvogel, 2013).

The first report describing the existence of extracellular vesicles (EVs) dated back in 1946. Chargaff and West, investigating the coagulation factors involved in the clotting process, found that human plasma exposed to a strong centrifugal field (30000*g*) forms sediments that they identified as "pro-coagulant platelet-derived particles" (Chargaff and West, 1946). Few years later another study by Wolf and colleagues described the presence of lipid-rich particles, they referred to them as "platelets dust" attributing no active role in the coagulation process (Wolf, 1967). An increasing interest and more focused research during the 1980s conducted by independent research groups showed that such particles could be found in different biological fluids, like serum, seminal plasma and prostatic fluid (Benz and Moses, 1974; Ronquist et al., 2009). A significant boost in these studies was brought about by the development of techniques that allow investigating this "dust" at the nano-scale. In 1983 Harding and colleagues while describing the maturation of reticulocytes, found that these cells also secretes nano-sized vesicle characterized by freeze-fracture electron microscopy (Harding et al., 1983). These vesicles were called exosomes and were hypothesized to be used in removing unneeded molecules, in particular proteins, from cells (Johnstone et al., 1987). It took almost two decades to demonstrate their importance in intercellular communication, starting from their capacity of antigen presentation in B lymphocytes of

immune system (Raposo et al., 1996; Théry et al., 2009), spreading to increasing numbers of specialized biological systems (Pant et al., 2012; Record et al., 2011; Simons and Raposo, 2009). The production and release of EVs has been shown in all eukaryotes, ranging from extremely simple organisms up to mammals and this alternative way of cellular signaling was shown to be conserved throughout the evolution, although it is still unknown how it may have actually evolved. For example, protists like *Dictyostelium discoideum* and *Trypanosoma cruzi* are able to exchange genetic material via EVs, indicating that these vehicles may effectively exchange genetic material between parasites (Regev-Rudzki et al., 2013), and between parasites and host cells (Bayer-Santos et al., 2013; Lavialle et al., 2009). The same observations were reported for fungi and plants, extending the pool of macromolecules transferred to lipids and polysaccharides by the same mechanisms of release and uptake. Interestingly in some fungi the EVs signaling is also a way to spread fungal virulence, demonstrating an involvement of this communication pathway not only in physiological but also in pathological conditions (Regente et al., 2012; Rodrigues et al., 2011). Moving to the animal kingdom, as expected, also invertebrates use EVs as a parallel way to exchange information, mainly during their development, for instance in the *Drosophila melanogaster* and *Caenorhabditis elegans*. In the first example the Wnt/Wingless signaling is mediated also by exosome-like vesicles containing the Wnt-binding protein Evenness Interrupted/Wntless/Sprinter (Beckett et al., 2013; Gross et al., 2012; Korkut et al., 2009) while in the second case a specific sector of *C. elegans* called V0 is able to secrete Hedgehog-related peptides through a multivesicular compartment capable of release exosomes (Liégeois et al., 2006). Given the increasing evidence and heterogeneity of EVs involvement in cell biology, I decided to introduce here a classification of this form of extracellular signaling system.

1.1 Classification

The generic term “extracellular vesicles” is currently used to refer to all the secreted membrane vesicles with a 30 and 1000 nm vast size range. This highly heterogeneous population can be broadly divided based on their biogenesis into two main categories: exosomes and microvesicles or ectosomes (Fig. 1).

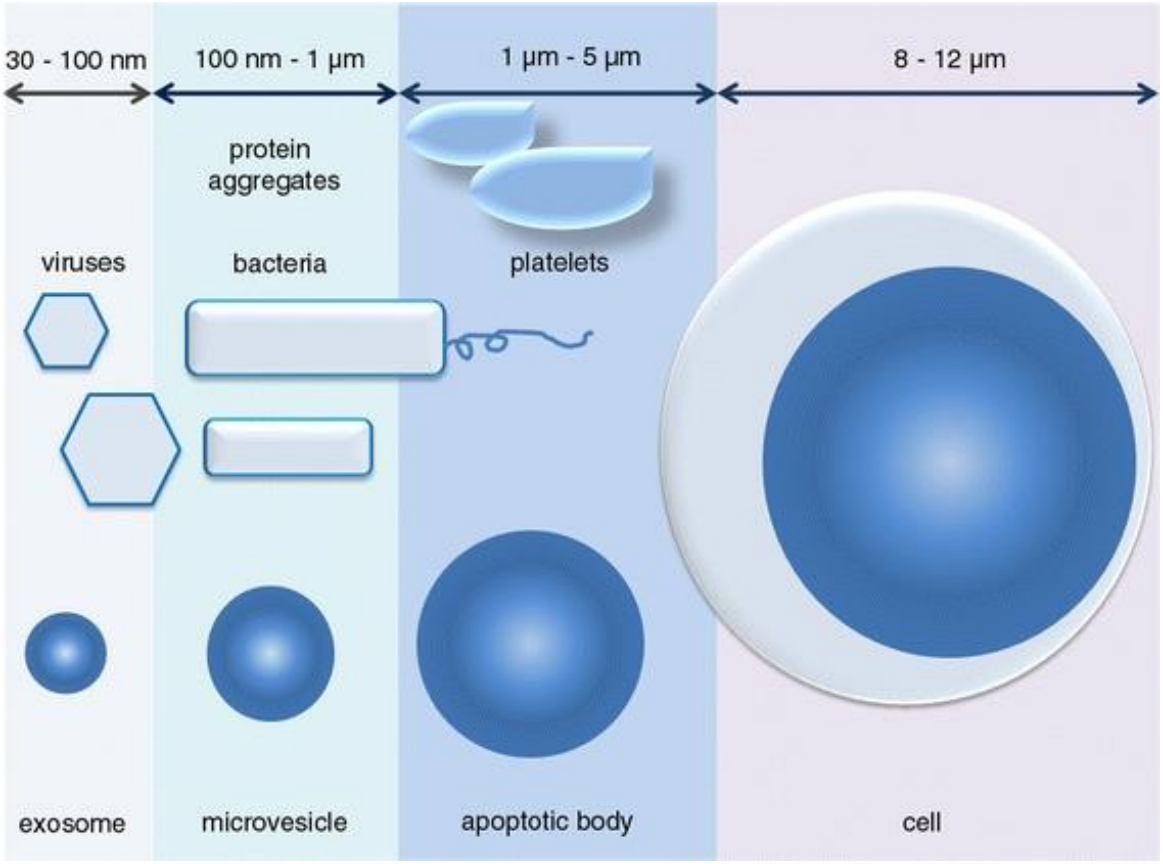

Figure 1

Schematic representation of the extracellular vesicles. Major populations include exosomes, microvesicles and apoptotic bodies (György et al., 2011).

The denomination exosome was used for the first time to refer to small membrane vesicles released by reticulocytes during their differentiation (Johnstone et al., 1987). Basically, exosomes are membrane vesicles of diameter comprised between 30 and 100 nm originating by the inward budding of endosomal membrane during the maturation of multivesicular endosomes (MVEs), intermediates of the endosomal pathway and they are secreted upon fusion of MVEs with the inner part of the plasma membrane of the cell (Simons and Raposo, 2009). The second category is represented by the microvesicles (MVs), firstly identified as subcellular product originating from platelets both in normal plasma and serum and formerly called "platelet dust" (Wolf, 1967). Differently from exosomes, MVs originates through direct outward budding and fission of the plasma membrane following different states of cell activation or during early stages of apoptosis (Tricarico et al., 2017). Even though MVs in

the past have been studied mainly for their role in blood coagulation (Satta et al., 1994; Sims et al., 1988), more recently they were reported to have a role in cell–cell communication comparable to that of exosomes, in several cell types, including cancer cells, where they are generally called oncosomes (Antonyak and Cerione, 2014). MVs are larger and more heterogeneous in size compared to exosomes, ranging from 50 to 1000 nm (Antonyak and Cerione, 2014; Raposo and Stoorvogel, 2013; van Niel et al., 2018) but they can be even larger, reaching a diameter of 10 μm in the case of oncosomes (Antonyak and Cerione, 2014; Minciacchi et al., 2015). This dimension-based identification is weaken by a clear overlapping of the size between exosomes and MVs, thus the mechanism of biogenesis is primarily used to distinguish MVs and exosomes (Akers et al., 2013; Antonyak and Cerione, 2014; György et al., 2011). In fact, the formation and release of MVs result from a dynamic process of phospholipid redistribution and cytoskeletal protein breakdown, in contrast with the more regulated biogenesis mechanism of exosomes.

There is also a third class of EVs that is not involved in the cellular crosstalk: the apoptotic bodies (ABs). ABs are the largest EVs, even larger than MVs, with a size range between 1 and 5 μm and are produced by nucleated cells undergoing programmed cell death. An apoptotic cell passes through several stages, beginning with condensation of the nuclear chromatin, followed by membrane blebbing, progressing to disintegration of the cellular content into the ABs (Akers et al., 2013).

1.2 EVs Biogenesis

The mechanisms involved in the biogenesis of exosomes and MVs are the main discriminating factor to distinguish these two classes of EVs (Fig. 2). Exosomes are firstly generated as intraluminal vesicles (ILVs) inside the lumen of endosomes, requiring a very precise molecular machine dedicated to sorting vesicles and their cargo, called endosomal sorting complex required for transport (ESCRT) (Hurley, 2008). This complex drives the assembling of exosomes by mediating the accumulation of distinct proteins, nucleic acids and bioactive lipids in the proximity of microdomains at the cytosolic side of the endosomes. The vesicles are successively generated by the inward budding of these microdomains with the formation of ILV (Colombo et al., 2014).

On the other hand, the biogenesis of MVs is still poorly understood compared to that of exosomes. The assembly of MVs takes place at the cytosolic side of specialized plasma membrane microdomains and requires the collection of macromolecules that will constitute their future cargo, which is slightly different from that of exosomes. Differently from the ILVs, the generation of MVs is the result of outward budding and shedding of these microdomains distributed across multiple and large plasma membrane areas. This mechanisms is probably mediated by the rearrangement of the asymmetric membrane phospholipid composition, induced by Ca^{2+} enzymes called flippase and floppase that cause a curvature of the plasma membrane promoting the budding and shedding of the vesicles (Akers et al., 2013; Cocucci and Meldolesi, 2015; Colombo et al., 2014). Other factors like the small GTPase Arf6, which mediates the vesicular trafficking and GTPase of Rho family are also involved in in this process (Antonyak et al., 2012; Muralidharan-Chari et al., 2009).

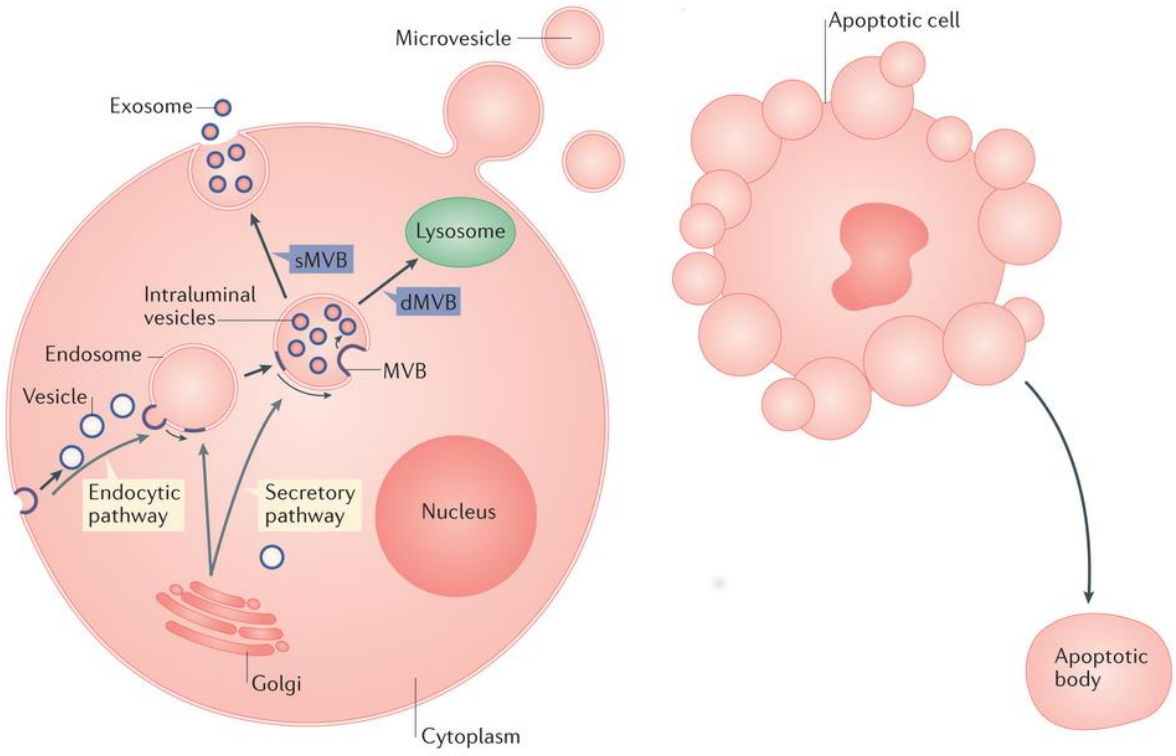

Figure 2

(left) Different pathways of EVs biogenesis. Exosomes form via the endocytic pathway by budding inwardly into the lumen of the endosome, generating the multivesicular bodies (MVBs). MVBs then fuse with the plasma membrane, releasing exosomes into the extracellular space. In contrast to

exosomes, microvesicles form by the outward budding of the plasma membrane surface. (right) Cell undergoing apoptosis sheds apoptotic bodies, which bud off from the plasma membrane (Budnik et al., 2016).

1.3 EVs Release and Uptake

Exosomes and MVs are released by parent cells into the extracellular environment usually triggered by specific internal or external stimuli, although a constitutive release in resting conditions has been proposed (Cocucci et al., 2009; Raposo and Stoorvogel, 2013; van Niel et al., 2018). Upon release, both types of EVs start navigating to reach their target cells. The release of exosomes, both at rest and under specific stimulations, may be variously delayed upon the biogenesis of intraluminal vesicles (ILVs) generated inside the MVBs, which, in many cells represents a store that prolong the release of this signal.

Conversely, prior to MVs generation the releasing cells accumulate specific molecules at their plasma membrane microdomains where the vesicles will be produced by the outward budding and consecutive shedding of plasma membrane (Akers et al., 2013; Cocucci and Meldolesi, 2015; Colombo et al., 2012) that is mostly induced. For example, in several cell types like macrophages and glial cells, the production of MVs in stimulated by the activation of the purinergic receptor-channel P_2X7 (Bianco et al., 2005; Wilson et al., 2004). In other cell types like the PC12 and platelets is the purinergic receptor P_2Y coupled with Gq protein (Kahner et al., 2008) that mediate the their release. Dependently to the type of stimulus applied, the shedding of MVs begins with some delay, ranging from few tens of second to 2 minutes(Antonyak and Cerione, 2014; Pilzer et al., 2005; Pizzirani et al., 2007).

An additional difference between the two EVs types may emerge from their kinetic of release. In the case of exosomes, upon appropriate stimuli MVBs translate from the perinuclear area (MVBs intracellular location) to the plasma to directly fuse with it by a process of exocytosis (Lopez-Verrilli and Court, 2013; Raposo and Stoorvogel, 2013). MVs release, if compared with exosomes, is much faster and this is probably due to the additional steps that the biogenesis and release of exosomes require.

However, the mechanisms involved in the formation of both exosomes and MVs require a dynamic remodeling of the membranes, for this reason the parental cell has to take important measures to preserve the equilibrium of the plasma membrane after the loss of its surface

necessary for the building of the EVs (Morris and Homann, 2001). If the shedding is slow, like in the case of exosomes, it is compensated by the trafficking of endosomes that are maintained in the equilibrium at the surface but in the case of MVs the rate of shedding is much higher and can rapidly affect cell volume, leading to a reduction of the plasma membrane area (Cocucci et al., 2009; Shifrin et al., 2013). This shrinkage is progressively compensated by exocytosis and subsequent fusion of intracellular vesicles called enlargeosome with the inner side of plasma membrane (Cocucci et al., 2007).

While the biogenesis and release of EVs is well regulated, once they are released in the extracellular space begin an unregulated navigation. As a consequence, a variable fraction of the released vesicle remains intact for a short period before the membrane breaks down. When this happens, their cargo, that is mostly composed by bioactive macromolecules like proteins, lipid and nucleic acids, becomes available for binding directly to their receptors on nearby cells inducing specific responses (Proia et al., 2008; Schiera et al., 2007). However most of released EVs are resistant enough to persist in the extracellular environment for long periods, such a resistance enable EVs to reach major body fluids such as blood serum or lymph and cerebrospinal fluid (Yoon et al., 2014) .

The most interesting part is how EVs can recognize specific cell phenotypes. The first evidence of this mechanisms were observed in platelets (Lösche et al., 2004). Losche and colleagues demonstrated how MVs released by these cells were able to bind selectively monocytes and not neutrophils. More recently, additional observations supported this notion, for example exosomes from cortical neurons are able to bind other cortical neurons, but not glial cells (Chivet et al., 2014) and exosomes released by oligodendrocytes are able to bind microglia, excluding other types of brain cells (Fitzner et al., 2011).

Once EVs identified their targets, they firstly interact with the cell surface to secondly fuse with the plasma membrane (Mulcahy et al., 2014) allowing the discharge of luminal cargoes into the cytosol (Fig. 3). However, there are some cases in which EVs can deliver their signal upon the bind and activation of surface receptors of the target cell (Gabrielli et al., 2015).

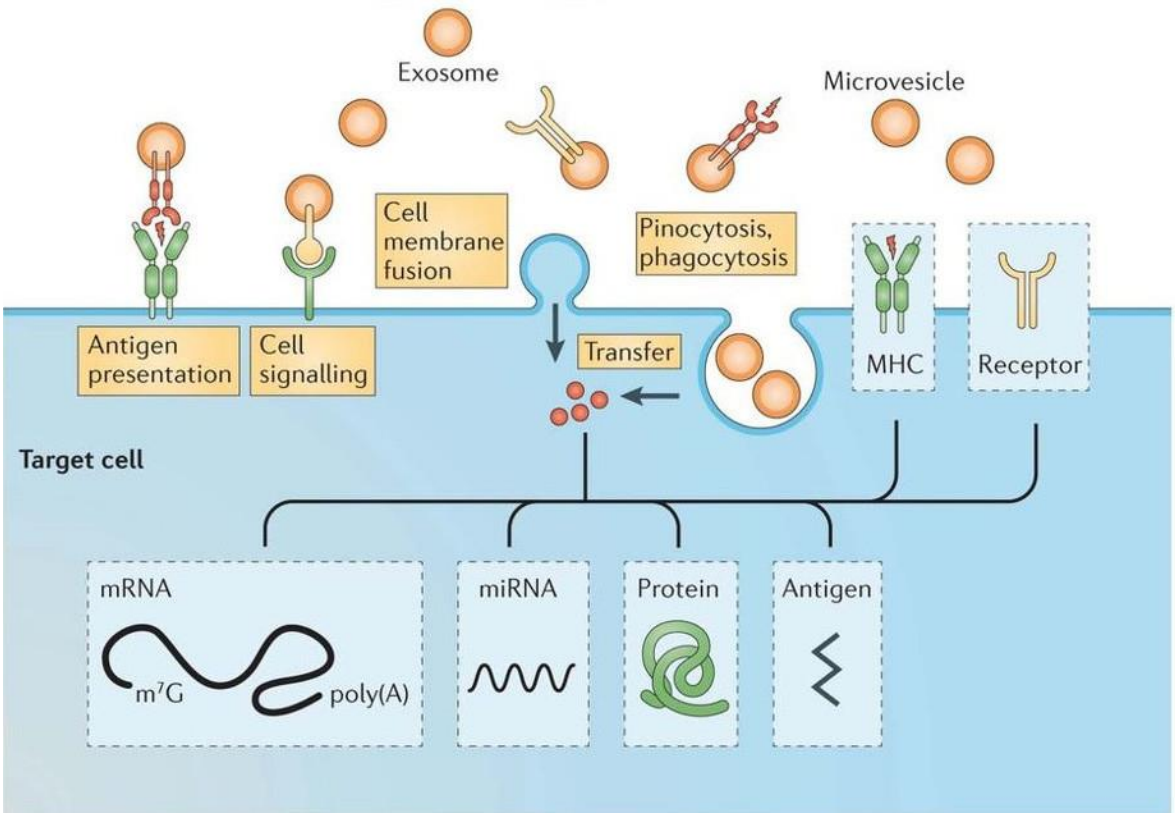

Figure 3

Schematic representation of EVs uptake by target cell. Extracellular vesicles can be regarded as signalosomes for several biological processes. They can be involved in antigen presentation and in the transfer of both major histocompatibility complex (MHC) molecules and antigens, thereby participating in immune regulation. Extracellular vesicles can directly activate cell surface receptors via protein and bioactive lipid ligands, transfer cell surface receptors or deliver effectors including transcription factors, oncogenes and infectious particles into recipient cells5. In addition, various RNA species including mRNAs and small regulatory RNAs (for example, microRNAs (miRNAs) and non-coding RNAs) are contained in extracellular vesicles and functionally delivered to recipient cells (EL Andaloussi et al., 2013).

1.4 Macromolecular Composition

Focusing on EVs composition, recent literature has highlighted that the two classes of EVs share some characteristics while differ in many others, in terms of molecular profile.

Exosome lipid bilayer consists of a high concentration of cholesterol and sphingomyelin plus ceramide and its products, which have a leading role in ILVs biogenesis. (Cocucci and Meldolesi, 2015; Raposo and Stoorvogel, 2013). Because of their endosomal origin,

membrane proteins are mostly represented by classes of proteins involved in membrane transport and fusion, like tretraspanins and integrins which also participate in cargo loading processes, biogenesis and release and have been conserved during evolution (Perez-Hernandez et al., 2013; Simons and Raposo, 2009; Urbanelli et al., 2013). Their cargo is mainly constituted by cystoskeletal and associated protein such as actin, chaperones, kinases and receptor. Together with proteins, exosomes transport also genetic material, mostly RNAs, such as miRNAs and mRNAs and in smaller quantity DNA (Gibbings et al., 2009; McKelvey et al., 2015) (Fig.4).

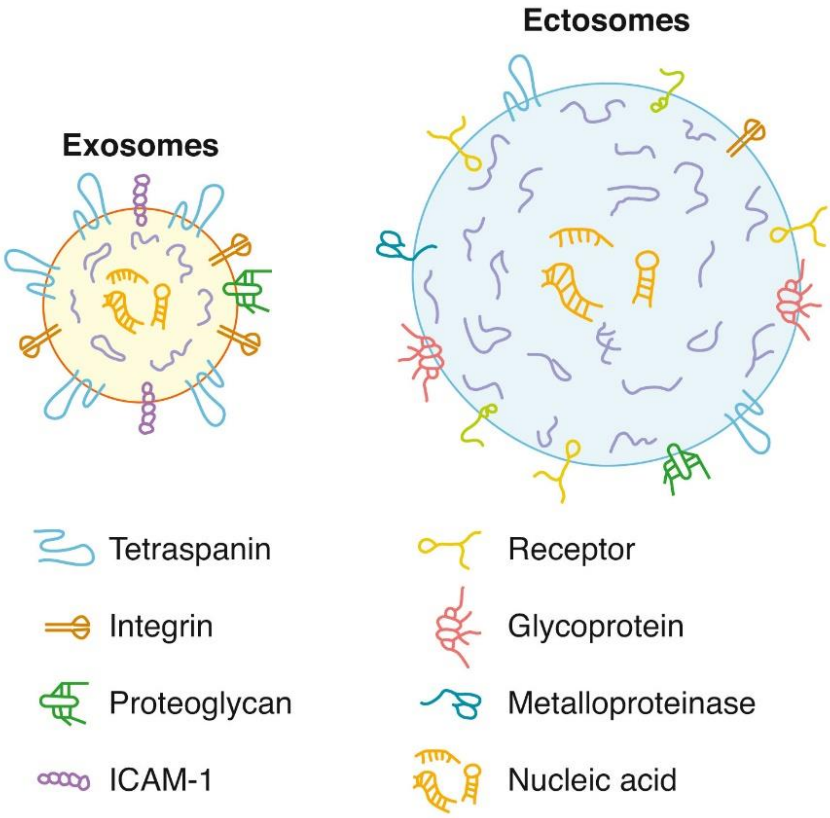

Figure 4

Structure and composition of exosomes and microvesicles (also known as ectosomes). In exosomes (yellow fill), the membranes are rich in tetraspanins, small transmembrane proteins important for membrane and luminal protein anchoring. In ectosomes (pale blue fill), the membrane contains many additional proteins like some receptors, glycoproteins and metalloproteinases. In orange are represented nucleic acids and in purple the proteins which constitutes EVs cargoes (Meldolesi, 2018).

MVs have a similar lipid membrane composition, with high levels of cholesterol, sphingomyelin and ceramide, but since they originate from the plasma membrane, their structure mostly depend on the lipid composition of parental cell. Ca^{2+}-dependent enzymes are able to perturbate the plasma membrane inducing a reorganization of phospholipid bilayer by translocating phosphatidylserine from the inner to the outer leaflet and these changes are also accompanied by changes in membrane proteins profile (Cocucci and Meldolesi, 2015; Tricarico et al., 2017). MVs cargoes differ from those of exosomes for the proteins, in fact MVs transport matrix metalloproteinase, glycoprotein receptors and other cytosolic proteins like those constituting the cytoskeleton in addition to centrosomal, ribosomal and mitochondrial proteins. As in exosomes, RNAs are also abundant within MVs consisting mostly of miRNAs but also mRNAs and non-coding RNAs.

A recent study suggested that, in line with the molecular species that the two classes of EVs transport, they exert different biological functionalities, in fact exosomes are mostly involved in signaling, antigen presentation and in the transfer of major histocompatibility complex while MVs are implicated in protein translation (Chang et al., 2013; Keerthikumar et al., 2015).

Even if a fraction of the cargoes-macromolecules is conserved throughout the evolution, the nature of EVs cargoes is strictly dependent on the donor cell-type and cargoes are often influenced by the cell physiological or pathological state, the stimuli that modulate their production and release and the molecular mechanisms that lead to their biogenesis (Kalra et al., 2016; Minciacchi et al., 2015).

1.5 EVs in Central Nervous System (CNS)

EVs as mediators of intercellular communication have been conserved throughout the evolution and for this reason virtually any cell is able to produce and release them (Akers et al., 2013; Maas et al., 2017; Minciacchi et al., 2015; Raposo and Stoorvogel, 2013). Even in the central nervous system (CNS), that is a relatively recent structure, EVs were shown to play an active role in cellular crosstalk and can be either taken up by neighbor cell or released into the cerebrospinal fluid (CSF) (Bianco et al., 2005; Colombo et al., 2012; Lugli et al., 2015). EVs released by neural cells share the same common features with all other EVs but

exert different functional effects on their targets and on the biological system they belong to, depending on the signals they deliver and then on the composition of their cargo. The functional role of EVs in the CNS has been shown in several aspects of neural biology, ranging from development to neurodegeneration (Fig. 5).

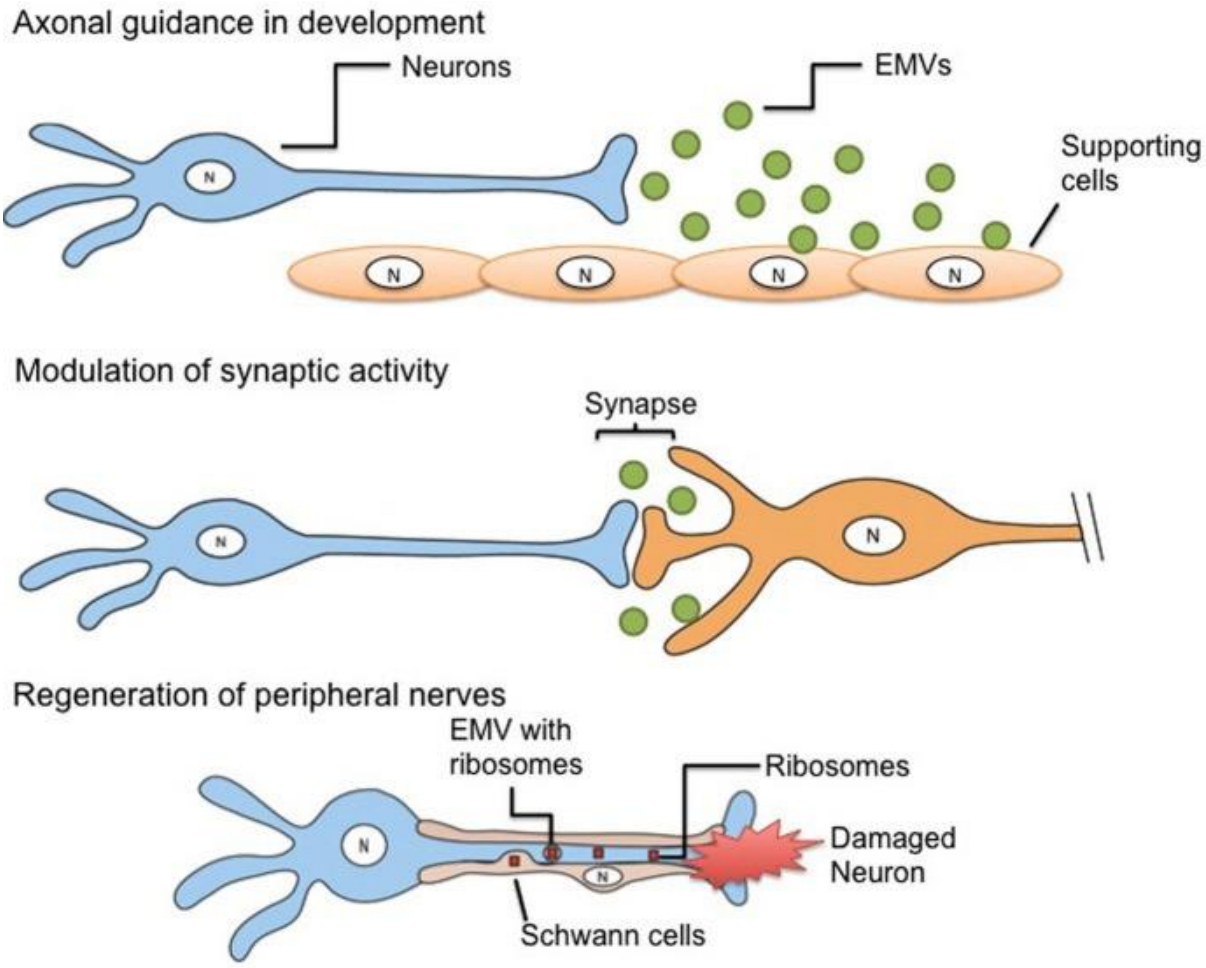

Figure 5

(top) Gradient of EVs can work as directional guide to axonal growth in the development of nervous system. (middle) EVs released from presynaptic nerve terminals and taken up by their postsynaptic partners can modulate synaptic activity. (bottom) Regeneration of peripheral nerves is enhanced by the transfer of ribosomes and mRNA mediated by EVs released from surrounding Schwann cells into the injured nerve to promote protein synthesis (Lai and Breakefield, 2012).

Development

EVs capacity to horizontally transfer various cargoes, especially genetic material and proteins, might significantly impact signaling during CNS development. Marzesco and colleagues in 2005 reported the presence of both exosomes and MVs in the luminal fluid of the neural tube of mice embryos (Marzesco et al., 2005). In cultured cortical neurons from mice embryos, EVs are released after the depolarization of immature neurons, apparently regulating synaptic activity via transported proteins like the L1 cell adhesion molecule (L1-CAM), the glycosylphosphatidyl-inositol–anchored (GPI-anchored) prion protein and the glutamate receptor subunit GluR1/3 (Fauré et al., 2006). Another and more recent study identified a pool of nanovesicles in embryonic cerebrospinal fluid (eCFS) of both rodents and humans, carrying protein and miRNA components of the insulin-like growth factor (IGF) signaling pathway which if isolated from eCFS and added to a mixed culture of embryonic neural stem cells (eNSC) were able to activate mTORC1 pathway enhancing the proliferation rate of these stem cells (Feliciano et al., 2014).

EVs generation in CNS is not limited to neurons or neural progenitors but involves virtually all kind of cell, comprising glial cell. In fact, another important role for EVs is the regulation of myelinogenesis, a complex and highly controlled process that takes place during development and regeneration. During CNS development the signals necessary to differentiate oligodendrocytes and those leading to the formation of myelin-membrane enwrapping axons are negatively regulated by EVs released by oligodendrocytes themselves. The release of this EVs and the resulting downregulation is dramatically inhibited at some point by neurons *via* the release of positive signals, thus initiating the maturation of oligodendrocytes and the following axonal myelinization (Bakhti et al., 2011). Astrocyte-derived EVs instead exhibited different effects on neurons during brain development, promoting neurite outgrowth and their survival, by delivering molecules like synapsin I and mediating neuronal differentiation (Wang et al., 2011). Another evidence of the strictly conserved nature of EVs is the identification of main cell-fate proteins, such as Wnt, TGF-β, EGF and FGF within EVs cargoes of both *Drosophila* and humans (Kalra et al., 2012).

Synaptic Communication

EVs may indeed modulate synapses and can be released in response to cortical neurons depolarization (Fauré et al., 2006; Lachenal et al., 2011). These neuron-derived exosomes can carry the GluR2 subunit of the glutamate receptor, suggesting EVs participation in regulating the amount of postsynaptic AMPA and NMDA receptors, modulating synaptic plasticity. EVs release after neuronal depolarization were also found to alter miRNA composition at both target-cellular and subcellular levels. They down-regulate and up-regulate the expression of brain-specific miRNA resulting in rapid changes in translation of mRNAs relevant to synaptic activity in postsynaptic region (Goldie et al., 2014).

EVs are exchanged not only among neurons but also between neurons and glial cells. Interestingly, neuronal synaptic activity and glutamate release appear to be necessary conditions to induce oligodendrocytes' EVs release, in fact the administration of calcium chelators like EDTA before exposure to glutamate completely abolishes exosomes release, indicating that entry of extracellular Ca^{2+} through ionotropic glutamate channels is essential to trigger exosome release in oligodendrocytes. A possible explanation is that mature oligodendrocytes express on their surface ligand-operated Ca^{2+} channels, such as NMDA receptors and their activation by glutamate released from depolarized neurons may stimulate the production of EVs in a calcium dependent way. This hypothesis is supported by the fact that pharmacological inhibition of NMDA receptors affected EVs release as EDTA did (Frühbeis et al., 2013a). This crosstalk between oligodendrocytes and neurons is not only necessary for the myelinogenesis during CNS development but is also thought to be crucial in maintaining axonal integrity in mature neurons.

Potentially all neuroglia cells might communicated with neurons via EVs. Antonucci and colleagues demonstrated in 2012 that MVs released by microglia interact with neurons, enhancing the miniature excitatory postsynaptic current (mEPSC) frequency without affecting the mEPSC amplitude (Antonucci et al., 2012). These authors investigated the effect of microglia-derived MVs *in vivo* by injecting them into the rat visual cortex and observed an acute increase in the amplitude of field potentials evoked by visual stimuli. The proposed mechanism underlying these effects on neurons is the capacity of MVs of regulating sphingolipid metabolism. Indeed, MVs promote ceramide and sphingosine

production in neurons which has been demonstrated to increase the probability of neurotransmitter release (Davletov and Montecucco, 2010).

Finally, astrocytes are known to scavenge extracellular glutamate, known to be neurotoxic when present at high concentrations, through excitatory amino acid transporters (EAAT-1 and EAAT-2), also crucial to regulate neurotransmission. Both these transporters have been identified in EVs released by astrocytes suggesting their role in synaptic transmission (Gosselin et al., 2013).

Axonal Regeneration

The ability to regenerate injured nerves is a peculiarity of peripheral nervous system (PNS) and axonal regeneration in adult PNS is finely regulated by a synergy of cellular and molecular processes that are mostly led by Schwann cells (SCs) (Bosse, 2012). A recent work demonstrated that exosomes produced by SCs are able to selectively target and be internalized by axons, both in dorsal root ganglia (DRG) cultures and in an *in vivo* model for sciatic nerve. SCs-derived exosomes have the capability to increase the regeneration rate of DRG neurons in both the models. The observed pro-regenerative effect depends either on proteins expressed on exosomal membrane that mediate the internalization by the targeted cell and on the cargo delivered (Lopez-Verrilli et al., 2013).

1.5.1 EVs in CNS diseases

EVs have a strong impact not only on physiological processes but contribute also to the development and spreading of cancer, neurodegeneration and neuroinflammation. Neurodegenerative diseases include: Alzheimer's disease (AD), Parkinson's disease (PD) and Prion diseases, which all share the common feature of protein accumulation and deposition in specific brain regions, called amyloid (Table 1).

Disease	Pathology	Possible roles for EVs		Key molecules carried by EVs
Prion disease	Conversion of the normal host PrPc to a misfolded aberrant conformation, PrPsc.	**Disease progression** ● Conversion of PrPc to PrPsc in MVBs ● Exosomes are the main pathway for prion, PrPsc, secretion and transmission to naïve cells.		PrPsc protein.
Alzheimer's disease (AD)	Accumulation of Aβ peptides in plaques derived from abnormal proteolytic processing of APP combined with NFT of hyperphosphorylated tau protein.	**Disease progression** ● Exosomes are related to pathology and propagation in the brain.	**Toxic clearance** ● Packaging and aggregation of Aβ peptides and tau proteins occur in exosomes; ● APP cleavage on early endosomes.	Hyperphosphorylated tau protein; Aβ peptide aggregates and fragments.
Parkinson's disease (PD)	Presence of Lewy Bodies, resulting from misfolded and fibrillar aggregation of α-syn. Degeneration of dopaminergic neurons in the *substantia nigra*.	**Disease progression** ● Exosomes secrete LRRK2 and catalyse α-syn aggregation; ● Exosomal α-syn is more efficiently delivered to cells comparing to free α-syn.		α-syn; LRRK2.
Huntington's disease (HD)	Expansion of a CAG triplet in huntingtin gene translated into a mutant htt with neurotoxic properties.	**Disease progression** ● Human exosomes carrying mutant htt trigger pathology in wild-type mice; ● Huntingtin aggregates phagocytized by glia, induce prion-like mechanisms of misfolding protein.	**Toxic clearance** ● Huntingtin aggregates can be phagocytized by glia.	Mutant htt
Amyotrophic lateral sclerosis (ALS)	Progressive disability of motor neurons caused by mutations in SOD1 and TDP43.	**Disease progression** ● Spreading of mutant SOD1 and TDP43 mediated by exosomes.	**Toxic clearance** ● Exosomal secretion of pathological TDP43 exerts a beneficial role in neuronal clearance.	SOD1; TDP43.
Multiple sclerosis (MS)	Progressive inflammation of myelin and axons leading to demyelination and oligodendrocytes loss.	**Disease progression** ● Pro-inflammatory cytokines promote EVs release; ● Myeloid EVs spread inflammation; ● EVs from oligodendrocytes inhibit myelin membrane sheath formation.		
Glioblastoma multiforme (GBM)	Several alterations in signal cascade pathways: RTK/RAS/PI3K, p53 and RB signaling.	**Disease progression** ● EVs released from GBM cells induce tumor growth in normal recipient cells; ● Tumor microenvironment is favored by the release of EVs from GBM.		EGFRvIII mRNA; EPHA2 RNA; miRNA-21; IDH1 RNA.

Table 1

Current knowledge of possible EVs roles in brain diseases.

Abbreviations: *MVBs - Multivesicular bodies; PrPc - cellular prion protein; PrPsc - scrapie prion protein; Aβ peptides - amyloid-beta peptides; APP - amyloid precursor protein; NFT - neurofibrillary tangles; α-syn - α-synuclein; LRRK2 - Leucine-rich repeat Kinase-2; mutant htt - mutant huntingtin protein; SOD1 - Cu/Zn superoxide dismutase 1; TDP43 - TAR DNA-binding protein 43; RTK - receptor tyrosine kinase; PI3K - phosphatidylinositol 3 kinase; RB - retinoblastoma protein; EGFR - epidermal growth factor receptor; EPHA2 - ephrin type-A receptor 2; IDH1 - isocitrate dehydrogenase 1. (Rufino-Ramos et al., 2017)*

Interestingly, there are evidences that EVs play a dual role in neurodegeneration: on one hand they promote the formation and spreading of these aggregates while on the other healthy cells use EVs to remove toxic proteins and amyloid aggregates from their cytoplasm. For example, it has been demonstrated that EVs released by neurons in a model of AD are able either to mediate aggregation and degradation of amyloid-beta (Aβ) and tau proteins (Asai et al., 2015; Rajendran et al., 2006).

The accumulation and transmission among cells of cytotoxic misfolded proteins like in AD is also the key mechanism of some prion diseases and it has been reported the presence of EVs carrying prion proteins, both the normal form (PrP^{c}) and scrapie form (PrP^{sc}) in biological fluids such as blood and CSF (Fevrier et al., 2004; Klöhn et al., 2013). In the case

of both PD and amyotrophic lateral sclerosis (ALS), the accumulation of α-synuclein and SOD1 respectively within EVs is a potential mechanism disease propagation, yet a causality has not been demonstrated (Basso et al., 2013; Danzer et al., 2012). Given the capacity of EVs to present antigens in the context of immune responses (Raposo et al., 1996; Théry et al., 2009), they are also able to carry tumor antigens promoting the oncogenesis and metastasis formation. By this mechanism, such EVs, known as oncosomes, may suppress the anti-cancer immune response (Czernek and Düchler, 2017). The most studied brain tumor in relation to EVs is the Glioblastoma (GBM), an extremely heterogeneous cancer, and several studies have demonstrated that GBM-derived EVs have a pivotal role in inducing malignant cell proliferation, angiogenesis, healthy tissue invasion and suppression of antitumor immune responses (Graner et al., 2009; van der Vos et al., 2011).

2. GLIA

The CNS is composed of two kinds of cells: neurons and neuroglia. Inthe human brain 10^{11} cells out of 10^{12} are neurons, while the remaining 9×10^{11} are glia.

The name *glia* was coined by Virchow at the end of 1850s when he described it as a "*connective substance formed in the brain, in the spinal cord, and in the higher sensory nerves, a sort of putty in which the nervous elements are embedded* " (Somjen, 1988). The name itself comes from the ancient Greek word "glia" meaning "glue". Since their discovery, glial cells were unfairly thought to only passively support neurons but we currently know that are more than just a glue keeping neurons stuck together. In fact glia actively participates to neurotransmission by modulating and responding to it and guides the development, maintenance and recovery of synapses (Fields and Stevens-Graham, 2002).

2.1 Classification and Functions

Glial cells are represented by several cell phenotypes that share the sole feature of not being neurons ultimately, being non-excitable cells. Neuroglia cells belong to four major phenotypes: astrocytes, oligodendrocytes, Schwann cells and microglia. These 4 cell types can be grouped, based on their origin, in macroglia and microglia (Fig. 6).

Macroglia includes astrocytes and oligodendrocytes (in the CNS) which arise from the neuroepithelium of embryonic neural tube and forebrain (Rowitch and Kriegstein, 2010) and

Schwann cells (in the PNS) which originate from the neural crest (Jacob, 2015). In contrast to macroglia, microglia has a mesodermal origin and is generated by the yolk sac during embryogenesis (Ginhoux and Prinz, 2015). As a first step hematopoietic stem cells generates primitive macrophages, which migrate in the developing CNS to be transformed into microglia.

Astrocytes most essential function in the CNS is related to neuronal survival, since these cells usually take up nutrients from the blood, thanks to their dual interaction with neurons and blood vessels of the blood brain barrier (BBB) (Pellerin et al., 2007). In response to neurotransmitter release by active neurons, they can also increase the blood flow to those brain regions where the metabolic needs are higher (Attwell et al., 2010). More recent evidences demonstrated the participation of astrocytes in synaptic maintenance, in addition to the already known capacity of scavenging neurotransmitter from the synaptic cleft and buffering extracellular potassium, they are able to control the formation, strength and turnover of synapses (Clarke and Barres, 2013). Lastly, astrocytes participate in the removal of exceeding synapses during CNS development where weak synapses were "pruned" and the strong ones kept (Allen, 2014).

Oligodendrocytes and Schwann cells are instead involved in myelinization of axons in CNS and PNS, respectively. Differentiating oligodendrocytes undergo complex morphological changes to generate numerous long processes that enwrap different axons forming the myelin sheaths (Snaidero and Simons, 2014). In PNS this job is carried out by Schwann cells, which constitute about the 80% of all cells in the peripheral nerves. In contrast to oligodendrocytes every Schwann cell surround only one axon and the myelin sheath is often thicker than CNS myelin (Salzer, 2015). Finally, as astrocytes participate in the removal of exceeding synapses in CNS, Schwann cells as well eliminate excess axons and synapses in the developing PNS by phagocytosis (Schuldiner and Yaron, 2015).

Microglia are the tissue-resident macrophages in the CNS and like macrophages, their role is to defend the nervous system against potential injuries. Resting microglia cells usually have a very ramified morphology, or surveillant state, to screen the environment in order to detect signs of injury. When needed, microglia rapidly migrate toward the lesion site and switch from the resting state to the activated one which is defined by an amoeboid morphology and production of cytokines and chemokines released in the injured site,

triggering a state of inflammation and cell apoptosis (Nimmerjahn et al., 2005). Also microglia, together with astrocytes and peripheral glia, is involved in synapse pruning in developing brain and this process, as for astrocytes, is strongly dependent on neuronal activity as demonstrated by the lack of synapse removal when action potential generation is pharmacologically blocked (Schafer and Stevens, 2015).

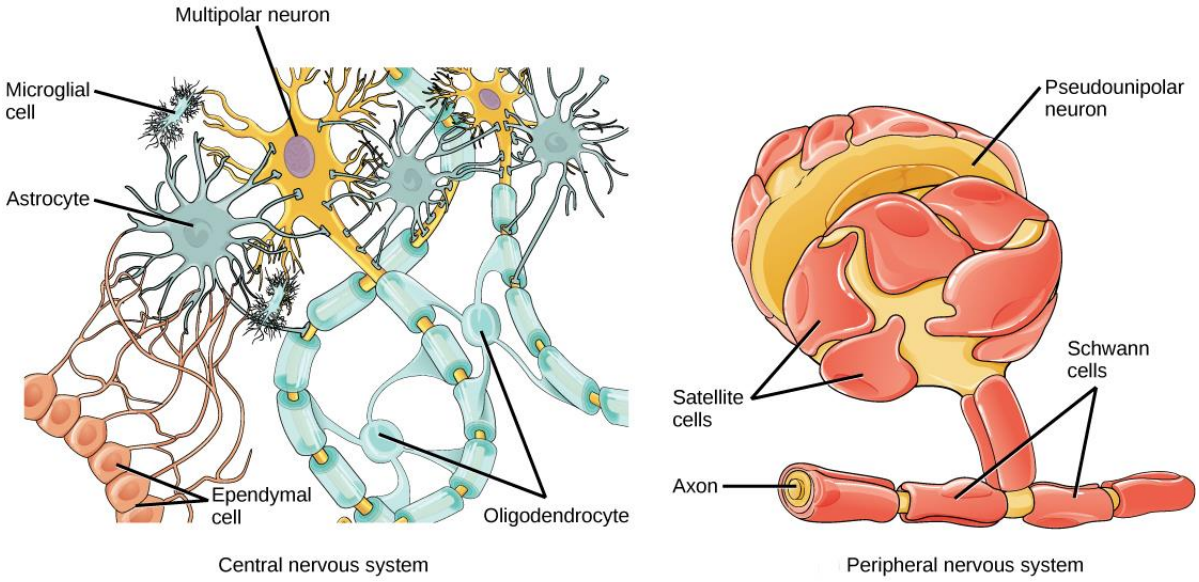

Figure 6

On the left are represented glial cells of the central nervous system including oligodendrocytes, astrocytes, ependymal cells, and microglial cells. Oligodendrocytes form the myelin sheath around axons. Astrocytes provide nutrients to neurons, maintain their extracellular environment, and provide structural support. Microglia scavenge pathogens and dead cells. Ependymal cells produce cerebrospinal fluid that cushions the neurons. On the right are represented glial cells of the peripheral nervous system, including Schwann cells, which form the myelin sheath, and satellite cells, which provide nutrients and structural support to neurons.

2.2 Glia-derived EVs

As synthesized in the previous paragraphs, neurons as well as neuroglia secrete EVs and the recent literature supports how intercellular communication through EVs has a strong functional impact in the nervous system both in physiological and pathological conditions, suggesting that the horizontal transfer of biomolecules may be a common mechanism of communication in the CNS (Frühbeis et al., 2012).

Astrocytes-derived EVs

EVs released by astrocytes are very heterogeneous in their composition and may have beneficial or pathological effects on CNS. For example, vesicles which are involved in physiological processes may carry heat-shock proteins like Hsp/Hsc 70 and synapsin I which have been suggested to have a neuroprotective function against oxidative stress (Taylor et al., 2007). Other molecules packaged inside EVs are factors that modulate angiogenesis, like FGF-2, VEGF endostatin and PED (Proia et al., 2008) and metalloproteinases which mediate astrocytes motility in physiological and pathological states (Sbai et al., 2010). A relevant role of astrocytes within the CNS is the regulation of glutamate homeostasis during synaptic transmission (Danbolt, 2001). This job is performed by the transporter EAAT-1 and EAAT-2 that are expressed on astrocytes plasma membrane, but recent evidences demonstrated that also astrocyte-derived EVs contain this class of transporters (Gosselin et al., 2013). EAATs use the electrochemical Na^+ gradient of the plasma membrane to transport glutamate and subsequently convert it to glutamine and their localization on astrocytes-derived EVs suggest a functional role in the elimination of exceeding glutamate from the extracellular environment (Rose et al., 2009). EVs released by astrocytes may also mediate the propagation of pathogenic proteins around the CNS, participating to the development of neurodegenerative diseases. Evidences were found in the context of disorders like ALS (Basso et al., 2013), AD (Wang et al., 2010, 2012) or HIV-associated neurological disorders (Hu et al., 2012).

Oligodendrocytes-derived EVs

EVs released by oligodendrocytes, as previously highlighted, are mostly involved in myelin formation and in the maintenance of axonal integrity. In fact, the presence of myelin proteins such as PLS, CNP, MAG and MOG has been detected as components of exosome cargo, essential for myelinogenesis during the early stages of development (Krämer-Albers et al., 2007). However, EVs have also a trophic function for neurons enwrapped in myelin sheath. They use exosomes as vehicle to deliver biomolecules such as metabolites, protective proteins, enzymes, mRNA and miRNA to neurons and this supportive action is regulated by neurons themselves. Glutamate released by active neurons induces Ca^{2+} entry through oligodendroglial ionotropic glutamate receptors with the consequent increase of intracellular

calcium which trigger EVs release (Frühbeis et al., 2013a) (Fig. 7). The same axonal support is mediated by Schwann cells in PNS (Lopez-Verrilli and Court, 2012).

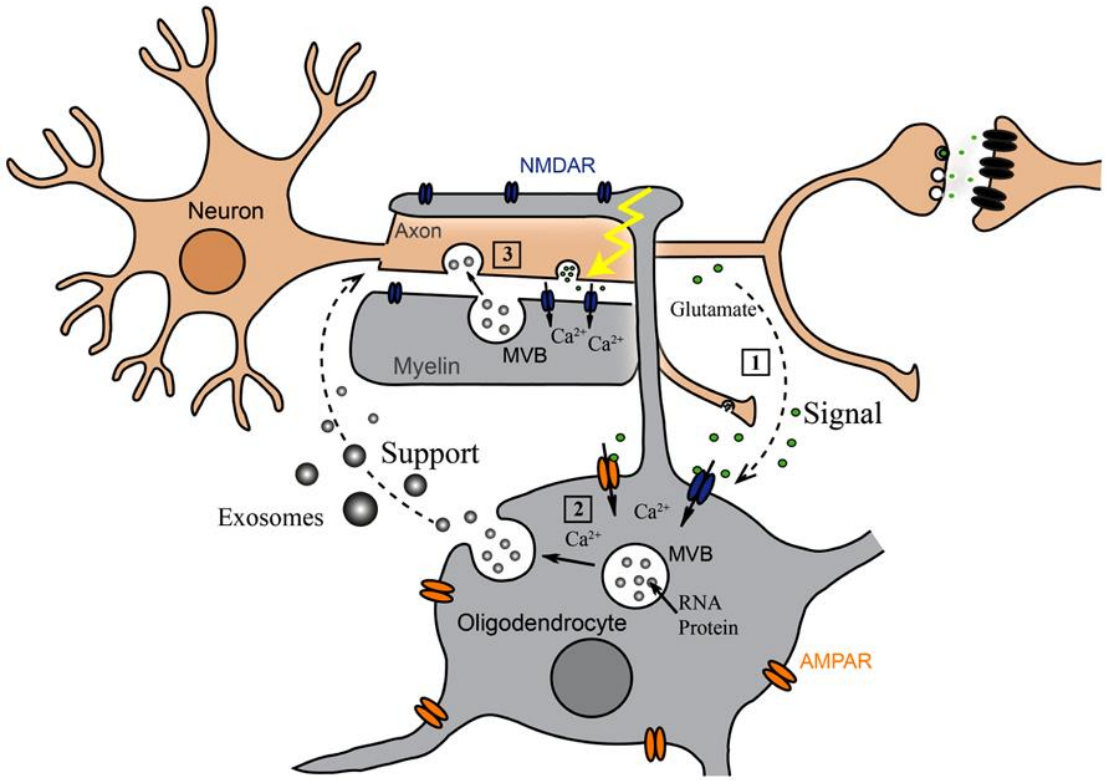

Figure 7

Oligodendrocyte-derived exosomes involved in neuron-glia communication. (1) Electrically active axons release glutamate that provokes Ca2+ entry through glutamate receptors present on oligodendrocytes surface. (2) Increase of intracellular Ca^{2+} levels induces exosome release from oligodendrocytes. (3) Exosomes internalization by neurons. (Frühbeis et al., 2013b)

Microglia-derived EVs

EVs released by microglia are mostly MVs and have the peculiarity of having irregular shape and size and are composed by high levels of phosphatidylserine and their shedding is induced upon activation of purinergic receptor P_2X7 by ATP (Bianco et al., 2005). Microglia-derived MVs transmit inflammatory signals such as interleukin-1β (IL-1β) to other microglial cells, resulting in an upregulation of proinflammatory genes like IL-1β, IL-6, cyclooxygenase-2 and nitric oxide synthase (Verderio et al., 2012). Given the role of microglia in the development of neuroinflammation, it is reasonable to consider also the involvement of MVs in this process. In fact, it has been observed how in multiple sclerosis and autoimmune

encephalomyelitis (EAE) the number of MVs dramatically increases and studies on rodents suggested that MVs enforce inflammation state in neuroinflammatory diseases. For this reason they also represent a promising diagnostic marker or therapeutic target (Colombo et al., 2012). Finally, experiments in vitro and in vivo demonstrated that microglia-derived MVs can stimulate spontaneous and evoked post-synaptic currents in hippocampal neurons through the modulation of ceramide metabolism at the pre-synaptic level (Antonucci et al., 2012).

3. TOOLS FOR INVESTIGATION OF EVs

At present, the role of EVs as fundamental mediators of intercellular communication is supported by an increasing number of studies in a large variety of biological systems, yet, their functions have not been fully elucidated. EVs contribution in either physiological or pathological processes makes them promising targets for the development of diagnostic and therapeutic applications, especially in the field of neuroscience (György et al., 2015). However, despite the promise of unveiling critical information of medical interest, working with these small particles represents a very tough scientific and technical challenge.

EVs are relatively new targets for bioassays and have peculiar biological and physical features in addition to their high heterogeneity (Yáñez-Mó et al., 2015). Such traits make them difficult to define and isolate with conventional analytical tools that possess sensitivity and throughput optimized for other biological targets (Witwer et al., 2013).

All these issues can be faced and partially overcome by using nanotechnological approaches. Nanotechnology indeed provides a set of materials, devices and systems whose functions are relevant for investigating very small scales of length, ranging from 1 nanometer to 1 micron that is the scale window where EVs are located (Whitesides, 2003).

The research on EVs may be subdivided in two main approaches: physical characterization and molecular composition analysis.

Physical characterization

Since EV is a generic word to identify a large variety of nanovesicles, heterogeneous in terms of origin and signals delivered, a first step in their study is the characterization for size, size distribution, concentration and morphology. However, conventional optical microscopies due to their diffraction limit, which is very close to that of EVs size, are not the best choice

to physically characterize them (van der Pol et al., 2010). High-resolution EV images are obtained through electron microscopy (EM) or atomic force microscopy (AFM).

The most popular EM technique for the study of EVs morphology are the transmission electron microscopy (TEM) and the scanning electron microscopy (SEM), with a preference for the first (Wu et al., 2015). In both techniques a focused beam of electrons hit the sample, but in the first case it is transmitted through the specimen to create a sample image, while in the second the beam scans the surface of the sample, interacting with atoms and providing a 3D surface topography information. There is also a third EM technique, that requires the sample to be analyzed at temperature around -100° C after a long fixation and staining, but with the advantage of avoiding the effect of dehydration and then the production of artifacts (Yuana et al., 2013).

Another high-resolution imaging technique for the characterization of EVs is AFM. AFM is a scanning probe technique based on the interaction of a very sharp tip directly with the sample, mounted on a mechanical cantilever with a laser beam that constantly hit the top of the cantilever and then reflected to a four-quadrant photodiode. While the tip passes over the sample, the deflection of the cantilever is measured by the displacement of the laser beam (Parisse et al., 2017). AFM does not require extensive preparation of the sample and provides two kind of information: surface topography and mechanical features (i.e. stiffness) of the sample (Sharma et al., 2010).

To note, these EM techniques do not allow studying the entire pool of EV. To do that there are techniques like dynamic light scattering (DLS) and nanoparticle tracking analysis (NTA) which are developed to study nanosized particles in suspension and therefore to gain information on, for example, an entire sample size distribution.

DLS measures the interference and intensity fluctuation of light scattered by EVs illuminated by a monochromatic light source and subjected to Brownian motion. The fluctuation rate is converted into the diffusivity of the vesicles in order to extrapolate the hydrodynamic radius (R_h). However the information obtained is intensity-related and proportional to R_h^6, meaning that larger objects can prevail over smaller ones, giving an inaccurate picture of EVs population (Palmieri et al., 2014). NTA is an optical method that calculates the size distribution and concentration of nanoparticles. In this technique the light scattered by

suspended EVs is captured by a camera that records their Brownian motion and tracking the single vesicle path and successively calculate size and concentration (Soo et al., 2012).

Molecular composition analysis

Another important aspect is the molecular composition of EV itself and of their cargo. The research over EVs focuses mainly on two macromolecules: proteins and nucleic acids.

Protein characterization is a fundamental step in the study of EVs not only to reconstruct their molecular profile but also for the identification of potential markers to use in biomedical research (Pant et al., 2012). A recent survey evidenced that the most widely used technique to characterize EVs is western blot (Gardiner et al., 2016), that together with the enzyme-linked immunoassay (ELISA) belong to the conventional protein assays which allow to easily demonstrate the presence of target proteins associated with EVs. However it requires a large amount and extensive pre-processing of the sample, which is very inconvenient for this kind of studies, especially in biomedical research (Witwer et al., 2013). In order to overcome the technical challenge of protein quantification related to low sensitivity of conventional techniques, new biosensors that require a smaller amount and minimal processing of the biological sample are under development. One of the more promising is the small particle flow cytometry, an enhancement of the conventional flow cytometry which can discriminate particles of around 100 nm in diameter versus the 500 nm of the classic one (Stoner et al., 2016) after they are stained with fluorescent antibodies in order to be characterized for their protein markers (Pospichalova et al., 2015). However, up to now other new biosensors have many limitations and are not still standardized for the study of EVs.

In addition to proteins, EVs transport also nucleic acids and RNA represents the major nucleic acid of their cargo. As with proteins, the total amount of nucleic acids inside EVs is very low and their study requires efficient extractions and very sensitive detection tools (Mateescu et al., 2017). The most used are the phenol-chloroform extraction and spin columns and both of them are standardized and provide well purified RNA (Enderle et al., 2015; Skog et al., 2008). Amplification and sequencing of nucleic acids allow to verify quality, yield and size but are typically sequence-dependent, meaning that we can amplify and detect only known sequences of DNA and RNA by using polymerase chain reaction (PCR) or real-time PCR (RT-PCR) (Balaj et al., 2011; Skog et al., 2008), resulting in a low throughput. Anyhow, next generation sequencing (NGS) now gives us the opportunity to

largely screen and characterize the transcriptome, including known and unknown RNA of EVs thanks to the generation of library shared among laboratories worldwide (Huang et al., 2013).

4. CARBON BASED NANOMATERIALS IN NEUROSCIENCE

In the last two decades we have witnessed an exponential interest in carbon based materials (CBMs) by the scientific community. Their unique physico-chemical properties coupled to the nano-size make them promising substrates for the development of biomedical applications in many fields of biomedicine, with a particular focus on neurosciences (Baldrighi et al., 2016b). The prospects that these materials opened to the scientific research range from the delivery to the CNS of molecules that usually cannot cross the blood brain barrier (BBB) (Saraiva et al., 2016) to the development of neuro-scaffolds for the regeneration of damaged nerves (John et al., 2015; Usmani et al., 2016).

The discovery of such materials begun in 1985 with fullerenes (Kroto et al., 1985), then with carbon nanotubes (Iijima, 1991) and finally with the synthesis of graphene (Novoselov et al., 2004) which are all composed of carbon atoms only but with different structures.

Carbon, constitutes the most versatile element of the periodic table, because of the variety of its allotropes and structures, given from the ability of the carbon valence orbitals to hybridize in sp, sp^2 and sp^3 configurations. The allotropes of carbon that are naturally produced are diamond, amorphous carbon and graphite but there are also carbon allotropes deriving from a synthetic process such as graphene, carbon nanotubes, fullerenes and nanodiamonds (Dresselhaus, 2012) (Fig. 8).

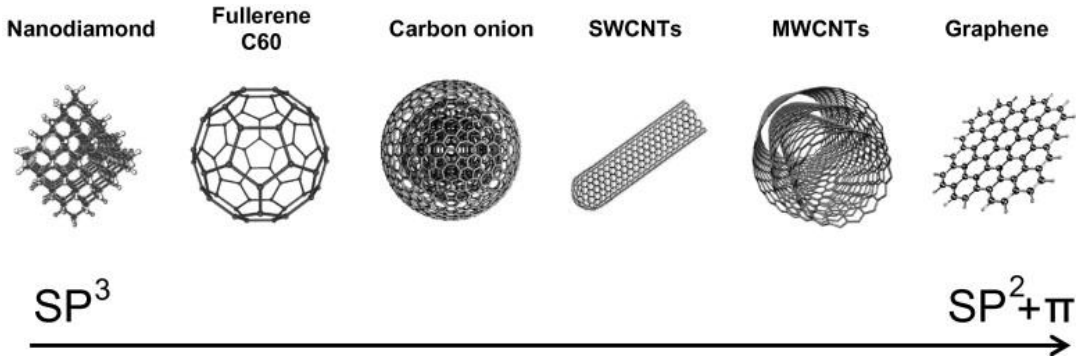

Figure 8

Hybridization states of carbon-based nanomaterials

All CBMs are naturally good electrical conductor with good biocompatibility, which make them excellent candidates for the development of electrically conductive scaffolds (Supronowicz et al., 2002). Among all kinds of CBMs, carbon nanotubes (CNTs) and graphene are the most popular that have been widely studied, since both possess excellent mechanical strength, electrical and thermal conductivity, and optical properties coupled with biocompatibility that is an imperative for biomedical applications. Lots of the research efforts have been focused on exploiting these advantageous properties for various applications including electronics, biological engineering, filtration, lightweight/strong composite materials, photovoltaic and energy storage (Esawi and Farag, 2007; Sreeprasad et al., 2011; Wang et al., 2010).

4.1 Graphene

Graphene (GR) is the thinnest compound known to man at one atom thick, the lightest material known (with 1 square meter coming in at around 0.77 milligrams), the strongest compound discovered (between 100-300 times stronger than steel and with a tensile stiffness of 150,000,000 psi), the best conductor of heat at room temperature (at $(4.84\pm0.44) \times 10^3$ to $(5.30\pm0.48) \times 10^3$ $W\times m^{-1}\times K^{-1}$) and also the best conductor of electricity known (studies have shown electron mobility at values of more than 15,000 $cm^2\times V^{-1}\times s^{-1}$) (Bolotin et al., 2008). The excellent physicochemical properties of graphene combined with its potential biocompatibility provide exciting opportunities for new biomedical applications. The different applications for which graphene have been proposed, lead to engineering not only graphene monolayers, but a wide variety of graphene-based materials (GBMs). The single layer graphene, bi-layer graphene, multilayer graphene, graphene oxide (GO), reduced graphene oxide (rGO) and chemically modified graphene are the members of the graphene-based nanomaterial family. GO and rGO are often preferred for biological applications because graphene itself is difficult to suspend in water solutions, due to its highly reactive surface. Research in neuroscience demonstrated how graphene films have excellent biocompatibility for primary culture of mouse hippocampal neurons and are even able to promote neurite sprouting and outgrowth, especially during the early stages of development (Li et al., 2011). GBMs are also able to preserve the basal physiological level of neuronal

activity as reported by Fabbro and colleagues (Fabbro et al., 2016). They highlighted uncommon properties of graphene-based substrates (GBSs) to support neuronal development, in terms of neuronal passive properties, spontaneous synaptic activity, synaptogenesis, and short-term synaptic plasticity (STP). Another amazing property of graphene is to tune the extracellular ions distribution at the interface with hippocampal neurons that is a key regulator of neuronal excitability. The interaction between graphene and ions are maximized when a single layer graphene is deposited on substrates electrically insulated. These biophysical changes caused a significant shift in neuronal firing phenotypes (Pampaloni et al., 2018).

One of the first observation related to the possible use of GR in the brain environment was that the biocompatibility and broad-spectrum transparency, flexibility and mass-producibility of graphene make it an ideal candidate for replacement of ITO in neural interfacing devices. Indeed, there are several examples of effective graphene-based electrode devices in the recent literature. A graphene-based, carbon-layered electrode array device was implanted in the brain surface in rodents for high-resolution neurophysiological recording. Its optical transparency of the device at >90% transmission over the ultraviolet to infrared spectrum was characterized and prove its utility through optical interface experiments that use this broad spectrum transparency. These experiments included optogenetic activation of focal cortical areas directly beneath electrodes, in vivo imaging of the cortical vasculature via fluorescence microscopy and 3D optical coherence tomography. GR is also being explored as a novel platform for the local delivery of therapeutic molecules with encouraging preliminary results. Functionalization of GR and GO can tailor their properties and enable their use as carriers of therapeutic molecules (Vincent et al., 2017) even because they potentially can deliver molecules that are usually rejected by the BBB.

In neurology, GR represents a promising tool for neuronal implants or bio-devices, with potential applications ranging from neuro-oncology to neuro-regeneration (Bitounis et al., 2013; Kuzum et al., 2014). It was also reported recently the ability of small graphene oxide nanosheets (s-GO) to interfere specifically with neuronal synapses, without affecting cell viability. In particular, in cultured neuronal networks, upon chronic s-GO exposure, glutamatergic release sites were sized down (Rauti et al., 2016a).

Among the different possible implementations of GBMs, building of graphene-based scaffolds for cell growth and differentiation is one of the most promising. 3D graphene foams (3D-GF) can be obtained using nickel foam template for chemical vapor deposition of graphene. Growing neural stem cells on these substrates allows not only a more physiological condition but also a substrate that can be electrically stimulated (Li et al., 2013). Growing neurons on 3D scaffold allows us also to recapitulate two basic properties of the complexity of the brain: firstly, the coexistence of local and global electrical activity, and secondly, the existence of neuronal assembly with a degree of correlated electrical activity varying in space and time (Ulloa Severino et al., 2016). A different strategy recently explored by Martìn and colleagues, these authors build hybrid hydrogel with polyacrylamide and graphene. Their study demonstrated that graphene improves the biocompatibility of the 3D scaffold (Martín et al., 2017).

4.1.1 Graphene Interaction with Cell Membrane

As observed with other nanosized particles, graphene and GBMs are able to interact with cell plasma membrane (Zhang et al., 2016). This interaction is the starting point for the development of biomedical interfaces between GBMs and mammalian cells but despite the recent increasing literature describing these interactions at different levels of living systems, there is still an unclear and incomplete picture of the mechanisms underlying (Bitounis et al., 2013; Kostarelos and Novoselov, 2014). Graphene interaction with cellular plasma membrane may be of two types: absorption or internalization (Kostarelos and Novoselov, 2014), however the nature of interaction depends on the characteristics of both the material and the biological system targeted. In fact, the internalization or adsorption of GBMs is strictly influenced by material size and surface chemistry. Smaller GO particles, for example, are mostly internalized by endocytosis but increasing the size of GO brings to a phagocytic way of uptake (Mu et al., 2012). Also its reduction state influences the internalization by increasing or decreasing the hydrophobicity of the material and then the capacity to interact with cell membrane component (Chatterjee et al., 2014). The type of cell targeted also affects the way GBMs can be internalized as demonstrated by Linares and colleagues in three different kind of cell treated with GO nanosheets (Linares et al., 2014). The cell uptake of graphene may alter the dynamic of plasma membrane and thus inducing biological effects

that in case of exposures at high concentrations can lead to neuroinflammatory response, as observed in macrophages (Zhou et al., 2012), or even cell death (Liao et al., 2011). It is therefore clear that the effects of graphene and its derivatives on cells are still not well elucidated and there are several biological processes happening in specific kind of cells or tissues which can be influenced by such interactions but have not been investigated yet.

In this context and considering the capacity of GO to influence plasma membrane equilibrium, we decided to investigate the effects that small GO flakes (s-GO) may exert on plasma membrane of glial cells, focusing membrane dynamics and MVs release. Since the release of MVs is a phenomenon that involves finely regulated alterations of plasma membrane lipids dynamics and given the previous report of the ability of s-GO to affect synaptic vesicles release in hippocampal neurons (Rauti et al., 2016a) we perform a sub-chronical exposure of glial cells to s-GO and measured the response to this stimulus in terms of MVs release. As reported in literature, MVs basal release is very low in physiological conditions but we demonstrated that a short treatment with s-GO at low concentrations boosted this spontaneous release without affecting cell viability. The ability of MVs to easily reach inaccessible regions due to the presence of biological barriers, like the blood brain barrier (BBB) of the brain might have a decisive role in the development of biomedical tools for the delivery of drugs or genetic material in these regions.

AIMS

This work is focused on the investigation of intercellular communication between glia and neurons of cerebral cortex. It is well established, since years, that glia has a leading role in the modulation and maintaining of synaptic connectivity and neuronal survival, starting from the early stages of development until the formation of a mature and stable network. The highly diversification of glial cell types allows the nervous system to mediate a wide range of functions critical for neuronal signaling. In particular, astrocytes represent the majority of glia and actively communicate with neurons in terms of survival and modulation of synaptic activity. In the context of astrocytes-neurons crosstalk there is a lack of knowledge regarding the role of newly discovered way of communication, alternative to the "classic" signaling, represented by extracellular vesicles.

The first aim of this study is to unveil the response of astrocytes to unconventional stimuli, understanding how these stimuli can affect the release of extracellular vesicles in rodent cerebral cortex. Once verified the capability of cortical astrocytes to release extracellular vesicles under pharmacological stimulation with agonists of purinergic receptor P_2X7 we investigated how the interaction of graphene based materials with glial cells could affect this signaling pathway. We focused on graphene and in particular small graphene oxide (s-GO) flakes, because of their ability to interact with plasma membranes and its unique physico-chemical properties which made s-GO extremely promising substrates for the development of biomedical application. Given the direct impact of s-GO on plasma membranes, we pointed our attention on the class of extracellular vesicles called microvesicles (MVs) due to the fact that their biogenesis is directly linked to plasma membrane perturbations. The literature about biological effects that MVs exert on neurons in terms of modulation of synaptic activity is currently very poor and incomplete, especially if we consider astrocytes-derive MVs. Some reports demonstrate the capability of extracellular vesicle to affect neuronal activity but are mostly focused on microglia-derived vesicles describing the effects of a mid-long exposure to them. We developed an efficient strategy to release MVs from astrocytes by s-GO exposure and MVs were systematically characterized by nano-technology based tools, and compared to ATP-released ones. Second aim of this study is to

investigate the effects of an acute exposure of cortical neurons to MVs isolated from astrocytes cultures, focusing not on the network activity but on the single neuron.
However, when we work with carbon based nanomaterials we must take in consideration also how the treated tissue could react. Tissue reactivity in response to GBMs is strictly dependent to many variables like: concentration, functionalization, size and shape of the material and with the perspective of a biomedical application it is mandatory to examine in depth also this aspect. For this reason, a collateral research was design to verify how the resident macrophages on central nervous system, represented by microglia, react to the presence of s-GO flakes, at the same concentration and conditions used for the treatment of astrocytes in order to evaluate possible long-term neurotoxic effects.
The results of this Thesis were in part published or submitted and are included as so in the following order:

Graphene Oxide Nanosheets Reshape Synaptic Function in Cultured Brain Networks. *ACS Nano* (2016)

Graphene Oxide Nanosheets and Neural System: from Synaptic Modulation to Neuroinflammation. *Frontiers in System Neuroscience* (2018) (submitted)

s-GO Nanoflakes Boost Microvesicle Production in Brain Cultured Astrocytes. *Nanoletters* (Manuscript in preparation)

Carbon Nanomaterials for Brain Interfaces (Review). *Carbon* (2018) (under revision)

ACSNANO
www.acsnano.org
ARTICLE

Graphene Oxide Nanosheets Reshape Synaptic Function in Cultured Brain Networks

Rossana Rauti,[†] Neus Lozano,[‡] Veronica León,[§] Denis Scaini,[†,⊥] Mattia Musto,[∥] Ilaria Rago,[⊥] Francesco P. Ulloa Severino,[∥] Alessandra Fabbro,[¶] Loredana Casalis,[⊥] Ester Vázquez,[§] Kostas Kostarelos,[‡] Maurizio Prato,[*,¶,#,△] and Laura Ballerini[*,†,∥]

[†]Life Science Department, University of Trieste, 34127 Trieste, Italy

[‡]Nanomedicine Lab, School of Medicine and National Graphene Institute, Faculty of Medical & Human Sciences, University of Manchester, M13 9PL Manchester, United Kingdom

[§]Departamento de Química Orgánica, Facultad de Ciencias y Tecnologías Químicas-IRICA, Universidad de Castilla La Mancha, 13071 Ciudad Real, Spain

[⊥]ELETTRA Synchrotron Light Source, 34149 Trieste, Italy

[∥]International School for Advanced Studies (SISSA), 34136 Trieste, Italy

[¶]Department of Chemical and Pharmaceutical Sciences, University of Trieste, 34127 Trieste, Italy

[#]CIC BiomaGUNE, Parque Tecnológico de San Sebastián, Paseo Miramón, 182, 20009 San Sebastián, Guipúzcoa, Spain

[△]Basque Foundation for Science, Ikerbasque, Bilbao 48013, Spain

Supporting Information

ABSTRACT: **Graphene offers promising advantages for biomedical applications. However, adoption of graphene technology in biomedicine also poses important challenges in terms of understanding cell responses, cellular uptake, or the intracellular fate of soluble graphene derivatives. In the biological microenvironment, graphene nanosheets might interact with exposed cellular and subcellular structures, resulting in unexpected regulation of sophisticated biological signaling. More broadly, biomedical devices based on the design of these 2D planar nanostructures for interventions in the central nervous system require an accurate understanding of their interactions with the neuronal milieu. Here, we describe the ability of graphene oxide nanosheets to down-regulate neuronal signaling without affecting cell viability.**

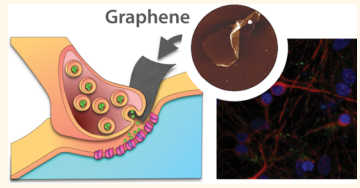

KEYWORDS: *nanotechnology, graphene, patch-clamp, synaptic terminals, exocytosis, FMI-43, microvesicles*

Graphene is a 2D plate-like material consisting of sp^2-hybridized carbon atoms organized in a hexagonal lattice and characterized by, among other properties, high electron mobility and mechanical flexibility.[1−3] In addition to the successful exploitation of graphene and graphene-based materials in an increasing number of industrial products, current applications of graphene hold the potential to revolutionize specific areas of medicine.[2−6] Biomedical developments, in general, in neurology, in particular, are focusing on few-layer graphene sheets to manufacture novel biodevices, including biosensors, interfaces, tissue scaffolds, drug delivery, and gene therapy vector systems.[4] The successful design of multifunctional graphene-based neurodevices will expose brain cells and neuronal circuits directly to this material by injection or implantation.[4,7] In this context, the exploration of the interactions between graphene nano- and microsheets with the sophisticated signaling machinery of nerve cells, with a particular focus on potential graphene flake interactions with the hydrophobic membrane domains, is of great importance.[1,8,9] Such interactions may favor graphene translocation or adhesion to cell membranes,[8,10] potentially interfering with exquisite membrane activities, such as the exocytic and endocytic trafficking systems, which are crucial to physiological synaptic transmission.[8,11]

Here, we explore by patch clamp and fluorescence imaging the ability of graphene (GR) and graphene oxide (GO) nanosheets to interfere with synaptic signaling once hippocampal cultured neurons are exposed for 1 week to a growth medium containing thin sheets of such materials at 1 or 10 μg/mL (concentrations reported not to induce cell death[12−14]). We further investigated whether, in the absence of explicit cell toxicity, such materials affected the ability of astrocytes to release synaptic-like microvesicles[15] (MVs) in pure glial cultures. Our results describe the potential of GO nanosheets to alter different modes of interneuronal communication systems in the central nervous system (CNS), hinting at

Received: January 7, 2016
Accepted: March 31, 2016
Published: March 31, 2016

DOI: 10.1021/acsnano.6b00130
ACS Nano 2016, 10, 4459−4471

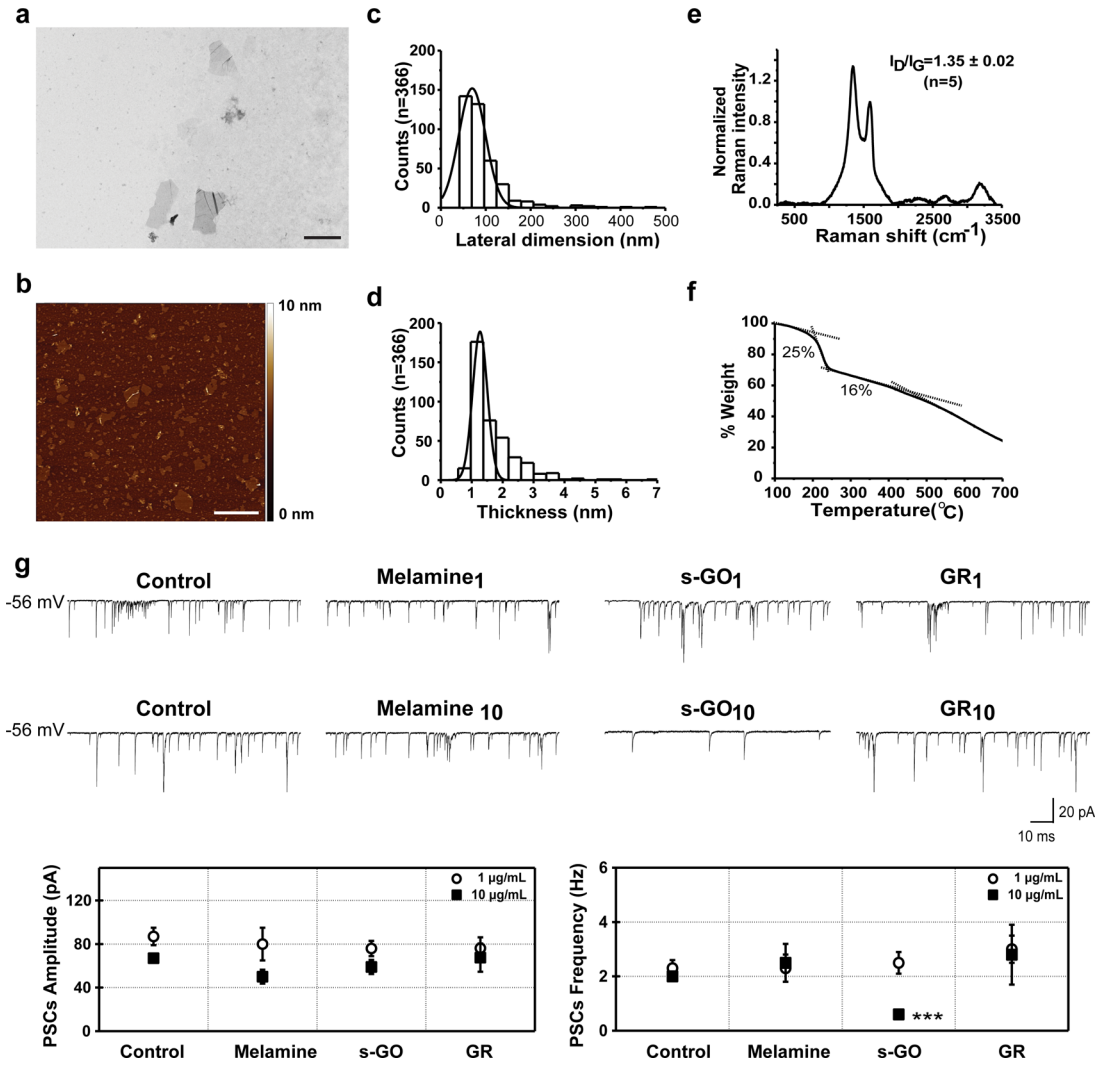

Figure 1. Characterization of small graphene oxide (s-GO) of biological grade; graphene oxide exposure at high concentration influences synaptic function. (a–f) Physicochemical characterization of s-GO: (a) TEM micrograph (scale bar 1 μm), (b) AFM height image (scale bar 1 μm), (c) lateral dimension distribution, and (d) thickness distribution analysis; (e) normalized Raman spectrum and (f) TGA analysis. (g) Graphene oxide exposure at high concentration influences synaptic function. Spontaneous synaptic activity recorded from hippocampal cultures in control, melamine, s-GO, and GR-treated cultures at 1 μg/mL (top traces) and 10 μg/mL (bottom traces) grown for 8–10 days *in vitro*. Postsynaptic currents (PSCs) were detected at −56 mV holding potential. Bottom plots represent pooled data and summarize average PSC amplitude and frequency; note the reduction in s-GO treatment (10 μg/mL, final concentration) of PSC frequency (* = $P < 0.001$ Student's *t* test; data are mean ± SEM).**

opportunities for neuromodulatory applications or highlighting subtle, but potentially unwanted, subcellular interactions.

RESULTS AND DISCUSSION

To address the issue of prolonged exposure of a functional brain network to graphene sheets, we used different materials. Graphene oxide sheets of large and small lateral dimensions (l-GO and s-GO, respectively) were synthesized using a modified Hummers method (see Methods). Following the reaction, the GO gel-like top layer was extracted carefully by using warm water, resulting in the large GO (l-GO). Final concentrations ranging between 1 and 2 mg/mL were obtained with a yield of *ca.* 10%. l-GO was freeze-dried, reconstituted in water for injection, sonicated for 5 min, and centrifuged at room temperature to generate the small GO (s-GO).The lateral dimension of the GO sheets was controlled by drying and sonicating the l-GO to obtain the s-GO sheets, which were always at least 1 order of magnitude smaller, without introducing any significant changes among their surface properties (see Table S1 in the Supporting Information).

The GO dispersions in aqueous media were homogeneous, of brownish color, and stable at room temperature for more than 6 months. The physicochemical characterization of the l-GO and s-GO dispersions is shown in Figure 1a–f and in the Supporting Information Figures S1 and S2. The structural properties (lateral dimension and thickness) were studied by optical microscopy, transmission electron microscopy (TEM), and atomic force microscopy (AFM). Optical properties were studied by UV–vis and fluorescence spectroscopy. Raman spectroscopy and laser Doppler electrophoresis (measuring ζ-potential) were used to assess the surface properties of the GO materials. The Raman spectroscopic analysis revealed D and G bands at 1319 and 1596 cm^{-1}, respectively, characteristic of most polyaromatic hydrocarbons. The D to G band intensity ratio (I_D/I_G) was calculated to be 1.3, corresponding to the metric of disorder in the graphitic structure. The surface charge

DOI: 10.1021/acsnano.6b00130
ACS Nano 2016, 10, 4459–4471

measured with a Zetasizer instrument showed an average ζ-potential of −50 mV, indicating flakes of high negative surface charge. To elucidate the degree of surface functionalization, thermogravimetric analysis (TGA) and X-ray photoelectron spectroscopy (XPS) were performed to quantify the purity of the GO (>99%) and the C/O ratio. XPS high-resolution C 1s spectra were recorded to elucidate the contribution of individual functional groups such as carboxylic, carbonyl, epoxide, and hydroxyl (Table S2b). All fittings shown were performed using the CasaXPS software, and the different regions were assigned according to NIST's XPS and lasurface databases. Deconvolution XPS spectra and assignment of the functional groups indicated that hydroxyls were the least abundant species in the GO material (see Supporting Information Table S2a).

Aqueous dispersions of graphene flakes were prepared using ball-milling for the exfoliation of graphite through interaction with melamine, as previously described[16,17] (see Methods). Due to the GR preparation process, graphene dispersions can contain traces of melamine. In order to determine the exact amount of these traces, final graphene dispersions (0.09 mg/mL) were evaluated by elemental analysis, which indicated 0.9 ppm of melamine. Experiments that involved incubation in neurons also included controls exposed to equal amounts of melamine alone (see Methods). The physicochemical characterization of GR dispersions is shown in Figure S3. The lateral size, studied by TEM, was found to range between 500 nm and 3 μm (Figure S3a,b in the Supporting Information). Optical properties were studied by UV−vis absorption spectroscopy. Dispersions were diluted, and the respective UV−vis absorption spectra were recorded (Figure S3). The spectra are featureless in the vis−NIR region, as expected. The absorbance at 660 nm, divided by cell length, is plotted against the concentration, exhibiting Lambert−Beer behavior (Figure S3d). Raman spectroscopy revealed differences between the GO and GR. Graphene exhibits G and 2D modes around 1573 and 2700 cm^{-1} that satisfy Raman selection rules, while the D peak, around 1345 cm^{-1}, requires a defect for its activation (Figure S3e). The D to G band intensity ratio was calculated at different locations, giving a significantly low value (0.22) in comparison with that of GO. TGA was also used to quantify the functionalization degree of GR. The low weight loss observed in GR (7%) corroborated the low quantity of oxygen groups generated by the exfoliation process (Figure S3f).

We used hippocampal neurons isolated and cultured for 8−10 days *in vitro* (DIV). Primary neuronal cultures were incubated for 2 DIV in the presence of GR or s-GO (at 1 and 10 μg/mL; see Methods) and maintained for 6−8 days. Afterward, visually identified neurons were patch clamped under a voltage clamp. Hippocampal neuron maturation and viability were assessed using single-cell recordings (see Methods) to measure the cell passive membrane properties that are accepted indicators of neuronal health[18−20] that allowed comparison among the recorded cells. These parameters (membrane capacitance and input resistance) displayed similar values in all treatment conditions (summarized in Table 1).

To investigate synapse formation and activity after *in vitro* growth of neurons, we monitored the occurrence of spontaneous postsynaptic currents (PSCs). The appearance of PSCs provided clear evidence of functional synapse formation, and it is a widely accepted index of network efficacy.[21,22]

Table 1. Neuronal Passive Membrane Properties upon GR and s-GO Exposure (1 and 10 μg/mL, Respectively)

	capacitance (pF)	input resistance (MΩ)
$control_1$ (n = 24)	59 ± 4	976 ± 138
$melamine_1$ (n = 28)	46 ± 5	1036 ± 132
$s\text{-}GO_1$ (n = 27)	62 ± 8	876 ± 145
GR_1 (n = 30)	50 ± 5	1029 ± 161
$control_{10}$ (n = 20)	57 ± 7	744 ± 82
$melamine_{10}$ (n = 25)	72 ± 16	717 ± 106
$s\text{-}GO_{10}$ (n = 18)	67 ± 6	997 ± 156
GR_{10} (n = 25)	59 ± 18	1223 ± 501

Figure 1g shows representative current tracings of the recorded electrical activity. In neurons exposed to low (1 μg/mL) s-GO and GR, spontaneous synaptic activity was not affected. In fact, measured PSC amplitude and frequency in s-GO and GR (79 ± 7 pA, 2.5 ± 0.4 Hz, n = 27 and 77 ± 8 pA, 3 ± 0.5 Hz, n = 30, respectively) were comparable to the corresponding control and control−melamine values (87 ± 8 pA and 2.3 ± 0.3 Hz, control, n = 24; 80 ± 15 pA and 2.3 ± 0.5 Hz melamine n = 28; plots in Figure 1g). In all tests, cell parameters measured in melamine were comparable to those expressed by control neurons (Figure 1g, bottom plots), thus the impact on cells of such a contaminant at the estimated concentration is negligible.

When investigating the impact of higher graphene doses (10 μg/mL), we detected a significant difference (P < 0.001; Student's t test) in PSC frequency when comparing control neurons (2.0 ± 0.1 Hz control, n = 20) with s-GO-treated ones (0.6 ± 0.1 Hz, n = 18), while in melamine and GR, PSC frequency values remained unchanged (2.5 ± 0.7 Hz, n = 25 for melamine and 2.8 ± 1.1 Hz, n = 25 for GR). In all treatments studied, the amplitude values of the PSCs were never affected (data are summarized in Figure 1g plots). We further tested synaptic responses when neurons were treated (1 and 10 μg/mL) with a commercially available GO provided by an industrial partner (A-GO; Supporting Information and Figure S4). Similar reduction in PSC frequency (Figure S5) was detected that validated the observation that GO nanosheets, differently than GR flakes, specifically interfered with synapses in cultured neurons, regardless of the starting material.

The impact of 10 μg/mL s-GO on synaptic activity was not related to a decreased number of surviving neurons in the presence of s-GO. In fact, we determined the cellular composition of control and s-GO-treated hippocampal cultures using immunofluorescence markers[23] for astrocytes (GFAP) and neurons (β-tubulin III). We observed both β-tubulin III and GFAP immunoreactive cells in all growing conditions (Figure 2a), and both cell groups were represented in a comparable proportion in all treatment groups (quantified by measuring the cell density in Figure 2a; n = 13 visual field per condition, three different culture series). Thus, s-GO at higher concentrations specifically altered synapse formation and/or function without affecting cell survival or the global network size.

To gain more insight into such processes, we further investigated s-GO-treated (10 μg/mL) cultures. We specifically addressed the distribution of neuronal excitation by measuring the activity of small clusters of neurons with fluorescence calcium imaging.[23−25] On average, 7 ± 2 fluorescent neurons (n = 26 fields), stained with the membrane-permeable Ca^{2+} dye Fura-2-AM (see Methods), were simultaneously visualized in

DOI: 10.1021/acsnano.6b00130
ACS Nano 2016, 10, 4459−4471

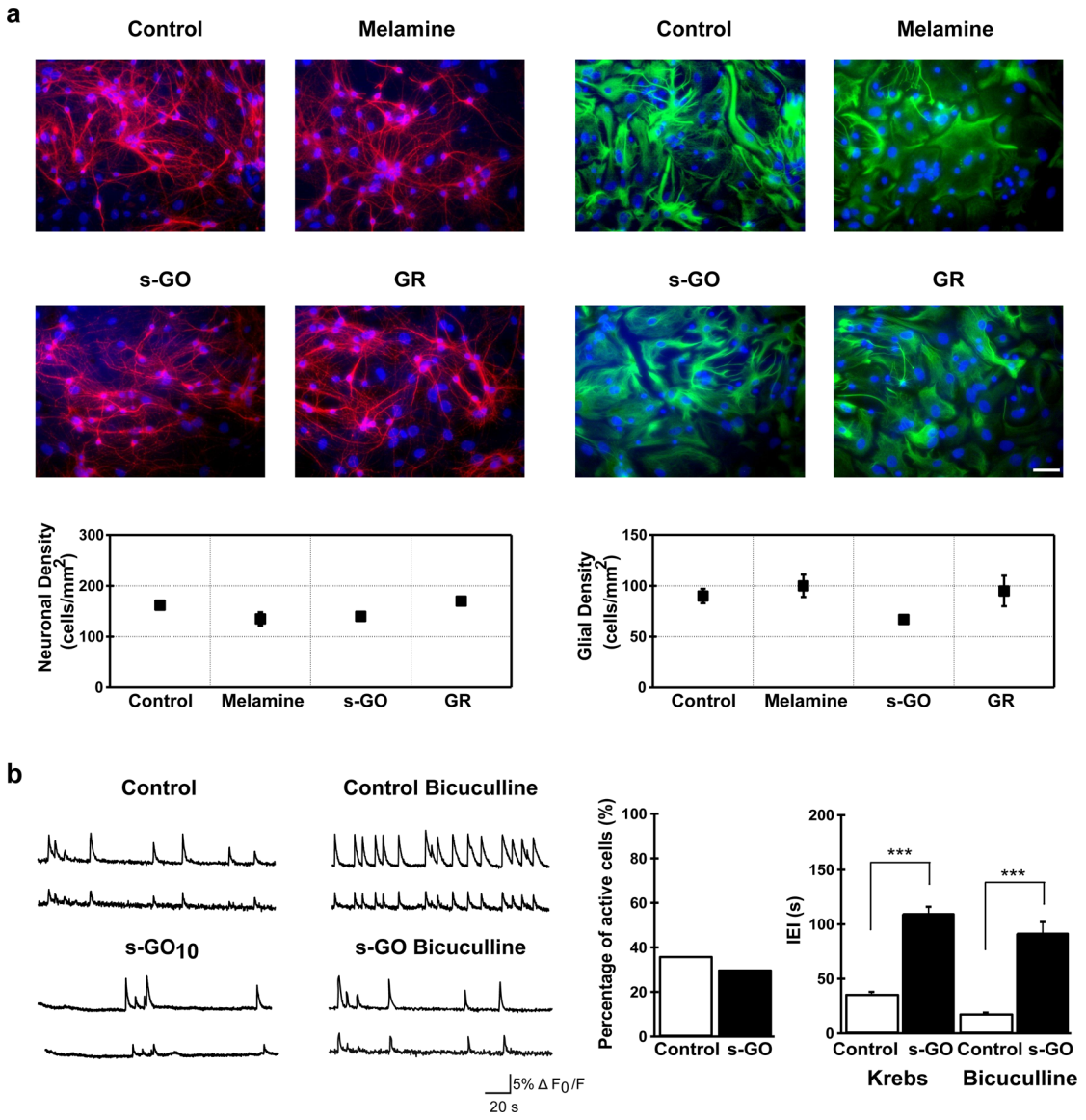

Figure 2. s-GO exposure at high concentration impaired network activity without changing network size. (a) Immunofluorescence images are shown to visualize neurons and glial cells in four different conditions (anti-β-tubulin III, in red, left panels; anti-GFAP, in green, right panels; in all, nuclei are visualized by DAPI in blue) (samples are for the 10 μg/mL protocol; scale bar 50 μm). The plots summarize neuronal (left) and glial (right) densities in all conditions. (b) Repetitive spontaneous Ca^{2+} (left panel) or bicuculline-induced (right panel) oscillations recorded in hippocampal cultures at 8−10 DIV (from each field sample, recordings of two cells were selected). Histograms summarize the percentage of spontaneous active cells (middle) and the average values of the interevent interval (IEI; right) in standard saline (Krebs) and in the presence of bicuculline (* = $P < 0.001$ Student's t test; data are mean ± SEM).**

the recorded field (120 × 160 μm^2). We compared and characterized the cell ability to generate repetitive Ca^{2+} oscillations.[23−25] In control conditions, all recorded fields (n = 8) displayed active cells, while in s-GO-treated cells, 56% (n = 10 out of 18) of the recorded fields did not display detectable cell activity. However, in the remaining s-GO fields (n = 8), we found an amount of neurons that were spontaneously generating repetitive Ca^{2+} oscillations comparable to that measured in controls (Figure 2b; 36% in control, 20 out of 56 neurons, n = 8 active fields and 30% in s-GO-treated, 18 out of 60 neurons, n = 8 active fields).

Figure 2b traces represent fluorescence recordings from active fields in control and s-GO-treated cultures (two sampled cells in each field). Episodes usually comprised spontaneous bursts of activity, fully blocked by tetrodotoxin (TTX, a blocker of voltage-gated, fast Na^+ channels) applications (1 μM; n = 8 fields, control and s-GO-treated; not shown). Control Ca^{2+} oscillations displayed an interevent interval (IEI) of 36 ± 2 s (n = 20 cells) that was significantly lower ($P < 0.001$; Student's t test) than that measured in s-GO-treated networks (110 ± 6 s, n = 18 cells, right plot in Figure 2b). When $GABA_A$ receptors were pharmacologically blocked by bicuculline (20 μM, 20 min), an antagonist of inhibitory connections known to potentiate rhythmic activity patterns,[23,26,27] the control IEI average value was still significantly lower ($P < 0.001$; Student's t test) than that measured in s-GO neurons in the presence of the $GABA_A$ receptor antagonist (18 ± 1 s, n = 20 in control cells *vs* 92 ± 10 s, n = 18 in s-GO cells; plot in Figure 2b, right). This indicated a direct reduction in the excitatory activity due to s-GO exposure.

DOI: 10.1021/acsnano.6b00130
ACS Nano 2016, 10, 4459−4471

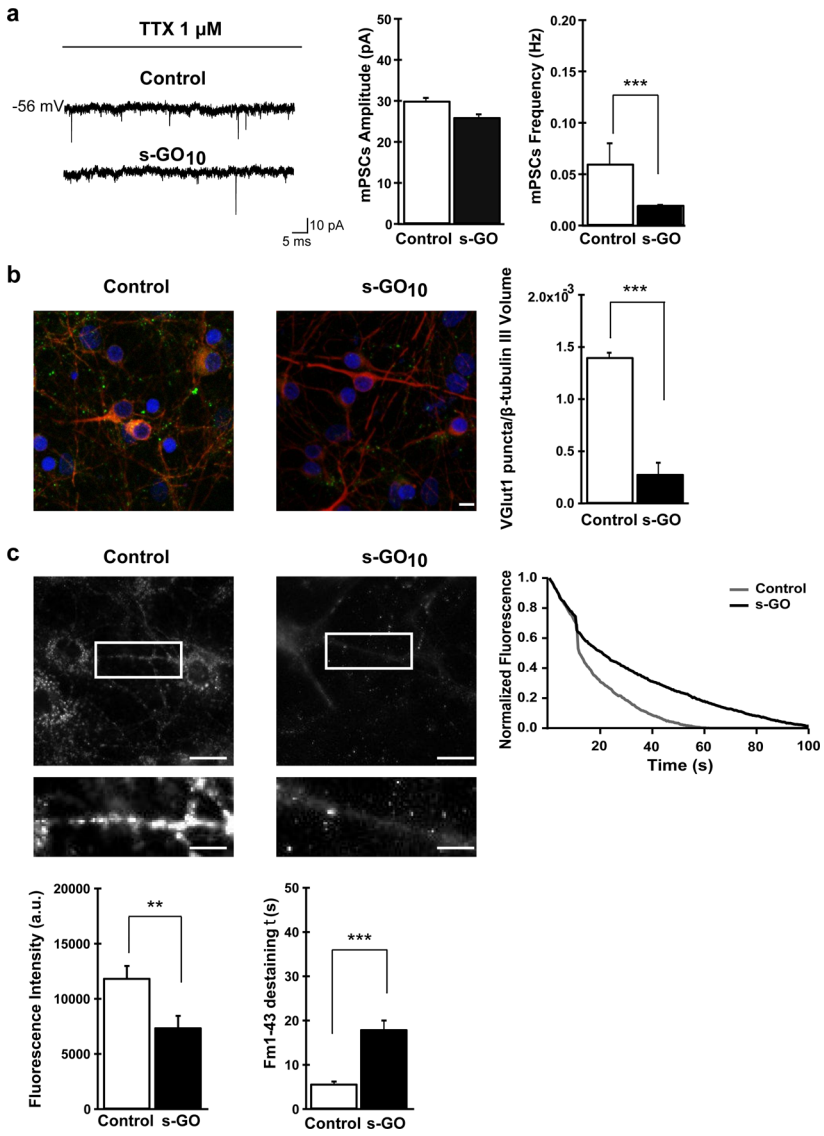

Figure 3. s-GO exposure at high concentration impaired excitatory synapses. (a) Sample tracings of mPSCs recorded in control and s-GO-treated cultures (left panel). Right panel: plots reporting mPSC amplitude and frequency values. s-GO treatment significantly decreased the frequency of mPSCs (* = $P < 0.001$ Student's t test). (b) Confocal reconstruction of control and s-GO-treated neurons immunolabeled for the vesicular glutamate transporter 1 (VGLUT1, green) and counterstained for cytoskeletal component β- tubulin III (red; nuclei are visualized by DAPI in blue; scale bar 10 μm). The plot shows the significant decrease of VGLUT1-positive puncta in s-GO-treated cultures (*** = $P < 0.001$ Student's t test). (c) Top: fluorescence images following staining with FM1-43, control, and s-GO-treated. Scale bar 50 μm. The areas in the boxes are higher magnifications to highlight the difference in vesicular staining between the two conditions (scale bar 100 μm). The plot (top right) reproduces the representative (control and s-GO) traces of FM1-43 destaining (please note that each trace has been normalized to the maximum fluorescence detected). Bottom: left plot summarizes the initial raw fluorescent intensities of hippocampal terminals from control and s-GO-treated cultures (** = $P < 0.01$ Mann–Whitney test); the right plot summarizes the decay time constant τ of FM1-43 destaining in the two conditions (*** = $P < 0.001$, Mann–Whitney test).**

Next, we recorded single-cell synaptic activity in the presence of TTX (1 μM, Figure 3a). Under these experimental conditions, synaptic currents, termed miniature PSCs (mPSCs), do not depend on action potential generation. mPSCs are due to the stochastic fusion of neurotransmitter vesicles at the presynaptic membrane, and their frequency is proportional to the number of synaptic contacts.[28] Despite the fact that in the recorded hippocampal neurons spontaneous synaptic activity was manifested as inward currents (in our recording conditions, see Methods[21]) made up by a mixed population of inhibitory ($GABA_A$ receptor-mediated) and excitatory (AMPA glutamate receptor-mediated) PSCs, virtually all mPSCs, as previously reported,[22] were identified as excitatory by their fast kinetics (decay time constant $\tau = 4 \pm 0.3$ ms; see Methods[22]). Notably, s-GO significantly decreased ($P < 0.001$, Student's t test; see plots in Figure 3a) the frequency of mPSCs without affecting their amplitude (0.06 ± 0.02 Hz and 30 ± 0.7 pA, control, $n = 15$; 0.02 ± 0.001 Hz and 26 ± 0.7 pA, s-GO-treated, $n = 9$; summarized in Figure 3a). To ascertain whether the s-GO interference with synaptic activity was selective on glutamate-mediated fast synaptic transmission, we tested the occurrence of evoked inhibitory PSCs by pair recordings of monosynaptically coupled neurons[22] (Methods and Figure S6a), and we observed that s-GO apparently did not impair $GABA_A$-mediated connections.

DOI: 10.1021/acsnano.6b00130
ACS Nano 2016, 10, 4459–4471

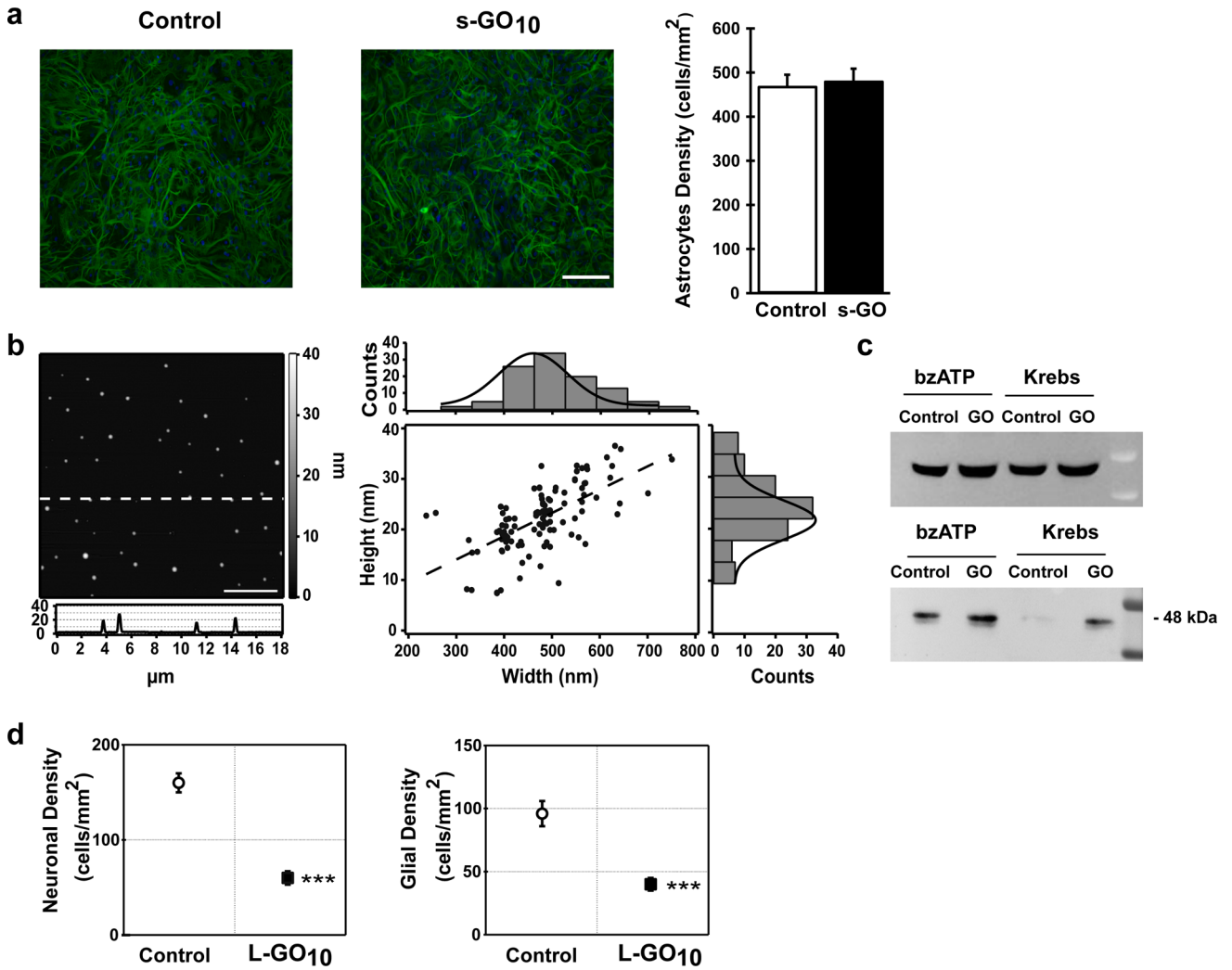

Figure 4. s-GO exposure and microvesicle release in glial cells. (a) Immunolabeling of primary rat astrocytes (3 weeks) in control and s-GO-treated cells (10 μg/mL, 6−8 days). Both cultures were immunostained for GFAP (green) and nuclei visualized by DAPI (blue; scale bar 100 μm). No statistical significance was found between the two conditions (top right). (b) AFM image of fixed MVs, where the differences in color are representative of height differences (brighter means higher). A representative height profile crossing three MVs is reported. The scatter plot (right) shows MV width *versus* height distribution and is fitted with a regression line represented by the equation $y = 0.046x + 0.218$. A frequency histogram, built upon experimental measurements of both width and height, was plotted over each axis of the scatter graph and fitted with Gaussian distributions. The frequency histograms revealed the highest number of occurrences to be about 490 and 24 nm for width and height, respectively. (c) Western blotting of the pellets (bottom row) and cell lysates (top row) for the MV marker flotillin-1. Pellets were obtained from the medium of glial cultures treated or untreated with s-GO under two different conditions: stimulated and not stimulated (Krebs) by 100 μM bzATP. Note the marked increase of the band for flotillin-1 in s-GO-treated cells. (d) Plots summarizing the decreased density of hippocampal cells when treated with l-GO (~10 μm lateral size; 10 μg/mL final concentration).

To determine whether changes in excitatory synaptic density may account for the reduction in fast mPSC frequency detected in s-GO-treated cultures, neurons were co-immunostained for β-tubulin III and the vesicular glutamate transporter (VGLUT1), a transmembrane protein localized at the glutamatergic presynaptic terminals.[29] Antibody to VGLUT1 labeled presynaptic boutons under both conditions (Figure 3b). Using β-tubulin III labeling to identify neuronal bodies and dendrites, we quantified VGLUT1-positive puncta, detecting a significant ($P < 0.001$; Student's t test) reduction in their density in s-GO-treated samples ($1.4 \times 10^{-3} \pm 0.045 \times 10^{-3}$, $n = 6$ fields for control and $0.28 \times 10^{-3} \pm 0.11 \times 10^{-3}$, $n = 6$ fields for s-GO; plot in Figure 3b). Parallel experiments were performed to quantify GABAergic synapses, by similar co-staining but for the vesicular GABA transporter (VGAT) to localize presynaptic GABAergic terminals.[22,30] These studies indicated that s-GO incubation did not alter the inhibitory connection density (Supporting Information and Figure S6b).

In the next set of experiments, we measured the kinetics of synaptic vesicle release by real-time imaging of vesicles labeled with FM dye to monitor the rate of presynaptic vesicle recycling from hippocampal neurons treated or untreated with s-GO. After being stained with the lipophilic dye FM1-43,[31−33] clusters of presynaptic terminals were visible as bright fluorescent spots (Figure 3c). The fluorescence intensity measured on FM-positive puncta following high KCl (50 mM[34]) depolarization is proportional to the number of vesicles endocytosed during synaptic vesicle recycling and thus allows estimation of the size of the recycling vesicle pool.[34] In s-GO-treated cells, upon a high-K^+-loading protocol, we detected a significant ($P < 0.01$; Mann−Whitney test) reduction in the raw fluorescence intensity of FM1-43-positive hippocampal

DOI: 10.1021/acsnano.6b00130
ACS Nano 2016, 10, 4459−4471

terminals (11876 ± 1100 arbitrary units (au), n = 7 fields for control and 7400 ± 1057 au, n = 6 fields for s-GO; three different culture series; Figure 3c), suggesting that chronic incubation with s-GO decreased the recycling vesicle pool. When analyzing the decay time constant (τ) of the FM1-43 fluorescence destaining profiles during vesicle exocytosis, we observed a significant (P < 0.001; Mann−Whitney test) difference in the kinetics displayed by control (τ = 5.7 ± 0.5 s, n = 205 terminals) and s-GO-treated (τ = 18 ± 2 s, n = 85 terminals) cells, as summarized in Figure 3c. In reference experiments, the image series captured on FM1-43-stained cells, but without the high-K^+ destaining stimulus, produced a baseline reference plot (not shown). Taken together, these results support the specific ability of chronic exposure to s-GO flakes to reduce the amount of excitatory synaptic contacts and to interfere with presynaptic vesicle recycling.

To test the ability of s-GO to impair cell membrane dynamics, in general, we investigated whether s-GO (10 μg/mL) was also reducing exocytosis and recycling of synaptic-like microvesicles[15] from cultured primary glial cells (see Methods). MVs are released into the extracellular space by direct budding from the plasma membrane of astrocytes and have been shown to contribute to intercellular communication.[15,35,36] We treated pure glial cell cultures with s-GO (10 μg/mL) for 6−8 days. In Figure 4a, immunofluorescence staining of control and s-GO-treated GFAP-positive cells are shown. s-GO incubation did not affect astrocyte density (Figure 4a, right histograms; n = 20 fields for both conditions), excluding any cytotoxic effect. In glial cultures, MV release was induced by bzATP incubation (100 μM, 30 min, n = 3 different series of cultures[37−39]), and MV release was detected and quantified by immunoblot analysis of the collected supernatant. In control, bzATP stimulation induced the appearance of the band corresponding to flotillin-1 (Figure 4c, bottom blot), a signature of MV release.[40−42] Surprisingly, in s-GO-treated astrocytes, the bzATP stimulation induced a marked increase in the size of the flotillin-1 band. This band was also detected in the absence of stimulation (Figure 4c, bottom blot), suggesting that s-GO *per se* induced the MVs' constitutive release.

AFM micrographs in Figure 4b (left panel) show the presence of vesicles in the stimulated control supernatant appearing as circular spots protruding from the ultraflat mica surface. For each of them, width and height were independently measured from particle crossing height profiles, and the resulting distributions were plotted (Figure 4b, right panel). Intriguingly, similar experiments with GR (10 μg/mL) did not induce shedding of MVs in glial cell cultures (Supporting Information and Figure S7).

We also attempted to investigate the effect of increased lateral size of GO (l-GO, with a lateral dimension in the few micromter range; 10 μg/mL final concentration) on cultured hippocampal cells. However, after 6−8 days of incubation, we measured a significant (P < 0.001; Student's t test; Figure 4d) reduction in both neuron and glial cell densities (160 ± 10 neurons/mm^2 and 96 ± 10 astrocytes/mm^2 for control and 96 ± 10 neurons/mm^2 and 40 ± 7 astrocytes/mm^2 for l-GO; n = 10 visual fields each, three series of cultures; Figure 4d), indicating cell toxicity that prevented any further functional measurements. We believe further investigations are warranted to explore such lateral size-dependent cytotoxic responses.

We report here the ability of s-GO nanosheets to interfere specifically with neuronal synapses, without affecting cell viability. In particular, in cultured neuronal networks, upon chronic s-GO exposure, glutamatergic release sites were sized down. This was shown by (i) the reduction in frequency of spontaneous synaptic activity (PSCs and mPSCs) together with the marked reduction in VGLUT1-positive labeling,[43] (ii) the reduced probability of finding active neurons when networks were explored by Ca^{2+} imaging,[23,44] and (iii) the decreased recycle vesicle pool quantified by FM1-43 measurements together with the altered kinetics of vesicle recycling.[34] This down-regulation of glutamate-mediated synapses was apparently not due to a general cell membrane disruption or to neuronal cell loss. In fact, we never detected alterations in basic electrophysiological parameters, reflecting neuronal health and membrane integrity.[18−20]

In addition, cell densities in treated cultures were comparable to control ones. The survival of GFAP-positive glial cells was also not affected by s-GO exposure, both in mixed neuronal and in pure neuroglial cultures. In the latter condition, MV release was indirectly monitored by the blot analysis of flotillin-1 protein,[40,41] and MV presence was confirmed by direct AFM measures. In these cultures, exposure to s-GO stimulated the basal release of shed vesicles and augmented the bzATP-induced one.[37−39] s-GO increase in MV release from neuroglia cells might be related to a general cell-stress condition[15] ultimately due to s-GO glial−membrane interactions or even internalization, depending on the flakes' shape, lateral dimension, and oxidization degree,[10] as well as the degree of protein adsorption from the culturing milieu.[45]

Based on our experimental evidence, we cannot rule out that treatment with s-GO down-regulated the synaptic function (in particular, presynaptic release) *via* MVs released in mixed neuronal−glial cultures, thus excluding a direct, membrane interference of s-GO nanosheets at the presynaptic glutamatergic terminals. MVs have long been reported as active messengers of intercellular communication, rather than mere inert debris;[37] however, to our knowledge, there are no reports of astrocyte shedding MVs acting as regulators of synaptic activity. On the contrary, MVs released by microglia have been reported to affect synaptic activity, mainly acting at the presynaptic site of the excitatory synapses, but increasing synaptic activity and release in primary cultures.[37] Against this neuroglial cell-mediated response to s-GO is also the fact that astrocyte density in mixed cultures is artificially kept at a low level by the culturing procedure itself, while the surviving microglia are even fewer.[46]

In contrast to s-GO, the inert nature of GR flakes regarding synaptic activity and MV release by glia is also of interest. This could be due to differences in shape and lateral size affecting flake−membrane interactions.[10] It is also interesting to consider that GR has a much less hydrophilic surface characteristic and overall poorer dispersibility in cell culture media[45] that may lead to the formation of aggregates potentially unable to interact with submicroscopic structures (such as the synaptic clefts).

The apparent selectivity in terms of the presynaptic terminals targeted by s-GO was also notable, with the inhibitory GABAergic ones that remained unaffected, as evidenced by pair recordings and the VGAT labeling.[22] Given the ability of graphene flakes to undergo motion and vibration that can lead to interaction with and possible piercing of lipid bilayers,[8] we propose an alternative mechanistic interpretation of our synaptic results. s-GO flakes may prevent the synaptic vesicle endocytotic cycle because their dimensions allow them to interact with the presynaptic cell membrane at the periphery of

DOI: 10.1021/acsnano.6b00130
ACS Nano 2016, 10, 4459−4471

the synaptic cleft and then be taken up by vesicles. In this process, the flakes may transiently trap vesicles in an open mode and prevent their closing and the subsequent endocytosis. This could affect synaptic release in the short term, inducing, in the long term, a down-regulation of glutamatergic release sites and synapses. Note that glutamatergic synaptic activity is specifically, and reversibly, affected also when neurons are transiently exposed to s-GO, with a short-term up-regulation of release, turned into a down-regulation within the first 3 days of chronic exposure (Figure S8 in Supporting Information). This observation further supports the hypothesis of the ability of s-GO to directly target synapses. The mechanism of such interaction among s-GO flakes and vesicles (including extra-synaptic ones) could be similar to what has been previously described for dispersed single-walled carbon nanotubes.[47] In this context, the unlikeliness of affecting GABAergic terminals may reside in the different dimensions of the excitatory (16 nm) and inhibitory (10 nm) synaptic clefts.[48] The latter are reported to be narrowed to 6 nm at the periphery of the clefts due to transcleft elements, while docked vesicles are concentrated at the central cleft domain.[48] On the contrary, docked vesicles in excitatory synapses are distributed evenly over the synaptic cleft.[48] It is tempting to speculate that these synaptic ultrastructural differences might explain why glutamatergic terminals became ideal targets of s-GO interactions. This selectivity is supported by the notion that, even when transiently exposed to s-GO *via* pressure-ejected brief pulses, GABAergic synapses are unaffected (see Supporting Information and Figure S8).

CONCLUSIONS

Regardless of the mechanisms involved, the described ability of s-GO to alter synapses and induce glial cell reaction has not been previously documented. This might compromise neuronal signaling and CNS functions and seems crucially dependent on the GO sheet dimensions since larger flakes were found unequivocally cytotoxic. In our experiments, 6 days of exposure of cultures to equal amounts of dispersed l-GO induced unequivocal hippocampal cell loss, both neuroglia and neurons, thus hampering any further evaluation of membrane/flake interactions.

These observations deserve further studies; in fact, altering synapses and inducing glia reactivity may raise concerns from a safety and nanotoxicity point of view.[49]

Beyond the safe design of nanomaterials, such a subtle interference affecting exquisite CNS signaling may offer possibilities in neuropharmacology when specific targeting of excitatory synapses is desired.[50−52] The use of nanoparticles as therapeutics is, in fact, fueled by their ability to circumvent biological barriers,[53] and targeting of synapses has created the basis for theranostics applications.[54] Our observations with thin s-GO flakes illustrate the potential of 2D nanosheet physical properties to engineer specific glutamate transmission modulators.

It is also relevant to note that synapse formation and function in neuronal networks, when interfaced to planar graphene-based materials, are not affected.[55] This strengthens the notion that when exploring the application of graphene in biology, studies should be performed with well-characterized types of materials because the materials' physical−chemical features, including geometry, are governing the potential interactions with specific biological components.[2]

METHODS

Synthesis and Characterization of Biological-Grade Thin Graphene Oxide of Different Lateral Size Distribution. For graphene oxide preparation, graphite flakes (Graflake 9580) were obtained from Nacional Grafite Ltd. (Brazil) and used for the preparation of large and small graphene oxide. Nitric acid 70%, sodium nitrate, potassium permanganate, sulfuric acid 99.999%, and hydrogen peroxide 30% were purchased from Sigma-Aldrich. Water for injection was obtained from Fresenius Kabi.

Graphene oxide sheets were synthesized using the modified Hummers method previously described[56] and under endotoxin-free conditions by using a laminar flow hood, water for injection, gloves, nonpyrogenic plastic containers, and depyrogenated glassware.[57] Briefly, 0.8 g of graphite flakes was mixed with 0.4 g of sodium nitrate in a round-bottom flask, and then 18.4 mL of sulfuric acid 99.999% was added slowly to the mixture. After a homogenized mixture was obtained, 2.4 g of potassium permanganate was slowly added and the mixture was maintained for 30 min. Next, 37 mL of water for injection was added dropwise due to the violent exothermic reaction, and the temperature was continuously monitored and kept at 98 °C for 30 min. The mixture was further diluted with 112 mL of water for injection, and 30% hydrogen peroxide was added for the reduction of the residual potassium permanganate, manganese dioxide, and manganese heptoxide to soluble manganese sulfate salts. The resulting mixture was purified by several centrifugation steps at 9000 rpm for 20 min until a viscous orange/brown layer of pure GO started to appear on top of the oxidation byproducts at neutral pH.[58]

This GO gel-like layer was extracted carefully with warm water, resulting in the large GO. Final concentrations ranging between 1 and 2 mg/mL were obtained with a yield of *ca.* 10%. l-GO was freeze-dried, reconstituted in water for injection, sonicated in a bath sonicator (VWR, 80W) for 5 min, and centrifuged at 13 000 rpm for 5 min at room temperature to prepare the s-GO. Structural properties such as lateral dimension and thickness of the GO materials have been studied by optical microscopy, TEM, and AFM. Optical properties such as absorbance and fluorescence have been studied by using UV−vis and fluorescence spectroscopy, respectively. Surface properties have also been studied by Raman spectroscopy and ζ-potential measurements. To elucidate the functionalization degree of the GO sheets, TGA was performed. X-ray photoelectron spectroscopy has been used to quantify the chemical composition of the GO sheets, C/O ratio, and the contribution of each individual functional group such as carboxylic, carbonyl, and epoxides.

Optical Microscopy. Bright-field microscopy using a Zeiss Primovert microscope was used to assess the lateral dimension distribution of the l-GO and to verify the size reduction of the s-GO.

Transmission Electron Microscopy. TEM was performed using a FEI Tecnai 12 Biotwin microscope (FEI, The Netherlands) at an acceleration voltage of 100 kV. Images were taken with Gatan Orius SC1000 CCD camera (GATAN, UK). One drop of sample was placed on a Formvar/carbon-coated copper grid. Filter paper was used to remove the excess material.

Atomic Force Microscopy. A multimode AFM was used on the tapping-mode with a J-type scanner, Nanoscope V8 controller (Veeco, Cambridge, UK), and an OTESPA silicon probe (Bruker, UK). Images were taken in air by depositing 20 μL of 100 μg/mL of GO on a freshly cleaved mica surface (Agar Scientific, Essex, UK) coated with poly-L-lysine 0.01% (Sigma-Aldrich, UK) and allowed to adsorb for 5 min. Excess unbound material was removed by washing with Milli-Q water and then allowed to dry in air; this step was repeated once. Lateral dimension and thickness distributions of GO were carried out using NanoScope Analysis software (version 1.40 Bruker, UK).

UV/Visible Spectroscopy. UV/visible absorbance spectra were obtained for GO samples from 7.5 to 20 μg/mL using a Varian Cary winUV 50 Bio spectrophotometer. Dual beam mode and baseline correction were used throughout the measurements to scan the peak wavelength and maximum absorbance between 200 and 800 nm.

Fluorescence Spectroscopy. Fluorescence emission spectroscopy was performed for GO samples from 75 to 200 μg/mL using a LS-50B

DOI: 10.1021/acsnano.6b00130
ACS Nano 2016, 10, 4459−4471

PerkinElmer spectrofluorimeter at the excitation wavelength of 525 nm, with both excitation and emission slits set at 20.

Raman Spectroscopy. Raman spectra were recorded for GO (20 μL of 100 μg/mL) on glass slides after complete evaporation of the water. Measurements were carried out using a 50× objective at 633 nm laser excitation using a micro-Raman spectrometer (ThermoScientific, UK). An average of five different locations within each sample was measured to calculate the I_D/I_G ratio.

Zeta-Potential Measurements. Electrophoretic mobility (μ) was measured by Malvern Zetasizer Nano ZS (UK) after dilution of samples with water in disposable Zetasizer cuvettes (Malvern Instruments). Default instrument settings and automatic analysis were used for all measurements, where the μ was converted automatically by the equipment software to zeta-potential (ζ) values as it is directly related to ζ-potential by Henry's equation. All values for samples prepared are triplicate measurements, and values were mean ± SD.

Thermogravimetric Analysis. The weight loss of GO samples was performed by TGA using a Pyris 6, PerkinElmer Ltd. GO (1−2 mg) was weighed into a ceramic crucible and analyzed from 100 to 995 °C at 10 °C/min with a nitrogen flow of 20 mL/min.

X-ray Photoelectron Spectroscopy. The composition of GO surfaces was studied by XPS at the NEXUS facility (the UK's National EPSRC XPS Users' Service, hosted by nanoLAB in Newcastle-upon-Tyne). XPS was recorded using a Thermo Theta Probe XPS spectrometer with a monochromatic Al Kα source of 1486.68 eV. The survey XPS spectra were acquired with pass energy (PE) of 200 eV, 1 eV step size, 50 ms dwell time, and averaged over five scans. The etching was 90 s. High-resolution C 1s XPS spectra were acquired with PE of 40 eV, 0.1 eV step size, 100 ms dwell time, and averaged over 20 scans. Spectra from insulating samples have been charge-corrected by shifting all peaks to the adventitious carbon C 1s spectral component binding energy set to 284.6 eV. CasaXPS software was used to process the spectra acquired at NEXUS. For the deconvolution of the different components, the CasaXPS software was used and the different regions were assigned according to NIST's XPS and lasurface databases:

$\pi-\pi^*$: 290.9−289.7
O−C═O: 288.8−288.0 eV
C═O: 287.6−286.6 eV
C−O−C: 286.7−286.3 eV
C−OH: 285.9−285.3 eV
C−C and C═C: 284.6 eV

For graphite samples, the CasaXPS software was able to properly fit the hydroxyl component at 285.6 eV, but for graphene oxide samples, it was not possible to fit six components where we should expect to have the epoxide and hydroxyl contributions separately. The amount of hydroxyls in the graphene oxide samples depends on the degree of oxidation, with the hydroxyl groups being the least oxidized, followed by epoxide, carbonyl, and carboxylic groups (the latter being the most oxidized).

Synthesis and Characterization of Pristine Graphene. The pristine graphene flakes used in this study were obtained by a methodology[16] that uses mechanochemical activation by ball-milling to exfoliate graphite through interactions with melamine (2,4,6-triamine-1,3,5-triazine) in solvent-free conditions. In a typical experiment, 7.5 mg of graphite (purchased from Bay Carbon, Inc. SP-1 graphite powder) and 0.16 mmol of melamine were ball-milled in a Retch PM100 planetary mill at 100 rpm for 30 min in air atmosphere. The resulting solid mixtures were dispersed in 20 mL of water to produce stable black suspensions. The as-prepared dispersions can be filtered and washed in hot water to remove melamine. Graphene water dispersions were obtained with a final concentration of 0.09 mg/mL in Milli-Q water. Melamine traces in the dispersions were analyzed by elemental analysis (LECO CHNS-932, model no. 601-800-500), giving 0.9 ppm of melamine. For TEM analyses, water dispersions were placed on a copper grid (3.00 mm, 200 mesh, coated with carbon film), and samples were investigated by high-resolution transmission electron microscopy (HRTEM) on a JEOL 2100. Lateral dimension distribution was carried out using Fiji-win32. UV−vis−NIR absorbance was performed for GR samples from 2.4 to 14.2 μg/mL using a 1 cm quartz cuvettes on a Cary 5000 UV−vis−NIR spectrophotometer. For Raman spectroscopy, the water dispersions are drop-cast onto a silicon surface (Si-Mat silicon wafers, CZ). Measurements were carried out using a 100× objective at 532 nm laser excitation using a SENTERRA Raman microscope. An average I_D/I_G ratio was measured from different locations in the sample. Thermogravimetric analyses were performed with a TGA Q50 (TA Instruments) at 10 °C/min in a nitrogen atmosphere.

Commercially Sourced Graphene Oxide. The graphene oxide was prepared by stirring powdered carbon fibers (GANF helical-ribbon carbon nanofibers manufactured by the Grupo Antolin Ingeniería, GANF) and sodium nitrate in sulfuric acid at 0 °C. While vigorous agitation was maintained, potassium permanganate was added to the suspension. After 30 min, water was slowly stirred into the paste. Then, the suspension was filtered and rinsed with copious amounts of water to remove the presence of acids.[59] For TEM analyses, water dispersions were placed on a copper grid (3.00 mm, 200 mesh, coated with carbon film). Samples were investigated by HRTEM on a JEOL 2100. Lateral dimension distribution was carried out using Fiji-win32. UV−vis−NIR absorbance was performed for GO samples from 7.5 to 20 μg/mL using a 1 cm quartz cuvettes on a Cary 5000 UV−vis−NIR spectrophotometer. For Raman spectroscopy, the water dispersions were drop-cast onto a silicon surface (Si-Mat silicon wafers, CZ). Measurements were carried out using a 100× objective at 532 nm laser excitation using a SENTERRA Raman microscope. An average I_D/I_G ratio was measured from different locations in the sample. The thermogravimetric analyses were performed with a TGA Q50 (TA Instruments) at 10 °C/min in a nitrogen atmosphere.

Preparation of Primary Cultures. Primary hippocampal cultures were prepared from 2 to 3 days postnatal (P_2-P_3) rats as previously reported.[21,22,60] All procedures were approved by the local veterinary authorities and performed in accordance with the Italian law (decree 116/92) and the UE guidelines (86/609/CE, 2007/526/CE, and 2010/63/UE). The animal use was approved by the Italian Ministry of Health. All efforts were made to minimize suffering and to reduce the number of animals used. All chemicals were purchased by Sigma unless stated otherwise. Briefly, enzymatically dissociated hippocampal neurons[21,22,60] were plated on poly-L-ornithine-coated glass coverslips (Kindler, EU) at a density of 200 000 ± 16 000 cells/mL (measure by sampling n = 4 culture series). Cultures were incubated (37 °C, 5% CO_2) in medium consisting of either 1× MEM (Gibco) or 10× MEM (Gibco) to compensate the volume of the added GR and GO water dispersion when treating cells at higher flakes concentrations (*i.e.*, 10 μg/mL). In both cases, the MEM was supplemented to reach 35 mM glucose, 1 mM Apo-transferrin, 15 mM HEPES, 48 μM insulin, 3 μM biotin, 1 mM vitamin B12, 500 nM gentamicin, and 10% fetal bovine serum (FBS; Invitrogen). For experiments involving chronic treatments, cultures were incubated at 2 DIV, with a medium containing 1 or 10 μg/mL of GR, either s-GO and A-GO, or l-GO, and controls were subjected to the same medium changes with addition of equivalent volumes of Milli-Q water or melamine alone. Cultures were used at days 8−10 (after 6−8 days of incubation).

Primary cortical glial cultures were prepared from P_2-P_3 rats as described in Calegari *et al.*[61] Briefly, dissociated cells were plated into plastic 75 cm^2 flasks, incubated (37 °C; 5% CO_2) in culture medium consisting of DMEM (Gibco), supplemented with 10% FBS, 100 IU/mL penicillin, and 10 mg/mL streptomycin. At 21 DIV, GR or s-GO (10 μg/mL) was added to the culture medium and cultures were used after 6−8 days of incubation.

Electrophysiological Recordings. Single and paired whole-cell recordings were obtained at room temperature (RT) with pipettes (5−7 MΩ) containing (in mM) 120 K gluconate, 20 KCl, 10 HEPES, 10 EGTA, 2 $MgCl_2$, 2 Na_2ATP, pH 7.3; osmolarity was adjusted to 300 mOsm. The extracellular solution contained (in mM) 150 NaCl, 4 KCl, 1 $MgCl_2$, 2 $CaCl_2$, 1 $MgCl_2$, 10 HEPES, 10 glucose (all Sigma), pH 7.4. Coverslips with cultures were positioned in a Perspex chamber mounted on an inverted microscope (Eclipse TE-200, Nikon, Japan). Data were collected by Multiclamp 700B patch amplifier (Axon CNS, Molecular Devices) and digitized at 10 kHz with the pClamp 10.2

DOI: 10.1021/acsnano.6b00130
ACS Nano 2016, 10, 4459−4471

acquisition software (Molecular Devices LLC, USA). The spontaneous synaptic activity was recorded by clamping the membrane voltage at −56 mV holding potential (not corrected for liquid junction potential, which was 14 mV). In paired recordings, the presynaptic neuron was held under current clamp mode at −70 mV (≤0.02 nA negative current injection), and action potentials were elicited by injecting short (4 ms) square current pulses (1 nA). The postsynaptic cell was voltage clamped usually at −56 mV holding potential. Monosynaptic connections were recognized by their short latency (<5 ms[62]), measured between the peak of the evoked action potential and the onset of the postsynaptic current response. All recorded events were analyzed offline with the AxoGraph 1.4.4 (Axon Instrument) event detection software (Axon CNS, Molecular Devices).

Calcium Imaging. Cultures were loaded for 1 h at RT with cell-permeable Fura-2-AM (2 μM) in the extracellular recording solution supplemented with 0.5% bovine serum albumin. The Fura-2-loaded cultures were observed with a 40× objective (0.6 NA, Nikon, Japan), and recordings were performed from visual fields (120 × 160 μm^2) containing on average 7 ± 2 neurons. Prior to recording Ca^{2+} signals, we selected the cells by drawing regions of interest (ROI) around their bodies to reduce any background.[23] Samples were excited at wavelengths of 340 and 380 nm generated by a monochromator device equipped with integrated light source (Polychrome IV, Till Photonics). Excitation light was separated from the light emitted from the sample using a 395 nm dichroic mirror. Images of emitted fluorescence >510 nm were acquired continuously for a maximum of 2400 s (200 ms individual exposure time) by a cooled slow-scan interline transfer camera (IMAGO CCD camera; Till Photonics). The camera was operated on 8 × 8 pixel binning mode, and the imaging system was controlled by an integrating imaging software package (TILLvisION; Till Photonics). To induce rhythmic bursts, 20 μM bicuculline methiodide was bath-applied after 15 min recording;[23] at the end of each experiment, tetrodotoxin (1 μM; Latoxan) was applied to confirm the neuronal nature of the recorded signals.[23] Recorded images were analyzed offline by Clampfit software (pClamp suite, 10.2 version; Molecular Devices LLC, US) and Igor Pro software (6.32A version; WaveMetrics, Lake Oswego, Oregon, USA). Intracellular Ca^{2+} transients were expressed as fractional amplitude increase ($\Delta F/F_0$, where F_0 is the baseline fluorescence level and ΔF is the rise over the baseline); elevations in calcium level were considered significant if they exceeded 5 times the standard deviation of the noise. We then computed the difference between consecutive onset times to obtain the IEI. Hence, after the IEI values were obtained from each active cell in the field, data were pooled for all fields recorded under the same experimental conditions and averaged for further comparison.

FM1-43 Loading and Destaining. Depolarization-dependent staining of synaptic terminals with the styryl dye *N*-(3-triethylammoniumpropyl)-4-(4-(dibutylamino)styryl)pyridinium dibromide (FM1-43, Molecular Probes, Life Technology) was obtained by incubating cultures (after 10 min saline buffer wash at RT) for 120 s with 50 mM KCl and FM1-43 (15 μM). The buffer was replaced with 2 mL of normal saline containing FM1-43, and cells were left to recover for 10 min to ensure complete recycling of the vesicles[63] and then incubated for 10 min with saline containing 6-cyano-7-nitroquinoxaline-2,3-dione (10 μM) and 2-aminophosphonovaleric acid (50 μM) to prevent network activity altering the rate of FM release. These antagonists were present throughout the experiment. After incubation with FM1-43 dye, cultures were transferred to the stage of a Nikon Eclipse Ti−U inverted microscope equipped with a piezoelectric table (Nano-ZI Series 500 μm range, Mad City Laboratories), HBO 103 W/2 mercury short lamp (Osram, Munich, Germany), mirror unit (exciter filter BP 465−495 nm, dichroic 505 nm, emission filter BP 515−555), and electron multiplier CCD camera C9100-13 (Hamamatsu Photonics, Japan). Images were acquired with an oil-immersion Plan Apo 100× (1.4 NA, Nikon, Japan) objective at a sampling of 2 Hz with a spatial resolution of 256 × 256 pixels. All experiments were performed at RT. Application of 50 mM KCl (5 s), followed by a 2 min washout, was used to stimulate vesicle exocytosis from the dye-containing terminals, measured as a fluorescence loss. The imaging system was controlled by an integrating imaging software package (NIS Element, Nikon, Japan). Offline analysis was performed on the image sequence with the image-processing package Fiji.[64] After background subtraction, images were analyzed using rounded ROIs of 4 pixels in diameter drawn on neural processes. Endocytosed vesicles during FM1-43 loading were measured by estimating the brightness of the total vesicle pool puncta (raw fluorescence intensity) in GO-treated and untreated cultures before the unloading stimulus. The decay time constant, τ, was measured by pClamp 10.2 software (Molecular Devices LLC, USA). To avoid imaging nonselective FM staining, only puncta that showed stimulus-dependent destaining were included in the analyses.

Immunofluorescence Labeling. Hippocampal neurons or glial cells, treated and untreated, were fixed in PBS containing 4% PFA for 20 min at RT. Cells were permeabilized with 1% Triton X-100 for 30 min, blocked with 5% FBS in PBS for 30 min at RT, and incubated with primary antibodies for 30 min. The primary antibodies used were rabbit polyclonal anti-β-tubulin III (Sigma T2200, 1:250 dilution), mouse monoclonal anti-GFAP (Sigma-Aldrich, 1:500 dilution), and guinea pig polyclonal antivesicular glutamate transporter (Millipore AB5905, dilution 1:2000). After the primary incubation and PBS washes, neurons were incubated for 30 min with the secondary antibodies AlexaFluor 594 goat anti-rabbit (Invitrogen, dilution 1:500), AlexaFluor 488 goat anti-mouse (Invitrogen, dilution 1:500), AlexaFluor 488 goat anti-guinea pig (Invitrogen, dilution 1:500), and DAPI (Invitrogen, dilution 1:200) to stain the nuclei. Samples were mounted in Vectashield (Vector Laboratories) on 1 mm thick coverslips. Cell densities were quantified at 20× (0.5 NA) magnification using a DM6000 Leica microscope (Leica Microsystems GmbH, Wetzlar, Germany), with random sampling of seven to ten fields (713 × 532 μm; control and treated, n = 3 culture series). For VGLUT1-positive terminals, image acquisition was performed using a confocal microscope (Leica Microsystems GmbH, Wetzlar, Germany) with 63× (1.4 NA) magnification (*Z*-stacks were acquired every 300 nm; 12 fields for control and untreated conditions). Offline analysis was performed using Volocity software (Volocity 3D image analysis software, PerkinElmer, USA). For each set of experiments, the images were acquired using identical exposure settings. The ROIs for the quantification were blindly chosen using the tubulin channel. For each analyzed field, we used the *Z*-stacks to quantify VGLUT1 puncta as 3D objects. The resulting numbers were normalized to the relative cellular volume calculated on the basis of β-tubulin III labeling.

Micovesicle Isolation and Characterization. Microvesicle shedding was induced in 21 DIV confluent glial cells (after washing in PBS, 37 °C) upon exposure to benzoyl-ATP (bzATP; 100 μM) in Krebs−Ringer solution with the following composition: 125 mM NaCl, 5 mM KCl, 1.2 mM $MgSO_4$, 1.2 mM KH_2PO_4, 2 mM $CaCl_2$, 6 mM D-glucose, and 25 mM HEPES/NaOH (pH adjusted to 7.4), for 30 min at 37 °C and 5% CO_2.[39] MVs were pelleted by centrifugation as described in Bianco *et al.*[39] Negative controls were incubated with Krebs−Ringer solution without the presence of bzATP. MVs isolated from confluent mixed glial cells were resuspended in lysis buffer (50 mM Tris-HCl, pH 8.0, 150 mM NaCl, 1% NP40, 0.1% SDS), sonicated 3 × 10 s, and then boiled at 95 °C for 5 min. Samples were run on a 10% polyacrylamide gel and were blotted onto nitrocellulose filters (Millipore, Italy). Filters were then blocked in PBS-Tween-20 (0.1%) plus 5% nonfat dry milk and incubated with the primary antibody antiflotillin-1 (dilution 1:1000) for 16 h at 4 °C. Specific MV marker flotillin-1[40,41] was detected with mouse monoclonal anti-flotillin-1 (dilution 1:1000). After three washes with PBS-Tween, filters were incubated with peroxidase-conjugated anti-mouse secondary antibody (dilution 1:1000). Optical density of immunolabeled ECL-exposed protein bands was measured with UVI-1D software.

For the AFM characterization, MVs were diluted 1:10 in PBS buffer solution and processed as described in Junker *et al.*[65] Briefly, a 15 μL drop of sample solution was placed and left to adsorb (15 min) onto a freshly peeled mica substrate, thereafter rinsed with PBS. In order to reduce vesicle collapsing during AFM analysis, vesicles were fixed with 1% formaldehyde for 1 h (RT). MVs were then washed with PBS and dried under a gentle stream of nitrogen. AFM was used in semicontact mode at RT in air using a commercial instrument (Solver Pro, NT-MDT, RU). Silicon tips (NSC36/CR-AU, MikroMash, USA) with a

DOI: 10.1021/acsnano.6b00130
ACS Nano 2016, 10, 4459−4471

typical force constant of 0.6 nN/nm and a resonance frequency of about 65 kHz were employed. Topographic height and phase images were recorded at 512 × 512 pixels at a scan rate of 0.5 Hz. Image processing was performed using Gwyddion freeware AFM analysis software, version 2.40.[66] For statistical analysis, 107 individual MVs were imaged in seven different fields and measured. In particular, width and height of each vesicle were evaluated from cross-line profiles, and results were statistically analyzed using Igor Pro software (Wavemetrics. USA).

ASSOCIATED CONTENT

Supporting Information

The Supporting Information is available free of charge on the ACS Publications website at DOI: 10.1021/acsnano.6b00130.

Supporting results, Figures S1−S8, and Tables S1 and S2 (PDF)

AUTHOR INFORMATION

Corresponding Authors

*E-mail: prato@units.it.

*E-mail: laura.ballerini@sissa.it.

Author Contributions

R.R. and A.F. performed cell biology, electrophysiology, and immunofluorescence experiments and analysis; R.R. and F.P.U.S. designed and performed imaging and real-time imaging experiments and analysis; N.L. and K.K. contributed to the synthesis and characterization of thin graphene oxide (l-GO and s-GO) of biological grade; V.L. and E.V. contributed to the synthesis and characterization of pristine graphene; M.M. performed glial cell experiments, immunofluorescence, and Western blot; D.S., I.R., and L.C. designed and performed the AFM experiments; L.B. and M.P. conceived the study; L.B. conceived the experimental design and contributed to the analysis of data; L.B. wrote the manuscript.

Notes

The authors declare no competing financial interest.

ACKNOWLEDGMENTS

We are especially grateful to Micaela Grandolfo, Jessica Franzot, and Beatrice Pastore for supervising the synaptic immune staining and quantification, the glial cell culturing, and Western Blot experiments. IOM-TASC National Laboratory (Trieste) is also gratefully acknowledged for AFM assistance. N.L. acknowledges Leon Newman for assistance with the TEM and Raman instrumentation. The authors acknowledge the staff in the Faculty of Life Sciences EM Facility and the Wellcome Trust for equipment grant support to the EM Facility. The University of Manchester Bioimaging Facility microscopes used in this study were purchased with grants from the BBSRC, Wellcome Trust, and the University of Manchester Strategic Fund. X-ray photoelectron spectroscopy was performed at the National EPSRC XPS User's Service (NEXUS) at Newcastle University, an EPSRC Mid-Range Facility. The Antolin group is also acknowledged for the provision of the commercial material. We acknowledge financial support from the EU FP7-ICT-2013-FET-F GRAPHENE Flagship project (No. 604391) from the NEUROSCAFFOLDS-FP7-NMP-604263 and PRIN-MIUR No. 2012MYESZW.

REFERENCES

(1) Sanchez, V. C.; Jachak, A.; Hurt, R. H.; Kane, A. B. Biological Interactions of Graphene-Family Nanomaterials: An Interdisciplinary Review. *Chem. Res. Toxicol.* **2012**, *25*, 15−34.

(2) Kostarelos, K.; Novoselov, K. S. Materials Science. Exploring the Interface of Graphene and Biology. *Science* **2014**, *344*, 261−263.

(3) Mao, H. Y.; Laurent, S.; Chen, W.; Akhavan, O.; Imani, M.; Ashkarran, A. A.; Mahmoudi, M. Graphene: Promises, Facts, Opportunities, and Challenges in Nanomedicine. *Chem. Rev.* **2013**, *113*, 3407−3424.

(4) Bitounis, D.; Ali-Boucetta, H.; Hong, B. H.; Min, D. H.; Kostarelos, K. Prospects and Challenges of Graphene in Biomedical Applications. *Adv. Mater.* **2013**, *25*, 2258−2268.

(5) Krishna, K. V.; Ménard-Moyon, C.; Verma, S.; Bianco, A. Graphene-Based Nanomaterials for Nanobiotechnology and Biomedical Applications. *Nanomedicine (London, U. K.)* **2013**, *8*, 1669−1688.

(6) Wang, Y.; Li, Z.; Wang, J.; Li, J.; Lin, Y. Graphene and Graphene Oxide: Biofunctionalization and Applications in Biotechnology. *Trends Biotechnol.* **2011**, *29*, 205−212.

(7) Kuzum, D.; Takano, H.; Shim, E.; Reed, J. C.; Juul, H.; Richardson, A. G.; de Vries, J.; Bink, H.; Dichter, M. A.; Lucas, T. H.; Coulter, D. A.; Cubukcu, E.; Litt, B. Transparent and Flexible Low Noise Graphene Electrodes for Simultaneous Electrophysiology and Neuroimaging. *Nat. Commun.* **2015**, *5*, 5259−5263.

(8) Li, Y.; Yuan, H.; von dem Bussche, A.; Creighton, M.; Hurt, R. H.; Kane, A. B.; Gao, H. Graphene Microsheets Enter Cells Through Spontaneous Membrane Penetration at Edge Asperities and Corner Sites. *Proc. Natl. Acad. Sci. U. S. A.* **2013**, *110*, 12295−12300.

(9) Tu, Y.; Lv, M.; Xiu, P.; Huynh, T.; Zhang, M.; Castelli, M.; Liu, Z.; Huang, Q.; Fan, C.; Fang, H.; Zhou, R. Destructive Extraction of Phospholipids from Escherichia Coli Membranes by Graphene Nanosheets. *Nat. Nanotechnol.* **2013**, *8*, 594−601.

(10) Mao, J.; Guo, R.; Yan, L. Simulations and Analysis of Cellular Internalization Pathways and Membrane Perturbation for Graphene Nanosheets. *Biomaterials* **2014**, *35*, 6069−6077.

(11) Rizzoli, S. O. Synaptic Vesicle Recycling: Steps and Principles. *EMBO J.* **2014**, *33*, 788−822.

(12) Bianco, A. Graphene: Safe or Toxic? The Two Faces of the Medal. *Angew. Chem., Int. Ed.* **2013**, *52*, 4986−4997.

(13) Yang, D.; Li, T.; Xu, M.; Gao, F.; Yang, J.; Yang, Z.; Le, W. Graphene Oxide Promotes the Differentiation of Mouse Embryonic Stem Cells to Dopamine Neurons. *Nanomedicine (London, U. K.)* **2014**, *9*, 2445−2455.

(14) Zhang, Y.; Ali, S. F.; Dervishi, E.; Xu, Y.; Li, Z.; Casciano, D.; Biris, A. S. Cytotoxicity Effects of Graphene and Single-Wall Carbon Nanotubes in Neural Phaeochromocytoma-Derived PC12 Cells. *ACS Nano* **2010**, *4*, 3181−3186.

(15) Falchi, A. M.; Sogos, V.; Saba, F.; Piras, M.; Congiu, T.; Piludu, M. Astrocytes Shed Large Membrane Vesicles that Contain Mitochondria, Lipid Doplets and ATP. *Histochem. Cell Biol.* **2013**, *139*, 221−231.

(16) León, V.; Quintana, M.; Herrero, M. A.; Fierro, J. L.; de la Hoz, A.; Prato, M.; Vázquez, E. Few-Layer Graphenes from Ball-Milling of Graphite with Melamine. *Chem. Commun. (Cambridge, U. K.)* **2011**, *47*, 10936−10938.

(17) León, V.; Rodriguez, A. M.; Prieto, P.; Prato, M.; Vázquez, E. Exfoliation of Graphite with Triazine Derivatives under Ball-Milling Conditions: Preparation of Few-Layer Graphene *via* Selective Noncovalent Interactions. *ACS Nano* **2014**, *8*, 563−571.

(18) Carp, J. S. Physiological Properties of Primate Lumbar Motoneurons. *J. Neurophysiol.* **1992**, *68*, 1121−1132.

(19) Gao, Y.; Liu, L.; Li, Q.; Wang, Y. Differential Alterations in the Morphology and Electrophysiology of Layer II Pyramidal Cells in the Primary Visual Cortex of a Mouse Model Prenatally Exposed to LPS. *Neurosci. Lett.* **2015**, *591*, 138−143.

(20) Djuric, U.; Cheung, A. Y.; Zhang, W.; Mok, R. S.; Lai, W.; Piekna, A.; Hendry, J. A.; Ross, P. J.; Pasceri, P.; Kim, D. S.; Salter, M. W.; Ellis, J. MECP2e1 Isoform Mutation Affects the Form and Function of Neurons Derived from Rett Syndrome Patient iPS Cells. *Neurobiol. Dis.* **2015**, *76*, 37−45.

(21) Lovat, V.; Pantarotto, D.; Lagostena, L.; Cacciari, B.; Grandolfo, M.; Righi, M.; Spalluto, G.; Prato, M.; Ballerini, L. Carbon Nanotube

DOI: 10.1021/acsnano.6b00130
ACS Nano 2016, 10, 4459−4471

Substrates Boost Neuronal Electrical Signaling. *Nano Lett.* **2005**, *5*, 1107−1110.
(22) Cellot, G.; Toma, F. M.; Varley, Z. K.; Laishram, J.; Villari, A.; Quintana, M.; Cipollone, S.; Prato, M.; Ballerini, L. Carbon Nanotube Scaffolds Tune Synaptic Strenght in Cultured Neural Circuits: Novel Frontiers in Nanomaterials-Tissue Interactions. *J. Neurosci.* **2011**, *31*, 12945−12953.
(23) Bosi, S.; Rauti, R.; Laishram, J.; Turco, A.; Lonardoni, D.; Nieus, T.; Prato, M.; Scaini, D.; Ballerini, L. From 2D to 3D: Novel Nanostructured Scaffolds to Investigate Signaling in Reconstructed Neuronal Networks. *Sci. Rep.* **2015**, *5*, 9562.
(24) Stetter, O.; Battaglia, D.; Soriano, J.; Geisel, T. Model-Free Reconstruction of Excitatory Neuronal Connectivity from Calcium Imaging Signals. *PLoS Comput. Biol.* **2012**, *8*, e1002653.
(25) Fabbro, A.; Pastore, B.; Nistri, A.; Ballerini, L. Activity-Independent Intracellular Ca^{2+} Oscillations are Spontaneously Generated by Ventral Spinal Neurons during Development *in vitro*. *Cell Calcium* **2007**, *41*, 317−329.
(26) Tibau, E.; Valencia, M.; Soriano, J. Identification of Neuronal Network Properties from the Spectral Analysis of Calcium Imaging Signals in Neuronal Cultures. *Front. Neural Circuits* **2013**, *7*, 199.
(27) Sokal, D. M.; Mason, R.; Parker, T. L. Multi-Neuronal Recordings Reveal a Differential Effect of Thapsigargin on Bicuculline- or Gabazine-Induced Epileptiform Excitability in Rat Hippocampal Neuronal Networks. *Neuropharmacology* **2000**, *39*, 2408−2417.
(28) Raastad, M.; Storm, J. F.; Andersen, P. Putative Single Quantum and Single Fibre Excitatory Postsynaptic Currents Show Similar Amplitude Range and Variability in Rat Hippocampal Slices. *Eur. J. Neurosci.* **1992**, *4*, 113−117.
(29) Bellocchio, E. E.; Reimer, R. J.; Fremeau, R. T., Jr; Edwards, R. H. Uptake of Glutamate into Synaptic Vesicles by an Inorganic Phosphate Transporter. *Science* **2000**, *289*, 957−960.
(30) Moulder, K. L.; Jiang, X.; Taylor, A. A.; Shin, W.; Gillis, K. D.; Mennerick, S. Vesicle Pool Heterogeneity at Hippocampal Glutamate and GABA Synapses. *J. Neurosci.* **2007**, *27*, 9846−9854.
(31) Betz, W. J.; Bewick, G. S. Optical Analysis of Synaptic Vesicle Recycling at the Frog Neuromuscular Junction. *Science* **1992**, *255*, 200−203.
(32) Ryan, T. A.; Reuter, H.; Wendland, B.; Schweizer, F. E.; Tsien, R. W.; Smith, S. J. The Kinetics of Synaptic Vesicle Recycling Measured at Single Presynaptic Boutons. *Neuron* **1993**, *11*, 713−724.
(33) Betz, W.; Mao, F.; Smith, C. Imaging Exocytosis and Endocytosis. *Curr. Opin. Neurobiol.* **1996**, *6*, 365−371.
(34) Ryan, T. A. Presynaptic Imaging Techniques. *Curr. Opin. Neurobiol.* **2001**, *11*, 544−549.
(35) Turola, E.; Furlan, R.; Bianco, F.; Matteoli, M.; Verderio, C. Microglial Microvesicles Secretion and Intercellular Signaling. *Front. Physiol.* **2012**, *3*, 149.
(36) Frühbeis, C.; Fröhlich, D.; Kuo, W. P.; Krämer-Albers, E. M. Extracellular Vesicles as Mediators of Neuron-Glia Communication. *Front. Cell. Neurosci.* **2013**, *7*, 182.
(37) Antonucci, F.; Turola, E.; Riganti, L.; Caleo, M.; Gabrielli, M.; Perrotta, C.; Novellino, L.; Clementi, E.; Giussani, P.; Viani, P.; Matteoli, M.; Verderio, C. Microvesicles Released from Microglia Stimulate Synaptic Activity *via* Enhanced Sphingolipid Metabolism. *EMBO J.* **2012**, *31*, 1231−1240.
(38) Bianco, F.; Pravettoni, E.; Colombo, A.; Schenk, U.; Möller, T.; Matteoli, M.; Verderio, C. Astrocyte-Derived ATP Induces Vesicle Shedding and IL-1 Beta Release from Microglia. *J. Immunol.* **2005**, *174*, 7268−7277.
(39) Bianco, F.; Perrotta, C.; Novellino, L.; Francolini, M.; Riganti, L.; Menna, E.; Saglietti, L.; Schuchman, E. H.; Furlan, R.; Clementi, E.; Matteoli, M.; Verderio, C. Acid Sphingomyelinase Activity Triggers Microparticle Release from Glial Cells. *EMBO J.* **2009**, *28*, 1043−1054.
(40) Del Conde, I.; Shrimpton, C. N.; Thiagarajan, P.; López, J. A. Tissue-Factor-Bearing Microvesicles Arise from Lipid Drafts and Fuse with Activated Platelets to Initiate Coagulation. *Blood* **2005**, *106*, 1604−1611.
(41) Al-Nedawi, K.; Meehan, B.; Micallef, J.; Lhotak, V.; May, L.; Guha, A.; Rak, J. Intercellular Transfer of the Oncogenic Receptor EGFRvIII by Microvesicles Derived from Tumour Cells. *Nat. Cell Biol.* **2008**, *10*, 619−624.
(42) Antonyak, M. A.; Cerione, R. A. Microvesicles as Mediators of Intercellular Communication in Cancer. *Methods Mol. Biol.* **2014**, *1165*, 147−173.
(43) Toyoshima, D.; Mandai, K.; Maruo, T.; Supriyanto, I.; Togashi, H.; Inoue, T.; Mori, M.; Takai, Y. Afadin Regulates Puncta Adherentia Junction Formation and Presynaptic Differentiation in Hippocampal Neurons. *PLoS One* **2014**, *9*, e89763.
(44) Aguado, F.; Carmona, M. A.; Pozas, E.; Aguiló, A.; Martínez-Guijarro, F. J.; Alcantara, S.; Borrell, V.; Yuste, R.; Ibañez, C. F.; Soriano, E. BDNF Regulates Spontaneous Correlated Activity at Early Developmental Stages by Increasing Synaptogenesis and Expression of the K^+/Cl^- Co-Transporter KCC2. *Development* **2003**, *130*, 1267−1280.
(45) Chong, Y.; Ge, C.; Yang, Z.; Garate, J. A.; Gu, Z.; Weber, J. K.; Liu, J.; Zhou, R. Reduced Cytotoxicity of Graphene Nanosheets Mediated by Blood-Protein Coating. *ACS Nano* **2015**, *9*, 5713−5724.
(46) Fabbro, A.; Sucapane, A.; Toma, F. M.; Calura, E.; Rizzetto, L.; Carrieri, C.; Roncaglia, P.; Martinelli, V.; Scaini, D.; Masten, L.; Turco, A.; Gustincich, S.; Prato, M.; Ballerini, L. Adhesion to Carbon Nanotube Conductive Scaffolds Forces Action-Potential Appearance in Immature Rat Spinal Neurons. *PLoS One* **2013**, *8*, e73621.
(47) Malarkey, E. B.; Reyes, R. C.; Zhao, B.; Haddon, R. C.; Parpura, V. Water Soluble Single-Walled Carbon Nanotubes Inhibit Stimulated Endocytosis in Neurons. *Nano Lett.* **2008**, *8*, 3538−3542.
(48) High, B.; Cole, A. A.; Chen, X.; Reese, T. S. Electron Microscopic Tomography Reveals Discrete Transcleft Elements at Excitatory and Inhibitory Synapses. *Front. Synaptic Neurosci.* **2015**, *7*, 9.
(49) Fedorovich, S. V.; Alekseenko, A. V.; Waseem, T. V. Are Synapses Targets of Nanoparticles? *Biochem. Soc. Trans.* **2010**, *38*, 536−538.
(50) Grados, M. A.; Atkins, E. B.; Kovacikova, G. I.; McVicar, E. A Selective Review of Glutamate Pharmacological Therapy in Obsessive-Compulsive and Related Disorders. *Psychology Res. and Behavior Management PRBM* **2015**, *8*, 115−131.
(51) Gardoni, F.; Di Luca, M. Targeting Glutamatergic Synapses in Parkinson's Disease. *Curr. Opin. Pharmacol.* **2015**, *20*, 24−28.
(52) Stone, J. M. Glutamatergic Antipsychotic Drugs: a New Dawn in the Treatment of Schizophrenia? *Ther. Adv. Psychopharmacol.* **2011**, *1*, 5−18.
(53) Meyer, R. A.; Sunshine, J. C.; Green, J. J. Biomimetic Particles as Therapeutics. *Trends Biotechnol.* **2015**, *33*, 514−524.
(54) Borisova, T.; Nazarova, A.; Dekaliuk, M.; Krisanova, N.; Pozdnyakova, N.; Borysov, A.; Sivko, R.; Demchenko, A. P. Neuromodulatory Properties of Fluorescent Carbon Dots: Effect on Exocytotic Release, Uptake and Ambient Level of Glutamate and GABA in Brain Nerve Terminals. *Int. J. Biochem. Cell Biol.* **2015**, *59*, 203−215.
(55) Fabbro, A.; Scaini, D.; León, V.; Vázquez, E.; Cellot, G.; Privitera, G.; Lombardi, L.; Torrisi, F.; Tomarchio, F.; Bonaccorso, F.; Bosi, S.; Ferrari, A. C.; Ballerini, L.; Prato, M. Graphene-Based Interfaces Do Not Alter Target Nerve Cells. *ACS Nano* **2016**, *10*, 615−23.
(56) Ali-Boucetta, H.; Bitounis, D.; Raveendran-Nair, R.; Servant, A.; Van den Bossche, J.; Kostarelos, K. Purified Graphene Oxide Dispersions Lack *in vitro* Cytotoxicity and *in vivo* Pathogenicity. *Adv. Healthcare Mater.* **2013**, *2*, 433−441.
(57) Mukherjee, S. P.; Lozano, N.; Kucki, M.; Del-Rio Castillo, A. E.; Vázquez, E.; Kostarelos, K.; Wick, P.; Fadeel, B. Detection of Endotoxin Contamination of Graphene Oxide Using the TNF-α Expression Test and Guidelines for Endotoxin-Free Graphene Oxide Production. Submitted for publication.
(58) Jasim, D. A.; Lozano, N.; Kostarelos, K. Synthesis of Few-Layered, High-Purity Graphene Oxide Sheets from Different Graphite Sources for Biology. *2D Mater.* **2016**, *3*, 014006.

DOI: 10.1021/acsnano.6b00130
ACS Nano 2016, 10, 4459−4471

(59) Varela-Rizo, H.; Rodriguez-Pastor, I.; Merino, C.; Martin-Gullon, I. Highly Crystalline Graphene Oxide Nano-Platelets Produced From Helical-Ribbon Carbon Nanofibers. *Carbon* **2010**, *48*, 3640−3643.
(60) Cellot, G.; Cilia, E.; Cipollone, S.; Rancic, V.; Sucapane, A.; Giordani, S.; Gambazzi, L.; Markram, H.; Grandolfo, M.; Scaini, D.; Gelain, F.; Casalis, L.; Prato, M.; Giugliano, M.; Ballerini, L. Carbon Nanotubes Might Improve Neuronal Performance by Favouring Electrical Shortcuts. *Nat. Nanotechnol.* **2009**, *4*, 126−133.
(61) Calegari, F.; Coco, S.; Taverna, E.; Bassetti, M.; Verderio, C.; Corradi, N.; Matteoli, M.; Rosa, P. A Regulated Secretory Pathway in Cultured Hippocampal Astrocytes. *J. Biol. Chem.* **1999**, *274*, 22539−22547.
(62) Pavlidis, P.; Montgomery, J.; Madison, D. V. Presynaptic Protein Kinase Activity Supports Long-Term Potentiation at Synapses Between Individual Hippocampal Neurons. *J. Neurosci.* **2000**, *20*, 4497−4505.
(63) Hoopmann, P.; Rizzoli, S. O.; Betz, W. J. Imaging Synaptic Vesicle Recycling by Staining and Destaining Vesicles with FM Dyes. *Cold Spring Harbor Protoc.* **2012**, *1*, 77−83.
(64) Schindelin, J.; Arganda-Carreras, I.; Frise, E.; Kaynig, V.; Longair, M.; Pietzsch, T.; Preibisch, S.; Rueden, C.; Saalfeld, S.; Schmid, B.; Tinevez, J. Y.; White, D. J.; Hartenstein, V.; Eliceiri, K.; Tomancak, P.; Cardona, A. Fiji: An Open-Source Platform for Biological-Image Analysis. *Nat. Methods* **2012**, *9*, 676−682.
(65) Junker, J. P.; Rief, M. Single-Molecule Force Spectroscopy Distinguishes Target Binding Modes of Calmodulin. *Proc. Natl. Acad. Sci. U. S. A.* **2009**, *106*, 14361−14366.
(66) Klapetek, P.; Valtr, M.; Nečas, D.; Salyk, O.; Dzik, P. Atomic Force Microscopy Analysis of Nanoparticles in Non-Ideal Conditions. *Nanoscale Res. Lett.* **2011**, *6*, 514.

DOI: 10.1021/acsnano.6b00130
ACS Nano 2016, 10, 4459−4471

Graphene Oxide Nanosheets and Neural System: from Synaptic Modulation to Neuroinflammation

Mattia Musto[1a], Rossana Rauti[1a], Neus Lozano[2], Elena Bonechi[3], Clara Ballerini[4*], Loredana Casalis[5], Kostas Kostarelos[2*], Laura Ballerini[1*]

[1]International School for Advanced Studies (SISSA), Trieste, Italy
[2]Nanomedicine Lab, School of Medicine and National Graphene Institute, Faculty of Medical & Human Sciences, University of Manchester, Manchester, United Kingdom
[3]Department NEUROFARBA, University of Florence, 50139 Florence, Italy
[4] Dipartimento di Medicina Sperimentale e Clinica, University of Firenze, Firenze, Italy
[5]Nanoinnovation Lab, ELETTRA Synchrotron Light Source, Trieste, Italy

[a] These authors equally contributed to the work

Correspondence:

E-mail: laura.ballerini@sissa.it, clara.ballerini@unifi.it and kostas.kostarelos@manchester.ac.uk

Keywords: graphene, organotypic cultures, patch-clamp, microglia, microvesicles

Abstract

Graphene-based nanomaterials represent potential tools in neuro-repair and are increasingly engineered as components of a variety of applications such as biosensors, interfaces or drug-delivery platforms. These developments necessitates addressing how this material affects biological systems and in particular, the interactions of 2D planar graphene with the neuronal tissue in physiological environment. In hippocampal cultures, we recently reported the ability of graphene oxide nano-sheets to interfere specifically with synapses, hampering excitatory neuro-transmission, and to alter glia reactivity, without affecting the viability of brain cells. Graphene oxide ability to specifically tune synapses might pose the basis for its exploitation in target applications in neuropharmacology. However, the potential neuroglia reactivity raises concerns from a toxicity point of view. To tailor graphene oxide nano-flakes safe developments, we need to model *in vitro* glial cell responses, and in particular the reactivity of microglia, a sub-population of neuroglia that acts as the first active immune response, when challenged by chronic graphene oxide

nano-flakes delivery at high doses. Here, we investigated the tissue reactivity upon long-term exposure to graphene oxide nano-sheets in 3D tissue models. We used the mouse organotypic spinal cord cultures, ideally suited for studying long-term interference with cues delivered at controlled times and concentrations. In cultured spinal segments, the normal presence, distribution and maturation of anatomically distinct classes of neurons and resident neuroglial cells are preserved. Organotypic explants were developed for two weeks embedded in fibrin glue alone or presenting graphene oxide nano-sheets at 10, 25 and 50 μg/mL. We addressed the impact of such treatments on premotor synaptic activity monitored by patch clamp recordings of ventral interneurons. We investigated by immunofluorescence and confocal microscopy the accompanying glial responses upon graphene oxide exposure, focusing on resident microglia, tested in organotypic spinal slices and in isolated neuroglia cultures. In the latter condition, we further tested the role of microglial micro-vesicle release in mediating cell responses to graphene oxide nano-sheets.

1. Introduction

Graphene is a honeycomb lattice structure consisting of sp^2 hybridized carbon atoms (Sanchez et al., 2012; Kostarelos and Novoselov, 2014), characterized by high mechanical strength and electrical conductivity, combined with optical transparency. In neurobiology, graphene has been used in surface engineering of regenerative scaffolds to control the neuro-induction of stem cells (Wang et al., 2012), and in that of neurological interfaces to improve the electrodes performance (Li et al., 2013; Kostarelos and Novoselov, 2014; Mao et al., 2013; Wang et al., 2011).

Graphene oxide (GO) is the most common derivative of graphene. Recently, GO materials have been successfully designed for drug delivery applications (Baldrighi et al., 2016). However, their potential persistency in biological tissues requires investigating their safety. We have previously (Rauti et al., 2016) reported the ability of small GO (<100 nm; s-GO) nano-sheets to reduce synaptic activity at glutamatergic synapses without affecting cultured hippocampal neurons survival. To date, only few studies addressed the interaction between s-GO nanosheets and synapses (Rauti et al., 2016; Bramini et al., 2016), while there are scarcely any data on the interactions between neural circuit function, s-GO tissue accumulation and inflammation. Before any further exploitation of s-GO in synaptic targeting, a detailed analysis of tissue responses to s-GO exposure is needed. Mechanistic studies of the interplay between s-GOs, the activation of microglia and synaptic function, may require in vitro models to test central nervous system (CNS) responses at cellular resolution. Organotypic slices are explant cultures that preserve key, structural elements of the tissue of origin (Medelin et al., 2016; Furlan et al., 2007; Avossa et al., 2003, 2006; Schermer and Humpel, 2002; Tscherter et al., 2001; Fischer et al., 1998; Hailer et al., 1996) allowing detailed studies of cellular and subcellular responses, such as inflammatory reactivity and synaptic efficacy, upon chronic treatments, including the exposure to

exogenous factors. In the CNS, the immune response is mediated by resident macrophages called microglia that are approximately 12 % of the total CNS cells originating from myeloid cells. This subpopulation of brain cells can switch between two different phenotypes: a ramified phenotype, typical of the resting/surveillant state, during which they "monitor" the surrounding environment (Nimmerjahn et al., 2005; Davalos et al., 2005; Cherry et al., 2014) and an amoeboid phenotype, which is induced by antigens-mediated stimulation. When activated, microglia rapidly changes its surface receptor expression and the production of molecules involved in the immune response, like cytokines and chemokines (Nimmerjahn et al., 2005; Fetler and Amigorena, 2005); activated microglia may represent an active player in neuron damage (Block et al., 2007). We used here mouse spinal organotypic cultures to mimic a chronic accumulation of s-GO in the spinal cord tissue. The s-GO nano-flakes were delivered to the spinal tissue upon dilution in the chicken plasma used to embed the explants for culturing, thus allowing s-GO to rapidly adsorb proteins (Bertrand et al., 2017), such a condition may mimic how nanosheets behave in a complex biological milieu. We patch-clamp ventral interneurons to monitor synaptic transmission. Contextually, by confocal microscopy we explored the effects of s-GO on innate immunity, in both organotypic slices and primary isolated microglial cultures. We conclude that chronic accumulation of s-GOs, due to delivery of high doses of the materials, significantly affected synaptic activity with a clear involvement of the microglia cell population. Our experiments in isolated microglia cells in culture support the direct activation by s-GO of immune responses in these experimental conditions.

2. Material and Methods

2.1 Preparation of spinal tissue slices and primary glial cultures

Organotypic cultures were obtained from spinal cords isolated from E12 embryonic mouse (C57Bl), as previously described (Avossa et al., 2003; Furlan et al., 2007; Furlan et al., 2005; Usmani et al., 2016). Briefly, pregnant mice were sacrificed by CO_2 overdose and decapitation and fetuses delivered by caesarean section. Isolated fetuses were decapitated and their backs were isolated from low thoracic and high lumbar regions and transversely sliced (275 µm) with a tissue chopper. Cultures were fixed on a glass coverslip (Kindler, EU) with fibrin glue, i.e. reconstituted chicken plasma (Rockland) clotted with thrombin (Merk). In graphene-treated cultures, s-GO (Rauti et al., 2016) nanosheets were embedded in the fibrin glue at 10, 25 and 50 µg/mL final concentration. Experiments were performed on control and s-GO treated cultures after 2 and 3 weeks *in vitro*.

All experiments were performed in accordance with the EU guidelines (2010/63/UE) and Italian law (decree 26/14) and were approved by the local authority veterinary service and by our institution (SISSA-ISAS) ethical committee. All efforts were made to minimize

animal suffering and to reduce the number of animal used. Animal use was approved by the Italian Ministry of Health, in agreement with the EU Recommendation 2007/526/CE.
Primary brain glial cultures were obtained from P2−P3 rats (Wistar) cortices, as previously described (Calegari et al., 1999; Rauti et al., 2016). Dissociated cells were plated into plastic 75 cm^2 flasks, incubated (37 °C; 5% CO_2) in culture medium consisting of DMEM (Invitrogen), supplemented with 10% FBS, 100 IU/ mL penicillin, and 10 mg/mL streptomycin.
Confluent mixed glial cultures from *days in vitro* (DIV) 21 to DIV 25 were treated with a trypsin solution (0.25% trypsin, 1 mM EDTA in HBSS) diluted 1:4 in PBS for 30 minutes at 37 °C and 5% CO_2. The medium was then collected and diluted 1:4 in DMEM supplemented with 10% FBS and centrifuged for 5 minutes at 200 x g. The pellet was then re-suspended in DMEM supplemented with 10% FBS and mixed glial cultures conditioned medium (50:50) and plated on poly-L-lysine-coated glass coverslips. Twenty-four hours after trypsinization half of the cultures were incubated with s-GO at a concentration of 10 µg/mL suspended in the culture medium for 1 or 5 days.

2.2 Electrophysiological Recordings

For patch-clamp recordings (whole-cell, voltage clamp mode), a coverslip with the spinal culture was positioned in a recording chamber, mounted on an inverted microscope (Eclipse TE-200, Nikon, Japan) and superfused with control physiological saline solution containing (in mM): 152 NaCl, 4 KCl, 1 $MgCl_2$, 2 $CaCl_2$, 10 HEPES and 10 Glucose. The pH was adjusted to 7.4 with NaOH (osmolarity 305 mosmol L^{-1}). Cells were patched with glass pipettes (4-7 MΩ) filled with a solution of the following composition (in mM): 120 Kgluconate, 20 KCl, 10 HEPES, 10 EGTA, 2 $MgCl_2$ and Na_2ATP. The pH was adjusted to 7.3 with KOH (295 mosmol L^{-1}). All electrophysiological recordings were performed at room temperature (RT; 20-22 °C) and the spontaneous synaptic activity was recorded by clamping the membrane voltage at –56 mV (not corrected for liquid junction potential, which was –14 mV). Recordings were performed from ventrally located spinal interneurons identified on the basis of previously reported criteria (Ballerini and Galante, 1998; Ballerini et al., 1999; Galante et al., 2000). We detected no differences between controls (n = 45) and s-GO (n = 39) neurons in cell membrane capacitance (70 ± 8 pF controls, 68 ± 6 pF s-GO) and membrane input resistance (250 ± 28 MΩ controls, 242 ± 20 MΩ s-GO). Spontaneous activity was also recorded in the presence of 6-cyano-7-nitroquinoxaline-2,3-dione (CNQX, 10 µM), bicuculline (20 µM) and strychnine (10 µM) to pharmacologically discriminate between glutamatergic and GABAergic PSCs, respectively. To detect miniature post-synaptic currents (mPSCs), TTX (1 µM; Latoxan, Valence, France) was added. All reagents were purchased from Sigma-Aldrich, if not otherwise indicated. Data were collected by Multiclamp 700B patch amplifier (Axon CNS,

Molecular Devices) and digitized at 10 kHz with the pClamp 10.2 software (Molecular Devices LLC, USA). All recorded events were analyzed offline with the AxoGraph 1.4.4 (Axon Instrument) event detection software (Axon CNS, Molecular Devices).

2.3 Immunofluorescence Labeling of spinal-cord slices

Organotypic cultures were fixed by 4% formaldehyde (prepared from fresh paraformaldehyde; Sigma) in PBS for 1 hour at RT and then washed in PBS. Free aldehyde groups were quenched in 0.1 M glycine in PBS for 5 min. The samples were blocked and permeabilized in 3 % fetal bovine serum (FBS), 3 % BSA and 0.3 % Triton-X 100 in PBS for 1 h at RT. Samples were incubated with primary antibodies (mouse anti-neurofilament H Smi 32, Biolegend, 1:250 dilution; mouse monoclonal anti-GFAP, Invitrogen, 1:500 dilution; rabbit monoclonal anti-caspase 3, Euroclone, 1: 200 dilution; rabbit polyclonal anti-β-tubulin III, Sigma-Aldrich, 1:250 dilution; rabbit anti Iba1, Wako, 1:250 dilution) diluted in PBS with 5 % FBS at 4 °C, overnight. Samples were then incubated in secondary antibodies (Alexa 488 goat anti-mouse, Invitrogen, 1:500 dilution; Alexa 594 goat anti-rabbit, Invitrogen, 1:500 dilution), and DAPI (Invitrogen, dilution 1:200) to stain the nuclei, for 2 h at RT and finally mounted on 1 mm glass coverslips using Vectashield hardset mounting medium (Vector Laboratories). Images were acquired using a Nikon C2 Confocal, equipped with Ar/Kr, He/Ne and UV lasers. Images were acquired with a 40× (1.4 NA) oil-objective (using oil mounting medium, 1.515 refractive index). Confocal sections were acquired every 500 nm and the total Z-stack thickness (50 µm) was set such that all emitted fluorescence was collected from the sample. Regions of interest were confined to the ventral part of slice. Offline analysis was performed using the open source image-processing package Fiji (Schindelin et al., 2012) and Volocity software (Volocity 3D image analysis software, PerkinElmer, USA).

2.4 Immunofluorescence Labeling of neuroglia primary cultures

Primary glial and microglial cultures were fixed with by 4 % formaldehyde (prepared from fresh paraformaldehyde) in PBS for 20 min at RT and then washed in PBS. Free aldehyde groups were quenched in 0.1 M glycine in PBS for 5 min. The samples were blocked and permeabilized in 5 % fetal bovine serum (FBS), 0.3 % Triton-X 100 in PBS for 30 min at RT. Samples were incubated with primary antibodies (mouse monoclonal anti-GFAP, Invitrogen, 1:500 dilution; rabbit anti Iba1, Wako, 1:250 dilution; mouse monoclonal anti-Brdu, Thermo Fisher, 1:200 dilution) diluted in PBS with 5 % FBS at 4 °C, overnight. Samples were then incubated in secondary antibodies (Alexa 488 goat anti-mouse, Invitrogen, 1:500 dilution; Alexa 594 goat anti-rabbit, Invitrogen, 1:500 dilution), and DAPI (Invitrogen, dilution 1:200) to stain the nuclei, for 45 minutes at RT and finally mounted on 1 mm thick glass coverslips using Vectashield mounting medium (Vector Laboratories). Cells densities were quantified at 20× (0.5 NA) magnification using a DM6000 Leica microscope (Leica Microsystems GmbH, Wetzlar, Germany). In order to investigate the internalization of s-GO in microglial cells, we used the reflection mode

property during the confocal acquisition. Images were acquired using a Nikon C2 Confocal, equipped with Ar/Kr, He/Ne and UV lasers. Images were acquired with a 40× (1.4 NA) oil-objective (using oil mounting medium, 1.515 refractive index). Confocal sections were acquired every 200 nm and the total Z-stack thickness 20µm.

2.5 Bromodeoxyuridine (BrdU) Incorporation

Microglial primary cultures were incubated with BrdU (Thermo Fisher) diluted in the culture medium at a final concentration of 10 µM for 24 hours. Cells were then washed with PBS and fixed by 4 % formaldehyde (prepared from fresh paraformaldehyde) for 20 minutes at RT and then washed with PBS (3 times, 2 minutes each). Free aldehyde groups were quenched in 0.1 M glycine in PBS for 5 min. Cells were then incubated with HCl 1 M for 1 minutes on ice and with HCl 2 M for 15 minutes at 37 °C. Acid was then neutralized with boric acid 0.1 M for 10 minutes at RT. The samples were then blocked and permeabilized in 3 % fetal bovine serum (FBS) and 0.3 % Triton-X 100 in PBS for 1h at RT. Samples were incubated with primary antibodies at 4 °C overnight (mouse monoclonal anti-BrdU, 1:200 dilution; rabbit anti-Iba1, 1:200 dilution). Samples were then incubated in secondary antibodies (Alexa 488 goat anti-mouse, Invitrogen, 1:500 dilution; Alexa 594 goat anti-rabbit, Invitrogen, 1:500 dilution), and DAPI (Invitrogen, dilution 1:200) to stain the nuclei, for 45 minutes at RT and mounted on 1 mm thick glass coverslips using Vectashield mounting medium (Vector Laboratories).

2.6 Microvesicles Isolation

Microvesicles shedding and detection by western blotting were performed as previously described (Rauti et al., 2016). The microvesicles release was induced in 21 DIV microglial cells by the stimulation with benzoyl-ATP (bzATP; 100 µM) in saline solution with the following composition: 125 mM NaCl, 5 mM KCl, 1.2 mM $MgSO_4$, 1.2 mM KH_2PO_4, 2 mM $CaCl_2$, 6 mM D-glucose, and 25 mM HEPES/NaOH (pH adjusted to 7.4), for 30 min at 37 °C and 5% CO_2. Microvesicles were then pelleted by centrifugation (Bianco et al., 2009). Negative controls were incubated with saline solution without the presence of bzATP. MVs were re-suspended in lysis buffer (50 mM Tris-HCl, pH 8.0, 150 mM NaCl, 1 % NP40, 0.1 % SDS), sonicated 3 × 10 s, and then boiled at 95 °C for 5 min. Samples were run on a 10 % polyacrylamide gel and were blotted onto nitrocellulose filters (Millipore, Italy). Filters were then blocked in PBS-Tween-20 (0.1 %) plus 5 % nonfat dry milk and incubated with the primary antibody antiflotillin-1 (dilution 1:1000) for 16 h at 4 °C. Specific MV marker flotillin-1 (Al-Nedawi et al., 2008; Del Conde et al., 2005) was detected with mouse monoclonal antiflotillin-1 (dilution 1:1000). After three washes with PBS-Tween, filters were incubated with peroxidase-conjugated anti-mouse secondary antibody (dilution 1:1000). Optical density of immunolabeled ECL-exposed protein bands was measured with UVI-1D software.

2.7 Microglial morphological analysis

For morphological analysis cells were fixed and immunostained for Iba1 and DAPI for nuclei, as described above and images were acquired with a 40 × oil objective. The quantitative analysis of cell morphology was performed with the particle analysis feature in Fiji (1.51v) to automatically measure the area, perimeter and Feret's maximum diameter. In particular, Feret's diameter is described as the greatest distance between any two points along cell perimeter and is considered as an index of cell length. A more ramified cell has a higher value for this parameter, while a more amoeboid shape is described by a lower value.

2.8 Measurement of cytokines and chemokines

Inflammatory reaction may be detected by cytokine and chemokine production. A panel of 12 out of cytokines or chemokines was measured in organotypic culture supernatants after 2 weeks culturing, by Luminex based technology, using a customized Procarta plex Immunoassy kit (Invitrogen), following the manufacturer's protocol. The following soluble factors were simultaneously measured in 50 µl of supernatant: Il4, IL6, IL10, IL17, IL21, BAFF, IFNγ, TNFα, CXCL1, CXCL2, CXCL10, MCP1.

2.9 Statistical Analysis

The results are presented as the mean ± SD, if not otherwise indicated. A statistically significant difference between two data sets was assessed by Student's *t*-test (after checking variances homogeneity by Leven's test) for parametric data and by Mann-Whitney's test for non-parametric ones. $P < 0.05$ was considered at a statistically significant.

3. Results

3.1 Long Term Exposure to High Doses of s-GO Impaired Network Activity in Spinal-Cord Organotypic Slices

We first explored the long-term (2 weeks) exposure of neural tissue to s-GO in 3D tissue cultures. s-GO was delivered to the neural tissue *via* the plasma clot that constitutes the explant growth environment. Figure 1A shows a reconstruction at low confocal magnification of a spinal cord slice after 14 days of growth, labelled for neurofilament H (Smi-32; in green) and for the nuclei (DAPI, in blue). The entire area of tissue growth is visualized, and it includes the spinal slice, at the centre, and the outgrowing area comprising the co-cultured dorsal root ganglia (DRG) and the typical, dense mesh of neurites in the surrounding outgrowth belt (Fabbro et al., 2012).

Spinal organotypic slices upon 2 weeks of culturing exhibit an intense spontaneous synaptic activity (Streit, 1993; Ballerini and Galante, 1998; Furlan et al., 2007). We patch-clamped (sketched in Figure 1B) visually identified ventral interneurons (at holding potential, V_h of –56 mV) in control cultures (n = 45) and in s-GO treated ones (n = 52), and we recorded spontaneous, basal postsynaptic currents (PSCs). Figure 1C shows

representative tracings in control (left) and after exposure to the higher dose (50 µg/mL) of s-GO (right). In all culture groups, PSCs appeared as heterogeneous inward currents of variable amplitudes, characterized by different kinetic properties (fast decaying, with decay time constant (τ) of 6 ± 2 ms and slow decaying with τ 22 ± 6, n = 15, see sample in Figure 1C insets; Medelin et al., 2018).

The chronic (2 weeks) exposure to low (10 µg/mL) s-GO doses did not affect PSCs amplitude and frequency values (39 ± 7 pA and 23 ± 5 Hz, n = 13) when compared to control ones (42 ± 6 pA and 24 ± 4 Hz, n = 15; plots in Figure 1D).

Conversely, higher s-GO doses significantly (25 and 50 µg/mL, $P < 0.05$ and $P < 0.01$, respectively; Student's *t* test) reduced PSCs frequency (from 24 ± 6 Hz in control to 14 ± 3 Hz, in s-GO 25 µg/mL, n = 15 and 13; from control 22 ± 8 Hz to 10 ± 2 Hz in s-GO 50 µg/mL, n = 15 and 13). PSCs decay kinetics (fast decaying, τ 5 ± 2 ms and slow decaying τ 26 ± 3, n = 13 at 50 µg/mL, see sample Figure 1C inset) and amplitudes were not altered by these treatments (Figure 1D). In 25 and 50 µg/mL s-GO treated cultures we investigated the amount of neuronal apoptosis in respect to aged-matched controls by measuring the expression of active caspase-3 (Cohen, 1997). Active caspase-3 positive cells were quantified in the ventral spinal horns (Figure 1E). We detected a comparative amount of apoptotic cells in all conditions (in control: 15 ± 3 Caspase-3 positive cells/mm^2 namely 3.7 % of the total amount of cells, n = 10 visual fields and in s-GO 50 µg/mL; 20 ± 3 Caspase-3 positive cells/mm^2, 4.3 % of the cells, n = 10 visual fields; plot in Figure 1E). Thus, s-GO only when delivered at higher concentrations altered synapse function, apparently without increasing neuronal cell death.

Miniature synaptic currents (mPSCs; Figure 2) were recorded in a subset of control (n = 12) and s-GO treated (n = 13) neurons by application of tetrodotoxin (TTX, 1 µM), to block voltage-gated sodium channels. As this treatment impairs the generation of action potentials, mPSCs reflect the stochastic release of vesicles from the presynaptic terminals at individual synapses impinging onto the recorded neuron: their frequency depends on the pre-synaptic release probability and on the number of synaptic contacts, while their amplitude depends on postsynaptic receptor sensitivity
(Raastad et al., 1992). In neurons exposed to low (10 µg/mL) s-GO, mPSCs frequency was not affected (from 19 ± 3 Hz in control to 15 ± 3 Hz in s-GO treated slices; plot in Figure 2). When investigating the impact of higher graphene doses (25 and 50 µg/mL), we detected a significant difference ($P < 0.05$ and $P < 0.01$, respectively; Student's *t* test) in mPSCs frequency (from 20 ± 3 Hz to 13 ± 2 Hz in s-GO 25µg/mL and from 16 ± 3 Hz to 6 ± 1 Hz in s-GO 50 µg/mL). s-GO did not affect the amplitude of the recorded events (from 27 ± 6 pA in controls to 32 ± 5 pA in s-GO 10 µg/mL; from 29 ± 5 pA in controls to 27 ± 4 pA in s-GO 25 µg/mL; from 33 ± 8 pA in controls to 30 ± 6 pA in s-GO 50 µg/mL).

In s-GO neurons (50 µg/mL) we pharmacologically (see Methods) isolated AMPA-receptor mediated glutamatergic mEPSCs (n = 13) and $GABA_A$- receptor mediated

mIPSCs (n = 13), both detected as inward currents in our recording conditions (Medelin et al., 2016). mEPSCs and mIPSCs frequency values were similarly reduced by s-GO when compared to control slices (for mEPSPs in controls 14 ± 4 Hz, n = 12; in s-GO 7 ± 2 Hz, n = 13; $P < 0.05$, Student's *t* test; histograms in Figure 2, bottom-left panel; for mIPSCs in controls 13 ± 4 Hz, n = 12; in s-GO 5 ± 2 Hz, n = 13; $P < 0.05$, Student's *t* test; histograms in Figure 2, bottom-right panel).

3.2 s-GO Exposure at High Doses Induced Microglial Proliferation

To investigate tissue reactivity accompanying s-GO ability to alter synaptic signalling, we used the highest dose tested, namely the s-GO at 50 μg/mL. In organotypic slice cultures, neuroglia resident cells are mainly represented by astrocytes (GFAP positive cells) and microglia (Iba1 positive cells; Medelin et al., 2018).

GFAP-positive astrocytes are not immune cells *per se*, but can, under certain conditions, contribute to the immune response (Farina et al., 2007). In organotypic cultures upon 2 weeks of culturing, these cells are usually characterized by a stellate-like morphology (Figure 3A; Avossa et al., 2003) and their density was not significantly altered by s-GO treatment (Figure 3A, right histograms; 500 ± 70 GFAP-positive cells/mm^2 in control and 650 ± 90 GFAP-positive cells in s-GO; n = 13 visual fields each).

Iba1-positive microglia cells are known mediators of CNS inflammation. In contrast to astrocytes, the density of Iba1-positive cells was significantly ($P < 0.01$, Student's *t* test) increased in slices exposed to s-GO (47 ± 17 Iba1-positive cells/mm^2, n = 10 fields in control and 150 ± 30 Iba1-positive cells/mm^2, n = 11 fields for s-GO; Figure 3B).

To further investigate glia cell activation in reaction to s-GO treatment in complex systems, we measured from the spinal cord cultures supernatant (n = 6 for each condition) the presence of cytokine and chemokine, after 2 weeks *in-vitro*. s-GO induced an increased expression, when compared to controls, of CXCL2, and MCP1, T lymphocytes and monocytes recall factors, and IL6, IL10, BAFF and TNFα, cytokines responsible for pro-inflammatory responses (IL6, TNFα), regulatory function (IL10) and homeostatic B cell survival (BAFF), however the profiles of soluble factors production obtained from our analysis, did not reach statistical significance (Figure 3C). These observations are in line with a partial activation of microglial cells toward both polarized forms: M1 and M2, or most probably toward an intermediate one (Kabba et al., 2017).

3.3 s-GO Exposure Induces Microglial Proliferation in Neuroglial Cultures

The presence of several signatures of microglial cell activation after 2 weeks exposure to high s-GO dose, prompt us to directly investigate the effects of s-GO on microglial cell types in isolated glial preparations. Due to the relatively low-cell density typical of cultures comprising isolated Iba1-positive cells, as shown in Figure 4A (control), we exposed the cells for 5 days to a lower (10 μg/mL) dose of s-GO. s-GO readily increased Iba1-positive cell-density, as shown in Figure 4A, a response reminiscent of the one observed in organotypic slices (Figure 3B). In order to assess whether s-GO flakes induced microglia

activation, we analysed the cellular shape, a traditionally accepted index of the phenotypes microglia acquires when entrained in cytotoxic responses. In particular, a highly ramified shape is linked to a quiescent state in which microglia actively monitors the surrounding environment. On the other hand, an amoeboid phenotype reveals the transition to the activated, pro-inflammatory state (Saijo and Glass, 2011). Consistent with a transformation from a ramified to an amoeboid phenotype, the Feret's maximum diameter (plot in Figure 4B) significantly decreased ($P < 0.05$, Student's *t* test) after 6 days of s-GO exposure ($mean_{GO} = 47.03 \pm 2.20$; n = 42 cells), compared to control ($mean_{control} = 55.43 \pm 2.25$; n = 46 cells) (n = 6 visual fields for both conditions; 3 different cultures series). This suggested that the exposure to s-GO caused an activation of microglial cells.

Next we analysed the number of cycling cells present in each culture group (control and s-GO). For this purpose, cells were pulsed at 24 h and at 5 days with 10 mM bromodeoxyuridine (BrdU) prior to fixation. The number of cells that had incorporated the nucleotide analogue was then assessed by immunofluorescence, using anti-BrdU-specific antibodies. In Figure 4C the box plot shows the $BrdU^+/Iba1^+$ ratio, an index of microglial cells that incorporated BrdU in the newly synthesized DNA during cell division, providing a quantitative measure of proliferative capacity of cells (Nowakowski et al., 1989). The higher $BrdU^+/Iba1^+$ ratio was already significant at 24 hours of s-GO exposure ($median_{GO}$= 0.85; $median_{control}$=0.08), suggesting an early interaction of microglia with small graphene flakes. The increased proliferation was more pronounced after five days of incubation with s-GO ($median_{GO}$= 0.2; $median_{control}$=0.45; $P < 0.001$, Mann-Whitney test, for both time points; n=10 fields for each condition; 4 different cultures).

Microvesicles (MVs), released from almost all cell brain types, are, in general, an emerging intercellular communication over long-range distance. In particular, MVs discharged by microglial cells represent a secretory pathway for inflammatory cytokine (Antonucci et al, 2012) potentially promoting propagation of neuroinflammatory responses in the brain. We measured the release of MVs from isolated microglial cultures in control or exposed to s-GO by western blot analysis for the protein flotillin-1, a marker of lipid rafts that are specific plasma membrane regions were the probability of MVs release is higher (Figure 4D; Rauti et al., 2016). Pharmacological stimulation by bzATP induces only a slight release of MVs in isolated microglial cells, as depicted by the particularly weak signal in the specific band (Figure 4D). Interestingly, bzATP stimulation in the presence of s-GO triggers a massive microglia shedding of MVs, shown by the high intensity of the band (Figure 4D).

3.4 Localization of s-GO in microglial cells

By confocal microscopy reconstructions, we directly investigated the fate of s-GO in isolated microglia cultures. Iba1-positive cells (2 different culture series) were exposed for 3 days to s-GO (10 μg/mL). We tested the presence of s-GO flakes within Iba1 positive cells by operating the confocal microscopy under reflection mode. Figure 5A shows

confocal reconstructions of control and treated Iba1 positive cells. In s-GO-treated cells, graphene flakes aggregates (in yellow, reflection mode) were detected inside microglial cells (in grey, Iba1^{+}) by z-stack reconstruction (Figure 5, top panels: 40 ×; 100 × 100 μm^2 visualized area). In Figure 5, high magnification confocal micrographs (control and s-GO treated, bottom panels) are shown (60 ×; 50 × 50 μm^2 visualized area) depicting a single microglia (grey) cell that co-localize with the reflected signal of graphene (yellow). The orthogonal view of the z-projection shows the XZ and YZ planes (bottom side and right side of the z-stack reconstructed image, respectively) of the acquired fields. As expected from cells that work as macrophages, the material were internalized and stocked inside the cell, forming small aggregates, appreciable by the orthogonal reconstruction. The signal of s-GO was not present in control cells, either in the z-stack reconstruction or in the orthogonal planes (Figure 5, left panels).

4. Discussion

We used here organotypic spinal cord cultures to test tissue responses to s-GO prolonged delivery. In particular, we were interested in assessing microglia reactivity in cultured neural explants, where immune resident cells are present, but not supported by the peripheral ones.

The major result of the present investigation is that the long-term accumulation of s-GO (when delivered at high doses) activates resident microglia and, in the absence of an effective clearance, may induce a subtle, although chronic, reactive state, ultimately trimming down synaptic activity.

In our experiments, both GABAR- and AMPAR-mediated mPSCs were reduced in frequency upon s-GO exposure at high concentrations. The reduction in miniatures' frequency, but not in their amplitude, strongly suggests a reduction in the number of synapses or of release sites (Rauti et al., 2016). This down-regulation of synapses is apparently not due to a general cell membrane disruption or to neuronal apoptosis. In fact, we never detected alterations in basic electrophysiological parameters, reflecting neuronal health and membrane integrity (Carp, 1992; Djuric et al., 2015), indicating, together with the absence of up-regulated apoptosis, that the synaptic events diminished not as a consequence of direct neuronal damage brought about by s-GO. These findings are in accordance with our previous report, where s-GO sized down release sites in hippocampal cultures (Rauti et al., 2016). However, in organotypic slices, both glutamate- and GABA-mediated synapses were down regulated by s-GO, excluding the presence of s-GO glutamate synapse-specificity as previously described. The lack of specific synaptic targeting may be related to the diverse CNS regions tested, i.e. ventral spinal cord *vs* hippocampus, to the more immature stage of network formation (embryonic *vs* postnatal) or to the s-GO high concentrations and delivery modality used here: in fact, s-GO accumulated in the fibrin glue embedding the spinal culture and, presumably, was from

here released along 2 weeks of culturing. Although we cannot exclude the diverse CNS synapse geometries, allowing s-GO to interact with heterogeneous synapses in the spinal cord, we favour the hypothesis that the potential formation of a protein corona might have affected the nanoparticle biological fate (Bertrand et al., Nat Comm 2017). In addition, the presence in the spinal explants of microglia resident cells may result in a tissue reactivity that regulates synapses (Kettenmann et al., 2011), an effect that could not be observed within the previous experimental settings (Rauti et al., 2016). In fact, active phagocytosis restricted to intrinsic microglia, without the involvement of blood cells such as macrophages, could have activated these resident cells leading to a generic microglia response, known as synaptic stripping, ultimately leading to indiscriminate synapse reduction (Kettenmann et al., 2013).

In spinal organotypic slices exposed to s-GO, the presence of mild tissue reactivity is supported by the observed increase in microglia cell-density, in the absence of astrocyte reactivity (Olson, 2010; Okada et al., 2018). In addition, although not significantly, the cytokines and chemokines profiles measured in organotypic cultures supernatant, were found altered after 2 weeks of s-GO exposure. Therefore, in this model, we may hypothesize that microglial activation, accompanied by proliferative response and variation of CKs production, does not involve a significant shift into the M1 phenotype.

In support of a direct activation of microglial cells, in response to active s-GO phagocytosis, are our results obtained with isolated $Iba1^+$ cells. s-GO boosted microglia proliferation leading to a significantly higher cell density in pure neuroglia cultures, accompanied by the typical morphological switch from a ramified to an amoeboid phenotype (Nimmerjahn et al., 2005; Saijo and Glass, 2011; Cherry et al., 2014), suggestive of an active role of Iba1-positive cells in the tissue reaction to graphene, even in the virtual absence of other cell types. The direct activation of microglia was apparently related to fast internalization of s-GO flake aggregates that occurs during the first 24h after the exposure.

We thus suggest that s-GO, accumulated via the fibrin glue, activates resident microglia and phagocytosis. This hypothesis is also supported by the observation that pure microglial cultures grown and exposed to s-GO in a serum-free medium did not show a proliferation boost comparable to that found in the presence of FBS (Figure S1). As already discussed above, the interaction of nanoparticles such as s-GO with biological fluids may affect their fate and effectiveness. In fact, the corona formation takes place not only in the presence of plasma proteins like fibrinogen but also with proteins present in the serum (Gräfe et al., 2016). Therefore, activation and proliferation response found in both pure microglial cultures and organotypic slices exposed to s-GO, despite their different origin and architecture, may be explained by an increase of the efficacy in the uptake of the material (Walkey et al., 2012) by microglia and mediated by s-GO interactions with the proteins pool of plasma and serum.

An additional indication of microglia reactivity in s-GO was provided by the increased release of shed vesicles induced by bzATP. MVs released by microglia have been reported to affect synaptic activity, mainly acting at the presynaptic site of the excitatory synapses, but increasing synaptic activity and release in primary cultures (Antonucci et al., 2012) thus it seems unfeasible that the down regulation in synapses is due to MVs release.
We favour the possibility that, in the current experimental conditions, the global reduction in synaptic activity accompanies tissue reactivity in general, more than being a specific targeting of synapses by s-GO (Rauti et al., 2016). However, we have to ask ourselves whether these data indicate a potential in vivo inflammatory response due to s-GO flakes. There are several relevant aspects that limit reporting it as an inflammatory response. First of all, the conditions we tested involved the delivering of s-GO to a "closed" biological system, allowing only resident macrophages to interact with it and limiting the contribution of neighbour tissues in the interaction with this material, how it would happen in an in vivo model. The lack of significance in the chemokines and cytokines concentration, that showed only a trend, suggest a mild immune response that may not necessary lead to a pathological inflammatory state or alternatively indicates a return to a physiological condition, from an intermediate immune activation. Last, astrocytes, which depend on microglia activation to be polarized to pro-inflammatory cells (Liddelow et al., 2017) did not show, in this context, reactive gliosis.
Microglia produces immune mediators secondary to neuronal stimulation, (i.e. tissue injury), or following a direct stimulus to microglia itself. Here we report an increased proliferation rate of Iba1-positive cells, suggestive of microglia activation, and consistent with morphological observations. However, the detected cell activation seems to involve a group of cells, not all of them, and this may explain the fact that we observed only a trend toward increased production of immune factors, without significant variations. We may hypothesize that the fraction of activated microglia includes cells in direct contact to s-GO. Indeed, microglia is often reported to function similarly to other myeloid cells, the macrophages, able to scavenge the environment, perform phagocytosis, antigen presentation and to react to contact with nano materials (Jin and Yamashita, 2016; Aldinucci et al., 2013) in order to maintain CNS homeostasis, with both detrimental and beneficial effects. It is important to underline that the pro-inflammatory molecules, increased after s-GO contact, were not enhancing astrogliosis. Therefore, as a side effect, our in vitro model not only allows the direct observation and study of material/neuron interactions in the presence of glial cells, but simulates accumulation of material in CNS and the possible consequences.

6. Figures

Figure 1. In (A) confocal micrograph of a spinal slice culture (14 DIV) immune-labelled for the neurofilament H (SMI-32; in green) and the nuclei (DAPI; in blue; scale bar 500

μm). In (B) sketch of the experimental setting for ventral interneuron recordings. In (C) spontaneous synaptic activity recorded from ventral interneurons in Control and s-GO treated slices (50 μg/mL). In the inset: isolated fast and slow events are shown superimposed (in white averaged tracings). In (D) the plots represent pooled data of average PSCs frequency and amplitude values; note the reduction in PSC frequency upon s-GO treatments (25 and 50 μg/mL) (* = $P < 0.05$ and ** = $P < 0.01$, respectively; Student's *t* test). In (E) confocal micrographs visualize caspase-3 positive cells (in red), counter-stained for β-tubulin III (in green, to visualize neurons) in Control (left) and s-GO (50 μg/mL; right) treated slices. Nuclei are visualized by DAPI (blue; scale bar: 50 μm). The histograms summarize the density of caspase and β-tubulin double positive cells; note the absence of statistical significant differences between the two conditions.

Figure 2. Sample tracings of mPSCs recorded in Control and s-GO (50 μg/mL) treated cultures (left panel). Right panel: plot reporting mPSCs frequency values in control and in the three different s-GO concentrations tested. s-GO treatment (25 and 50 μg/mL) significantly decreased the frequency of mPSCs (* = $P < 0.05$ and ** = $P < 0.01$, respectively; Student's *t* test). Bottom: histograms summarize the average values of AMPA-glutamate (left panel) and $GABA_A$ (right panel) receptor mediated mPSCs pharmacologically isolated. In s-GO treatments (50 μg/mL) a significant decrease in the frequency of both mPSCs was detecetd (* = $P < 0.05$ and ** = $P < 0.01$, respectively; Student's *t* test).

Figure 3. In (A) immune-labelling of astrocytes in Control and s-GO treated slices (50 μg/mL). Both cultures were labelled for GFAP (in green) and nuclei (visualized by DAPI; in blue; scale bar 100 μm). GFAP+ cell density did not differ between the two conditions (right plot). In (B) immunofluorescence images are shown to visualize glial and microglial cells in the two different conditions, Control and s-GO (50 μg/mL) treated slices (anti-Iba1, in red; anti-GFAP in green; nuclei are visualized by DAPI in blue; scale bar 50 μm). Note that Iba1+ cell density was significantly ($P < 0.01$, Student's *t* test) increased by s-GO (50 μg/mL; right histograms). In (C) In organotypic culture supernatant we detected by Milliplex assay the production of the following cytokines: IL6, IL10, TNF and BAFF and chemokines: CXCL1, CXCL2, CXCL10 and MCP1 in the presence or absence of s-GO, after 2 weeks *in vitro*. Column graphs report mean values ± SEM of 6 independent experiments. We observed a trend toward IL-6, IL10. TNF and BAFF increase in s-GO supernatant.

Figure 4. Cell density analysis (A) of microglial cells in control and s-GO treated microglial cultures (10 μg/mL). Both cultures were immunostained for Iba1 (red) to visualize microglia. The microglial density is significantly higher in cultures treated with s-GO (right plot) ($P < 0.001$, Student's *t* test). In (B) high magnification of Iba1+ cells highlight the different morphology detected in s-GO treated cultures, the right plot

summarizes the Ferret's maximum diameter, an index of cellular ramification, that is significantly decreased ($P < 0.05$, Student's *t*-test) after s-GO exposure.
In (C) box plots show the brdU+/Iba1+ ratio measured in isolated microglial cultures 24h and 5 days after s-GO exposure (10 µg/mL) ($P < 0.001$, Mann-Whitney test, for both timepoints) Note the statistical significant differences ($P<0.001$). In (D) western blot analysis for the MVs marker flotillin-1 of each condition. Microvesicles were isolated from glial cultures incubated with s-GO (10 µg/mL) for 6 days and then treated or not with bzATP.
Figure 5. Representative confocal reconstructions of microglial cells in Control or treated with s-GO (10 µg/mL), scale bar 20 µm. In the bottom panel, for both conditions a 60 × zoom (50 × 50 µm field) of a single microglial cell (scale bar 20 µm) is shown. Cultures are immunostained for Iba1 (in grey), and DAPI (in blue), s-GO is visualized by the reflection mode of the confocal system (in yellow). s-GO flakes are visible as aggregates coloured in yellow inside the cell.

6. Conflict of Interest

The authors declare that the research was conducted in the absence of any commercial or financial relationships that could be construed as a potential conflict of interest.

7. Author Contributions

M.M. and R.R. performed all cell biology, electrophysiology, and confocal experiments and analysis; N.L. and K.K. contributed to the synthesis and characterization of thin graphene oxide (s-GO); E.B. and C.B. designed and performed the supernatant measures; L.C. contributed to the MVs analysis; C. B. and L.B. conceived the experimental design and wrote the manuscript.

8. Funding

We acknowledged financial support from the European Union's Horizon 2020 research and innovation programme under grant agreement No 696656.

9. Acknowledgments

We are especially grateful to Gabriele Baj for the confocal reconstructions of microglial cells generated at the Light Microscopy Imaging Center (LMIC) of the University of Trieste - Life Sciences Department.

10. References

1. Al-Nedawi, K., Meehan, B., Micallef, J., Lhotak, V., May, L., Guha, A., Rak, J. (2008). Intercellular Transfer of the Oncogenic Receptor EGFRvIII by Microvesicles Derived from Tumour Cells. *Nat. Cell Biol.* 10, 619−624. doi: 10.1038/ncb1725.
2. Aldinucci, A., Turco, A., Biagioli, T., Toma, F. M., Bani, D., Guasti, D., Manuelli, C., Rizzetto, L., Cavalieri, D., Massacesi, L., Mello, T., Scaini, D., Bianco, A., Ballerini, L., Prato, M., Ballerini, C. (2013). Carbon nanotube scaffolds instruct human dendritic cells: modulating immune responses by contacts at the nanoscale. *Nano Lett*. 13, 6098-6105. doi:10.1021/nl403396e.
3. Aloisi, F. (1999). The role of microglia and astrocytes in cns immune surveillance and immunopathology. *Adv. Exp. Med. Biol.* 468, 123-133.
4. Antonucci, F., Turola, E., Riganti, L., Caleo, M., Gabrielli, M., Perrotta, C., Novellino, S., Clementi, E., Giussani, P., Viani, P., Matteoli, M., Verderio, C. (2012). Microvesicles released from microglia stimulate synaptic activity via enhanced sphingolipid metabolism. *EMBO J*. 31, 1231-1240.
5. Avossa, D., Grandolfo, M., Mazzarol, F., Zatta, M., Ballerini, L. (2006). Early signs of motoneuron vulnerability in a disease model system: Characterization of transverse slice cultures of spinal cord isolated from embryonic ALS mice. *Neuroscience* 138, 1179-1194. doi: 10.1016/j.neuroscience.2005.12.009.
6. Avossa, D., Rosato-Siri, M.D., Mazzarol, F., Ballerini, L. (2003). Spinal circuits formation: A study of developmentally regulated markers in organotypic cultures of embryonic mouse spinal cord. *Neuroscience* 122, 391-405. doi:10.1016/j.neuroscience.2003.07.006.
7. Baldrighi, M., Trusel, M., Tonini, R., Giordani, S. (2016). Carbon Nanomaterials Interfacing with Neurons: An In vivo Perspective. *Front. Neurosci.* 10:250. doi: 10.3389/fnins.2016.00250.
8. Ballerini, L., Galante, M. (1998). Network bursting by organotypic spinal slice cultures in the presence of bicuculline and/or strychnine is developmentally regulated. *Eur. J. Neurosci*. 10, 2871-2879. doi: 10.1111/j.1460-9568.1998.00296.x.
9. Ballerini, L., Galante, M., Grandolfo, M., Nistri, A. (1999). Generation of rhythmic patterns of activity by ventral interneurons in rat organotypic spinal slice culture. *J. Physiol*. 517, 459-475. doi: 10.1111/j.1469-7793.1999.0459.t.x.
10. Bertrand, N., Grenier, P., Mahmoudi, M., Lima, E. M., Appel, E. A., Dormont, F., Lim, J. M., Karnik, R., Langer, R., Farokhzad, O. C. (2017). Mechanistic understanding of in vivo protein corona formation on polymeric nanoparticles and impact on pharmacokinetics. *Nat. Commun.* 8:777. doi: 10.1038/s41467-017-00600-w.

11. Bianco, F., Perrotta, C, Novellino, L., Francolini, M., Riganti, L., Menna, E., Saglietti, L., Schuchman, Eh., Furlan, R., Clementi, E., Matteoli, M., Verderio, C. (2009). Acid sphingomyelinase activity triggers microparticle release from glial cells. *EMBO J.* 28, 1374. doi: 10.1038/emboj.2009.45.
12. Block, M. L., Zecca, L., Hong, J. S. (2007). Microglia-mediated neurotoxicity: uncovering the molecular mechanisms. *Nat. Rev. Neurosci.* 8, 57-69. doi: 10.1038/nrn2038.
13. Bosi, S., Rauti, R., Laishram, J., Turco, A., Lonardoni, D., Nieus, T., Prato, M., Scaini, D., Ballerini, L. (2015). From 2D to 3D: novel nanostructured scaffolds to investigate signalling in reconstructed neuronal networks. *Sci. Rep.* 5, 9562. doi: 10.1038/srep09562.
14. Bramini, M., Sacchetti, S., Armirotti, A., Rocchi, A., Vázquez, E., León Castellanos, V., Bandiera, T., Cesca, F., Benfenati, F. (2016). Graphene Oxide Nanosheets Disrupt Lipid Composition, $Ca^{(2+)}$ Homeostasis, and Synaptic Transmission in Primary Cortical Neurons. *ACS Nano* 10, 7154-7171. doi: 10.1021/acsnano.6b03438.
15. Calegari, F., Coco, S., Taverna, E., Bassetti, M.; Verderio, C., Corradi, N., Matteoli, M., Rosa, P. A. (1999). Regulated Secretory Pathway in Cultured Hippocampal Astrocytes. *J. Biol. Chem.* 274, 22539−22547. doi: 10.1074/jbc.274.32.22539.
16. Carp, J. S. (1992). Physiological properties of primate lumbar motoneurons. *J. Neurophysiol*. 68, 1121-1132. doi: org/10.1152/jn.1992.68.4.1121.
17. Cherry, J. D., Olschowka, J. A., O'Banion, M. K. (2014). Neuroinflammation and M2 microglia: the good, the bad, and the inflamed. *J. Neuroinflammation* 11, 98. doi: 10.1186/1742-2094-11-98.
18. Cohen, P. (1997). The search for physiological substrates of MAP and SAP kinases in mammalian cells. *Trends Cell Biol.* 7, 353-361. doi: 10.1016/S0962-8924(97)01105-7
19. Davalos, D., Grutzendler, J., Yang, G., Kim, J. V., Zuo, Y., Jung, S., Littman, D. R., Dustin, M. L., Gan, W. B. (2005). ATP mediates rapid microglial response to local brain injury in vivo. *Nat. Neurosci*. 8, 752-758. doi: 10.1038/nn1472.
20. Del Conde, I., Shrimpton, C. N., Thiagarajan, P.; López, J. A. (2005) Tissue-Factor-Bearing Microvesicles Arise from Lipid Drafts and Fuse with Activated Platelets to Initiate Coagulation. *Blood* 106, 1604−1611. doi: 10.1182/blood-2004-03-1095.
21. Djuric, U., Cheung, A. Y., Zhang, W., Mok, R. S., Lai, W., Piekna, A., Hendry, J. A., Ross, P. J., Pasceri, P., Kim, D. S., Salter, M. W., Ellis, . (2015). MECP2e1 isoform mutation affects the form and function of neurons derived from Rett syndrome patient iPS cells. *Neurobiol. Dis*. 76, 37-45. doi: 10.1016/j.nbd.2015.01.001.
22. Fabbro A., Scaini D., León V., Vázquez E., Cellot G., Privitera G., Lombardi L., Torrisi F., Tomarchio F., Bonaccorso F., Bosi S., Ferrari A. C., Ballerini L., Prato M.

Graphene-based interfaces do not alter target nerve cells. (2016). *ACS Nano* 10, 615-623. doi: 10.1021/acsnano.5b05647.

23. Farina, C., Aloisi, F., Meinl, E. (2007). Astrocytes are active players in cerebral innate immunity. *Trends Immunol.* 28, 138-145. doi: 10.1016/j.it.2007.01.005.
24. Fetler, L., Amigorena, S. (2005). Neuroscience. Brain under surveillance: the microglia patrol. *Science* 309, 392-393. doi: 10.1126/science.1114852.
25. Fischer, H. P., Marksteiner, J., Ransmayr, G., Saria, A., Humpel, C. (1998). NGF but not GDNF or neurturin enhance acetylcholine tissue levels in striatal organotypic brain slices. *Int. J. Dev. Neurosci.* 16, 391-401. doi: 10.1016/S0736-5748(98)00039-2.
26. Furlan, F., Guasti, L., Avossa, D., Becchetti, A., Cilia, E., Ballerini, L., Arcangeli, A. (2005). Interneurons transiently express the ERG K+ channels during development of mouse spinal networks in vitro. *Neuroscience* 135, 1179-1192. doi: 10.1016/j.neuroscience.2005.06.040.
27. Furlan, F., Taccola, G., Grandolfo, M., Guasti, L., Arcangeli, A., Nistri, A., Ballerini, L. (2007). ERG conductance expression modulates the excitability of ventral horn GABAergic interneurons that control rhythmic oscillations in the developing mouse spinal cord. *J. Neurosci.* 27, 919-928. doi: 10.1523/JNEUROSCI.4035-06.2007.
28. Gähwiler, B. H. (1981). Organotypic monolayer cultures of nervous tissue. *J. Neurosci. Methods* 4, 329-342.
29. Galante, M., Avossa, D., Rosato-Siri, M., Ballerini, L. (2001). Homeostatic plasticity induced by chronic block of AMPA/kainite receptors modulates the generation of rhythmic bursting in rat spinal cord organotypic cultures. *Eur. J. Neurosci*. 14, 903-917. doi: 10.1046/j.0953-816x.2001.01710.x.
30. Galante, M., Nistri, A., Ballerini, L. (2000). Opposite changes in synaptic activity of organotypic rat spinal cord cultures after chronic block of AMPA/kainate or glycine and $GABA_A$ receptors. *J. Physiol*. 523, 639-651. doi: 10.1111/j.1469-7793.2000.t01-1-00639.x.
31. Gräfe, C., Weidner, A., v.d Lühe, M., Bergermann, C., Schacher, F. H., Clement, J., Dutz, S. (2016). Intentional formation of a protein corona on nanoparticles: Serum concentration affects protein corona mass, surface charge, and nanoparticle–cell interaction. *Int. J. Biochem. Cell Biol*. 75:196-202. doi: 10.1016/j.biocel.2015.11.005.
32. Hailer, N. P., Jarhult, J. D., Nitsch, R. (1996). Resting microglial cells in vitro: analysis of morphology and adhesion molecule expression in organotypic hippocampal slice cultures. *Glia* 18, 319-331.
33. Hanisch, U.K. (2002). Microglia as a source and target of cytokines. *Glia* 40, 140-155 doi: 10.1002/glia.10161.

34. Hanisch, U. K., Kettenmann, H. (2007). Microglia: active sensor and versatile effector cells in the normal and pathologic brain. *Nat. Neurosci.* 10, 1387-1394. doi:10.1038/nn1997.
35. Hu, W., Peng, C., Luo, W., Lv, M., Li, X., Li, D., Huang, Q., Fan, C. (2010). Graphene-based antibacterial paper. *ACS Nano* 4, 4317-4323. doi: 10.1021/nn101097v.
36. Jin, X., Yamashita, T. (2016). Microglia in central nervous system repair after injury. *J. Biochem*. 159, 491-496. doi: 10.1093/jb/mvw009.
37. Kabba, J. A., Xu, Y., Christian, H., Ruan, W., Chenai, K., Xiang, Y., Zhang, L., Saavedra, J. M., Pang, T. (2017). Microglia: Housekeeper of the Central Nervous System. *Cell Mol. Neurobiol.* doi: 10.1007/s10571-017-0504-2.
38. Kettenmann, H., Hanisch, U. K., Noda, M., Verkhratsky, A. (2011). Physiology of microglia. *Physiol. Rev.* 91, 461-553. doi: 10.1152/physrev.00011.2010.
39. Kettenmann H., Kirchhoff F., Verkhratsky A. (2013). Microglia: new roles for the synaptic stripper. *Neuron* 77, 10-18. doi: 10.1016/j.neuron.2012.12.023.
40. Kostarelos, K., Novoselov, K. S. (2014). Materials science. Exploring the interface of graphene and biology. *Science* 344, 261-263. doi: 10.1126/science.1246736.
41. Liddelow S. A., Guttenplan K. A., Clarke L. E., Bennett F. C., Bohlen C. J., Schirmer L., Bennett M. L., Münch A. E., Chung W. S., Peterson T. C., Wilton D. K., Frouin A., Napier B. A., Panicker N., Kumar M., Buckwalter M. S., Rowitch D. H., Dawson V. L., Dawson T. M., Stevens B., Barres B. A. (2017). *Nature* 541, 481-487. doi: 10.1038/nature21029.
42. Li, N., Zhang, Q., Gao, S., Song, Q., Huang, R., Wang, L., Liu, L., Dai, J., Tang, M., Cheng, G. (2013). Three-dimensional graphene foam as a biocompatible and conductive scaffold for neural stem cells. *Sci Rep*. 3. doi: 10.1038/srep01604.
43. Mao, H. Y., Laurent, S., Chen, W., Akhavan, O., Imani, M., Ashkarran, A. A., Mahmoudi, M. (2013). Graphene: promises, facts, opportunities, and challenges in nanomedicine. *Chem. Rev*. 113, 3407-3424. doi: 10.1021/cr300335p.
44. Medelin, M., Rancic, V., Cellot, G., Laishram, J., Veeraraghavan, P., Rossi, C., Muzio, L., Sivilotti, L., Ballerini L. (2016). Altered development in GABA co-release shapes glycinergic synaptic currents in cultured spinal slices of the SOD1(G93A) mouse model of amyotrophic lateral sclerosis. *J. Physiol.* 594, 3827-3840. doi: 10.1113/JP272382.
45. Medelin M., Giacco V., Aldinucci A., Castronovo G., Bonechi E., Sibilla A., Tanturli M., Torcia M., Ballerini L., Cozzolino F., Ballerini C. (2018). Bridging pro-inflammatory signals, synaptic transmission and protection in spinal explants in vitro. *Mol. Brain.* 11. doi: 10.1186/s13041-018-0347-x.

46. Nimmerjahn, A., Kirchhoff, F., Helmchen, F. (2005). Resting microglial cells are highly dynamic surveillants of brain parenchyma in vivo. *Science* 308, 1314-1318. doi: 10.1126/science.1110647.
47. Nowakowski, R. S., Lewin, S. B., Miller, M. W. (1989). Bromodeoxyuridine immunohistochemical determination of cell lenghts of the cell cycle and the DNA-syntetic phase for an anatomically defined population. *J. Neurocytol.* 18, 311-318.
48. Okada, S., Hara, M., Kobayakawa, K., Matsumoto, Y., Nakashima, Y. Astrocyte reactivity and astrogliosis after spinal cord injury. (2018). *Neurosci. Res.* 126, 39-43.
49. Olson, J. K. Immune response by microglia in the spinal cord. (2010). *Ann. N. Y. Acad. Sci.* 1198, 271-278.
50. Qian, J., Wang, D., Cai, F. H., Xi, W., Peng, L., Zhu, Z. F., He, H., Hu, M. L., He, S. (2012). Observation of multiphoton-induced fluorescence from graphene oxide nanoparticles and applications in in vivo functional bioimaging. *Angew. Chem. Int. Ed. Engl.* 51, 10570-10575. doi: 10.1002/anie.201206107.
51. Raastad, M., Storm, J. F., Andresen, P. (1992). Putative single quantum and single fibre excitatory postsynaptic currents show similar amplitude range and variability in rat hippocampal slices. *Eur. J. Neurosci*. 4, 113-117. doi: 10.1111/j.1460-9568.1992.tb00114.x.
52. Rauti, R., Lozano, N., León, V., Scaini, D., Musto, M., Rago, I., Ulloa Severino, F. P., Fabbro, A., Casalis, L., Vázquez. E., Kostarelos, K., Prato, M., Ballerini, L. (2016). Graphene Oxide Nanosheets Reshape Synaptic Function in Cultured Brain Networks. *ACS Nano*. 10, 4459-4471. doi: 10.1021/acsnano.6b00130.
53. Rosato-Siri, M., Grandolfo, M., Ballerini, L. (2002). Activity-dependent modulation of GABAergic synapses in developing rat spinal networks in vitro. *Eur. J. Neurosci*. 16, 2123-2135. doi: 10.1046/j.1460-9568.2002.02291.x.
54. Rothman, S. M., Samaie, M. (1985). Physiology of excitatory synaptic transmission in cultures of dissociated rat hippocampus. *J. Neurophysiol.* 54, 701-713 doi.org/10.1152/jn.1985.54.3.701.
55. Ryoo, S. R., Kim, Y. K., Kim, M. H., Min, D. H. (2010). Behaviors of NIH-3T3 fibroblasts on graphene/carbon nanotubes: proliferation, focal adhesion, and gene transfection studies. *ACS Nano* 4, 6587-6598. doi: 10.1021/nn1018279.
56. Saijo, K., Glass. C. K. (2011). Microglial cell origin and phenotypes in health and disease. *Nat. Rev. Immunol.* 11, 775-787. doi: 10.1038/nri3086.
57. Sanchez, V. C., Jachak, A., Hurt, R. H., Kane, A. B. (2012). Biological interactions of graphene-family nanomaterials: an interdisciplinary review. *Chem. Res. Toxicol*. 25, 15-34. doi: 10.1021/tx200339h.
58. Schermer, C., Humpel, C. (2002). Granulocyte macrophage-colony stimulating factor activates microglia in rat cortex organotypic brain slices. *Neurosci. Lett.* 328, 180-184. doi: 10.1016/S0304-3940(02)00496-2.

59. Schindelin, J., Arganda-Carreras, I., Frise, E., Kaynig, V., Longair, M., Pietzsch, T., Preibisch, S., Rueden, C., Saalfeld, S., Schmid, B., Tinevez, J. Y., White, D. J. Hartenstein, V., Eliceiri, K., Tomancak, P., Cardona, A. (2012). Fiji: an open-source platform for biological-image analysis. *Nat Methods* 9, 676-682. doi: 10.1038/nmeth.2019.
60. Segal, M., Barker, J. L. (1984). Rat hippocampal neurons in culture: properties of GABA-activated Cl- ion conductance. *J. Neurophysiol.* 51, 500-515. doi: 10.1152/jn.1984.51.3.500.
61. Song, Q., Jiang, Z., Li, N., Liu, P., Liu, L., Tang, M., Cheng, G. (2014). Anti-inflammatory effects of three-dimensional graphene foams cultured with microglial cells. *Biomaterials* 35, 6930-6940. doi: 10.1016/j.biomaterials.2014.05.002.
62. Streit, J. (1993). Regular oscillations of synaptic activity in spinal networks in vitro. *J. Neurophysiol*. 70, 871-878. doi: 10.1152/jn.1993.70.3.871.
63. Tian, L., Ma, L., Kaarela, T., Li, Z. (2012). Neuroimmune crosstalk in the central nervous system and its significance for neurological diseases. *J. Neuroinflammation*. 9, 155. doi: 10.1186/1742-2094-9-155.
64. Tscherter, A., Heuschkel, M. O., Renaud, P., Streit, J. (2001). Spatiotemporal characterization of rhythmic activity in rat spinal cord slice cultures. *Eur. J. Neurosci.* 14, 179-190. doi: 10.1046/j.0953-816x.2001.01635.x.
65. Usmani, S., Aurand, E. R., Medelin, M., Fabbro, A., Scaini, D., Laishram, J., Rosselli, F. B., Ansuini, A., Zoccolan, D., Scarselli, M., De Crescenzi, M., Bosi, S., Prato, M., Ballerini, L. (2016). 3D meshes of carbon nanotubes guide functional reconnection of segregated spinal explants. *Sci Adv.* 2, e1600087. doi: 10.1126/sciadv.1600087.
66. Walkey, C. D., Olsen, J. B., Guo, H., Emili, A., Chan, W. C. W. (2012). Nanoparticle size and surface chemistry determine serum protein adsorption and macrophage uptake. *J. Am. Chem. Soc*. 134(4):2139-47. doi: 10.1021/ja2084338.
67. Wang, Y., Lee, W. C., Manga, K. K., Ang, P. K., Lu, J., Liu, Y. P., Lim, C. T., Loh, K. P. (2012). Fluorinated graphene for promoting neuro-induction of stem cells. *Adv. Mater.* 24, 4285-4290. doi: 10.1002/adma.201200846.
68. Wang, Y., Li, Z., Wang, J., Li, J., Lin, Y. (2011). Graphene and graphene oxide: biofunctionalization and applications in biotechnology. *Trends Biotechnol*. 29, 205-212. doi: 10.1016/j.tibtech.2011.01.008.
69. Zhang, Y., Ali, S. F., Dervishi, E., Xu, Y., Li, Z., Casciano, D., Biris, A. S. (2010). Cytotoxicity effects of graphene and single-wall carbon nanotubes in neural phaeochromocytoma-derived PC12 cells. *ACS Nano* 4, 3181-3186. doi: 10.1021/nn1007176.

FIGURE 1

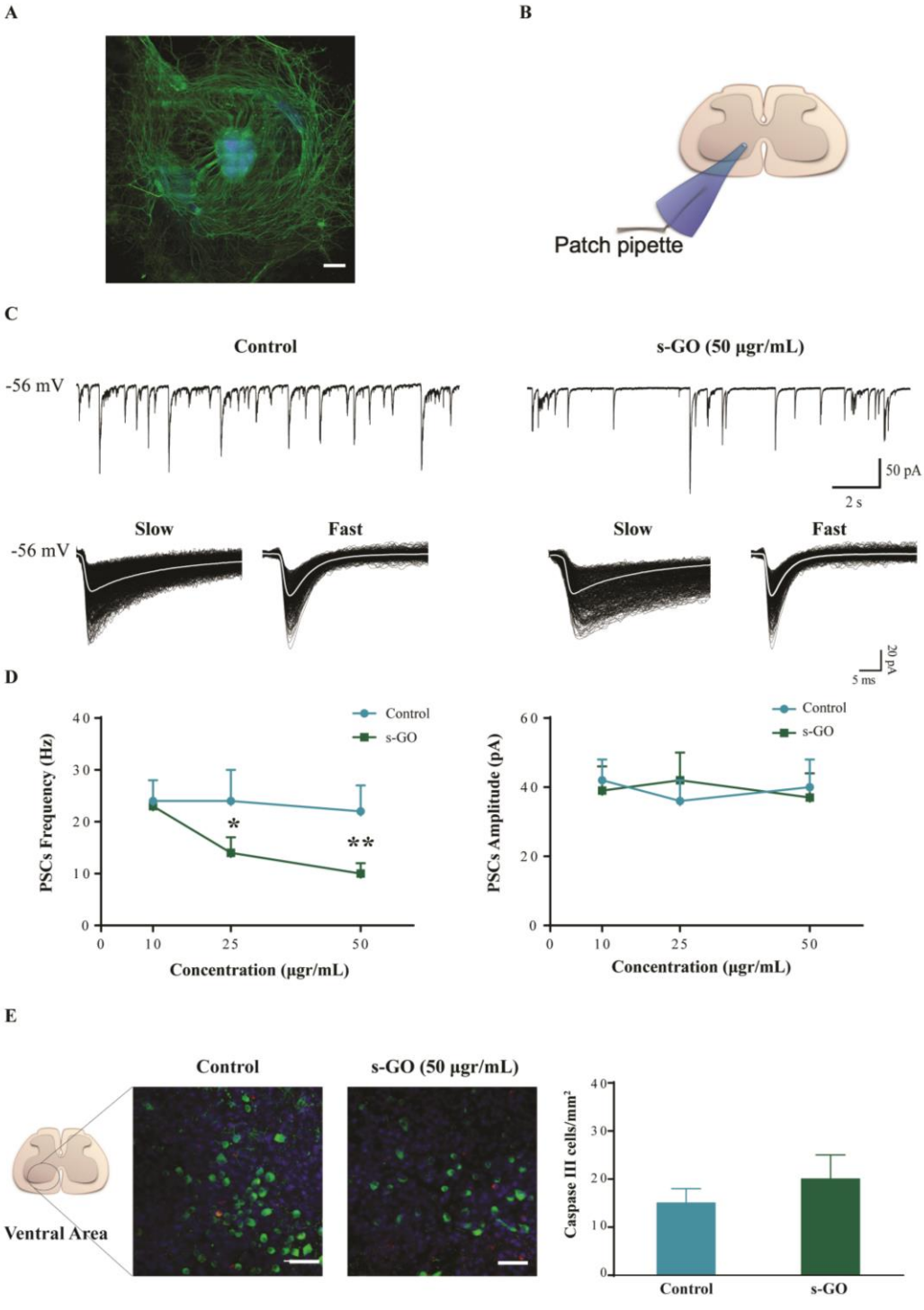
A
B
Patch pipette
C
Control
s-GO (50 µgr/mL)
-56 mV
50 pA
2 s
Slow
Fast
-56 mV
20 pA
5 ms
D
Control
s-GO
PSCs Frequency (Hz)
PSCs Amplitude (pA)
Concentration (µgr/mL)
*
**
E
Control
s-GO (50 µgr/mL)
Ventral Area
Caspase III cells/mm²
Control
s-GO

FIGURE 2

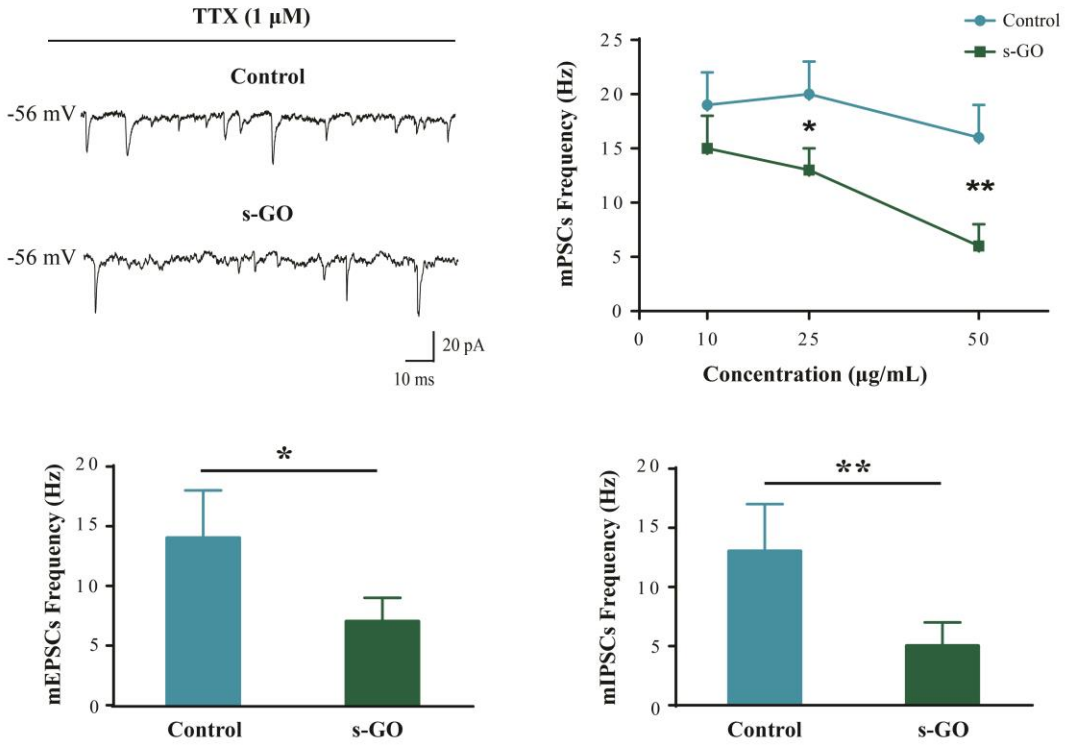
TTX (1 µM)
Control
-56 mV
s-GO
-56 mV
20 pA
10 ms
Control
s-GO
mPSCs Frequency (Hz)
Concentration (µg/mL)
*
**
mEPSCs Frequency (Hz)
Control
s-GO
*
mIPSCs Frequency (Hz)
Control
s-GO
**

FIGURE 3

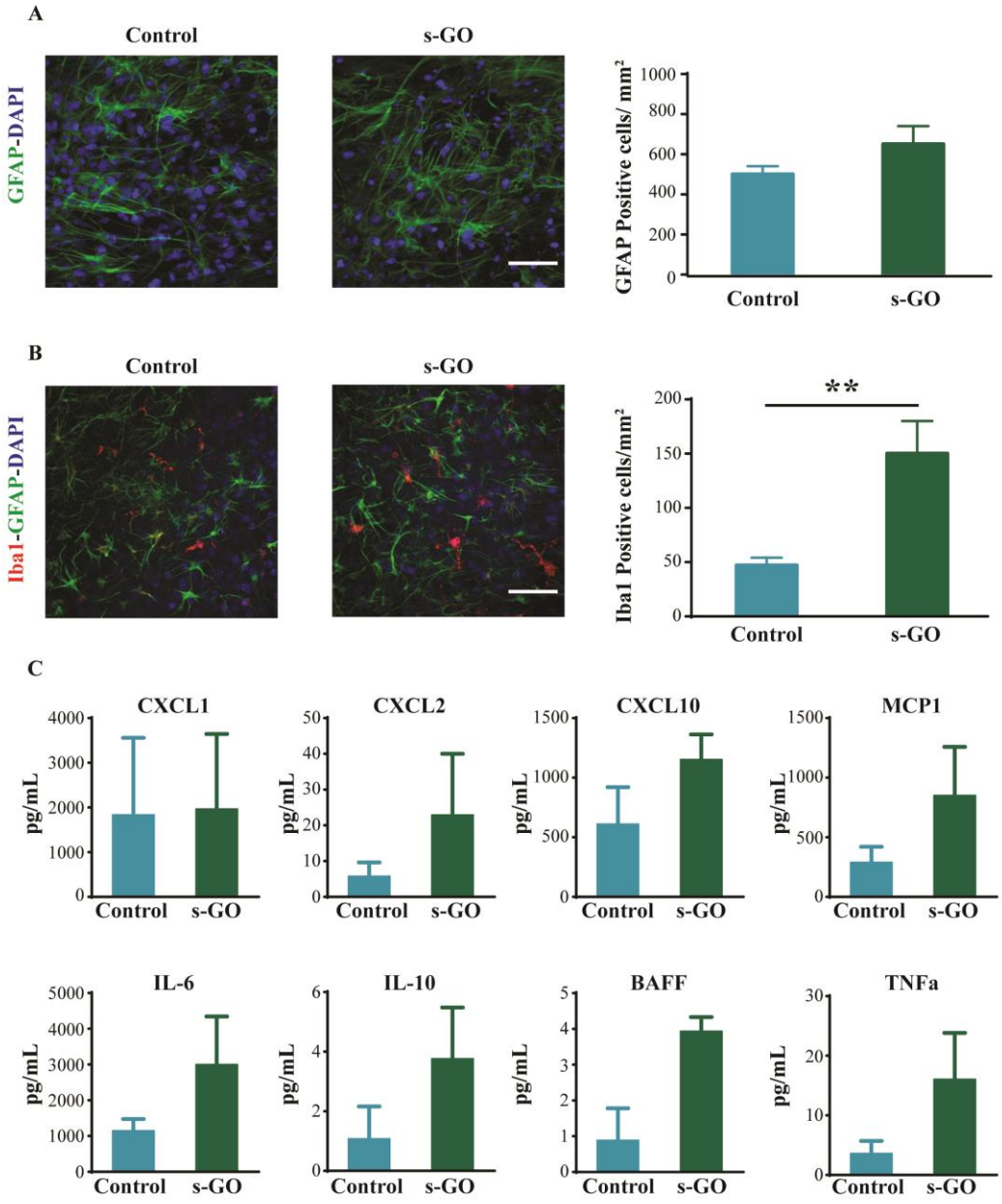
A
Control
s-GO
GFAP-DAPI
GFAP Positive cells/ mm²
1000
800
600
400
200
0
Control
s-GO
B
Control
s-GO
Iba1-GFAP-DAPI
Iba1 Positive cells/mm²
**
200
150
100
50
0
Control
s-GO
C
CXCL1
CXCL2
CXCL10
MCP1
pg/mL
4000
3000
2000
1000
0
50
40
30
20
10
1500
1000
500
Control
s-GO
IL-6
IL-10
BAFF
TNFa
5000
6
4
2
5
3
1
30
20
10

FIGURE 4

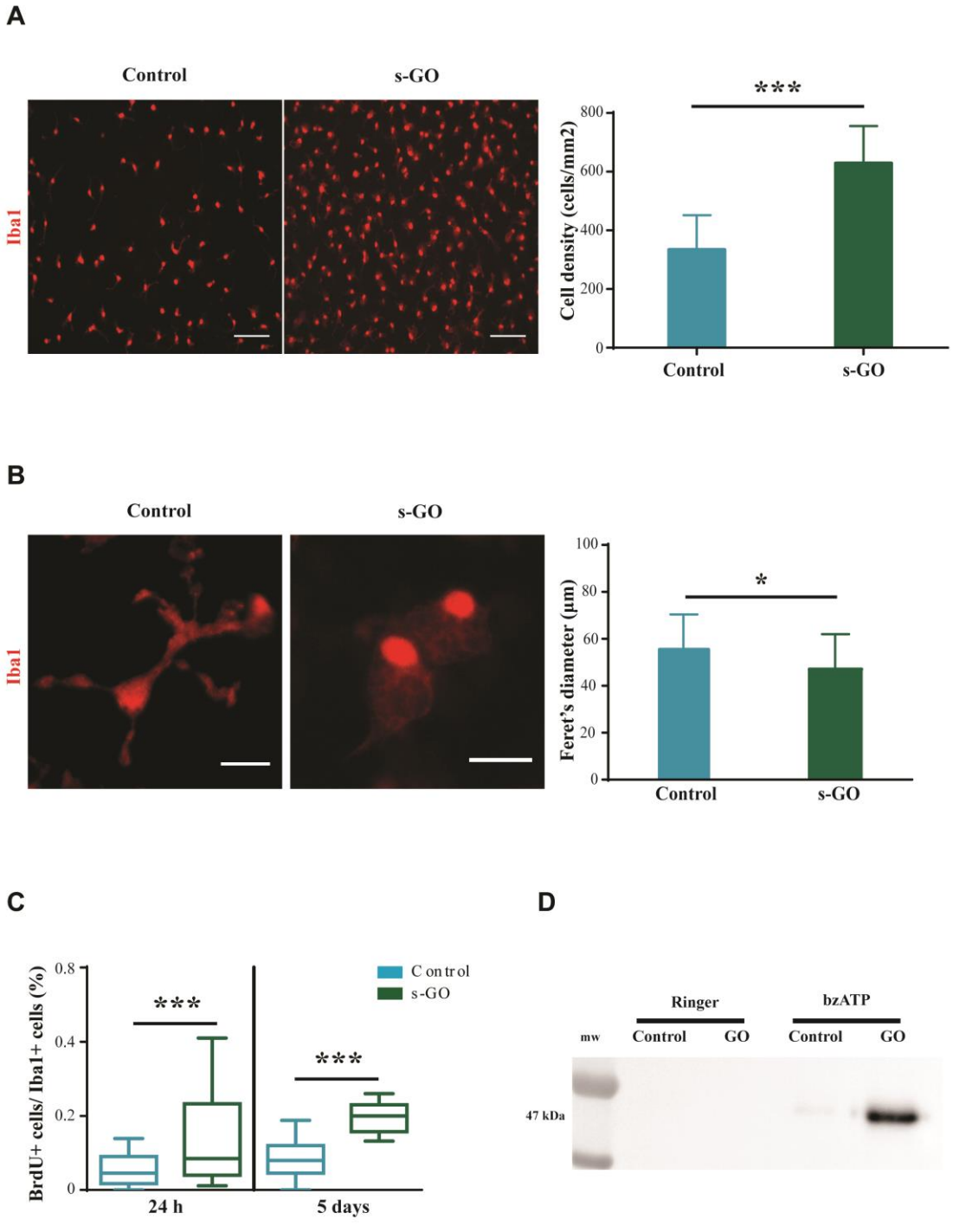
A
Control
s-GO
Iba1
***
Cell density (cells/mm2)
800
600
400
200
0
Control
s-GO
B
Control
s-GO
Iba1
*
Feret's diameter (µm)
100
80
60
40
20
0
Control
s-GO
C
BrdU+ cells/ Iba1+ cells (%)
0.8
0.4
0.2
0
***
***
Control
s-GO
24 h
5 days
D
Ringer
bzATP
mw
Control
GO
Control
GO
47 kDa

FIGURE 5

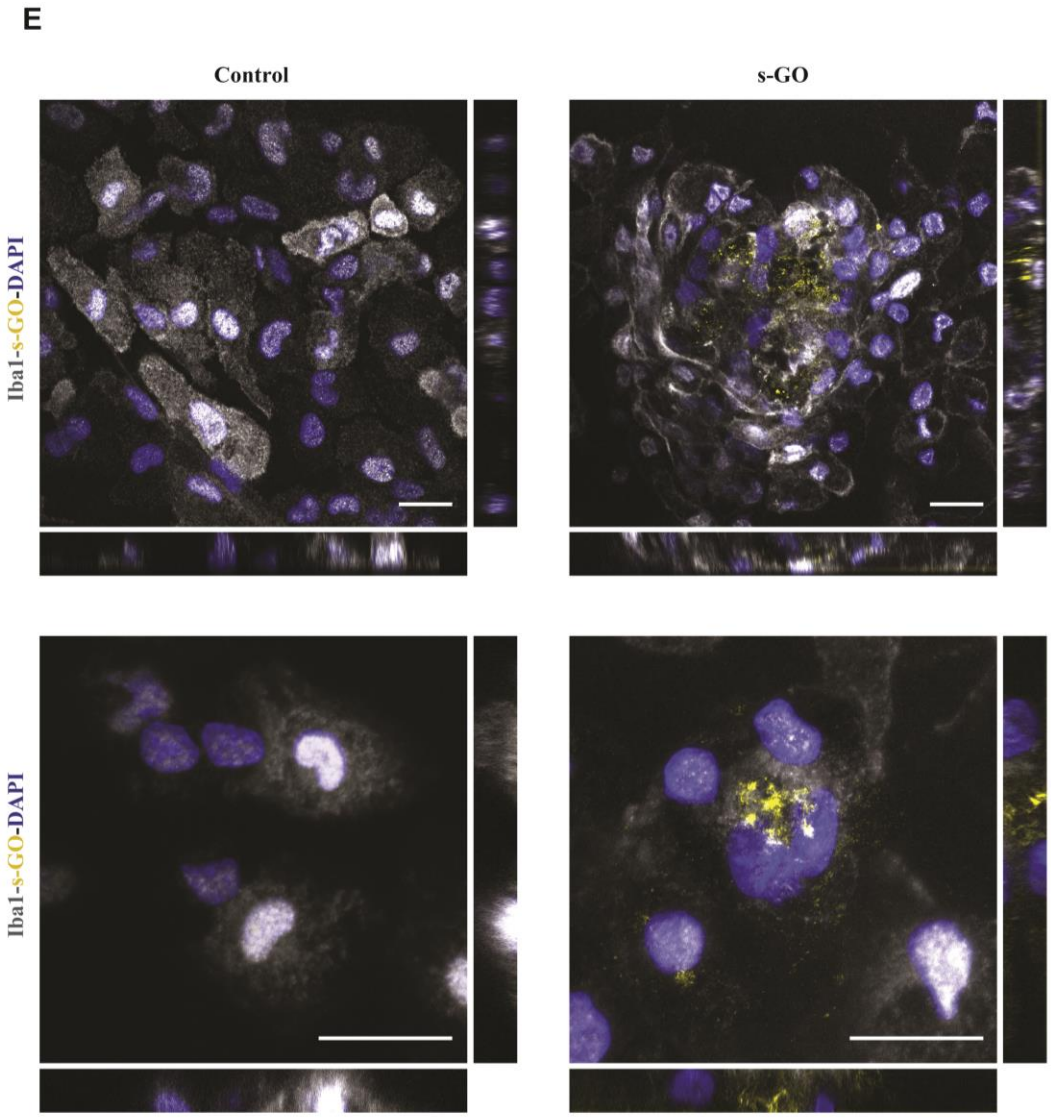

FIGURE S1

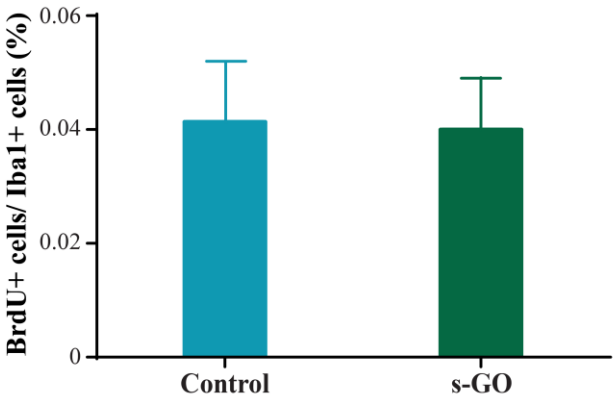

s-GO Nanoflakes Boost Microvesicle Production In Brain Cultured Astrocytes

Mattia Musto[1], Pietro Parisse[2], Neus Lozano[3], Kostas Kostarelos[3], Loredana Casalis[2] and Laura Ballerini[1*]*

[1]International School for Advanced Studies (SISSA), Neuroscience, Trieste, Italy; [2]ELETTRA Synchrotron Light Source, Nanoinnovation Lab, Trieste, Italy; [3]Nanomedicine Lab, School of Medicine and National Graphene Institute, Faculty of Medical & Human Sciences, University of Manchester, Manchester, United Kingdom

ABSTRACT

Natural microvesicles (MVs) derived from astrocytes are increasingly considered crucial in contributing to intercellular communication, able to actively transfer biological materials between neuroglia and neurons. To investigate the features of such glio-signalling requires the applications of new tools in generating MVs and in measuring their properties. Here, we used small graphene nanoflakes (s-GO) to artificially generate MVs from astrocytes in cultures and we compared s-GO generated MVs with those generated by ATP stimulation. We used atomic force microscopy, light scattering and spectroscopy to investigated the morphological and structural features of MVs produced by means of different stimuli. Finally, we set up a functional test to compare the impact of mvG delivery with that of mvA on synaptic activity, when neuronal networks are acutely and transiently exposed to MVs. Our results indicate a substantial similarity between MVs generated by the two different stressors, however by AFM a difference in MV dimensions when vesicles are induced by s-GO is detected. Regardless the smaller dimension, acute exposure to MVs of both groups alters spontaneous synaptic current frequency, inducing a stable increase in network activity.

MAIN TEXT

In biology, newly described forms of intercellular communication [1,2] comprise the release of vesicles, named exosomes, from specific cell types, including neuroglia phenotypes such as astrocytes. These vesicles store signalling molecules within their cargo or embed them in the plasma membrane [3] to modulate relevant processes in the development, physiology and pathology of the central nervous system (CNS). Extracellular vesicles comprise shedding microvesicles (MVs), exosome and apoptotic bodies, characterized by different size, membrane composition, cargo and origin [4,5].

MVs are nanovesicles able to interact specifically with cells at local or distant sites [6]. In maintaining CNS functions, glial cells intensely communicate with neurons, also *via* the release of extracellular vesicles, which represents a highly versatile tool to functionally impact the CNS [7–9]. MVs are considered a mighty "vectorized" signalling system [10] able to bind to target cells to transmit their information.

Graphene oxide (GO) is the most common derivative of graphene. GO properties can be tailored to adapt to new physical and biological applications [11] and, more recently, GO flakes have been successfully designed for drug delivery applications in biomedicine [12]. In the CNS, small GO nano-flakes (s-GO) were shown to induce constitutive MVs release from cultured astrocytes and to potentiate evoked MVs release induced by bzATP applications [13].

Unarguably, to elucidate MVs properties and in particular to characterize whether the ambient conditions used to release and harvest MVs from the same cell type, i.e. astrocytes, influence their signalling ability, will impact our understanding of MVs physiology and the design of MV-based biomedical applications in the CNS [14,15]. Here, we exploited the ability of s-GO to substantially increase the production of MVs from astrocytes to provide, for the first time, a robust and comparative vesicle characterization by means of ultra microscopy and infra-red spectroscopy combined to electrophysiology.

Astrocytes were isolated from postnatal (2-3 days) rats (Wistar) cortices, as previously described [13,16]. We used visually homogenous s-GO dispersions containing s-GO nanosheets with lateral dimensions predominantly between 50 – 500 nm [13,17]. We treated pure glial cell cultures with s-GO (10 μg/mL) for 6−8 days [13]. Immunofluorescence labelling by antigen against glial-fibrillary acidic protein (GFAP), an intermediate filament

protein that is highly specific for cells of the astroglial lineage [18], was used to visualize control and s-GO-treated neuroglial cultures (GFAP, in green; Figure 1A). s-GO treatment did not impair astrocyte morphology and density when compared with matched control cultures (box-plot in Figure 1A; ref). MVs are released into the extracellular space by direct budding from the plasma membrane of astrocytes [19]. To determine the dynamic of MVs release, we measured the presence of changes in membrane trafficking by briefly incubating cultures with the fluorescent styryl dye FM1-43 and then quantifying the membrane-fluorescence decay to provide a cumulative measure of exocytosis [19].

FM dyes are fluorescent probes that reversibly stain membranes, and are largely used for optical real-time measurements of secretory dynamics [20–22]. Incubation with the FM dye (2 μM, 2 min) resulted in clear surface membrane staining of control and s-GO treated cultures, highlighted in Figure 1 B (left panels). Both bright and weak FM-stained plasma membrane domains were present along the whole cytoplasmic surface and became visible within 2 min treatment (Figure 1B), due to this initial intensity variability all FM de-staining measures were normalized to the relative time 0 (see Supplementary Methods). Once astrocytes' membranes were labelled by the fluorescent dye FM1-43 we measured the plasma membrane de-staining over a fixed time (10 min) in control, in s-GO treated cultures or during acute exposure to bzATP (100 μM, 10 min), an agent known to evoke massive MVs release [19], also in our culturing conditions [13]. Representative fluorescence intensity traces are shown in Figure 1C; the dynamic of the fluorescence decay showed a faster rate in s-GO and bzATP groups, in respect to controls. This is also visualized by the time-lapse images framed at time 0, 300 s and 600 s of the recordings (Figure 1B middle and right panels). We quantified the fluorescence decay time constant (τ) values (box plot of Figure 1C) and detected shorter decay values in both bzATP and s-GO groups ($median_{control}$= 219 sec; $median_{bzATP}$= 184.2 sec; $median_{s\text{-}GO}$= 163.9 sec). This result suggested that the membrane de-staining was actually related to MVs release, as expected in bzATP treated cells, more than to other membrane turnover activities. Such a release was comparable between bzATP and s-GO, both significantly faster than controls.

The release of MVs suggested by FM1-43 measures was confirmed by immunoblot analysis for the biomarker flotillin-1 [23] of the supernatant collected from control and treated cultures. As expected [13,19], bzATP stimulation (100 μM, 30 min) and s-GO induced

the appearance of a thick band corresponding to flottillin-1 (Figure 1D), a signature of MVs release by neuroglia, with a clear synergy between s-GO exposure and pharmacological stimulation with bzATP, compared with the other two conditions. In control conditions only a weak band was perceived, indicating a poorly detectable MVs constitutive release in culture. Atomic force microscopy (AFM) topographic reconstruction of re-suspended MVs pellet (Figure 1E) confirmed the presence of MVs detected by the immunoblot in both bzATP and s-GO groups.

We systematically investigated and compared the MVs size distribution. When analyzed by AFM (Figure 2A, right), s-GO-derived MVs (mvG) were significantly smaller (n = 72, $median_{mvG}$= 244 nm) than bzATP-derived ones (mvA; n = 107, $median_{mvA}$= 479 nm). Conversely, we detected no differences in MVs height values ($median_{mvG}$= 19 nm; $median_{mvA}$= 22 nm). Within each group, the distribution of size values detected was not negatively correlated to the height, shown in Figure 2A (left; r_{mvG}= 0.8808 and r_{mvA}= 0.4039). However, AFM experiments were performed in air, thus a not specific flattening of MVs caused by vesicle collapsing might have influenced their measurements. In addition, AFM representativeness could have been affected by the reduced size of the analyzed samples, given the limited number of MVs collected by this procedure, potentially not reflecting the entire population. We enforced large-scale measurement in the next set of experiments, by adopting dynamic light scattering (DLS) and nanoparticle tracking analysis (NTA) to analyze the entire population of MVs in aqueous suspension. NTA tracks single particle Brownian motion, within a dark field microscope, derives mean square vesicles velocity and translates them into size distribution [24]. DLS analysis showed a similar diameter profile for both the populations of MVs (Figure 2B) with a single peak located around 140 nm. However, NTA revealed a more complex pattern of size distribution (Figure 2C): in the case of mvA we observed three subpopulations of vesicles at 115 nm, 235 nm and 400 nm respectively while in the case of mvG we found two partially overlapping peaks at 135 nm and 168 nm, plus two distinct peaks at 275 nm and 385 nm (Figure 2C, left). The diameter analysis revealed a slight, but not significant, difference between the two populations with the diameter of mvG smaller and less distributed, compared to those of mvA ($median_{mvA}$ = 235.4; $median_{mvG}$ = 183.6). These results convincingly suggested a comparable size distribution in both MVs populations and

subpopulations, however, we detected a significant difference in the number of vesicles released within the same time window (Figure 2C, right), with cultures treated with s-GO that produced more MVs when compared to cultures stimulated with bzATP (mvA= 3.32 x 10^8 vesicle/mL; mvG= 8.19 x 10^8 vesicles/mL), consistently with our results obtained by MVs release analysis and immunoblot. Regardless the size of the global MVs population, s-GO is more efficient in generating MVs from astrocytes.

Finally, in order to analyse the macromolecular composition of MVs we performed an infrared-ATR measurement of the two pools of vesicles isolated with the same protocol of differential centrifugation used before. However, to avoid the absorption contribution of phosphate groups and sugars, we removed glucose from the buffer solutions and used a solution of NaCl (150 mM) for the washing and dilution of MVs. We have not found any significant difference between the two condition of release suggesting a similar structural composition and cargoes content. Both the absorbance spectra revealed a clear contribution of the amide I located at 1650 cm^{-1} and then of proteins. Lipids signatures are present in traces: the methyl and methylene stretching modes are quite suppress and the carbonyl ester of phospholipids is visible at about 1740 cm^{-1}. There are contributions from poly-sugars as visible from the bands related to C-O-C (1045 cm^{-1}) and C-OH (1178 cm^{-1}), probably related to the presence of genetic material. Because of the low concentration of sample and the consequent low signal-noise ratio, we were not able to perform second derivative analysis of the spectra to better elucidate the nature of protein material present.

In summary, we compared, for the first time, the morphological and structural features of MVs produced by means of different stimuli and we documented a substantial similarity between mvA and mvG, with the only exception of AFM measures. Yet, besides the bias introduced by the small size of the AFM samples, we cannot exclude the influence of differences in MVs elastic properties, potentially related to diverse membrane components, leading to a variable collapsing of MVs when measured in air.

Finally, we set up a functional test to compare the impact of mvG delivery with that of mvA on synaptic activity, when neuronal networks are acutely and transiently exposed to MVs. To this aim we isolated cortical neurons and glial cells from postnatal rat cortices and

cultured them for 10 days. Figure 3A shows confocal high magnification micrograph of cortical cultures where neurons are visualised by labelling Class III β-tubulin (in red), a microtubule component expressed exclusively in neurons [25], and astrocytes are visualised by GFAP labelling (in green). We patch-clamped visually identified cortical neurons (in voltage clamp configuration, holding potential – 70 mV) while a second pipette for the local delivery of saline solution was positioned at a distance of 200 μm (under microscopy visual control) from the recorded cell (sketched in Figure 3B). We estimated that, at this distance, the application of a brief (500 ms) pulse of pressure should result in a local (i.e. on the recorded neuron) and transient delivery of standard saline solution alone or containing mvG or mvA (re-suspended in saline; see Supporting Information). A typical feature of these cultures is the prominent expression of spontaneous synaptic activity, represented by heterogeneous postsynaptic currents (PSCs) of variable frequency and amplitude (box plots in Figure 3C). Baseline PSCs were recorded before (10 min) and after (15 min) the local saline or mvG or mvA ejection. Figure 3D shows representative current tracings where standard saline was ejected (light grey, top), or where mvA solution (orange, middle) and mvG (black, bottom) were administered. Since spontaneous fluctuations in PSCs frequency ≤ 15 % of baseline were frequently detected, we took this as threshold value to estimate changes when comparing PSCs before and after pressure ejections of saline. In the large majority (n= 16/18; histograms in Figure 3E, left) of neurons exposed to saline solution alone, spontaneous PSCs frequency did not change. On the contrary, within 5-8 min from the acute mvA and mvG ejections, PSCs frequency was stably increased in 64 % (n= 16/25, mvA) and 54 % (13/24, mvG; summarized in the histograms of Figure 3E, left) of neurons. The plot in Figure 3E (right) shows the increases in PSCs frequency in individual experiments and highlights the variability of such changes when administering MVs, with increased frequencies ranging from 20 % to 200 %. Since we could not experimentally control the amount of MVs collected by primary astrocytes and delivered by pressure ejection (see Methods in Supporting Information), neurons were exposed to different amounts of MVs and this can in part explain the detected variability. PSCs frequency increases due to MVs exposures were not reversible upon 20 min washout. From our functional investigation, gliosignalling generated by ATP or s-GO affected similarly neuronal synapses upon transient, direct exposure. This is the first attempt to

investigate the effects of MVs generated by astrocytes when locally delivered to neurons. Neuroglia extracellular vesicles have been described to provide support on synaptic activity [26,27], with the majority of studies focused on microglia and inflammation, apparently regulating neural transmission at the pre-synaptic level [28,29]. Besides inflammatory or degenerative contests [30], astrocytes MVs have been proposed to exert neuroprotective effects and to support neuronal energy metabolism, however the role of astrocytes or of discrete astrocyte populations in delivering different messages via MVs release has yet to be elucidated [31].

FIGURE CAPTION

Figure 1. Cultured astrocytes release microvesicles (MVs) upon ATP or s-GO stimulation. **A.** Confocal images are shown to visualize cultured astrocytes in control and after s-GO (10 μg/mL; 6 days) treatment; anti-GFAP, in green, and DAPI (to visualize nuclei), in blue; scale bar 50 μm. Box plot summarizes the cell density measures, note the similar values in both groups. **B.** Surface membrane staining and activity dependent de-staining of FM1-43 in cultured astrocytes; scale bar 25 μm. Brighter spots are adherent debris and were excluded form the analysis. **C.** Plot of normalized FM1-43 de-staining traces in control astrocytes (light grey), in bzATP treated once (orange) and in s-GO treated once (black). Box plot summarizes the decay time constant τ of FM1-43 de-staining in the three conditions ($median_{control}$ = 219.2; $median_{bzATP}$ = 184.2; $median_{s\text{-}GO}$ = 163.9. Thick horizontal bars in the box plots indicate median value; boxed area extends from the 25th to 75th percentiles, whiskers from 2.5th to the 97.5th percentiles. Significance: ** P<0.01 ***P<0.001, Kruskal-Wallis test, Dunn's post hoc test) **D.** Western blotting of the pellets (top row) and cell lysates (bottom row) for the MV marker flotillin-1. Pellets were obtained from the medium of glial cultures treated or untreated with s-GO under two different conditions: stimulated and not stimulated (saline) by 100 μM bzATP. **E.** AFM topographic reconstruction of MVs isolated from cultured primary astrocytes treated with bzATP (100 μM) and s-GO (10μg/mL) and performed in air (semi-contact mode). Scale bar 500 nm.

Figure 2. Microvesicle produced by glial cells by bzATP or s-GO exposure characterized by ultra-resolution approaches. **A.** AFM measures of lateral size is plotted against AFM

measures of height of MVs isolated from glial cells treated with bzATP (100 μM; mvA; orange) or with s-GO (10μg/mL; mvG; black). Right plot illustrate lateral size values distribution and median values for both groups, note that mvG lateral size is significantly smaller than that of mvA ($median_{mvA}$ = 479; $median_{mvA}$ = 244.1. Significance: P>0.001, Mann-Whitney test. **B.** Size distribution of MVs measured by Dynamic Light Scattering (DLS). **C.** Size distribution of MVs measured by nanoparticle tracking analysis (NTA). Values of the peaks are expressed in nm. **D.** Representative ATR-FTIR spectra of MV. Values of the peaks are expressed in arbitrary unit of infrared light absorbance.

Figure 3. Potentiation of PSCs frequency upon local applications of MVs in cortical cultures. A. Confocal micrograph visualizing cortical primary cultures at 8 days in vitro; anti-class III β-tubulin is used to visualize neurons (in red), anti-GFAP for astrocytes (in green) and DAPI (in blue) to visualize neurons. Scale bar 50 μm. **B.** (A) Sketch of the experimental setting for the simultaneous MVs pressure-release (puff) and cell recording from cultured neurons. **C.** Box plot summarizes the PSCs frequency and amplitude values. **D.** Top: diagram of the experimental protocol; bottom: representative tracings of the spontaneous synaptic activity detected prior and after puff applications of control saline (light grey) or mvA (orange) or mvG (black). **E.** Histograms of pooled data summarize the % of cells displaying PSCs frequency increase in the three conditions. The plot summarizes the distribution of the % of increase in PCSs frequency detected within the three groups.

METHODS

Cell Cultures.

Primary glial cultures were obtained from cortices isolated from neonatal rats (Wistar) at postnatal day 2-3 (P2−P3), as previously described (Calegari et al., 1999; Rauti et al., 2016). Dissociated cells were plated into plastic 150 cm^2 flasks and incubated at 37 °C; 5 % CO_2 in culture medium composed of DMEM (Invitrogen), supplemented with 10 % fetal bovine serum (FBS; Thermo Fisher), 100 IU/ mL penicillin, and 10 mg/mL streptomycin.

Cortical neurons were isolated from from neonatal rats cortices (Wistar) at postnatal day 0-1 (P0−P1). Dissociated cells were then plated on poly-L-ornithine (Sigma) coated coverslips (Kindler, EU) at a concentration of 150000 cells in a volume of 200 μL and incubated at 37 °C; 5 % CO_2 in a culture medium composed of Neurobasal-A (Thermo

Fischer) containing 2% B27 (Gibco), 10 mM Glutamax and 0.5 μM Gentamycin (Gibco) for 8-10 DIV before performing electrophysiological experiments.

MVs Isolation

MVs shedding and isolation was performed as previously described (Rauti et al., 2016). MVs were collected from 21-24 DIV glial cultures previously treated with graphene oxide nanoflakes (s-GO) for 6 days at a concentration of 10 μg/mL or with benzoyl-ATP (bzATP; 100 μM) diluited in physiological saline solution with the following composition: 152 mM NaCl, 4 mM KCl, 1 mM $MgCl_2$, 2 mM $CaCl_2$, 10 mM HEPES and 10 mM Glucose (pH adjusted to 7.4), and left for 30 min at 37 °C and 5 % CO_2 before the harvest. Negative controls were incubated with physiological solution without the presence of bzATP or s-GO. After the incubation period, cell medium was collected and centrifuged for 15 min at a speed of 300 x *g* in order to remove cell debris. Supernatant was then collected MVs were pelleted by centrifugation at 300 x g for 15 min and at 20000 x g for 2 hours.

Western blot analysis

MVs were prepared as previously reported , briefly they were re-suspended in lysis buffer (50 mM Tris-HCl, pH 8.0, 150 mM NaCl, 1 % NP40, 0.1 % SDS), sonicated for 30 s, and then boiled at 95 °C for 5 min. Samples were run on a 10 % polyacrylamide gel and blotted onto nitrocellulose membranes (Millipore, Italy). Membranes were then blocked in PBS-Tween-20 (0.1 %) plus 5 % nonfat dry milk and incubated with the primary antibody antiflotillin-1 (dilution 1:1000) for 16 h at 4 °C. Membranes were then washed with PBS-Tween and incubated with peroxidase-conjugated anti-mouse secondary antibody (dilution 1:1000). Detection of immunolabeled ECL-exposed protein bands was measured with UVI-1D software.

Immunofluorescence and confocal microscopy

Primary glial and cortical neurons cultures were fixed in 4 % formaldehyde (prepared from fresh paraformaldehyde) in PBS for 60 min at room temperature (RT) and then washed in PBS. Free aldehyde groups were quenched in 0.1 M glycine solution for 5 min. The samples were permeabilized in 5 % FBS, 0.3 % Triton-X 100 in PBS for 30 min at RT. Samples were then incubated with primary antibodies (mouse monoclonal anti-GFAP, Invitrogen, 1:500 dilution; rabbit polyclonal anti-β-tubulin III, Sigma-Aldrich, 1:500

dilution) diluted in PBS with 5 % FBS at 4 °C for 1 hours. Samples were then incubated with secondary antibodies (Alexa 488 goat anti-mouse, Invitrogen, 1:500 dilution; Alexa 594 goat anti-rabbit, Invitrogen, 1:500 dilution), and DAPI (Invitrogen, dilution 1:200) to stain the nuclei, for 45 minutes at RT and finally mounted on 1 mm thick glass coverslips using Fluoromount mounting medium (Sigma-Andrich). Images were acquired using a Nikon C2 Confocal, equipped with Ar/Kr, He/Ne and UV lasers with a 40 × (1.4 NA) oil-objective (using oil mounting medium, 1.515 refractive index).

FM1-43 staining

Glial cells were incubated with the fluorescent styryl dye FM1-43 (2 μM) for 2 minutes in order to completely stain plasma membrane, then extensively washed with PBS and exposed for 10 minutes to bzATP (100 μM concentration) or to standard extracellular solution. Samples were placed in a recording chamber mounted on an inverted microscope (Nikon Eclipse Ti-U) and observed with a 40 × objective (0.6 NA, PlanFluor, Nikon). Images (512x512 px) were acquired for 10 min with an exposure time of 150 ms (6.6 Hz) by a Hamamatsu Orca-Flash 4.0 digital camera controlled by an integrating imaging software package (HCImage, Hamamatsu). Recorded images were analyzed offline with the Clampfit software (pClamp suite, 10.2 version; Axon Instruments). Image time stacks were analyzed in selected regions of interest (ROI) to measure the variations in FM1-43 fluorescence intensity over time.

AFM Analysis

AFM characterization was performed as previously described (Rauti et al., 2016). Briefly, the pellet of MVs was re-suspended in PBS solution after isolation from cell cultures and a 15 μL drop of sample solution was placed and left to adsorb (30 min) onto a freshly peeled mica substrate. Vesicles were then fixed with 1% formaldehyde for 1 h (RT) in order to prevent their collapse during AFM acquisition. MVs were then washed with PBS and dried under a gentle stream of nitrogen. AFM analysis was performed in air at RT, using the semicontact mode of a commercial instrument (Solver Pro, NT-MDT, RU). Silicon tips (NSC36/CR-AU, MikroMash, USA) with a typical force constant of 0.6 nN/nm and a resonance frequency of about 65 kHz were employed. Topographic height and phase images were recorded at 512 × 512 pixels at a scan rate of 0.5 Hz. Image processing was performed using Gwyddion freeware AFM analysis software, version 2.40. Diameter and

height of each vesicle were evaluated from cross-line profiles, and results were statistically analysed using Prism (Graphpad software).

Nanoparticle Tracking analysis (NTA)

Measurement and analysis of MVs size distribution by NTA was performed on a NanoSight LM10 system (Malvern) using approximately 500 μL of MVs of both conditions (bzATP-derived and s-GO-derived) diluited 1:20 in MilliQ H_2O. Individual videos of 60 seconds for each sample were acquired using the maximum camera gain and analyzed by the NanoSight particle tracking software to calculate size and vesicles concentration.

Dynamic Light Scattering (DLS)

DLS measurements were carried out on a Zetasizer Nano ZS (Malvern Panalytical Ltd, UK), working in back scattering mode at a fixed scattering angle of 173°. The concentration of the vesicle solution was adjusted with regard to the scattering intensity. With sufficient photocounts, the lowest concentration was used for experiments. The samples were prepared 1 day the measurements and the analysis was conducted at 25°C in folded capillary cells. Each sample was tested three times.

FTIR-ATR Spectroscopy Measurements

MVs were isolated from 21-24 DIV glial cultures by centrifugation as described above and MVs pellet was successively washed with NaCl solution (150mM) and finally resuspended in 50 μL of the same solution in order to avoid contribution of phosphate and sugar groups to the absorbance spectra. For each experiment, 10 μL of sample solution were spread over the whole area of a round germanium ATR plate and left to dry forming a thin film of sample. 30 repeated spectra were acquired for monitoring the complete drying of the sample. Every spectrum was collected at 2 cm-1, repeating 256 scans in the range 3000÷700 cm-1. Measurements were performed at SISSI (Synchrotron Infrared Source for Spectroscopy and Imaging, Elettra-Sincrotrone Beamlines, Basovizza, Trieste, Italy).

Electrophysiological Recordings

Patch-clamp recordings (whole-cell, voltage clamp mode) were performed from visually identified (under DIC microscopy) cortical neurons (DIV 9-11) placed in a recording chamber, mounted on an inverted microscope (Eclipse Ti-U, Nikon, Japan) and superfused with control physiological saline solution of the following concentration: 152 mM NaCl, 4

mM KCl, 1 mM MgCl2, 2 mM CaCl2, 10 mM HEPES and 10 mM Glucose (pH adjusted to 7.4). Cells were patched with glass pipettes (4-7 MΩ) containing: 120 mM potassium gluconate, 20 mM KCl, 10 mM HEPES, 10 mM EGTA, 2 mM $MgCl_2$ and 2 mM Na_2ATP, pH 7.35; osmolarity was adjusted to 300 mOsm. All electrophysiological recordings were performed at RT and the spontaneous synaptic activity was recorded by clamping the membrane voltage at –56 mV (not corrected for liquid junction potential, which was –14 mV). To investigate the acute effect on cortical neurons of glia-derived MVs, an injection pipette (patch pipette with resistance of 1–4 MΩ) filled with MVs previously isolated glial cultures as described above and resuspended in 100 μL of physiological saline solution was positioned at 200μm from the cell soma and connected to a pico-spritzer (PDES-02DX, npi Electronics) with 0.3 psi in-line pressure. The concentration of MVs used was approximately 6.64×10^9 for MVs obtained by bzATP stimulation and 1.64×10^{10} for MVs isolated from s-GO treated cultures. Baseline spontaneous synaptic activity was recorded for the 10 minutes prior delivering the puff (500 ms) of MVs and followed up for 20 minutes to verify changes in post synaptic current (PSC) frequency and amplitude induced by the fusion of MVs with neuronal membranes.

Data were collected by Multiclamp 700B patch amplifier (Axon CNS, Molecular Devices) and digitized at 10 kHz with the pClamp 10.2 software (Molecular Devices LLC, USA).

All recorded events were analysed offline with the AxoGraph 1.4.4 (Axon Instrument) event detection software (Axon CNS, Molecular Devices).

Statistical Analysis

Data sets found to follow a non-normal distribution, were represented as box plot. The central thick horizontal bar in the box plots indicates the median value, while the boxed area extends from the 25th to 75th percentiles with the whiskers ranging from the 2.5th to the 97.5th percentiles. Statistically significant differences between two non-parametric data sets was assessed by Mann-Whitney's test, while to assess statistically significant differences among three data sets was used the Kruskal-Wallis test and Dunn's post hoc test. $P < 0.05$ was considered at a statistically significant.

Funding Sources

This project has received funding from the European Union's Horizon 2020 research and innovation programme under grant agreement No 696656

REFERENCES

(1) Shifrin, D. A.; Beckler, M. D.; Coffey, R. J.; Tyska, M. J. Extracellular Vesicles: Communication, Coercion, and Conditioning. *Mol. Biol. Cell* **2013**, *24* (9), 1253–1259.

(2) Yoon, Y. J.; Kim, O. Y.; Gho, Y. S. Extracellular Vesicles as Emerging Intercellular Communicasomes. *BMB Rep.* **2014**, *47* (10), 531–539.

(3) Zappulli, V.; Friis, K. P.; Fitzpatrick, Z.; Maguire, C. A.; Breakefield, X. O. Extracellular Vesicles and Intercellular Communication within the Nervous System. *J. Clin. Invest.* **2016**, *126* (4), 1198–1207.

(4) Cocucci, E.; Meldolesi, J. Ectosomes and Exosomes: Shedding the Confusion between Extracellular Vesicles. *Trends Cell Biol.* **2015**, *25* (6), 364–372.

(5) Raposo, G.; Stoorvogel, W. Extracellular Vesicles: Exosomes, Microvesicles, and Friends. *J. Cell Biol.* **2013**, *200* (4), 373–383.

(6) Maas, S. L. N.; Breakefield, X. O.; Weaver, A. M. Extracellular Vesicles: Unique Intercellular Delivery Vehicles. *Trends Cell Biol.* **2017**, *27* (3), 172–188.

(7) Frühbeis, C.; Fröhlich, D.; Krämer-Albers, E.-M. Emerging Roles of Exosomes in Neuron–Glia Communication. *Front. Physiol.* **2012**, *3*, 119.

(8) Lachenal, G.; Pernet-Gallay, K.; Chivet, M.; Hemming, F. J.; Belly, A.; Bodon, G.; Blot, B.; Haase, G.; Goldberg, Y.; Sadoul, R. Release of Exosomes from Differentiated Neurons and Its Regulation by Synaptic Glutamatergic Activity. *Mol. Cell. Neurosci.* **2011**, *46* (2), 409–418.

(9) van der Vos, K. E.; Balaj, L.; Skog, J.; Breakefield, X. O. Brain Tumor Microvesicles: Insights into Intercellular Communication in the Nervous System. *Cell. Mol. Neurobiol.* **2011**, *31* (6), 949–959.

(10) Ha, D.; Yang, N.; Nadithe, V. Exosomes as Therapeutic Drug Carriers and Delivery Vehicles across Biological Membranes: Current Perspectives and Future Challenges.

Acta Pharm. Sin. B **2016**, *6* (4), 287–296.

(11) Loh, K. P.; Bao, Q.; Eda, G.; Chhowalla, M. Graphene Oxide as a Chemically Tunable Platform for Optical Applications. *Nat. Chem.* **2010**, *2* (12), 1015–1024.

(12) Baldrighi, M.; Trusel, M.; Tonini, R.; Giordani, S. Carbon Nanomaterials Interfacing with Neurons: An In Vivo Perspective. *Front. Neurosci.* **2016**, *10*, 250.

(13) Rauti, R.; Lozano, N.; León, V.; Scaini, D.; Musto, M.; Rago, I.; Ulloa Severino, F. P.; Fabbro, A.; Casalis, L.; Vázquez, E.; et al. Graphene Oxide Nanosheets Reshape Synaptic Function in Cultured Brain Networks. *ACS Nano* **2016**, *10* (4).

(14) Verderio, C.; Muzio, L.; Turola, E.; Bergami, A.; Novellino, L.; Ruffini, F.; Riganti, L.; Corradini, I.; Francolini, M.; Garzetti, L.; et al. Myeloid Microvesicles Are a Marker and Therapeutic Target for Neuroinflammation. *Ann. Neurol.* **2012**, *72* (4), 610–624.

(15) EL Andaloussi, S.; Mäger, I.; Breakefield, X. O.; Wood, M. J. A. Extracellular Vesicles: Biology and Emerging Therapeutic Opportunities. *Nat. Rev. Drug Discov.* **2013**, *12* (5), 347–357.

(16) Calegari, F.; Coco, S.; Taverna, E.; Bassetti, M.; Verderio, C.; Corradi, N.; Matteoli, M.; Rosa, P. A Regulated Secretory Pathway in Cultured Hippocampal Astrocytes. *J. Biol. Chem.* **1999**, *274* (32), 22539–22547.

(17) Jasim, D. A.; Lozano, N.; Kostarelos, K. Synthesis of Few-Layered, High-Purity Graphene Oxide Sheets from Different Graphite Sources for Biology. *2D Mater.* **2016**, *3* (1), 014006.

(18) Bignami, A.; Eng, L. F.; Dahl, D.; Uyeda, C. T. Localization of the Glial Fibrillary Acidic Protein in Astrocytes by Immunofluorescence. *Brain Res.* **1972**, *43* (2), 429–435.

(19) Bianco, F.; Perrotta, C.; Novellino, L.; Francolini, M.; Riganti, L.; Menna, E.; Saglietti, L.; Schuchman, E. H.; Furlan, R.; Clementi, E.; et al. Acid Sphingomyelinase Activity Triggers Microparticle Release from Glial Cells. *EMBO J.* **2009**, *28* (8), 1043–1054.

(20) Amaral, E.; Guatimosim, S.; Guatimosim, C. Using the Fluorescent Styryl Dye FM1-43 to Visualize Synaptic Vesicles Exocytosis and Endocytosis in Motor Nerve Terminals. In *Methods in molecular biology (Clifton, N.J.)*; 2011; Vol. 689, pp 137–

148.

(21) Betz, W. J.; Mao, F.; Smith, C. B. Imaging Exocytosis and Endocytosis. *Curr. Opin. Neurobiol.* **1996**, *6* (3), 365–371.

(22) Brumback, A.; Lieber, J. L.; Angleson, J. K.; Betz, W. J. Using FM1-43 to Study Neuropeptide Granule Dynamics and Exocytosis. *Methods* **2004**, *33* (4), 287–294.

(23) Yoshioka, Y.; Konishi, Y.; Kosaka, N.; Katsuda, T.; Kato, T.; Ochiya, T. Comparative Marker Analysis of Extracellular Vesicles in Different Human Cancer Types. *J. Extracell. vesicles* **2013**, *2*.

(24) Dragovic, R. A.; Gardiner, C.; Brooks, A. S.; Tannetta, D. S.; Ferguson, D. J. P.; Hole, P.; Carr, B.; Redman, C. W. G.; Harris, A. L.; Dobson, P. J.; et al. Sizing and Phenotyping of Cellular Vesicles Using Nanoparticle Tracking Analysis. *Nanomedicine* **2011**, *7* (6), 780–788.

(25) Caccamo, D. V; Herman, M. M.; Frankfurter, A.; Katsetos, C. D.; Collins, V. P.; Rubinstein, L. J. An Immunohistochemical Study of Neuropeptides and Neuronal Cytoskeletal Proteins in the Neuroepithelial Component of a Spontaneous Murine Ovarian Teratoma. Primitive Neuroepithelium Displays Immunoreactivity for Neuropeptides and Neuron-Associated Beta-Tubulin Isotype. *Am. J. Pathol.* **1989**, *135* (5), 801–813.

(26) Antonucci, F.; Turola, E.; Riganti, L.; Caleo, M.; Gabrielli, M.; Perrotta, C.; Novellino, L.; Clementi, E.; Giussani, P.; Viani, P.; et al. Microvesicles Released from Microglia Stimulate Synaptic Activity via Enhanced Sphingolipid Metabolism. *EMBO J.* **2012**, *31* (5), 1231–1240.

(27) Budnik, V.; Ruiz-Cañada, C.; Wendler, F. Extracellular Vesicles Round off Communication in the Nervous System. *Nat. Rev. Neurosci.* **2016**, *17* (3), 160–172.

(28) Paolicelli, R. C.; Bergamini, G.; Rajendran, L. Cell-to-Cell Communication by Extracellular Vesicles: Focus on Microglia. *Neuroscience* **2018**.

(29) Yang, Y.; Boza-Serrano, A.; Dunning, C. J. R.; Clausen, B. H.; Lambertsen, K. L.; Deierborg, T. Inflammation Leads to Distinct Populations of Extracellular Vesicles from Microglia. *J. Neuroinflammation* **2018**, *15* (1), 168.

(30) Carson, M. J.; Thrash, J. C.; Walter, B. The Cellular Response in Neuroinflammation: The Role of Leukocytes, Microglia and Astrocytes in Neuronal

Death and Survival. *Clin. Neurosci. Res.* **2006**, *6* (5), 237–245.

(31) Holm, M. M.; Kaiser, J.; Schwab, M. E. Extracellular Vesicles: Multimodal Envoys in Neural Maintenance and Repair. *Trends Neurosci.* **2018**, *41* (6), 360–372.

FIGURE 1

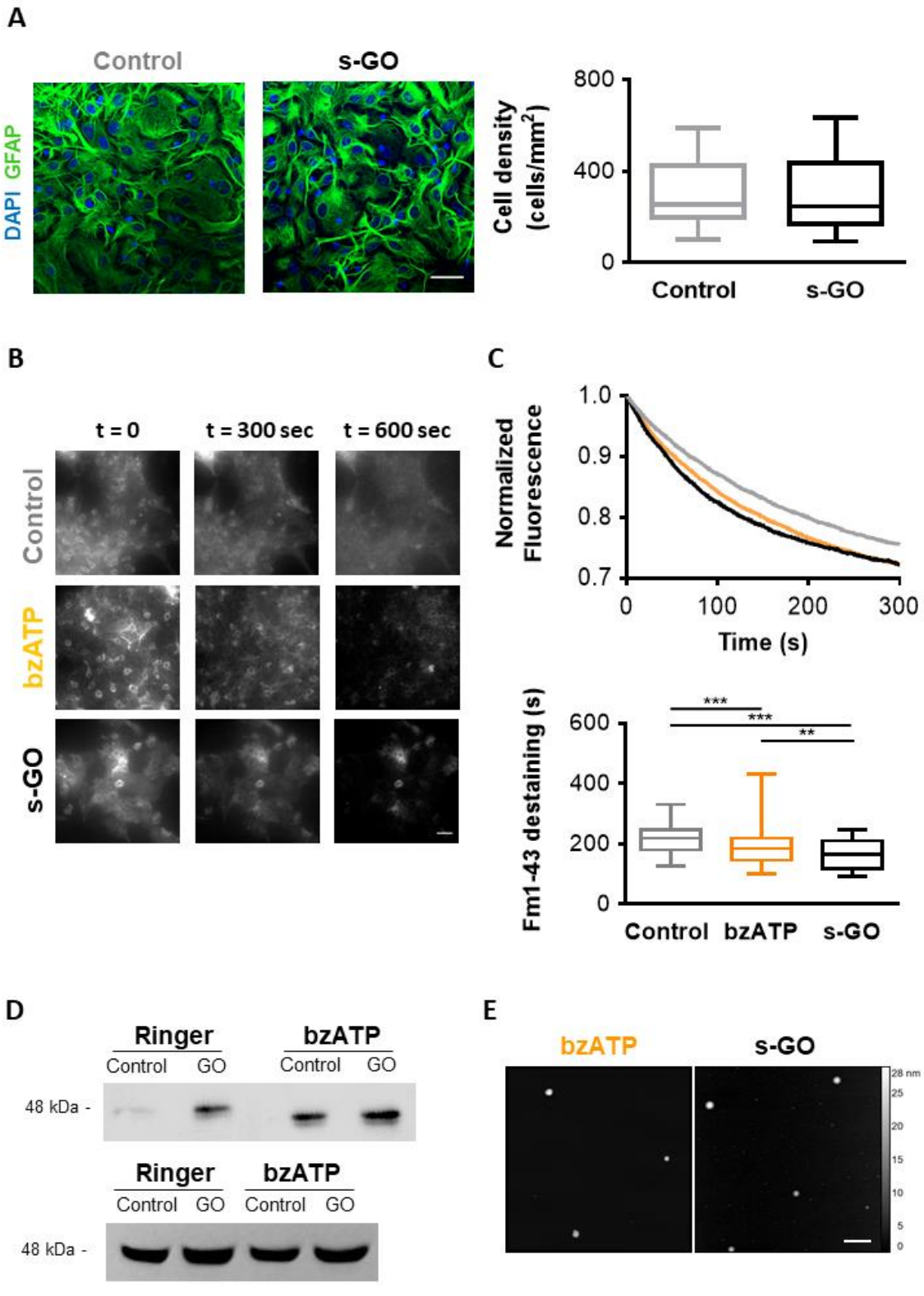
A
Control
s-GO
DAPI GFAP
Cell density (cells/mm²)
800
400
0
Control
s-GO
B
t = 0
t = 300 sec
t = 600 sec
Control
bzATP
s-GO
C
Normalized Fluorescence
1.0
0.9
0.8
0.7
0
100
200
300
Time (s)
Fm1-43 destaining (s)
600
400
200
0
***
***
**
Control
bzATP
s-GO
D
Ringer
bzATP
Control
GO
Control
GO
48 kDa -
Ringer
bzATP
Control
GO
Control
GO
48 kDa -
E
bzATP
s-GO
28 nm
25
20
15
10
5
0

FIGURE 2

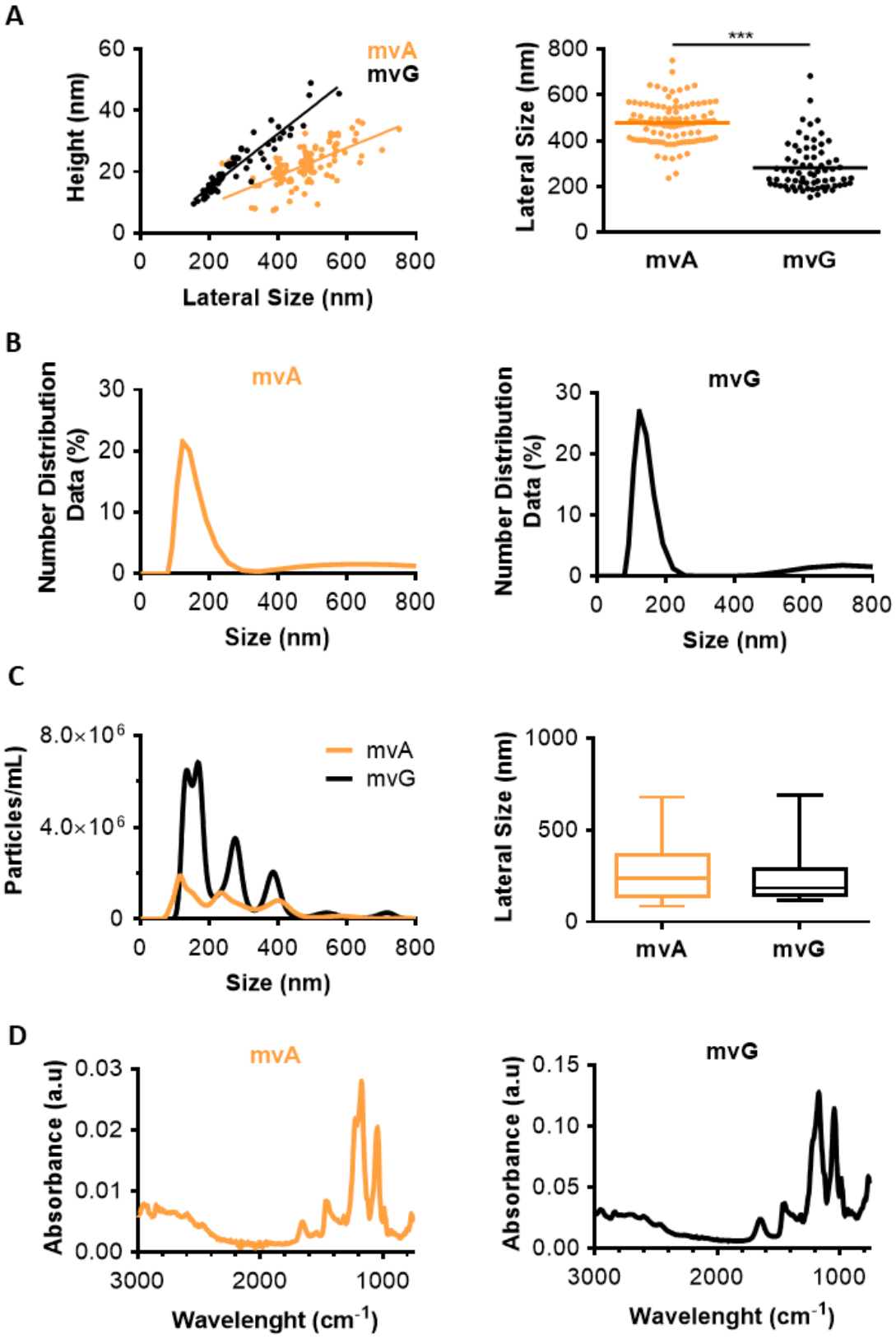
A
mvA
mvG
Height (nm)
Lateral Size (nm)
***
mvA
mvG
B
mvA
mvG
Number Distribution Data (%)
Size (nm)
C
Particles/mL
8.0×10⁶
4.0×10⁶
mvA
mvG
Size (nm)
Lateral Size (nm)
D
mvA
mvG
Absorbance (a.u)
Wavelenght (cm⁻¹)

FIGURE 3

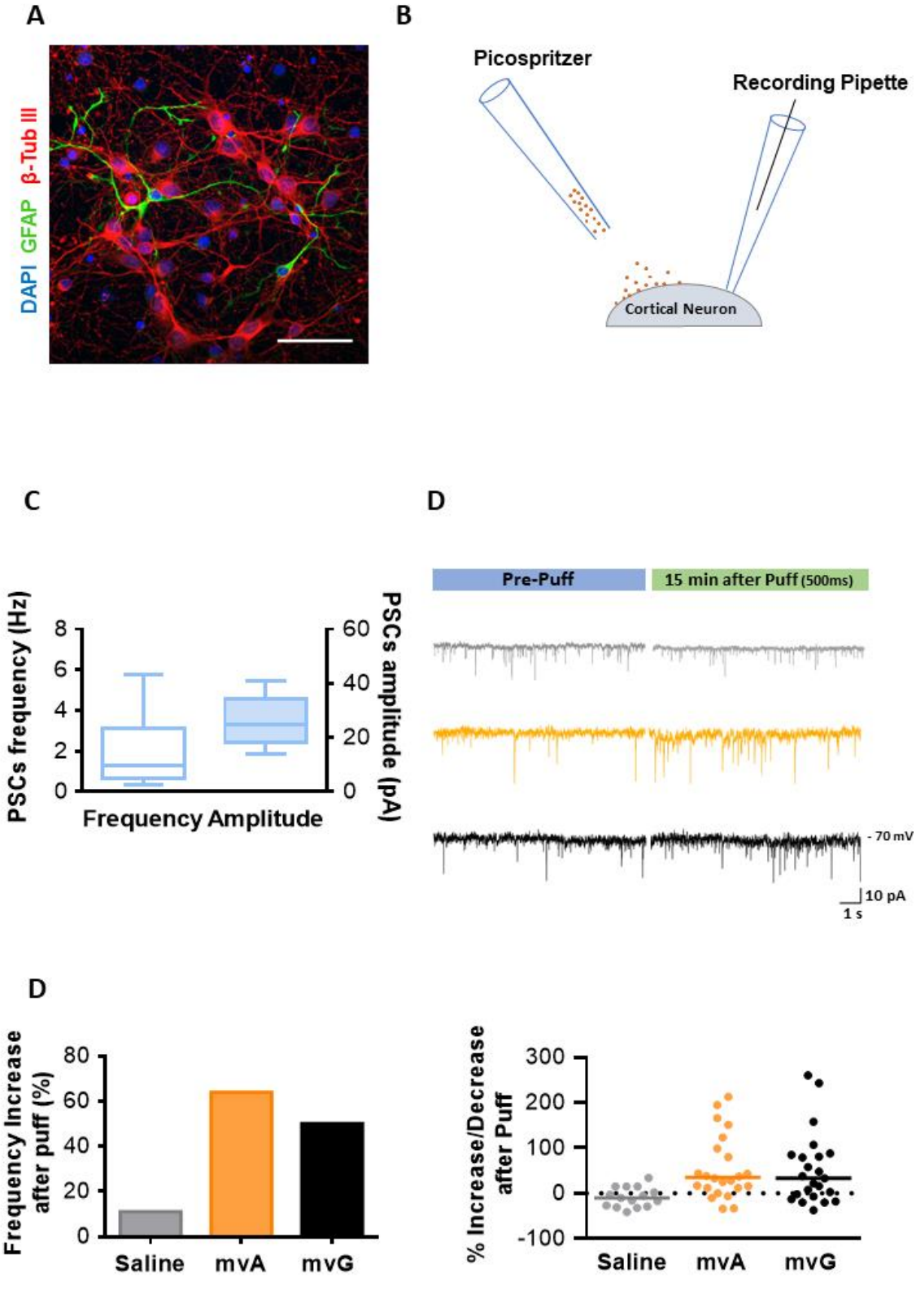
A
DAPI GFAP β-Tub III
B
Picospritzer
Recording Pipette
Cortical Neuron
C
PSCs frequency (Hz)
PSCs amplitude (pA)
Frequency Amplitude
D
Pre-Puff
15 min after Puff (500ms)
- 70 mV
10 pA
1 s
D
Frequency Increase after puff (%)
Saline
mvA
mvG
% Increase/Decrease after Puff
Saline
mvA
mvG

Carbon Nanomaterials For Brain Interfaces

Rossana Rauti[1]*, Mattia Musto[1], Susanna Bosi[2], Maurizio Prato[2,3,4]*, Laura Ballerini[1]

[1]International School for Advanced Studies (SISSA), Neuroscience, Trieste, Italy
[2]Department of Chemical and Pharmaceutical Sciences, University of Trieste, Trieste, Italy
[3]Nanobiotechnology Laboratory, CIC biomaGUNE, -San Sebastiàn, Spain
[4]Ikerbasque, Basque Foundation for Science, Bilbao, Spain

*Corresponding Author:
E-mail: prato@units.it
E-mail: rossana.rauti@sissa.it

Abstract

In the last decades we have witnessed an exponential increase in the engineering of carbon-based (nano)-materials towards biomedical applications in neurology. Carbon constitutes one of the most versatile elements, characterized by a variety of allotropes and structures expressing different properties due to sp, sp^2 and sp^3 hybridizations. Carbon nano-materials are naturally excellent electrical conductors and were shown to possess variable degrees of biocompatibility, which make them promising candidates for the development of neural devices such as neural interfaces. Successful interfacing of the nervous system with devices that record or modulate neuronal electrical activity requires stable device/neuronal electrical coupling, favored by tight interactions between the electrode surface and the cell membrane. Such interactions as well as the efficient electrical coupling might be improved significantly by the use of conductive, ad hoc designed, nano-materials. Here we review the diverse carbon-based nanomaterials currently used in basic and applied neuroscience, the recent discoveries in this research field, focusing in particular on *in vitro* and *in vivo* neural interfaces.

List of Contents

1. Introduction.

In the past decades, increasing attention to nanotechnology has fostered the development of diverse nanomaterials and nanostructures, from quantum dots [1], to nanofibers, nanotubes [2] and nanowires [3,4]. These nanomaterials are particularly promising in neuroscience applications, due to their ability to promote electrical and chemical communication within the nervous system at micro- and nanoscale levels. Applications of nanostructures to neuroscience rapidly expanded from molecular imaging [5], to neuro-regenerative scaffolds [6] and neural interfaces [7-9].

In the framework of nanotechnologies, carbon-based nanomaterials (CBNs) deserve particular attention. These materials, composed of pure carbon with different hybridization or structures [10], were recently introduced and became instrumental to the development of nanotechnology based research in neuroscience.

2. Carbon and carbon-based nanomaterials

Carbon [11] is the most versatile element in the periodic table, owing to the large number of bonds of different type and strength that can form with itself and with many different elements. Within the periodic table, carbon constitutes a versatile element, because of the variety of its allotropes and structures, given by the ability of the carbon valence orbitals to hybridize in sp, sp^2 and sp^3 configurations. To date, the three naturally occurring allotropes of carbon (diamond, amorphous carbon and graphite) have been joined by allotropes deriving from synthetic process (such as graphene, carbon nanotubes, fullerenes, nanodiamonds) [12; Figure 1].

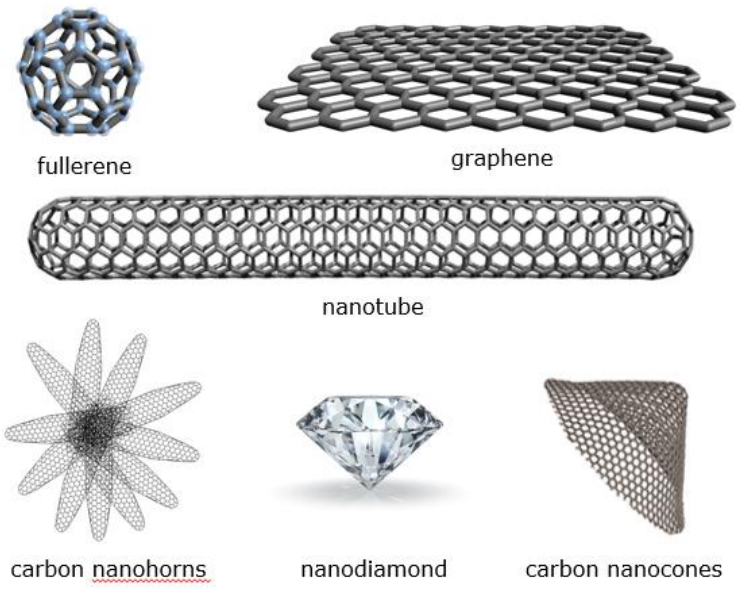

Figure 1. *Carbon allotropes derived from synthetic process.*

The interest in CBNs increased exponentially in the last decades, first with the discovery of fullerenes (1985), then with carbon nanotubes (1991) and finally with the synthesis of graphene (2004). Carbon nanomaterials are naturally good electrical conductor and have good biocompatibility, which make them excellent candidates for electrically conductive scaffolds [14].

The unique properties of CBNs make them widely used in many fields ranging within material science [15], energy [16], environment [17,18], biology [19-22], medicine [23,24], and so forth.

Among all kinds of carbon nanomaterials, carbon nanotubes (CNTs) and graphene are the most popular that have been extensively studied, since both possess excellent mechanical strength, electrical and thermal conductivity, and optical properties. The Young's modulus and tensile strength of CNTs and graphene can reach 1 TPa and 130 GPa [25]. Electron mobility of graphene is more than 15000 $cm^2 \times V^{-1} \times s^{-1}$, and the current density of metallic CNTs is orders of magnitude higher than those of metals such as copper [26,27]. Thermal conductivities of CNTs and graphene are about 3000-3500 W/mK and 5000 W/mK respectively [28]. The light absorption ratio of single-layer graphene is just 2.5% [29]. Lots of the research efforts have been focused on utilizing these advantageous properties for various applications including electronics, biological engineering, filtration, lightweight/strong composite materials, photovoltaic and energy storage [30-32].

3. Carbon nanotubes (CNTs)

CNTs have been discovered by Ijima in 1991 [33] and exhibit outstanding mechanical, thermal, and conductive properties. They are unique nano-objects made of one-atom-thick sheets of carbon (graphene) rolled in a cylindrical shape.

In their simplest geometry, they are generally constituted by a single side-wall, made of benzene rings, and two end caps, presenting fullerene-like structures. CNTs can be classified mainly into two categories: single walled CNTs (SWNTs) and multi walled CNTs (MWNTs). SWNTs are formed of a single layer of graphene and their diameter ranges from 0.7 to 1.4 nm depending on the temperature at which they have been synthesized, while their length can vary from few hundreds of nm up to some μm. MWNT consist of many rolled layers of graphite, leading to tubes with larger diameter, up to 100 nm.

They possess high surface area, high mechanical strength but ultralight weight, rich electronic properties, and excellent chemical and thermal stability [34]. These properties make CNTs very promising in different fields: they have been used in conductive composites, for energy storage and energy conversion devices, sensors, field emission displays and radiation sources, hydrogen storage media and nanometer-sized semiconductor devices, probes, and interconnects [35]. Their poor solubility and their apparently high toxicity have been faced in the past decade via functionalization of the CNTs surface by means of many different approaches aimed at increasing their solubility and lowering their toxic effects to promote biomedical applications [36]. CNTs have been proposed as biosensors [37], ion channel blockers [38], biocatalysts [39] tools in cancer diagnosis and therapy [40] and nanovectors [41].

Among the number of possible biological applications of carbon nanotubes, tissue engineering has emerged as one of the more promising [42]. In particular, due to their peculiar features, CNTs appear to be suitable for the interaction with electrically active tissues, like neuronal and cardiac tissues. For example, many studies have demonstrated that CNT substrates are able to sustain neuronal survival and to promote neuronal process outgrowth [43-47].

An emerging application of CNTs to the nervous system is related to the issue of brain machine interfaces. These devices are designed to provide a direct communication pathway between Central Nervous System (CNS) structures and an external effector in order to restore abilities to patients who have lost sensory or motor function because of disease or injury.

In this context, electrical recording or stimulation of nerve cells is widely employed in neural prostheses (for hearing, vision, and limb-movement recovery), in clinical therapies (treating Parkinson's disease, dystonia, and chronic pain), as well as in basic neuroscience studies. In all

these applications, individual electrodes or microelectrode arrays (MEA), characterized by various shapes and dimensions, stimulate neurons and/or record their activity to modulate their behavior.

Ideally, an implanted stimulation electrode should maintain stability over time with a high spatio-temporal resolution of signals, being safe for the patient. Often these requirements are conflicting, because small electrodes, useful to reduce brain damage in the site of implantation, need high current density to be efficacious and this can cause abnormalities in neural functions and cell structures [48]. CNTs, thanks of their nanometer size and their conductive properties, might be advantageous for designing novel brain machine interfaces.

A first series of studies have addressed the ability of CNTs to deliver electrical stimuli to nerve cells. The first example of neuronal electrical stimulation through CNTs is reported by Liopo and colleagues [49]. CNTs were deposited onto polyethylene terephthalate films and a separated stimulation chamber was created by putting a ring in the middle of the film to contain dorsal root ganglion neurons, while the stimulating electrodes were attached to the CNTs substrate outside of the ring. It has been found that a current step of 1 μA amplitude, applied directly to the CNTs substrate, elicited a neuronal response, monitored as inward trans-membrane current by whole-cell patch recordings; such an inward current was indistinguishable from those induced by direct patch-clamp electrode-mediated depolarizing voltage steps.

Similarly, Gheith and coworkers [50] showed that neurons were activated by steps of electrical stimulation delivered through SWNT films, made by the layer- by-layer method, which consists in alternate layering with a negatively charged polyacrylic acid polymer and positive charged SWNTs.

Although these were the pieces of evidence of successful stimulation of neurons via CNTs substrates, the nature of the interaction between neurons and nanotubes was still poorly understood.

New insights about this issue were obtained by the work of Mazzatenta and coauthors [51]: by using an experimental setting similar to that reported by Liopo, these authors found that neuronal circuits, chronically grown on SWNT substrates, could be effectively stimulated via the SWNT-layers. In fact, they observed that the delivery of voltage steps via Ag wire-SWNT layer induced the appearance of fast inward currents in hippocampal cultured neurons, monitored in voltage-clamp mode, which were abolished by tetrodotoxin (TTX), a selective blocker of voltage gated fast sodium channels. When recording in current clamp, supra-threshold stimulations elicited repetitive action potentials (APs). However the effective stimulation of neural network via SWNT was proved by monitoring the emergence of monosynaptic responses in neurons connected with ones in which presumably CNT mediated stimulation induced APs.

In addition, the presence of tight contacts between neuronal membranes and CNTs were imaged by means of SEM [51], indicating, together with electrophysiological experiments, the presence of an electrical coupling between CNTs and neural membranes.

The next advance in CNT-based neuronal interfaces was reported by Wang and collaborators [52]. These authors designed a prototype of neural interface, using vertically aligned MWNTs pillars as microelectrodes (VACNF), which offered a high charge injection limit (1-1.6 mC/cm^2) without faradic reactions. Then, they cultured rat hippocampal primary cultures on the device and, while neurons were stimulated via CNTs electrodes, neuronal activity was optically monitored by observing intracellular Ca^{2+} level changes using a fluorescent calcium indicator. This study outlined that CNTs could be applied to provide safer and more efficient solutions for neural prostheses than previous metal electrode approaches [52].

In addition, CNTs forming the neuronal interfaces can be layered by electrically conductive polymers, such as polypyrrole, in order to improve the mechanical properties of the substrate and the efficacy of the electrical stimulation, together with their biocompatibility [53]; potentially, this might provide also a method for controlled drug release into the local environments [54]. Carbon nanofibers electrode architectures have been further employed to provide long-term, neuron-electro-analytical measurements of the dynamic processes of intercellular communication between excitable cells. Multi-element electrode arrays composed of individually addressed VACNF were used as substrates for culturing of both neuronal-like derived cell lines (PC12) and primary cells (rat hippocampus) over extended periods (days to weeks) [55]. Neuronal activity was monitored at the electrode site in terms of detection of easily oxidized species generated by the cultured cells, i.e. neurotransmitters. Preliminary data also suggested that quantal release (in vesicular quanta) of easily oxidized transmitters could be observed at nanofiber electrodes following direct culture and differentiation on the arrays for periods of at least 16 days [55].

Recently, researchers are focusing on the optimization of production process in order to obtain CNT-based MEA systems more easily and with a high degree of reproducibility. Shein and collaborators [56] prepared CNTs-MEA systems by means of a conventional micro-fabrication technique, where CNTs were deposited through a chemical vapor deposition growth procedure utilizing metal electrodes as catalyst. These authors tested chips by culturing rat cortical neurons on them: they observed that, after several days in culture, neurons and glial cells aggregated and accumulated on CNT covered regions allowing the detection of neuronal activity via CNT electrodes up to 60 days *in-vitro* with high stability. Electrical stimulations were delivered by an electrode and the evoked neuronal responses recorded by adjacent ones. This work showed how

CNTs can be exploited to design biocompatible, long lasting stimulation/recording systems, where micro-fabrication technique allows the design of patterned network.

Shoval and coauthors [57] employed a similar procedure to develop CNT-MEA devices, which were exploited to record the activity of whole-mount neonatal mouse retinas. After minutes from the placement of retinas on electrodes, the authors could monitor neural spontaneous activity as typical bursting and propagating waves with a higher signal-to-noise ratio in comparison with commercially available electrodes. Interestingly, the recorded signals underwent over a period of minutes to hours to a gradual increase in APs amplitude, suggesting a dynamic interaction between CNTs and neurons, which resulted in an improvement in cell electrode coupling.

Recently, another fascinating view is emerging in the field of CNT-based neuronal interfaces, namely that they provide not only a better quality in spatio- temporal resolution of recorded signals, but that CNTs might influence the fate of cells, thanks to the CNT intrinsic properties.

In fact, it has been observed that the electrical activity of rat hippocampal neuronal network developed on CNTs immobilized microelectrodes is characterized by an earlier onset (4 days after seeding) in comparison to the ones of cultures grown on control electrodes. The authors suggested that the increase in surface roughness in CNT immobilized microelectrodes provides cells with a larger surface area to adhere leading to an increase in the activation of adhesion integrins, which might promote a faster neuronal differentiation [58].

Much of the understanding of neural interfaces has been gained by studying 2D structures/devices, however more recently biologists have come to understand the dissimilarity between the flat surfaces and the 3D topographical complexes i.e. the extracellular environment in which cells routinely operate in vivo [59]. Ghibaudo and team in 2009 [60] reported differences in cellular interactions between 2D and 3D substrates. They assessed cellular adhesion and migration of fibroblasts in both conditions. Cells interfaced to 3D microenvironment showed more elongated and branched shapes. Thus, 3D offers more control on size and shape of the substrate and cellular morphology than traditional 2D substrates [60].

CNTs fortunately present tunable properties that can lead to modification of their dimensions. Gui et al., [61] have molded CNTs into a porous sponge of 3D with a very high porosity while retaining desired mechanical properties. The sponge structure obtained was very stable and in fact allowed excellent compressibility and ability to recover volume by free expansion. 3D scaffold discussed in the literature maintained good contact and percolation and polymer infiltration [61].

Moreover, CNTs as implantable materials can also easily be tagged with biomolecules or polymers. Using a polymer incorporated with CNTs can provide the desired mechanical and physical properties as well as offer favorable electrical environment elicited by CNTs. Due to their

biological applications, and resistance to biodegradation, CNTs have proved to be one of the promising choices for brain or spinal implantable materials or devices e.g scaffold, electrodes, other neural interfaces. In order to further enhance neuronal performance or detect existing neuronal connections, optimized electrical stimulations can be delivered to CNTs or CNTs-entrapped-polymer. These strategies can be exploited all together to build scaffolds that can trigger improvements in neuronal network formations and functional tissues.

CNTs have also been used to enhance the functional reconnections of separated spinal explants [62; Figure 2] and reconstruct 3D hippocampal network in vitro [63, Figure 3]. Bosi and collaborators were able to fabricate 3D PDMS scaffolds with pores layered by an irregular carbon nanotube carpet stably entrapped in the PDMS matrix. These mixed 3D scaffolds were applied not only to study the activity of primary hippocampal neurons in vitro [63], but also as scaffolds for the growth and functional reconnection of separated spinal cord organotypic slices and in vivo implant in the adult rats visual cortex, where they show a limited tissue reaction [64].

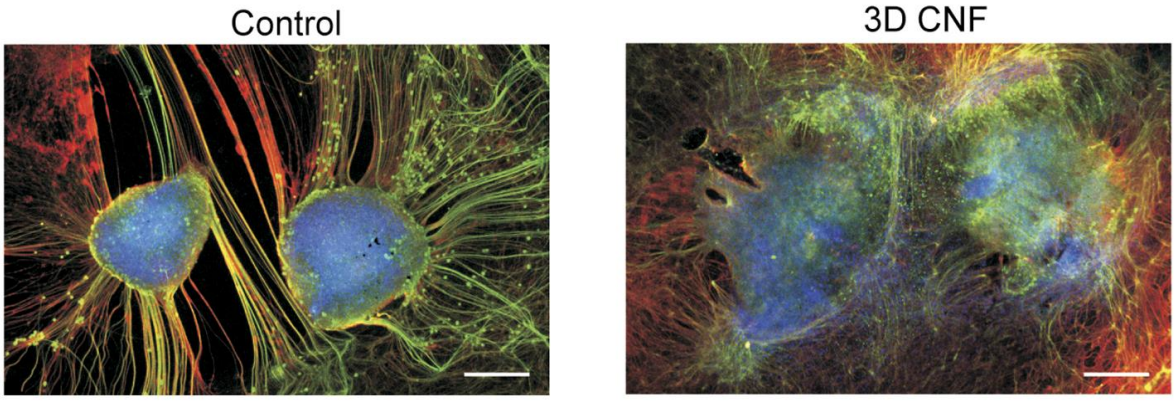

Figure 2. *Spinal organotypic slices cocultured in Control and in 3D CNF after 14 days of growth. Immunofluorescence is for neuron-specific microtubules (β-tubulin III; red), neurofilament H (SMI-32; green), and nuclei (DAPI; blue). (Modified with permission from Usmani et al. 2016 [62])*

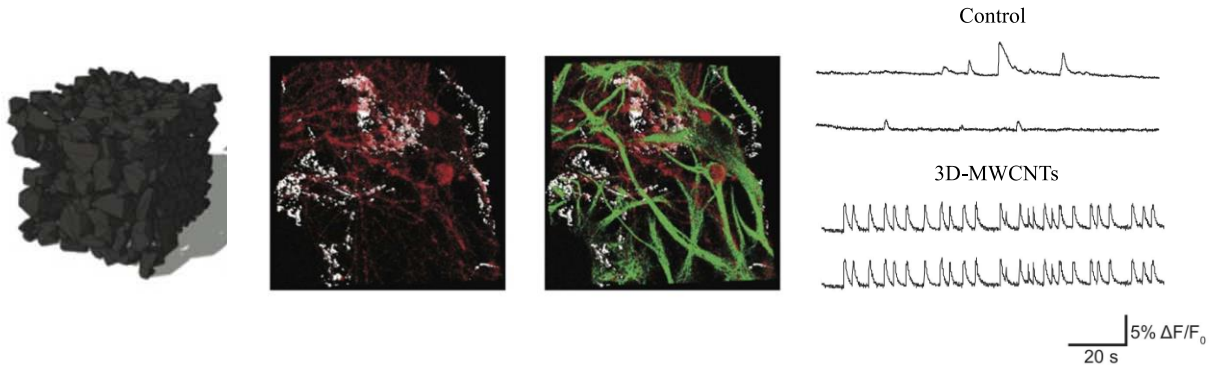

Figure 3*. Confocal micrographs show hippocampal cultures grown (9 DIV) on 2D-PDMS (left) and 3D-MWCNTS (right) immune-stained for β-tubulin III (in red), GFAP (green) and DAPI (blue). Scale bar: 100 μm. Repetitive Ca2+ activities spontaneously (middle) or bicuculline induced (right) recorded in 2D- and 3D-MWCNT. (Modified with the permission from Bosi et al. 2015 [63]).*

4. Graphene

The CBN that is nowadays taking the stage is graphene (GR): this carbon allotrope consists of a single layer of carbon atoms arranged in a hexagonal honeycomb lattice and can be considered the founder of many other allotropes of carbon, such as graphite, diamond, charcoal, carbon nanotubes and fullerenes. Graphene is the thinnest compound known to man at one atom thick, the lightest material known (with 1 square meter coming in at around 0.77 milligrams), the strongest compound discovered (between 100-300 times stronger than steel and with a tensile stiffness of 150,000,000 psi), the best conductor of heat at room temperature (around 5000 W/mK) and also the best conductor of electricity known (studies have shown electron mobility at values of more than 15,000 $cm^2 \times V^{-1} \times s^{-1}$ [25]). Being able to create super-capacitors out of graphene will possibly be the big step in electronic engineering in a very long time, when the development of electronic components has been progressing at a very high rate over the last 20 years. However, the excellent electrical and chemical properties of graphene combined with its biocompatibility provide exciting opportunities for new biomedical applications. After the groundbreaking experiments of Geim and Novoselov [65] on graphene, research on this carbon allotrope has grown exponentially with more than 30000 publications in the last ten years. Its simple molecular architecture and the ability to combine with other existing nano- and biomaterials make graphene suitable for a variety of purposes. The different applications for which graphene has been proposed, lead to the engineering of not only graphene monolayers, but a wide variety of graphene-based materials. Single layer graphene, bi-layer graphene, multilayer graphene, graphene oxide (GO), reduced graphene oxide (rGO) and chemically modified graphene are the members of the graphene-based nanomaterial family: each

member of this family possesses its own features in terms of oxygen content, number of layers, surface chemistry, purity, lateral dimensions, defect density and composition. Due to its highly reactive surface, single layer defect-free graphene production is challenging and it is also difficult to suspend in solution. These are the main reasons why GO and rGO are often preferred for biological applications.

However, graphene has already been engineered for a variety of biomedical applications, including cellular imaging and drug delivery [66], bio-analysis [67], stem cell research [68,69] and even photothermal therapy for tumor [70].

It has been demonstrated that graphene films have excellent biocompatibility for primary cultures of mouse hippocampal neurons and are even capable of promoting neurite sprouting and outgrowth, especially during the early developmental phase [71]. Fabbro et al. observed that graphene-based materials are inert neuron-interfacing materials, able to preserve the basal physiological level of neuronal activity [72]. They noticed uncommon ability of Graphene-based substrates (GBSs) to support neuronal development (in terms of neuronal passive properties, spontaneous synaptic activity, synaptogenesis, and short-term synaptic plasticity) without pre-coating with adhesion-promoting peptides (e.g., polylysine or polyornithine). More recently, graphene was reported to tune the extracellular ion distribution at the interface with hippocampal neurons, key regulator of neuronal excitability. The ability to trap ions by graphene is maximized when a single layer graphene is deposited on substrates electrically insulated. These biophysical changes caused a significant shift in neuronal firing phenotypes and affected network activity [73].

One of the first observations related to the possible use of GR in the brain environment was that the biocompatibility and broad-spectrum transparency, flexibility and mass-producibility makes GR an ideal candidate for replacement of ITO in neural interfacing devices. Indeed, there are several examples of effective graphene-based electrode devices in the recent literature. A graphene-based, carbon-layered electrode array device was implanted on the brain surface in rodents for high-resolution neurophysiological recording. The optical transparency of the device at >90% transmission over the ultraviolet to infrared spectrum demonstrated its utility through optical interface experiments that use this broad spectrum transparency. These experiments included optogenetic activation of focal cortical areas directly beneath electrodes, in vivo imaging of the cortical vasculature via fluorescence microscopy and 3D optical coherence tomography [74; Figure 4].

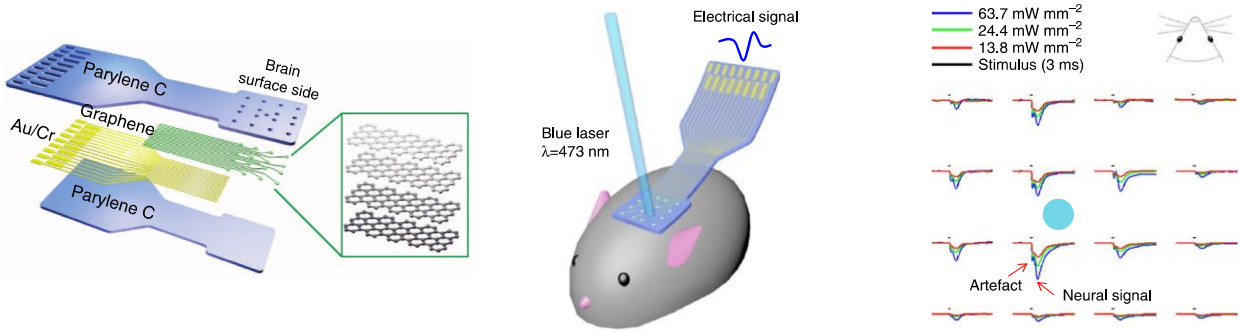

Figure 4. *Left panel: diagram of CLEAR device construction showing the layered structures; middle panel: schematic drawing of opto-experimental setup, showing the CLEAR device implanted on the cerebral cortex of a mouse, with an optical fibre delivering blue light stimuli to the neural cells; right panel: optical evoked potentials recorded by the CLEAR device. X-scale bars represent 50 ms, y-scale bars represent 100 mV (Modified with the permission from Park et al. 2014 [74]).*

Graphene and related materials (GRMs) offer several benefits as novel components for the engineering of neural interfaces, including multifunctionality and biocompatibility. Kostarelos et al., [75] have reported flexible neural implants with very low noise levels. Using a flexible array of graphene field-effect transistors, the implants successfully detected slow-wave activity, synchronous epileptic activity and audio-visual responses in rats, matching the performance of state-of-the-art platinum electrode implants [76].

GR is also explored as a novel platform for the local delivery of therapeutic molecules with encouraging preliminary results. Functionalization of GR and GO can tailor their properties and enable their use as carriers of therapeutic molecules, while their biosensing, optical and photothermal properties are also being exploited for combinatory interventions [77]. As an electroactive material, graphene is considered emerging as a next-generation neuronal tissue engineering scaffolds to enhance neuronal regeneration and functional recovery after brain injury. Electrospun microfiber scaffolds coated with self-assembled colloidal graphene were implanted into the striatum or into the subventricular zone of adult rats [78], while microglia and astrocytes activation levels were suppressed with graphene functionalization. In addition, self-assembled graphene implants prevented glial scarring in the brain 7 weeks following implantation. Astrocytes guidance within the scaffold and redirection of neuroblasts from the subventricular zone along the implants was also demonstrated. Song et al. observed [79] that 3D graphene supported the growth of microglia and showed good biocompatibility. Microglia is a macrophage like phagocytic cell normally inactive unless provoked by damaging xenobiotics. These cells are derived from myeloid cells and constitute 12% of brain cells [80]. The observations indicated that 3D graphene offered milder neuroinflammation on microglial cells compared to 2D graphene, which further suggested

that the topographical features could affect inflammatory behaviors. Additionally, the 3D graphene foams facilitated the growth of neural stem cells and PC-12 cells (originated from neural crest) and proved that they can be used for neural repairing and neurogenesis.

Several other studies demonstrated the ability of GR substrates to promote neurites sprouting and outgrowth [71], to enhance neuron electrical signaling [81] and to reduce the inflammatory response [79]. In neurology, GR represents a promising tool for neuronal implants or bio-devices, with potential applications that range from neurooncology to neuroregeneration [82,83]. It was also reported recently the ability of small graphene oxide nanosheets (s-GO) to interfere specifically with neuronal synapses, without affecting cell viability. In particular, in cultured neuronal networks, upon chronic s-GO exposure, glutamatergic release sites were sized down [84]. Different studies reported the use of GBMs at the CNS for cell labeling and real-time live-cell monitoring [85,86]; delivery to the brain of molecules that are usually rejected by the Blood Brain Barrier (BBB) [87,88], and cell analysis based on G-electrodes [89,90]. In addition, interfacing graphene with neural cells was also proposed to be extremely advantageous for exploring their electrical behavior or facilitating neuronal regeneration by promoting controlled elongation of neuronal processes [71,72,91,92, Figure 5].

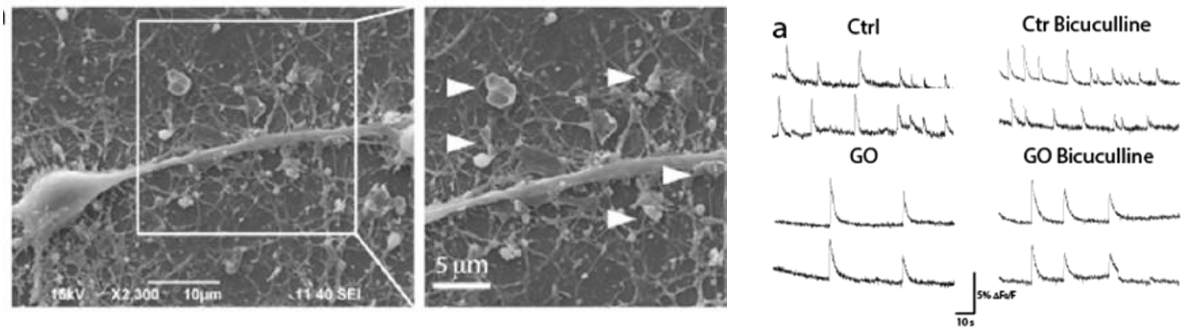

Figure 5. *SEM images showing large number of graphene oxide flakes (white arrowheads) in contact with the neuronal cortical cell membrane, exposed to GO flakes for 14 days. On the right panel, representative spontaneous (left panels) or bicuculline-evoked (right panels) Ca^{2+} oscillations recorded in 14 DIV cortical cultures in control or GO conditions. (Reprinted with the permission from Bramini et al. 2016 [92], American Chemical Society).*

Among the different possible implementations of GBMs, building of graphene-based scaffolds for cell growth and differentiation is one of the most promising. 3D graphene foams (3D-GF) can be obtained using nickel foam template for chemical vapor deposition of graphene. Growing neural

stem cells on these substrates allows not only a more physiological condition but also a substrate that can be electrically stimulated [93; Figure 6].

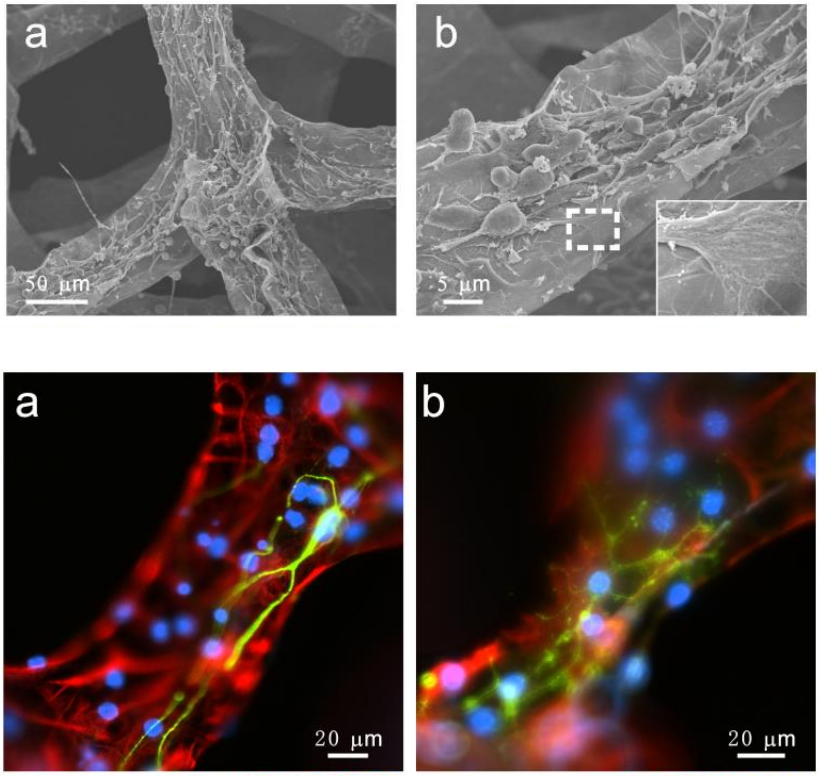

***Figure 6**. Top panel: low- (a) and high- (b) magnified SEM images of NSCs cultured on 3D-GFs. The inset illustrates the interaction between the cell filopodia and 3D-GF surface. Bottom panel: Representative fluorescence images of differentiated NSCs under differentiation conditions, the cells were immunostained with Tuj-1 for neuron (green, a), GFAP for astrocyte (red, a&b), O4 for oligodendrocyte (green, b) and DAPI for nuclei (blue, a&b) (Modified from Li et al., 2013 [93])*

Neuronal dissociated hippocampal cultures, grown on 3D-GFs built as previously described, were also able to recapitulate two basic properties of the complexity of the brain: firstly, the coexistence of local and global electrical activity, and secondly, the existence of neuronal assembly with a degree of correlated electrical activity varying in space and time [94]. In a different strategy Martìn et al. built hybrid hydrogels with polyacrylamide and graphene. This study demonstrates that graphene improves the biocompatibility of 3D scaffold [95].

5. Diamond

Diamond, a natural as well as a synthetic material, has captured researchers' attention more than 10 years ago. From any list summarizing the specific material properties, diamond is often at the

extreme [96]: crystalline diamond shows the highest atomic density of any bulk crystal, the highest bulk modulus and high thermal conductivity. Diamond, a wide band gap semiconductor, is optically transparent from the far infrared to the ultraviolet, making it an ideal candidate for optical applications [97]. The attractiveness of diamond is that different morphologies and forms can be obtained from this sp^3-hybridized material. Indeed, modulation of the growth parameters results in microcrystalline to ultra-nanocrystalline CVD diamond films. Ultra-nanocrystalline films have the advantage of possessing smooth surfaces, lower strain and improved fracture resistance. Such films are characterized by diamond domains that are ≈10 nm or less in size, with thin sp^2 boundaries. Nanoscale diamond particles (also termed nanodiamonds, NDs) represent another interesting form of diamond, largely explored for applications in drug delivery or medical diagnostics.

Due to its chemical and biochemical inertness, diamond is generally considered as a biocompatible material, meaning that it is chemically non-cytotoxic when in contact with biological cells [98]. This makes diamond a material of interest for coating medical devices, building artificial organs, and as a growth support for biological cells. ND particles and thin film have been used as substrates for cultivation of different cell phenotypes including neurons [99], fibroblasts [100], osteoblasts [101] and many other cell lines [102]. Guarina and collaborators [103] used fluorescent nanodiamonds (FND) to evaluate their functional implications on hippocampal neurons, using MEA recordings. The firing frequency of neurons was differently affected depending on the developmental stage of incubation with FNDs (7 versus 14). When FNDs were applied at 14 days in vitro they drastically reduced the neuronal frequency (Figure 7).

In all cases diamond exhibited no measurable cytotoxicity and, in some cases, appeared to promote cell adhesion and proliferation over conventional materials such as glass or tissue culture polystyrene.

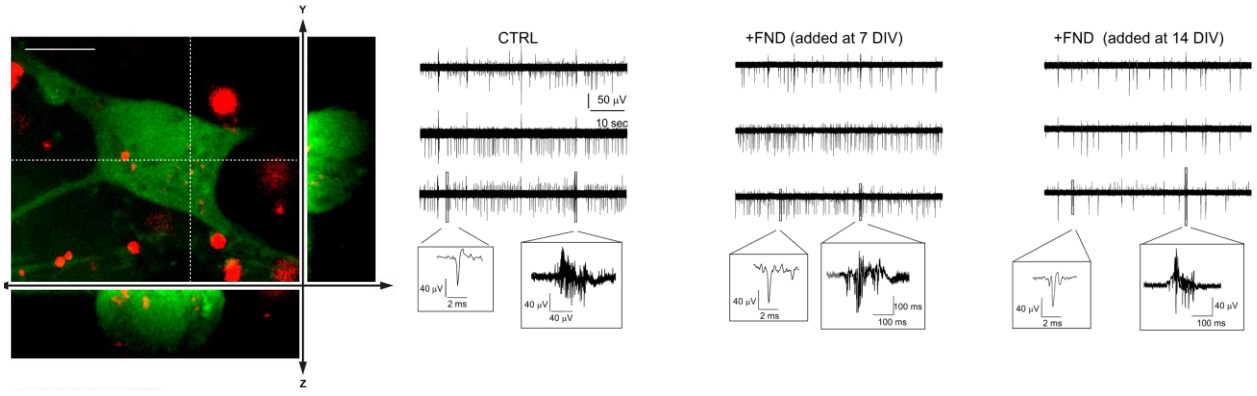

Figure 7*. Confocal fluorescence micrograph of cultured hippocampal neurons (14 DIV), exposed to 40 µg/ml FND for 2 days, and stained in green with the cytoplasmic labelling dye (CellTracker™ Green CMFDA). Red emission is from FNDs. The entire field and cross-sections (XZ and YZ) were shown. Representative traces of spontaneous firing at 18 DIV (data from 3 representative MEA channels) under control conditions (CTRL), without FNDs, with FNDs seeded at*

7 DIV and at 14 DIV. Insets: higher magnification of single spikes and bursts. (Modified with the permission from Guarina et al. 2018 [103]).

In neuroscience, in addition to the employment as growing substrate, NDs were applied in the development of biosensors for recording neuronal activity, thanks to their peculiar electrical and chemical properties and stability [104,105]. Its high biocompatibility and low cytotoxicity make ND an excellent candidate for the development of neural interfaces in biological systems with different levels of complexity.

The increasing interest and the recent development of new techniques for constructing micro/nanodevices [106-110] has rapidly broadened the number of diamond-based MEAs (DBMs) employed for electrical recording and stimulation and for detecting neurotransmitter release [111]. DBMs can now be used to either resolve the electrical activity in complex neuronal networks (low-density MEAs) [112,113], to identify the extension of cell microdomains (active zones) where neurosecretion occurs (high-density MEAs) [114] or to assay the protein content of the physiological liquids that condition the growth, formation, and maturation of complex neuronal networks [115,116].

Ariano and colleagues fabricated a device to record extracellular activity of cultured neurons, based on hydrogen terminated (H-terminated) conductive diamonds. The device allows to record the entire activity of the network in a way similar to conventional microelectrode array (MEA) and with comparable neuronal activity signals [104]. 2D and 3D MEA systems based on diamond and consisting of 256 electrodes on a surface of 28.8 mm^2 have also been developed with the purpose of studying ex-vivo models, in order to obtain more information from a more complex neuronal network [117]. Finally, Halpern and colleagues successfully implanted diamond electrodes in *Aplysia californica* attaching it on the buccal nerve 2, a primary nerve involved in the feeding behavior of Aplysia and recording extracellular electrical activity for up to 9 days after the implantation [118].

Diamond in the form of nanowires should also be considered. The use of diamond nanowires is believed to address positively issues related to improving the overall performance of sensors, including sensitivity and selectivity [119-122].

In the field of cellular sensing, diamond-based substrates offer unique advantages in comparison to conventional materials (silicon, glass, metals, and polymers), [123] which directly derive from the extreme physical properties of this material, i.e., mechanical robustness, wide optical transparency and thermal conductivity [124].

In-vitro tests demonstrated that diamond-based substrates are non-cytotoxic and display a significantly better cell adhesion and growth in comparison with standard substrates [125,126].

Furthermore, the chemical inertness of the pristine diamond surface does not prevent its efficient chemical functionalization upon the termination with specific covalent bonds that allows the attachment of a broad variety of molecules, including DNA strands [127-129].

The H-termination of the diamond surface favors the formation of an electrically conductive two-dimensional layer in contrast with the insulating O-terminated surface [130]. These transparent electrodes have been exploited to record the activity of cultured neuronal cells with a single macroelectrode [104] and subsequently to record the activity of cultured cardiomyocyte-like and human embryonic kidney cells using arrays of solution-gated field-effect transistors.

6. Carbon nanofibers

The typical lengths and diameters of carbon nanofibers are in the ranges of 5–100 mm and 5–500 nm, respectively [131]. Compared to the conventional technologies, carbon nanofibers (CNFs) have great potential as neural interfaces, for their superior electrical, chemical, and physical properties [1]: chemically stable and inert in physiological environment [2], biocompatible for long-term implantation due to their solid carbon skeleton [3], electrically robust and conductive for signal detection [4], 3D structures that allow intra-tissue and intracellular penetration [132], with high surface-to-volume ratio, which reduces contacting electrical impedance greatly, and [5] high spatial resolution due to their ultra-micro scale sizes.

In addition, carbon nanofiber materials have been developed as electroconductive scaffolds for neural tissues to facilitate communication through neural interfaces. Electrical fields are able to enhance and direct nerve growth [133], therefore electroconductive scaffolds have been applied to enhance the nerve regeneration process, not only providing physical support for cell growth but also delivering the functional stimulus. Moreover, CNFs have great potential as multiplexing and intracellular neural interfaces, capable of dual-mode detecting electrophysiological and neurochemical signals, not only at the extracellular level with high spatial resolution, but also at the intracellular level by penetrating into single neurons [9].

7. Fullerenes

The first fullerene C60 came to life in 1985 [134] but the family of fullerenes includes a wide range of carbon-based molecules with different number of carbon atoms and symmetries. The most common fullerene is also called buckyball and consists of 60 carbon atoms arranged into 12 pentagons and 20 hexagons to create a structure with the geometry of a hollow sphere [134-136]. C_{60} attracted great attention because of its very stable and symmetric structure [137].

Fullerenes are considered zero-dimensional materials which possess very interesting physical and chemical properties [138-142] for medicine and technology.

The main issue the biomedical field faced was the natural water repulsion of C_{60} and its resulting hydrophobicity. This insolubility in aqueous media induces fullerenes to aggregate [143] and this led to develop several strategies to overcome the problem. Hydroxyl and malonic acid functionalized fullerenes found important applications in neuroprotection against free radicals generated by fatty acid aerobic metabolism, which neurons are rich of [144], after brain injury or inflammatory response to diseases. These derivatives of fullerene can interrupt chain reactions generating the radicals by removing intermediate peroxyl radicals and showing robust neuroprotection activity in several in vitro models of CNS injury and neurological disease including Parkinson's disease [145]. This ability has also important clinical applications, in fact, it can prevent excitotoxicity produced by the leak of neurotransmitters and excitatory ions following the free radical damage even present after neuroprosthetic surgery and this effect is probably due in part by its ability to inhibit glutamate channels [146].

8. Other carbon nanomaterials

Single wall carbon nanohorns (SWCNHs), reported by Ijima in 1999, are tiny graphene sheets, wrapped up to form horn-shaped cones with a half fullerene cap, having 30-50 nm length and 2-5 nm diameter. They have the tendency to group together and form aggregates (spherical clusters or bundles) like "dahlia" flowers or buds, with an overall diameter of 80-100 nanometers.

Being their structure similar to tiny carbon nanotubes, SWCNHs maintain most of the typical properties of nanotubes: high electrical conductivity, high thermal conductivity and possibility of functionalization. SWCNHs peapods (functionalized with CdSe/ZnSe QDs), encapsulating Gd3N@C80 fullerenes and delivered to U87 tumor bearing mice by convection-enhanced delivery intratumoral infusion [147], enabled tumor imaging either in vivo by MRI (thanks to Gd3+) and ex vivo by confocal microscopy (owing to the presence of QDs). SWCNHs showed to be retained inside the tumor for at least 3 days. Although this study indicates SWCNHs as a possible brain drug delivery nanoplatform, other reports on the in vivo bio-distribution of SWCNHs have demonstrated that they could not cross the BBB [148,149]. This precludes the SWCNHs to be delivered i.v. to the brain, leaving the more dangerous and complicated intracranial administration as the only feasible option available at the moment. Carbon dots (CDs) are a recently discovered class of discrete, quasi-spherical CBNs [150], which essentially combine the presence of an amorphous core and a graphitic shell. CDs are expected to have a huge impact in biotechnological and environmental applications, based on their high potential as a nontoxic, fluorescent alternative to the popular

semiconductor-based QDs. Their peculiar properties have been exploited in photocatalysis [151], electrocatalysis [152], as sensitizers for solar cells [153], as well as for sensing applications [154]. Due to their high intrinsic fluorescence that can span from the VIS to the NIR [155,156], CDs were considered particularly appealing for bioimaging applications (for a review see Peng Z. et al. 2017 [157]). Depending on the synthetic strategy adopted, they might expose functional groups on their surface, allowing surface passivation with biocompatible polymers or grafting additional biomolecules [158,159]. Finally, molecules like anticancer drugs and nucleic acids can be non-covalently loaded on their surface, allowing the use of these nanomaterials for delivery purposes [160,161]. Among all the carbon nanomaterials described so far, CDs seem to display the highest biocompatibility [162]. One important contribution to this effect seems to be the high density of charged groups on their surface, which provides high stability of their suspensions in water and biological fluids. Several authors have reported that carbon dots penetrate cell lines in vitro [163-167;]. No toxicity was observed in various studies conducted on cell lines [162,165] and on animals [168]. However, Borisova et al. reported that these nanoparticles could interfere with exocytotic mechanisms, and therefore hamper the normal neuronal and brain functions [169]. However, the effect of CDs on cellular biochemistry has not been completely explored.

Given their recent discovery, only a few studies have applied CDs to the CNS with the aim of diagnosis and therapy. Interestingly, the CDs used in in vivo biodistribution studies exhibited very good BBB crossing capabilities and a strong tendency to accumulate in the brain even if they were not specifically functionalized: 100 nm fluorescent CDs, prepared via the inexpensive and efficient pyrolysis of a glucose and glutamic acid mixture, were uptaken by cerebral tissues after i.v. administration in mice [170]. Epifluorescence imaging, made possible thanks to the CDs bright fluorescence emission, revealed that they crossed readily the BBB after systemic injection and diffused in the brain tissues, where they reached the highest concentration within 1 h. Ex vivo imaging of brain slices indicated that CDs were predominantly accumulated at the cortex surface, in the hippocampus and in the ventricles. The authors hypothesized that the presence of still intact glucose and glutamine molecules on the CDs surface endowed the nanoparticles of “CNS-targeting” capabilities. From the available epifluorescence images, the nanomaterial did not show diffusion in other specific body regions apart from the brain and the blood. Interestingly, the nanomaterial was also rapidly cleared from the CNS. In vitro studies [171,172] have demonstrated that CDs dispersions in plasma had high stability, and good hemocompatibility with moderate cytotoxicity for brain endothelial cells, detected only at very high concentrations. In summary they provided in vivo data, although referring only to early time-points, suggested that the nanomaterial had an adequate safety profile for biomedical applications in the CNS.

Also 3–4 nm glycine-derived CDs were able to cross very efficiently the BBB and accumulate in the brain. Moreover, they were able to target a human glioma tumor xenographted in mice brain [173]. Epifluorescence imaging indicated that they displayed a maximum brain uptake just 5 min after tail vein injection, and strongly localized inside the tumor mass to be then rapidly cleared. Systemically, CDs distributed in the liver, kidneys and hearth. In vitro hemolysis, plasma stability and cytotoxicity studies indicated a high biocompatibility of this nanomaterials [168,174]. Although these CDs displayed fast and consistent accumulation inside the tumor, their potential use as vectors for delivering antitumor drugs in the CNS is not suggested at the moment because of their fast excretion from the tumor lesion and their accumulation in the heart, which is a known target of anticancer drugs toxicity.

These nanomaterials are in the very early stages of development for biomedical applications: suitable chemical modification with molecules able to increase their plasma circulation time and/or with targeting moieties might improve their retention in the brain allowing future applications in tumor therapy. A deep toxicological evaluation of their effects in the CNS in particular but also in the whole body is needed since current available data, albeit very promising, are not sufficient to draw clear conclusions.

9. Conclusions

In the past few years, CBNs have been studied in a wide range of technological fields, including biomedical applications. Many CBNs have demonstrated to possess unexpected and outstanding properties towards electrically active systems, such as the neuronal and the cardiac tissues. In particular, CNTs are in the spotlight for having a powerful influence on the physiological activity of neuronal tissue. The precise biophysical mechanisms of these special interactions are not completely understood, but the features and the remarkable applications of such materials, together with their ability to manipulate neural activity, hold strong promise in manufacturing interfaces enriched by artificial cues that can guide tissue reconstruction. The ability of CNT-based 3D structures to dictate neurite web morphology toward successful reconnection of segregated spinal explants has been explored in vitro [62] and the same material has been implanted in vivo in the rat brain with a limited tissue reaction surrounding the implants [64]. The new protagonist among CBNs, graphene, has also displayed interesting features that can be exploited at the interface with neurons and other CBNs are under investigation for their own peculiar properties.

We strongly believe that a great future awaits CBNs in machine-brain interfaces and in tissue engineering. For this reason, in this review, we have reported some of the more recent CBN applications related to engineer brain interfaces. We have discussed their properties and their

performances in improving and boosting neuronal growth, in developing new research lines in neurophysiology and neurobiology and in providing novel methods to explore brain function.

10. Author Contributions

RR, MM, SB, MP and LB conceived, structured and participated in writing the review.

11. Conflict of Interest Statement

The authors declare that the research was conducted in the absence of any commercial or financial relationship that could be constructed as a potential conflict of interest.

12. Acknowledgments

We acknowledge the financial support from the European Union's Horizon 2020 research and innovation program under grant agreements No. 696656 and No.785219 (Graphene Flagship). MP, as the recipient of the AXA Chair, is grateful to the AXA Research Fund for financial support. MP was also supported by the Spanish Ministry of Economy and Competitiveness MINECO (project CTQ2016-76721-R), by the University of Trieste and by Diputación Foral de Gipuzkoa program Red (101).

13. References

1. G. A. Posthuma-Trumpie, J. H. Wichers, M. Koets, L. B. Berendsen, A. Van Amerongen, Amorphous carbon nanoparticles: a versatile label for rapid diagnostic (immuno)assays, Anal Bioanal Chem, 402 (2012), 593-600
2. L. Zhang, L. Chen, T. Wells, M. El-Gomati, Bamboo and herringbone shaped carbon nanotubes and carbon nanofibres synthesized in direct current-plasma enhanced chemical vapour deposition, J Nanosci Nanotechnol, 9 (2009), 4502-4506
3. M. F. De Volder, R. Vansweevelt, P. Wagner, D. Reynaerts, C. Van Hoof, A. J. Hart, Hierarchical carbon nanowire microarchitectures made by plasma-assisted pyrolysis of photoresist, ACS Nano, 5 (2011), 6593-6600
4. X. Cao, Q. He, W. Shi, B. Li, Z. Zeng, Y. Shi, Q. Yan, H. Zhang, Graphene oxide as a carbon source for controlled growth of carbon nanowires, Small, 7 (2011), 1199-1202
5. K. Seekell, M. J. Crow, S. Marinakos, J. Ostrander, A. Chilkoti, A. Wax, Hyperspectral molecular imaging of multiple receptors using immunolabeled plasmonic nanoparticles, J Biomed Opt, 16 (2011), 116003
6. J. Y. Lee, C. A. Bashur, A. S. Goldstein, C. E. Schmidt, Polypyrrole-coated electrospun PLGA nanofibers for neural tissue applications, Biomaterials, 30 (2009), 4325-4335
7. O. Onaca, R. Enea, D. W. Hughes, W. Meier, Stimuli-responsive polymersomes as nanocarriers for drug and gene delivery, Macromol Biosci, 9 (2009), 129-139
8. J. H. Kim, G. Kang, Y. Nam, Y. K. Choi, Surface-modified microelectrode array with flake nanostructure for neural recording and stimulation, Nanotechnology, 21 (2010), 085303

9. H. Zhang, M. Yu, L. Xie, L. Jin, Z. Yu, Carbon-Nanofibers-Based Micro-/Nanodevices for Neural-Electrical and Neural-Chemical Interfaces, Journal of Nanomaterials, 2012 (2012), Article ID 280902
10. M. S. Dresselhaus, Fifty years in studying carbon-based materials, Phys. Scr. 2012 (2012) T146
11. G. A. Silva, Nanotechnology approaches to crossing the blood-brain barrier and drug delivery to the CNS. BMC Neurosci. (2008) 3:S4
12. D. Pantarotto, J. P. Briand, M. Prato, A. Bianco, Translocation of bioactive peptides across cell membranes by carbon nanotubes, Chem Commun (Camb) 1 (2004), 16-7
13. M. S. Mauter and M. Elimelech, Environmental Applications of Carbon-Based Nanomaterials, Environ. Sci. Technol 42 (2008), 5843–5859
14. P. R. Supronowicz, P. M. Ajayan, K. R. Ullmann, B. P. Arulanandam, D. W. Metzger, R. Bizios, Novel current-conducting composite substrates for exposing osteoblasts to alternating current stimulation, J. Biomed. Mater. Res. 59 (2002) 499-506
15. Q. Li, J. Song, F. Besenbacher, M. Dong, Two-dimensional material confined water, Acc Chem Res, 48 (2015) 119-127
16. D. Yu, K. Goh, H. Wang, L. Wei, W. Jiang, Q. Zhang, L. Dai, Y. Chen, Scalable synthesis of hierarchically structured carbon nanotube-graphene fibres for capacitive energy storage, Nat Nanotechnol, 9 (2014) 555-562
17. Q. Xue, H. Chen, Q. Li, K. Yan, F. Besenbacher, M. Dong, Room-temperature high-sensitivity detection of ammonia gas using the capacitance of carbon/silicon heterojunctions, Energy Environ Sci, 3 (2010) 288-291
18. H. Sun, X. You, J. Deng, X. Chen, Z. Yang, J. Ren, H. Peng, Novel graphene/carbon nanotube composite fibers for efficient wire-shaped miniature energy devices, Adv Mater, 26 (2014) 2868-2873
19. C. Ge, J. Du, L. Zhao et al., Binding of blood proteins to carbon nanotubes reduces cytotoxicity, Proc Natl Acad Sci U. S. A., 108 (2011), 16968-16973
20. X. Zhang, W. Hu, J. Li, L. Tao, Y. Wei, A comparative study of cellular uptake and cytotoxicity of multi-walled carbon nanotubes, graphene oxide, and nanodiamond, Toxicol Res, 1 (2012), 62-68
21. M. V. Khodakovskaya, K. de Silva, A. S. Biris, E. Dervishi, H. Villagarcia, Carbon nanotubes induce growth enhancement of tobacco cells, ACS Nano, 6 (2012), 2128-2135
22. Y. Liu, X. Dong, P. Chen, Biological and chemical sensors based on graphene materials, Chem Soc Rev, 41 (2012), 2283-2307
23. M. Adeli, R. Soleyman, Z. Beiranvand, F. Madani, Carbon nanotubes in cancer therapy: a more precise look at the role of carbon nanotube-polymer interactions, Chem Soc Rev, 42 (2013), 5231-5256
24. M. Zheng, S. Liu, J. Li et al., Integrating oxaliplatin with highly luminescent carbon dots: an unprecedented theranostic agent for personalized medicine, Adv Mater, 26 (2014), 3554-3560
25. B. G. Demczyk, Y. M. Wang, J. Cumings, M. Hetman, W. Han, A. Zettl, R. O. Ritchie, Direct mechanical measurement of the tensile strength and elastic modulus of multiwalled carbon nanotubes, Mater. Sci. Eng. A. 334 (2002), 173-178
26. K. I. Bolotin, K. J. Sikes, Z. Jiang, M. Klima, G. Fudenberg, J. Hone, P. Kim, H. L. Stormer, Ultrahigh electron mobility in suspended graphene, Solid State Commun. 146 (2008), 351-355
27. F. Kreupl, A. P. Graham, G. S. Duesberg, W. Steinhögl, M. Liebau, E. Unger, W. Hönlein, Carbon nanotubes in interconnect applications, Microelectron. Eng. 64 (2002), 399-408
28. A. A. Balandin, S. Ghosh, W. Bao, I. Calizo, D. Teweldebrhan, F. Miao, C. N. Lau, Superior Thermal Conductivity of Single-Layer Graphene, Nano Lett. 8 (2008), 902-907

29. L. Gomez De Arco, Y. Zhang, C. W. Schlenker, K. Ryu, M. E. Thompson, C. Zhou, Continuous, highly flexible, and transparent graphene films by chemical vapor deposition for organic photovoltaics, ACS Nano 4 (2010), 2865-2873
30. S. Wang, P. K. Ang, Z. Wang, A. L. Tang, J. T. Thong, K. P. Loh, High mobility, printable, and solution-processed graphene electronics, Nano Lett. 10 (2010), 92-98
31. T. S. Sreeprasad, S. M. Maliyekkal, K. P. Lisha, T. Pradeep, Reduced graphene oxide-metal/metal oxide composites: Facile synthesis and application in water purification, J. Hazard. Mater. 186 (2011), 921-931
32. A. M. K. Esawi, M. M. Farag, Carbon nanotube reinforced composites: Potential and current challenges, Mater. Des. 28 (2007), 2394-2401
33. S. Iijima, Helical microtubules of graphitic carbon, Nature 354, (1991) 56-58
34. P. M. Ajayan, Nanotubes from carbon, Chem. Rev. 99 (1999), 1787-1799
35. S. Prithu, A. Prerit, Recent advances in carbon nanotube-based electronics, Mater. Res. Bull. 43 (2008), 2517-2526
36. A. Bianco, K. Kostarelos, M. Prato, Making carbon nanotubes biocompatible and biodegradable, Chem. Commun. (Cambridge, U.K.) 47 (2011), 10182-10188
37. N. Yang, X. Chena, T. Ren, P. Zhang, D. Yang, Sensors and Actuators B: Chemical 207, Part A, 2015, 690-715
38. H. E. Unalan, M. Chhowalla, Investigation of single-walled carbon nanotube growth parameters using alcohol catalytic chemical vapour deposition, Nanotechnology 16 (2005), 2153-2163
39. W. Feng, P. Ji, Enzymes immobilized on carbon nanotubes. Biotechnol. Adv. 29 (2011), 889-895
40. S. R. Ji, C. Liu, B. Zhang, F. Yang, J. Xu, J. Long, C. Jin, D. L. Fu, Q. X. Ni, X. J. Yu, Carbon nanotubes in cancer diagnosis and therapy, Biochim Biophys Acta. 1806 (2010), 29-35
41. H. He, L. A. Pham-Huy, P. Dramou, D. Xiao, P. Zuo, C. Pham-Huy, Carbon Nanotubes: Applications in Pharmacy and Medicine, Biomed. Res. Int. 8 (2013), 578290
42. S. Bosi, A. Fabbro, L. Ballerini, M. Prato, Carbon nanotubes: a promise for nerve tissue engineering? Nanotechnol. Rev., 2 (2013), 47-57
43. M. P. Mattson, R. C. Haddon, M. Rao, Molecular functionalization of carbon nanotubes and use as substrates for neuronal growth, J. Mol. Neurosci. 14 (2000), 175-182
44. H. Hu, Y. Ni, V. Montana, R. C. Haddon, V. Parpura, Chemically functionalized carbon nanotubes as substrates for neuronal growth, Nano Lett. 4 (2004), 507-511
45. A. Fabbro, F. M. Toma, G. Cellot, M. Prato, L. Ballerini, Carbon nanotubes and neuronal performance, Nanomedicine and the Nervous System 2010, 183-206;
46. N. A. Kotov, J. O. Winter, I. P. Clements, E. Jan, B. P. Timko, S. Campidelli, et al. Nanomaterials for neural interfaces, Adv. Mater. 21 (2009), 3970-4004
47. V. Lovat, D. Pantarotto, L. Lagostena, B. Cacciari, M. Grandolfo, M. Righi, et al. Carbon nanotube substrates boost neuronal electrical signaling, Nano Lett. 5 (2005), 1107-1110
48. S. B. Brummer, M. J. Turner, Electrical stimulation with Pt electrodes: II-estimation of maximum surface redox (theoretical non-gassing) limits, IEEE Trans. Biomed. Eng. 24 (1977), 440-443
49. A. V. Liopo, M. P. Stewart, J. Hudson, J. M. Tour, T. C. Pappas, Biocompatibility of native functionalized single-walled carbon nanotubes for neuronal interface, J. Nanosci. Nanotechnol. 6 (2006), 1365-1374
50. M. K. Gheith, T. C. Pappas, A. V. Liopo, V. Sinani, B. S. Shim, M. Motamedi, J. P. Wicksted, N. A. Kotov, Stimulation of neural cells by lateral layer-by-layer films of single-walled currents in conductive carbon nanotubes, Adv. Mater. 18 (2006), 2975

51. A. Mazzatenta, M. Giugliano, S. Campidelli, L. Gambazzi, L. Businaro, H. Markram, M. Prato, L. Ballerini, Interfacing neurons with carbon nanotubes: electrical signal transfer and synaptic stimulation in cultured brain circuits, J. Neurosci. 27 (2007) 6931-6936
52. K. Wang, H. A. Fishman, H. Dai, J. S. Harris, Neural stimulation with a carbon nanotube microelectrode array, Nano Lett. 6 (2006), 2043-2048
53. T. D. Nguyen-Vu, H. Chen, A. M. Cassell, R. J. Andrews, M. Meyyappan, J. Li, Vertically aligned carbon nanofiber architecture as a multifunctional 3-D neural electrical interface, IEEE Trans. Biomed. Eng. 4 (2007), 1121-1128
54. M. Abidian, D. C. Martin, Conducting-polymer nanotubes for controlled drug release. Adv. Mater. 18 (2006), 405-409
55. T. E. McKnight, A. V. Melechko, B. L. Fletcher, S. W. Jones, D. K. Hensley, D. B. Peckys, G. D. Griffin, M. L. Simpson, M. N. Ericson, Resident neuroelectrochemical interfacing using carbon nanofiber arrays, J. Phys. Chem. B. 110 (2006), 15317-15327
56. M. Shein, A. Greenbaum, T. Gabay, R. Sorkin, M. David-Pur, E. Ben-Jacob, Y. Hanein, Engineered neuronal circuits shaped and interfaced with carbon nanotube microelectrode arrays, Biomed. Microdevices. 11 (2009), 495-501
57. A. Shoval, C. Adams, M. David-Pur, M. Shein, Y. Hanein, E. Sernagor, Carbon nanotube electrodes for effective interfacing with retinal tissue, Front. Neuroeng. 2 (2009), 4
58. M. Khraiche, N. Jackson, J. Muthuswamy, Early onset of electrical activity in developing neurons cultured on carbon nanotube immobilized microelectrodes. Conf. Proc. IEEE Eng. Med. Biol. Soc. (2009), 777-80
59. B. M. Baker, C. S. Chen, Deconstructing the third dimension: how 3D culture microenvironments alter cellular cues, J. Cell Sci. 125 (2012) 3015-3024
60. M. Ghibaudo, L. Trichet, J. Le Digabel, A. Richert, P. Hersen, B. Ladoux, Substrate topography induces a crossover from 2D to 3D behavior in fibroblast migration, Biophys J. 97 (2009), 357-368
61. X. Gui, J. Wei, K. Wang, A. Cao, H. Zhu, Y. Jia, Q. Shu, D. Wu, Carbon nanotube sponges, Adv Mater. 22 (2010), 617-621
62. S. Usmani, E. R. Aurand, M. Medelin, A. Fabbro, D. Scaini, J. Laishram, F. B. Rosselli, A. Ansuini, D. Zoccolan, M. Scarselli, M. De Crescenzi, S. Bosi, M. Prato, L. Ballerini, 3D meshes of carbon nanotubes guide functional reconnection of segregated spinal explants, Sci Adv. 2 (2016), e1600087
63. S. Bosi, R. Rauti, J. Laishram, A. Turco, D. Lonardoni, T. Nieus, M. Prato, D. Scaini, L. Ballerini, From 2D to 3D: novel nanostructured scaffolds to investigate signalling in reconstructed neuronal networks, Sci Rep. 5 (2015), 9562
64. E. R. Aurand, S. Usmani, M. Medelin, D. Scaini, S. Bosi, F. B. Rosselli, S. Donato, G. Tromba, M. Prato, L. Ballerini, Nanostructures to Engineer 3D Neural ‐ Interfaces: Directing Axonal Navigation toward Successful Bridging of Spinal Segments, Adv. Funct. Mater. 28 (2018), 1700550
65. K. S. Novoselov, A. K. Geim, S. V. Morozov, D. Jiang, Y. Zhang, S. V. Dubonos, I. V. Grigorieva, A. A. Firsov, Electric field effect in atomically thin carbon films, Science 306, (2004), 666-669
66. X. Sun, Z. Liu, K. Welsher, J. T. Robinson, A. Goodwin, S. Zaric, H. Dai, Nano-graphene oxide for cellular imaging and drug delivery, Nano. Res. 1 (2008), 203-212
67. T. Cohen-Karni, Q. Qing, Q. Li, Y. Fang, C. M. Lieber, Graphene and nanowire transistors for cellular interfaces and electrical recording, Nano. Lett. 10 (2010), 1098-1102
68. M. Kalbacova, A. Broz, J. Kong, M. Kalbac, Graphene substrates promote adherence of human osteoblasts and mesenchymal stromal cells, Carbon, 48 (2010), 4323-4329
69. S. Y. Park, J. Park, S. H. Sim, M. G. Sung, K. S. Kim, B. H. Hong, S. Hong, Enhanced differentiation of human neural stem cells into neurons on graphene, Adv. Mater. 23 (2011), H263-7

70. K. Yang, S. Zhang, G. Zhang, X. Sun, S. T. Lee, Z. Liu, Graphene in mice: ultrahigh in vivo tumor uptake and efficient photothermal therapy, Nano Lett. 10 (2010), 3318-3323
71. N. Li, X. Zhang, Q. Song, R. Su, Q. Zhang, T. Kong, L. Liu, G. Jin, M. Tang, G. Cheng, The promotion of neurite sprouting and outgrowth of mouse hippocampal cells in culture by graphene substrates, Biomaterials, 32 (2011), 9374-9382
72. A. Fabbro, D. Scaini, V. León, E. Vázquez, G. Cellot, G. Privitera, L. Lombardi, F. Torrisi, F. Tomarchio, F. Bonaccorso, S. Bosi, A. C. Ferrari, L. Ballerini, M. Prato, Graphene-based interfaces do not alter target nerve cells, ACS Nano 10, (2016) 615-623
73. N.P. Pampaloni, M. Lottner, M. Giugliano, A. Matruglio, F. D'Amico, M. Prato, G.J. Antonio, L. Ballerini, D. Scaini, Single-layer graphene modulates neuronal communication and augments membrane ion currents. Nature Nanotech. (2018), Doi: 10.1038/s41565-018-0163-6
74. D. W. Park, A. A. Schendel, S. Mikael, S. K. Brodnick, T. J. Richner, J. P. Ness, M. R. Hayat, F. Atry, S. T. Frye, R. Pashaie, S. Thongpang, Z. Ma, J. C. Williams, Graphene-based carbon-layered electrode array technology for neural imaging and optogenetic applications, Nat Commun. 5 (2014), 5258
75. K. Kostarelos, M. Vincent, C. Hebert, J. A. Garrido, Graphene in the Design and Engineering of Next-Generation Neural Interfaces, Adv Mater. 29 (2017)
76. C. Hébert, E. Masvidal-Codina, A. Suarez-Perez, A. B. Calia, G. Piret, R. Garcia-Cortadella, X. Illa, E. Del Corro Garcia, J. M. De la Cruz Sanchez, D. V. Casals, E. Prats-Alfonso, J. Bousquet, P. Godignon, B. Yvert, R. Villa, M. V. Sanchez-Vives, A. Guimerà-Brunet, J. A. Garrido, Flexible Graphene Solution-Gated Field-Effect Transistors: Efficient Transducers for Micro-Electrocorticography, Adv. Funct. Mater. 28 (2018), 1703976
77. M. Vincent, I. de Lázaro, K. Kostarelos, Graphene materials as 2D non-viral gene transfer vector platforms, Gene Ther. 24 (2017), 123-132
78. K. Zhou, S. Motamed, G. A. Thouas, C. C. Bernard, D. Li, H. C. Parkington, H. A. Coleman, D. I. Finkelstein, J. S. Forsythe, Graphene functionalized scaffolds reduce the inflammatory response and supports endogenous neuroblast migration when implanted in the adult brain, PloS one, 11 (2016), e0151589
79. Q. Song, Z. Jiang, N. Li, P. Liu, L. Liu, M. Tang, G. Cheng, Anti-inflammatory effects of three-dimensional graphene foams cultured with microglial cells, Biomaterials 35 (2014), 6930-6940
80. A. Verkhratsky, M. Noda, V. Parpura, Microglia: structure and function, Anatomy and Physiology, Systems 2 (2015), 109-113
81. M. Tang, Q. Song, N. Li, Z. Jiang, R. Huang, G. Cheng, Enhancement of electrical signaling in neural networks on graphene films, Biomaterials 34 (2013), 6402-6411
82. D. Bitounis, H. Ali-Boucetta, B. H. Hong, D. H. Min, K. Kostarelos, Prospects and challenges of graphene in biomedical applications Adv Mater. 25 (2013), 2258-2268
83. D. Kuzum, H. Takano, E. Shim, J. C. Reed, H. Juul, A. G. Richardson, J. de Vries, H. Bink, M. A. Dichter, T. H. Lucas, D. A. Coulter, E. Cubukcu, B. Litt, Transparent and flexible low noise graphene electrodes for simultaneous electrophysiology and neuroimaging Nat Commun. 5 (2014), 5259
84. R. Rauti, N. Lozano, V. León, D. Scaini, M. Musto, I. Rago, F. P. Ulloa Severino, A. Fabbro, L. Casalis, E. Vázquez, K. Kostarelos, M. Prato, L. Ballerini, Graphene Oxide Nanosheets Reshape Synaptic Function in Cultured Brain Networks ACS Nano 10 (2016), 4459-4471
85. X. Wang, X. Sun, J. Lao, H. He, T. Cheng, M. Wang, et al., Multifunctional graphene quantum dots for simultaneous targeted cellular imaging and drug delivery Colloids Surf. B Biointerfaces 122 (2014) 638-644

86. L. Zuccaro, C. Tesauro, T. Kurkina, P. Fiorani, H. K. Yu, B. R. Knudsen B, et al., Real-time label-free direct electronic monitoring of topoisomerase enzyme binding kinetics on graphene ACS Nano 9 (2015), 11166-11176
87. F. M. Tonelli, V. A. Goulart, K. N. Gomes, M. S. Ladeira, A. K. Santos, E. Lorencon, et al., Graphene-based nanomaterials: biological and medical applications and toxicity Nanomedicine 10 (2015), 2423-2450
88. H. Dong, M. Jin, Z. Liu, H. Xiong, X. Qiu, W. Zhang, et al., In vitro and in vivo brain-targeting chemo-photothermal therapy using graphene oxide conjugated with transferrin for Gliomas Lasers Med. Sci 31 (2016), 1123-1131
89. M. Medina-Sánchez, S. Miserere, A. Merkoci, Nanomaterials and lab-on-a-chip technologies Lab Chip 12 (2012), 1932-1943
90. N. Li, T. Xiao, Z. Zhang, R. He, D. Wen, Y. Cao, et al., A 3D graphene oxide microchip and a Au-enwrapped silica nanocomposite-based supersandwich cytosensor toward capture and analysis of circulating tumor cells Nanoscale 7 (2015), 16354-16360
91. Q. Tu, L. Pang, Y. Chen, Y. Zhang, R. Zhang, B. Lu, et al., Effects of surface charges of graphene oxide on neuronal outgrowth and branching, Analyst 139 (2014), 105-115
92. M. Bramini, G. Alberini, E. Colombo, M. Chiacchiaretta, M. L. DiFrancesco, J. F. Maya-Vetencourt, L. Maragliano, F. Benfenati, F. Cesca, Interfacing Graphene-Based Materials With Neural Cells, Front Syst Neurosci. 11 (2018),12
93. N. Li, Q. Zhang, S. Gao, Q. Song, R. Huang, L. Wang, L. Liu, J. Dai, M. Tang, G. Cheng, Three-dimensional graphene foam as a biocompatible and conductive scaffold for neural stem cells Sci Rep. 3 (2013), 1604
94. F. P. Ulloa Severino, J. Ban, Q. Song, M. Tang, G. Bianconi, G. Cheng, V. Torre, The role of dimensionality in neuronal network dynamics Sci Rep. 6 (2016), 29640
95. C. Martín, S. Merino, J. M. González-Domínguez, R. Rauti, L. Ballerini, M. Prato, E. Vázquez, Graphene Improves the Biocompatibility of Polyacrylamide Hydrogels: 3D Polymeric Scaffolds for Neuronal Growth Sci Rep. 7 (2017), 10942
96. R. J. Nemanich, J. A. Carlisle, A. Hirata, K. Haenen, CVD diamond-Research, applications, and challenges. MRS Bull. 39 (2014), 490-548
97. S. Szunerits, Y. Coffinier, R. Boukherroub, Diamond Nanowires: A Novel Platform for Electrochemistry and Matrix-Free Mass Spectrometry. Sensors 15 (2015), 12573-12593
98. D.A. Garrett, W. Tong, D. A. Simpson, H. Meffin, Diamond for neural interfacing: A review, Carbon 102 (2016), 437-454
99. C. G. Specht, O. A. Williams, R. B. Jackman, R. Schoepfer, Ordered growth of neurons on diamond, Biomaterials 25 (2004), 4073-4078
100. B. Shi, Q. L. Jin, L. H. Chen, O. Auciello, Fundamentals of ultrananocrystalline diamond (UNCD) thin films as biomaterials for developmental biology: embryonic fibroblasts growth on the surface of (UNCD) films, Diam. Relat. Mat. 18 (2009), 596-600
101. B. Shi, Q. Jin, L. Chen, A. S. Woods, A. J. Schultz, O. Auciello, Cell growth on different types of ultrananocrystalline diamond thin films, J. Funct. Biomater 3 (2012), 588
102. P. Bajaj, D. Akin, A. Gupta, D. Sherman, B. Shi, O. Auciello, R. Bashir, Ultrananocrystalline diamond film as an optimal cell interface for biomedical applications, Biomed. Microdevices 9 (2007), 787-794
103. L. Guarina, C. Calorio, D. Gavello, E. Moreva et al., Nanodiamonds-induced effects on neuronal firing of mouse hippocampal microcircuits, Sci Rep. 8 (2018) 2221
104. P. Ariano, A. Lo Giudice, A. Marcantoni, E. Vittone, E. Carbone, D. Lovisolo, A diamond-based biosensor for the recording of neuronal activity, Biosens. Bioelectron. 24 (2009), 2046-2050
105. C. Ho-Yin, D. M. Aslam, J. A. Wiler, B. Casey, A novel diamond microprobe for neuro-chemical and -electrical recording in neural prosthesis, J. Microelectromech. Syst. 18 (2009), 511-521

106. M. Dankerl, S. Eick, B. Hofmann, M. Hauf, S. Ingebrandt, A. Offenhäusser, M. Stutzmann, J. A. Garrido, Diamond Transistor Array for Extracellular Recording From Electrogenic Cells, Adv. Funct. Mater 19 (2009), 2915-2923
107. V. Carabelli, S. Gosso, A. Marcantoni, Y. Xu, E. Colombo, Z. Gao, E. Vittone, E. Kohn, A. Pasquarelli, E. Carbone, Nanocrystalline diamond microelectrode arrays fabricated on sapphire technology for high-time resolution of quantal catecholamine secretion from chromaffin cells, Biosens. Bioelectron. 26 (2010), 92-98
108. F. Picollo, A. Battiato, E. Bernardi, L. Boarino, E. Enrico, J. Forneris, D. Gatto Monticone, P. Olivero, Realization of a diamond based high density multi electrode array by means of Deep Ion Beam Lithography Nucl. Instrum. Methods Phys. Res., Sect. B 348 (2015), 199-202
109. C. Hebert, J. Warnking, A. Depaulis, L. A. Garcon, M. Mermoux, D. Eon, P. Mailley, F. Omnes, Microfabrication, characterization and in vivo MRI compatibility of diamond microelectrodes array for neural interfacing, Mater. Sci. Eng., C 46 (2015), 25-31
110. G. Piret, C. Hebert, J. P. Mazellier, L. Rousseau, E. Scorsone, M. Cottance, G. Lissorgues, M. O. Heuschkel, S. Picaud, P. Bergonzo, B. Yvert, 3D-nanostructured boron-doped diamond for microelectrode array neural interfacing, Biomaterials 53 (2015), 173-183
111. V. Carabelli, A. Marcantoni, F. Picollo, A. Battiato, E. Bernardi, A. Pasquarelli, P. Olivero, E. Carbone, Planar Diamond-Based Multiarrays to Monitor Neurotransmitter Release and Action Potential Firing: New Perspectives in Cellular Neuroscience, ACS Chemical Neuroscience 8 (2017), 252-26
112. K. Fox, H. Meffin, O. Burns, C. J. Abbott, P. J. Allen, N. L. Opie, C. McGowan, J. Yeoh, A. Ahnood, C. D. Luu, R. Cicione, A. L. Saunders, M. McPhedran, L. Cardamone, et al., Development of a Magnetic Attachment Method for Bionic Eye Applications Artif. Organs 40 (2016), E12-24
113. K. Ganesan, D. J. Garrett, A. Ahnood, M. N. Shivdasani, W. Tong, A. M. Turnley, K. Fox, H. Meffin, S. Prawer, An all-diamond, hermetic electrical feedthrough array for a retinal prosthesis, Biomaterials 35 (2014), 908-915
114. S. Gosso, M. Turturici, C. Franchino, E. Colombo, A. Pasquarelli, E. Carbone, V. Carabelli, Heterogeneous distribution of exocytotic microdomains in adrenal chromaffin cells resolved by high-density diamond ultra-microelectrode arrays, J. Physiol 592 (2014), 3215-3230
115. P. A. Nistor, P. W. May, F. Tamagnini, A. D. Randall, M. A. Caldwell, Long-term culture of pluripotent stem-cell-derived human neurons on diamond - A substrate for neurodegeneration research and therapy, Biomaterials 61 (2015), 139-149
116. A. Thalhammer, R. J. Edgington, L. A. Cingolani, R. Schoepfer, R. B. Jackman, The use of nanodiamond monolayer coatings to promote the formation of functional neuronal networks, Biomaterials 31 (2010), 2097-3104
117. M. Bonnauron, S. Saada, C. Mer, C. Gesset, O. A. Williams, L. Rousseau, E. Scorsone, P. Mailley, M. Nesladek, J. C. Arnault, P. Bergonzo, Transparent diamond-on-glass micro-electrode arrays for ex-vivo neuronal study, Phys. Stat. Sol. 205 (2008), 2126-2129
118. J. M. Halpern, M. J. Cullins, H. J. Chiel, H. B. Martin, Chronic in vivo nerve electrical recordings of Aplysia californica using a boron-doped polycrystalline diamond electrode, Diamond and Related Materials 19 (2010), 178-181
119. S. Szunerits, Y. Coffinier, E. Galopin, J. Brenner, R. Boukherroub, Preparation of boron-doped diamond nanowires and their application for sensitive electrochemical detection of tryptophan. Electrochem. Commun. 12 (2010), 438-441

120. D. Luo, L. Wu, J. Zhi, Fabrication of boron-doped diamond nanorod forest electrodes and their application in nonenzymatic amperometric glucose sensing. ACS Nano 3 (2009), 2121-2128
121. N. Yang, H. Uetsuka, E. Osawa, C. E. Nebel, Vertically aligned diamond nanowires for DNA sensing. Angew. Chem. Int. Ed. 47 (2008), 5183-5185
122. Q. Wang, P. Subramanian, M. Li, W. S. Yeap, K. Haenen, Y. Coffinier, R. Boukherroub, S. Szunerits, Non-enzymatic glucose sensing on long and short diamond nanowires electrodes, Electrochem. Commun. 34 (2013), 286-290
123. F. Lemaître, M. Guille Collignon, C. Amatore, Recent advances in Electrochemical Detection of Exocytosis, Electrochim. Acta, 140 (2014), 457-466
124. J. E. Field, The mechanical and strength properties of diamond, Rep Prog Phys. 75 (2012), 126505
125. M. Jelínek, K. Smetana, T. Kocourek, B. Dvořánková, J. Zemek, J. Remsa, T. Luxbacher, Biocompatibility and sp3/sp2 ratio of laser created DLC films, Mater. Sci. Eng., B 169 (2010), 89-93
126. M. Kopecek, L. Bacakova, J. Vacik, F. Fendrych, V. Vorlicek, I. Kratochvilova, V. Lisa, E. Van Hove, C. Mer, P. Bergonzo, M. Nesladek, Improved adhesion, growth and maturation of human bone-derived cells on nanocrystalline diamond films, Phys. Status Solidi A 205 (2008), 2146-2153
127. J. A. Garrido, (2009) Biofunctionalization of Diamond Surfaces: Fundamentals and Applications. In CVD Diamond for Electronic Devices and Sensors, R.S. Sussman (ed.), 399-437
128. T. C. Kuo, R. L. McCreery, G. M. Swain, Electrochemical Modification of Boron-Doped Chemical Vapor Deposited Diamond Surfaces with Covalently Bonded Monolayers, Electrochem. Solid-State Lett. 2 (1999), 288-290
129. W. Yang, O. Auciello, J. E. Butler, W. Cai, J. A. Carlisle, J. E. Gerbi, D. M. Gruen, T. Knickerbocker, T. L. Lasseter, J. N. Russell, L. M. Smith, R. J. Hamers, DNA-modified nanocrystalline diamond thin-films as stable, biologically active substrates, Nat. Mater. 1 (2002), 253-257
130. K. Sugata, M. Tachiki, T. Fukuda, H. Seo, H. Kawarada, Nanoscale Modification of the Hydrogen-Terminated Diamond Surface Using Atomic Force Microscope, Jpn. J. Appl. Phys. 41 (2002), 4983
131. A. Fraczek-Szczypta, Carbon nanomaterials for nerve tissue stimulation and regeneration, Mater Sci Eng C Mater Biol Appl. 34 (2014), 35-49
132. W. Kubo, H. Hayakawa, K. Miyoshi, S. Fujikawa, Size-controlled simple fabrication of free-standing, ultralong metal nanobelt array, J. Nanosci Nanotechnol 11 (2011), 131-137
133. C. D. McCaig, A. M. Rajnicek, B. Song, M. Zhao, Controlling cell behavior electrically: current views and future potential, Physiol. Rev. 85 (2005), 943-978
134. H. W. Kroto, J. R. Heath, S. C. O'Brien, R. F. Curl, R. E. Smalley, C60: Buckminsterfullerene, Nature 318 (1985), 162-163
135. R. Taylor, D. R. M. Walton, The Chemistry of Fullerenes, Nature 363 (1993), 685-693
136. D. S. Bethune, R. D. Johnson, J. R. Salem, M. S. de Vries, C. S. Yannoni, Atoms in Carbon Cages: The Structure and Properties of Endohedral Fullerenes, Nature 366 (1993), 123-128
137. H. W. Kroto, The Stability of the Fullerenes Cn, with n = 24, 28, 32, 36, 50, 60 and 70, Nature 329 (1987), 529-531
138. D. M. Guldi, M. Prato, Excited-State Properties of C60 Fullerene Derivatives, Acc. Chem. Res. 33 (2000), 695-703

139. S. Kirner, M. Sekita, D. M. Guldi, 25th Anniversary Article: 25 Years of Fullerene Research in Electron Transfer Chemistry, Adv. Mater. 26 (2014), 1482-1493
140. A. W. Jensen, S. R. Wilson, D. I. Schuster, Biological Applications of Fullerenes, Bioorgan. Med. Chem. 4 (1996), 767-779
141. J. E. Anthony, A. Facchetti, M. Heeney, S. R. Marder, X. Zhan, N-Type Organic Semiconductors in Organic Electronics, Adv. Mater. 22 (2010), 3876-3892
142. R. Gaudiana, C. Brabec, Organic Materials: Fantastic Plastic, Nat. Photonics 2 (2008), 287-289
143. A. Montellano, T. Da Ros, A. Bianco, M. Prato, Fullerene C_{60} as a multifunctional system for drug and gene delivery, Nanoscale 3 (2011), 4035-4041
144. B. Halliwell, Reactive oxygen species and the central nervous system, J. Neurochem. 59 (1992), 1609-1623
145. L. L. Dugan, D. M. C. Turetsky Du, D. Lobner, M. Wheeler, C. R. Almli, C. K. Shen, T. Y. Luh, D. W. Choi, T. S. Lin, Carboxyfullerenes as neuroprotective agents, Proc. Natl. Acad. Sci. U S A. 94 (1997), 9434-9439
146. H. Jin, W. Q. Chen, X. W. Tang, L. Y. Chiang, C. Y. Yang, J. V. Schloss, J. Y. Wu, Polyhydroxylated C60, fullerenols, as glutamate receptor antagonists and neuroprotective agents, J Neurosci Res. 62 (2000), 600-607
147. J. Zhang, J. Ge, M. D. Shultz, E. Chung, G. Singh, C. Shu, *et al*., In vitro and in vivo studies of single-walled carbon nanohorns with encapsulated metallofullerenes and exohedrally functionalized quantum dots, Nano Lett. 10 (2010), 2843-2848
148. J. Miyawaki, S. Matsumura, R. Yuge, T. Murakami, S. Sato, A. Tomida, *et al*., Biodistribution and ultrastructural localization of single-walled carbon nanohorns determined in vivo with embedded Gd2O3 labels, ACS Nano 3 (2009), 1399-1406
149. Y. Tahara, J. Miyawaki, M. Zhang, M. Yang, I. Waga, S. Iijima, *et al.*, Histological assessments for toxicity and functionalization-dependent biodistribution of carbon nanohorns, Nanotechnology (2011), 22:265106
150. X. Xu, R. Ray, Y. Gu, H. J. Ploehn, L. Gearheart, K. Raker, *et al.*, Electrophoretic analysis and purification of fluorescent single-walled carbon nanotube fragments, J. Am. Chem. Soc. 126 (2004), 12736-12737
151. K. A. S. Fernando, S. Sahu, Y. Liu, W. K. Lewis, E. A. Guliants, A. Jafariyan, *et al*., Carbon quantum dots and applications in photocatalytic energy conversion, ACS Appl. Mater. Interfaces 7 (2015), 8363-8376
152. J. Shen, Y. Li, Y. Su, Y. Zhu, H. Jiang, X. Yang, *et al*., Photoluminescent carbon-nitrogen quantum dots as efficient electrocatalysts for oxygen reduction, Nanoscale 7, (2015), 2003-2008
153. J. Briscoe, A. Marinovic, M. Sevilla, S. Dunn, M. Titirici, Biomass-derived carbon quantum dot sensitizers for solid-state nanostructured solar cells, Angew. Chemie Int. 54, (2015), 4463-4468
154. A. Zhao, Z. Chen, C. Zhao, N. Gao, J. Ren, X. Qu, Recent advances in bioapplications of C-dots, Carbon 85, (2015), 309-327
155. H. Li, Z. Kang, Y. Liu, S. T. Lee, Carbon nanodots: synthesis, properties and applications, J. Mater. Chem. 22, (2012), 24230-24253
156. V. Strauss, J. T. Margraf, C. Dolle, B. Butz, T. J. Nacken, J. Walter, *et al*., Carbon Nanodots: toward a comprehensive understanding of their photoluminescence, J. Am. Chem. Soc. 136, (2014), 17308-17316
157. Z. Peng, X. H. Shanghao, L. Abdulrahman, O. Al-Youbi, A. S. Bashammakh, M. S. El-Shahawi, R. M. Leblanc, Carbon dots: Biomacromolecule interaction, bioimaging and nanomedicine, Coordination Chemistry Reviews 343, (2017), 256-277

158. M. C. Kim, K. S. Yu, S. Y. Han, J. Kim, J. W. Lee, N. S. Lee, Y. G. Jeong, D. K. Kim, Highly photoluminescent N-isopropylacrylamide (NIPAAM) passivated carbon dots for multicolor bioimaging applications, European Polymer Journal 98, (2018),191-198
159. A. Kundu, J. Lee, B. Park, C. Ray, K. V. Sankar, W. S. Kim, S. H. Lee, I. J. Cho, S. C. Jun, Facile approach to synthesize highly fluorescent multicolor emissive carbon dots via surface functionalization for cellular imaging, J Colloid Interface Sci. 513, (2018), 505-514
160. Q. Zeng, D. Shao, X. He, Z. Ren , W. Ji, C. Shan, S. Qu, J. Li, L. Chen, Q. Li, Carbon dots as a trackable drug delivery carrier for localized cancer therapy in vivo, J. Mater. Chem. B 4, (2016), 5119-5126
161. S. Singh, A. Mishra, R. Kumari, K. K. Sinha, M. K. Singh, P. Das, Carbon dots assisted formation of DNA hydrogel for sustained release of drug, Carbon 114, (2017), 169-176
162. J. Wang, J. Qiu, A review of carbon dots in biological applications, Journal of Materials Science 51, (2016), 4728-4738
163. N. Zhou, S. Zhu, S. Maharjan, Z. Hao, Y. Song, X. Zhao, Y. Jiang, B. Yang, L. Lu, Elucidating the Endocytosis, Intracellular Trafficking, and Exocytosis of Carbon Dots in Neural Cells. RSC Adv. 4, (2014), 62086-62095
164. E. J. Goh, K. S. Kim, Y. R. Kim, H. S. Jung, S. Beack, W. H. Kong, G. Scarcelli, S. H. Yun, S. K. Hahn, Bioimaging of Hyaluronic Acid Derivatives Using Nanosized Carbon Dots, Biomacromolecules 13, (2012), 2554-2561
165. C. Liu, P. Zhang, X. Zhai, F. Tian, W. Li, J. Yang, Y. Liu, H. Wang, W. Wang, W. Liu, Nano-Carrier for Gene Delivery and Bioimaging Based on Carbon Dots with PEI-Passivation Enhanced Fluorescence, Biomaterials 33, (2012), 3604-3613
166. N. Li, X. Liang, L. Wang, Z. Li, P. Li, Y. Zhu, J. Song, Biodistribution Study of Carbogenic Dots in Cells and in Vivo for Optical Imaging, J. Nanopart. Res. 14, (2012), 1-9
167. Q. X. Mao, S. E, J. M. Xia, R. S. Song, Y. Shu, X. W. Chen, J. H. Wang, Hydrophobic Carbon Nanodots with Rapid Cell Penetrability and Tunable Photoluminescence Behavior for in Vitro and in Vivo Imaging, Langmuir 32, (2016), 12221-12229
168. H. Tao, K. Yang, Z. Ma, J. Wan, Y. Zhang, Z. Kang, Z. Liu, In Vivo NIR Fluorescence Imaging, Biodistribution, and Toxicology of Photoluminescent Carbon Dots Produced from Carbon Nanotubes and Graphite, Small, 8 (2012) 281-290
169. T. Borisova, A. Nazarova, M. Dekaliuk, N. Krisanova, N. Pozdnyakova, A. Borysov, et al., Neuromodulatory properties of fluorescent carbon dots: effect on exocytotic release, uptake and ambient level of glutamate and GABA in brain nerve terminals, Int. J. Biochem. Cell Biol. 59, (2015), 203-215
170. J. Qian, S. Ruan, X. Cao, X. Cun, J. Chen, S. Shen, X. Jiang, Q. He, J. Zhu, H. Gao, Fluorescent carbonaceous nanospheres as biological probe for noninvasive brain imaging, J Colloid Interface Sc. 436 (2014) 227-233
171. X. Huang, F. Zhang, L. Zhu, K. Y. Cho, N. Guo, J. Guo, K. Tackett, P. Anilkumar, G. Liu, Q. Quan, H. S. Choi, G. Niu, Y. Sun, S. Lee, X. Chen, Effect of injection routes on the biodistribution, clearance, and tumor uptake of carbon dots, ACS Nano 7, (2013) 5684-5693
172. M. Zheng, S. Ruan, S. Liu, T. Sun, D. Qu, H. Zhao, Z. Xie, H. Gao, X. Jing, Z. Sun, Self-Targeting Fluorescent Carbon Dots for Diagnosis of Brain Cancer Cells, ACS Nano 9, (2015) 11455-11461
173. S. Ruan, J. Qian, S. Shen, J. Chen, J. Zhu, X. Jiang, Q. He, W. Yang, H. Gao, Fluorescent carbonaceous nanodots for noninvasive glioma imaging after angiopep-2 decoration, Bioconjug Chem. 25 (2014) 2252-9

174. K.Wang, Z. Gao, G. Gao, Y. Wo, Y. Wang, G. Shen, D. Cui, Systematic safety evaluation on photoluminescent carbon dots, Nanoscale Res. Lett., 8 (2013) 122

DISCUSSION

EVs discovery represents a breakthrough in the understanding of signaling among cells, unveiling an alternative and complementary way every cell phenotype may adopt to communicate either with neighbor or distant targets, not only circumscribed to a single tissue. EVs structure allows the organisms to deliver complex signals mediated by macromolecules in a stable environment and avoiding potential interactions with external agents. Their conservation over the evolution suggests a fundamental role in many aspects of functioning of biological systems, at different levels of complexity (Lawson et al., 2017).

However one of the main issue in the study of these particles is their isolation, detection and measurement (Witwer et al., 2013). The recent increasing studies on EVs coincides in fact with the rising of technologies and tools for the investigation of the nanoscale and synthesis of nanosized materials, the so-called "nanotechnologies" (Wong et al., 2013). In the vast panorama of nanomaterials, an extraordinary scientific interest is growing up on carbon-based materials, driven by the immense variety of possibilities that these materials can provide to the development of biomedical interfaces, especially in the field of neuroscience (Baldrighi et al., 2016a; John et al., 2015).

What we have done was to study the interfacing of nanomaterials with glial cells, focusing on s-GO flakes. s-GO flakes are nanosized fragments of graphene oxide which directly interact with cellular plasma membrane by adsorbing on it or being internalized by the cell. This interaction is known to alter the equilibrium of the membrane and in some conditions, mostly correlated with concentration and exposure-time, also its integrity (Zhang et al., 2016).

We already know from literature that glial cells, both astrocytes and microglia, are able to release MVs under pharmacological stimulation with bzATP (Bianco et al., 2005, 2009) and as first step we confirmed this data (Rauti et al., 2016b). However the massive release of MVs evoked by bzATP represents a stressful condition for cells that could not be maintained over time, due to the long-term cytotoxic effects of bzATP. On the other hand, MVs basal release has been known to be very weak in resting condition, as also shown by the western blot analysis. Therefore, starting from the fact that s-GO flakes interacts with plasma membrane and considering the biogenesis and origin of MVs, we tested the capacity of those

flakes to modulate the release of vesicles by simply exposing glial cell to it for a short-term period. The treatment did not visibly affect glia viability, as demonstrated by the cell density analysis, however significantly affected basal MVs release. s-GO flakes indeed boosted MVs basal release to a level totally comparable to that of bzATP and significantly higher than the basal release measured in the untreated cultures, as demonstrated by western blot. Since this way of inducing MVs release by this specific kind of cell was not reported before, we investigated the nature of those MVs by comparing them with MVs released by a well-known model of release, represented by bzATP stimulation. We investigated similarities and differences to better understand the nature of this alternative pool of MVs by characterizing them for structure, composition and physiological effects exerted. Once we identified MVs by AFM measurement and verified that MVs released from s-GO-treated cultures were completely similar to those isolated after bzATP stimulation, proving that s-GO effectively induced release of MVs from glial cells we investigated the dynamic of the release by staining plasma membranes with FM1-43 styryl dye in both the condition of release. The plasma membrane de-staining revealed a faster decay of fluorescence equivalent in both the treated cultures when compared with controls, suggesting that this was actually related to MVs budding from the cell surface and not the result of lipid membrane physiological turnover and finally verifying the flotillin-1 positive signals obtained from treated cultures culture media. Once the hypothesis of the enhanced MVs basal release induced by s-GO was confirmed, we investigated the nature of MVs obtained by comparing the two populations. Size measurement revealed a comparable size distribution with the exception of AFM measurements, where s-GO-derived MVs were significantly smaller than the bzATP-derived ones. This result could be related to the small number of vesicles analysed, if compared with the large scale measurement of DLS and NTA. However, the smaller diameter reported for s-GO-derived MVs may also suggest a difference in the elastic properties between the two population of vesicles, in fact the AFM measures performed in air may cause MVs to collapse under the atmospheric pressure; the different size observed could then represent a higher resistance of s-GO-derived MVs to this pressure. Also the analysis of macromolecular composition performed with infrared-ATR measurement revealed an equivalent nature for MVs isolated from the two conditions of release. The absorption peaks highlighted the presence of nucleic acids, mostly represented by RNAs, proteins and lipids, even if the low

signal-noise ratio did not allow a deeper analysis of the spectrum aimed to identify which specific class of nucleic acids and proteins they carry. These data together suggest that even if the stimulus that triggers the production of vesicles is different, the product of release is similar and reinforce the hypothesis that s-GO potentiate the MVs pathway of release, without affecting the vesicles makeup.

Finally, the role of MVs and EVs in general is to deliver complex messages that are stored in their cargo as macromolecules like nucleic acids, proteins and bioactive lipids which, once uptaken by target cells, may affect their physiology at different level and with different timings. In literature there are several studies on different cellular models which investigate the biological effects mediated by EVs on other cells and only few of them focuses on nervous system. The effects reported, studied both in physiological and pathological conditions, are usually the result of a long-time exposure to EVs (Antonucci et al., 2012; Emmanouilidou et al., 2010; Simeoli et al., 2017) but almost nothing is known about the short-time effects that take place few minutes after the interaction of EVs with the target. In the last part of the work we investigated how an acute administration of MVs to cortical neurons affects their synaptic activity. We found that over 50% of the neurons exposed to MVs, isolated from both conditions, showed an increase in PSCs frequencies 15 minutes after the puff of MVs, revealing however a large variability. The cause of this variability may be attributed to at least three factors: the concentration of MVs really delivered is variable by definition because we cannot actually control the number of vesicles released by a single culture of glial cell, even if MVs density is localized in a fixed range, the intrinsic variability could affect the response of cells targeted; the number of MVs that actually reach and fuse with the plasma membrane may also variate and finally the mechanism of signaling itself involves the synergy of several pathways that cooperate all together to generate a biological output (Rhoads, 1999). One of those is RNA translation and protein synthesis, which require a variable time span of the order of minutes, significantly slower and less precise than the response mediated by the activation of receptors by their ligands.

In conclusion, MVs and more in general EVs are a field of research that has to be explored more in depth since the comprehension of underlying mechanisms is still at an embryonic stage. They represent a great opportunity to better understand the physiology of intercellular

communication even in a pathological environment, and provide a powerful tool to modulate and possibly control the signaling among cells. On the other hand, in the field of cellular engineering, gene therapy and drug delivery, EVs constitute a promising strategy for the development of applications in biomedicine and bioengineering. However, the fulfillment of these goals cannot be reached without the integration of biological sciences with nanotechnologies. High throughput instruments and nanosized substrates are essential to create efficient interfaces able to control those processes that were uncontrollable until few years ago. In this context we cannot overlook the capacity of such nanomaterials to be integrated in biological systems without affecting their physiology. For this reason, studies of biocompatibility must be conducted in parallel, in order to minimize possible adverse reaction and maximize the outputs.

REFERENCES

Akers, J. C., Gonda, D., Kim, R., Carter, B. S., and Chen, C. C. (2013). Biogenesis of extracellular vesicles (EV): exosomes, microvesicles, retrovirus-like vesicles, and apoptotic bodies. *J. Neurooncol.* 113, 1–11. doi:10.1007/s11060-013-1084-8.

Allen, N. J. (2014). Astrocyte Regulation of Synaptic Behavior. *Annu. Rev. Cell Dev. Biol.* 30, 439–463. doi:10.1146/annurev-cellbio-100913-013053.

Antonucci, F., Turola, E., Riganti, L., Caleo, M., Gabrielli, M., Perrotta, C., et al. (2012). Microvesicles released from microglia stimulate synaptic activity via enhanced sphingolipid metabolism. *EMBO J.* 31, 1231–40. doi:10.1038/emboj.2011.489.

Antonyak, M. A., and Cerione, R. A. (2014). "Microvesicles as Mediators of Intercellular Communication in Cancer," in *Methods in molecular biology (Clifton, N.J.)*, 147–173. doi:10.1007/978-1-4939-0856-1_11.

Antonyak, M. A., Wilson, K. F., and Cerione, R. A. (2012). R(h)oads to microvesicles. *Small GTPases* 3, 219–24. doi:10.4161/sgtp.20755.

Asai, H., Ikezu, S., Tsunoda, S., Medalla, M., Luebke, J., Haydar, T., et al. (2015). Depletion of microglia and inhibition of exosome synthesis halt tau propagation. *Nat. Neurosci.* 18, 1584–93. doi:10.1038/nn.4132.

Attwell, D., Buchan, A. M., Charpak, S., Lauritzen, M., MacVicar, B. A., and Newman, E. A. (2010). Glial and neuronal control of brain blood flow. *Nature* 468, 232–243. doi:10.1038/nature09613.

Bakhti, M., Winter, C., and Simons, M. (2011). Inhibition of myelin membrane sheath formation by oligodendrocyte-derived exosome-like vesicles. *J. Biol. Chem.* 286, 787–96. doi:10.1074/jbc.M110.190009.

Balaj, L., Lessard, R., Dai, L., Cho, Y.-J., Pomeroy, S. L., Breakefield, X. O., et al. (2011). Tumour microvesicles contain retrotransposon elements and amplified oncogene sequences. *Nat. Commun.* 2, 180. doi:10.1038/ncomms1180.

Baldrighi, M., Trusel, M., Tonini, R., and Giordani, S. (2016a). Carbon Nanomaterials

Interfacing with Neurons: An In vivo Perspective. *Front. Neurosci.* 10, 250. doi:10.3389/fnins.2016.00250.

Baldrighi, M., Trusel, M., Tonini, R., and Giordani, S. (2016b). Carbon Nanomaterials Interfacing with Neurons: An In vivo Perspective. *Front. Neurosci.* 10, 250. doi:10.3389/fnins.2016.00250.

Basso, M., Pozzi, S., Tortarolo, M., Fiordaliso, F., Bisighini, C., Pasetto, L., et al. (2013). Mutant copper-zinc superoxide dismutase (SOD1) induces protein secretion pathway alterations and exosome release in astrocytes: implications for disease spreading and motor neuron pathology in amyotrophic lateral sclerosis. *J. Biol. Chem.* 288, 15699–711. doi:10.1074/jbc.M112.425066.

Bayer-Santos, E., Aguilar-Bonavides, C., Rodrigues, S. P., Cordero, E. M., Marques, A. F., Varela-Ramirez, A., et al. (2013). Proteomic analysis of Trypanosoma cruzi secretome: characterization of two populations of extracellular vesicles and soluble proteins. *J. Proteome Res.* 12, 883–97. doi:10.1021/pr300947g.

Beckett, K., Monier, S., Palmer, L., Alexandre, C., Green, H., Bonneil, E., et al. (2013). Drosophila S2 Cells Secrete Wingless on Exosome-Like Vesicles but the Wingless Gradient Forms Independently of Exosomes. *Traffic* 14, 82–96. doi:10.1111/tra.12016.

Benz, E. W., and Moses, H. L. (1974). Small, virus-like particles detected in bovine sera by electron microscopy. *J. Natl. Cancer Inst.* 52, 1931–4. Available at: http://www.ncbi.nlm.nih.gov/pubmed/4834422 [Accessed June 10, 2018].

Bianco, F., Perrotta, C., Novellino, L., Francolini, M., Riganti, L., Menna, E., et al. (2009). Acid sphingomyelinase activity triggers microparticle release from glial cells. *EMBO J.* 28, 1043–54. doi:10.1038/emboj.2009.45.

Bianco, F., Pravettoni, E., Colombo, A., Schenk, U., Möller, T., Matteoli, M., et al. (2005). Astrocyte-derived ATP induces vesicle shedding and IL-1 beta release from microglia. *J. Immunol.* 174, 7268–77. Available at: http://www.ncbi.nlm.nih.gov/pubmed/15905573 [Accessed June 12, 2018].

Bitounis, D., Ali-Boucetta, H., Hong, B. H., Min, D.-H., and Kostarelos, K. (2013). Prospects and Challenges of Graphene in Biomedical Applications. *Adv. Mater.* 25, 2258–2268. doi:10.1002/adma.201203700.

Bolotin, K. I., Sikes, K. J., Jiang, Z., Klima, M., Fudenberg, G., Hone, J., et al. (2008). Ultrahigh electron mobility in suspended graphene. *Solid State Commun.* 146, 351–355. doi:10.1016/J.SSC.2008.02.024.

Bosse, F. (2012). Extrinsic cellular and molecular mediators of peripheral axonal regeneration. *Cell Tissue Res.* 349, 5–14. doi:10.1007/s00441-012-1389-5.

Budnik, V., Ruiz-Cañada, C., and Wendler, F. (2016). Extracellular vesicles round off communication in the nervous system. *Nat. Rev. Neurosci.* 17, 160–72. doi:10.1038/nrn.2015.29.

Chang, C., Lang, H., Geng, N., Wang, J., Li, N., and Wang, X. (2013). Exosomes of BV-2 cells induced by alpha-synuclein: important mediator of neurodegeneration in PD. *Neurosci. Lett.* 548, 190–5. doi:10.1016/j.neulet.2013.06.009.

Chargaff, E., and West, R. (1946). The biological significance of the thromboplastic protein of blood. *J. Biol. Chem.* 166, 189–197. Available at: http://www.ncbi.nlm.nih.gov/pubmed/20273687 [Accessed June 8, 2018].

Chatterjee, N., Eom, H.-J., and Choi, J. (2014). A systems toxicology approach to the surface functionality control of graphene–cell interactions. *Biomaterials* 35, 1109–1127. doi:10.1016/J.BIOMATERIALS.2013.09.108.

Chivet, M., Javalet, C., Laulagnier, K., Blot, B., Hemming, F. J., and Sadoul, R. (2014). Exosomes secreted by cortical neurons upon glutamatergic synapse activation specifically interact with neurons. *J. Extracell. Vesicles* 3, 24722. doi:10.3402/jev.v3.24722.

Clarke, L. E., and Barres, B. A. (2013). Emerging roles of astrocytes in neural circuit development. *Nat. Rev. Neurosci.* 14, 311–321. doi:10.1038/nrn3484.

Cocucci, E., and Meldolesi, J. (2015). Ectosomes and exosomes: shedding the confusion between extracellular vesicles. *Trends Cell Biol.* 25, 364–72.

doi:10.1016/j.tcb.2015.01.004.

Cocucci, E., Racchetti, G., and Meldolesi, J. (2009). Shedding microvesicles: artefacts no more. *Trends Cell Biol.* 19, 43–51. doi:10.1016/j.tcb.2008.11.003.

Cocucci, E., Racchetti, G., Podini, P., and Meldolesi, J. (2007). Enlargeosome traffic: exocytosis triggered by various signals is followed by endocytosis, membrane shedding or both. *Traffic* 8, 742–57. doi:10.1111/j.1600-0854.2007.00566.x.

Colombo, E., Borgiani, B., Verderio, C., and Furlan, R. (2012). Microvesicles: Novel Biomarkers for Neurological Disorders. *Front. Physiol.* 3, 63. doi:10.3389/fphys.2012.00063.

Colombo, M., Raposo, G., and Théry, C. (2014). Biogenesis, Secretion, and Intercellular Interactions of Exosomes and Other Extracellular Vesicles. *Annu. Rev. Cell Dev. Biol.* 30, 255–289. doi:10.1146/annurev-cellbio-101512-122326.

Czernek, L., and Düchler, M. (2017). Functions of Cancer-Derived Extracellular Vesicles in Immunosuppression. *Arch. Immunol. Ther. Exp. (Warsz).* 65, 311–323. doi:10.1007/s00005-016-0453-3.

Danbolt, N. C. (2001). Glutamate uptake. *Prog. Neurobiol.* 65, 1–105. Available at: http://www.ncbi.nlm.nih.gov/pubmed/11369436 [Accessed August 12, 2018].

Danzer, K. M., Kranich, L. R., Ruf, W. P., Cagsal-Getkin, O., Winslow, A. R., Zhu, L., et al. (2012). Exosomal cell-to-cell transmission of alpha synuclein oligomers. *Mol. Neurodegener.* 7, 42. doi:10.1186/1750-1326-7-42.

Davletov, B., and Montecucco, C. (2010). Lipid function at synapses. *Curr. Opin. Neurobiol.* 20, 543–549. doi:10.1016/j.conb.2010.06.008.

Dresselhaus, M. S. (2012). Fifty years in studying carbon-based materials. *Phys. Scr.* T146, 014002. doi:10.1088/0031-8949/2012/T146/014002.

EL Andaloussi, S., Mäger, I., Breakefield, X. O., and Wood, M. J. A. (2013). Extracellular vesicles: biology and emerging therapeutic opportunities. *Nat. Rev. Drug Discov.* 12, 347–357. doi:10.1038/nrd3978.

Emmanouilidou, E., Melachroinou, K., Roumeliotis, T., Garbis, S. D., Ntzouni, M., Margaritis, L. H., et al. (2010). Cell-produced alpha-synuclein is secreted in a calcium-dependent manner by exosomes and impacts neuronal survival. *J. Neurosci.* 30, 6838–51. doi:10.1523/JNEUROSCI.5699-09.2010.

Enderle, D., Spiel, A., Coticchia, C. M., Berghoff, E., Mueller, R., Schlumpberger, M., et al. (2015). Characterization of RNA from Exosomes and Other Extracellular Vesicles Isolated by a Novel Spin Column-Based Method. *PLoS One* 10, e0136133. doi:10.1371/journal.pone.0136133.

Esawi, A. M. K., and Farag, M. M. (2007). Carbon nanotube reinforced composites: Potential and current challenges. *Mater. Des.* 28, 2394–2401. doi:10.1016/J.MATDES.2006.09.022.

Fabbro, A., Scaini, D., León, V., Vázquez, E., Cellot, G., Privitera, G., et al. (2016). Graphene-Based Interfaces Do Not Alter Target Nerve Cells. *ACS Nano* 10, 615–623. doi:10.1021/acsnano.5b05647.

Fauré, J., Lachenal, G., Court, M., Hirrlinger, J., Chatellard-Causse, C., Blot, B., et al. (2006). Exosomes are released by cultured cortical neurones. *Mol. Cell. Neurosci.* 31, 642–8. doi:10.1016/j.mcn.2005.12.003.

Feliciano, D. M., Zhang, S., Nasrallah, C. M., Lisgo, S. N., and Bordey, A. (2014). Embryonic cerebrospinal fluid nanovesicles carry evolutionarily conserved molecules and promote neural stem cell amplification. *PLoS One* 9, e88810. doi:10.1371/journal.pone.0088810.

Fevrier, B., Vilette, D., Archer, F., Loew, D., Faigle, W., Vidal, M., et al. (2004). Cells release prions in association with exosomes. *Proc. Natl. Acad. Sci. U. S. A.* 101, 9683–8. doi:10.1073/pnas.0308413101.

Fields, R. D., and Stevens-Graham, B. (2002). New Insights into Neuron-Glia Communication. *Science (80-.).* 298, 556–562. doi:10.1126/science.298.5593.556.

Fitzner, D., Schnaars, M., van Rossum, D., Krishnamoorthy, G., Dibaj, P., Bakhti, M., et al. (2011). Selective transfer of exosomes from oligodendrocytes to microglia by

macropinocytosis. *J. Cell Sci.* 124, 447–58. doi:10.1242/jcs.074088.

Frühbeis, C., Fröhlich, D., and Krämer-Albers, E.-M. (2012). Emerging Roles of Exosomes in Neuron–Glia Communication. *Front. Physiol.* 3, 119. doi:10.3389/fphys.2012.00119.

Frühbeis, C., Fröhlich, D., Kuo, W. P., Amphornrat, J., Thilemann, S., Saab, A. S., et al. (2013a). Neurotransmitter-triggered transfer of exosomes mediates oligodendrocyte-neuron communication. *PLoS Biol.* 11, e1001604. doi:10.1371/journal.pbio.1001604.

Frühbeis, C., Fröhlich, D., Kuo, W. P., and Krämer-Albers, E.-M. (2013b). Extracellular vesicles as mediators of neuron-glia communication. *Front. Cell. Neurosci.* 7, 182. doi:10.3389/fncel.2013.00182.

Gabrielli, M., Battista, N., Riganti, L., Prada, I., Antonucci, F., Cantone, L., et al. (2015). Active endocannabinoids are secreted on extracellular membrane vesicles. *EMBO Rep.* 16, 213–20. doi:10.15252/embr.201439668.

Gardiner, C., Vizio, D. Di, Sahoo, S., Théry, C., Witwer, K. W., Wauben, M., et al. (2016). Techniques used for the isolation and characterization of extracellular vesicles: results of a worldwide survey. *J. Extracell. Vesicles* 5, 32945. doi:10.3402/jev.v5.32945.

Gibbings, D. J., Ciaudo, C., Erhardt, M., and Voinnet, O. (2009). Multivesicular bodies associate with components of miRNA effector complexes and modulate miRNA activity. *Nat. Cell Biol.* 11, 1143–9. doi:10.1038/ncb1929.

Ginhoux, F., and Prinz, M. (2015). Origin of microglia: current concepts and past controversies. *Cold Spring Harb. Perspect. Biol.* 7, a020537. doi:10.1101/cshperspect.a020537.

Goldie, B. J., Dun, M. D., Lin, M., Smith, N. D., Verrills, N. M., Dayas, C. V, et al. (2014). Activity-associated miRNA are packaged in Map1b-enriched exosomes released from depolarized neurons. *Nucleic Acids Res.* 42, 9195–208. doi:10.1093/nar/gku594.

Gosselin, R.-D., Meylan, P., and Decosterd, I. (2013). Extracellular microvesicles from astrocytes contain functional glutamate transporters: regulation by protein kinase C and cell activation. *Front. Cell. Neurosci.* 7, 251. doi:10.3389/fncel.2013.00251.

Graner, M. W., Alzate, O., Dechkovskaia, A. M., Keene, J. D., Sampson, J. H., Mitchell, D. A., et al. (2009). Proteomic and immunologic analyses of brain tumor exosomes. *FASEB J.* 23, 1541–57. doi:10.1096/fj.08-122184.

Gross, J. C., Chaudhary, V., Bartscherer, K., and Boutros, M. (2012). Active Wnt proteins are secreted on exosomes. *Nat. Cell Biol.* 14, 1036–1045. doi:10.1038/ncb2574.

Gundacker, N. C., Haudek, V. J., Wimmer, H., Slany, A., Griss, J., Bochkov, V., et al. (2009). Cytoplasmic proteome and secretome profiles of differently stimulated human dendritic cells. *J. Proteome Res.* 8, 2799–811. doi:10.1021/pr8011039.

György, B., Hung, M. E., Breakefield, X. O., and Leonard, J. N. (2015). Therapeutic Applications of Extracellular Vesicles: Clinical Promise and Open Questions. *Annu. Rev. Pharmacol. Toxicol.* 55, 439–464. doi:10.1146/annurev-pharmtox-010814-124630.

György, B., Szabó, T. G., Pásztói, M., Pál, Z., Misják, P., Aradi, B., et al. (2011). Membrane vesicles, current state-of-the-art: emerging role of extracellular vesicles. *Cell. Mol. Life Sci.* 68, 2667–2688. doi:10.1007/s00018-011-0689-3.

Harding, C., Heuser, J., and Stahl, P. (1983). Receptor-mediated endocytosis of transferrin and recycling of the transferrin receptor in rat reticulocytes. *J. Cell Biol.* 97, 329–39. Available at: http://www.ncbi.nlm.nih.gov/pubmed/6309857 [Accessed May 18, 2018].

Hess, C., Sadallah, S., Hefti, A., Landmann, R., and Schifferli, J. A. (1999). Ectosomes released by human neutrophils are specialized functional units. *J. Immunol.* 163, 4564–73. Available at: http://www.ncbi.nlm.nih.gov/pubmed/10510400 [Accessed May 3, 2018].

Holme, P. A., Solum, N. O., Brosstad, F., Røger, M., and Abdelnoor, M. (1994). Demonstration of platelet-derived microvesicles in blood from patients with activated coagulation and fibrinolysis using a filtration technique and western blotting. *Thromb. Haemost.* 72, 666–71. Available at: http://www.ncbi.nlm.nih.gov/pubmed/7900071 [Accessed May 3, 2018].

Hu, G., Yao, H., Chaudhuri, A. D., Duan, M., Yelamanchili, S. V, Wen, H., et al. (2012). Exosome-mediated shuttling of microRNA-29 regulates HIV Tat and morphine-mediated neuronal dysfunction. *Cell Death Dis.* 3, e381. doi:10.1038/cddis.2012.114.

Huang, X., Yuan, T., Tschannen, M., Sun, Z., Jacob, H., Du, M., et al. (2013). Characterization of human plasma-derived exosomal RNAs by deep sequencing. *BMC Genomics* 14, 319. doi:10.1186/1471-2164-14-319.

Hurley, J. H. (2008). ESCRT complexes and the biogenesis of multivesicular bodies. *Curr. Opin. Cell Biol.* 20, 4–11. doi:10.1016/j.ceb.2007.12.002.

Iijima, S. (1991). Helical microtubules of graphitic carbon. *Nature* 354, 56–58. doi:10.1038/354056a0.

Jacob, C. (2015). Transcriptional control of neural crest specification into peripheral glia. *Glia* 63, 1883–1896. doi:10.1002/glia.22816.

John, A. A., Subramanian, A. P., Vellayappan, M. V., Balaji, A., Mohandas, H., and Jaganathan, S. K. (2015). Carbon nanotubes and graphene as emerging candidates in neuroregeneration and neurodrug delivery. *Int. J. Nanomedicine* 10, 4267–77. doi:10.2147/IJN.S83777.

Johnstone, R. M., Adam, M., Hammond, J. R., Orr, L., and Turbide, C. (1987). Vesicle formation during reticulocyte maturation. Association of plasma membrane activities with released vesicles (exosomes). *J. Biol. Chem.* 262, 9412–20. Available at: http://www.ncbi.nlm.nih.gov/pubmed/3597417 [Accessed June 10, 2018].

Kahner, B. N., Dorsam, R. T., and Kunapuli, S. P. (2008). Role of P2Y receptor subtypes in platelet-derived microparticle generation. *Front. Biosci.* 13, 433–9. Available at: http://www.ncbi.nlm.nih.gov/pubmed/17981558 [Accessed June 12, 2018].

Kalra, H., Drummen, G. P. C., and Mathivanan, S. (2016). Focus on Extracellular Vesicles: Introducing the Next Small Big Thing. *Int. J. Mol. Sci.* 17, 170. doi:10.3390/ijms17020170.

Kalra, H., Simpson, R. J., Ji, H., Aikawa, E., Altevogt, P., Askenase, P., et al. (2012). Vesiclepedia: a compendium for extracellular vesicles with continuous community

annotation. *PLoS Biol.* 10, e1001450. doi:10.1371/journal.pbio.1001450.

Keerthikumar, S., Gangoda, L., Liem, M., Fonseka, P., Atukorala, I., Ozcitti, C., et al. (2015). Proteogenomic analysis reveals exosomes are more oncogenic than ectosomes. *Oncotarget* 6, 15375–96. doi:10.18632/oncotarget.3801.

Klöhn, P.-C., Castro-Seoane, R., and Collinge, J. (2013). Exosome release from infected dendritic cells: a clue for a fast spread of prions in the periphery? *J. Infect.* 67, 359–68. doi:10.1016/j.jinf.2013.07.024.

Korkut, C., Ataman, B., Ramachandran, P., Ashley, J., Barria, R., Gherbesi, N., et al. (2009). Trans-Synaptic Transmission of Vesicular Wnt Signals through Evi/Wntless. *Cell* 139, 393–404. doi:10.1016/j.cell.2009.07.051.

Kostarelos, K., and Novoselov, K. S. (2014). Exploring the Interface of Graphene and Biology. *Science (80-.).* 344, 261–263. doi:10.1126/science.1246736.

Krämer-Albers, E.-M., Bretz, N., Tenzer, S., Winterstein, C., Möbius, W., Berger, H., et al. (2007). Oligodendrocytes secrete exosomes containing major myelin and stress-protective proteins: Trophic support for axons? *PROTEOMICS – Clin. Appl.* 1, 1446–1461. doi:10.1002/prca.200700522.

Kroto, H. W., Heath, J. R., O'Brien, S. C., Curl, R. F., and Smalley, R. E. (1985). C60: Buckminsterfullerene. *Nature* 318, 162–163. doi:10.1038/318162a0.

Kuzum, D., Takano, H., Shim, E., Reed, J. C., Juul, H., Richardson, A. G., et al. (2014). Transparent and flexible low noise graphene electrodes for simultaneous electrophysiology and neuroimaging. *Nat. Commun.* 5, 5259. doi:10.1038/ncomms6259.

Lachenal, G., Pernet-Gallay, K., Chivet, M., Hemming, F. J., Belly, A., Bodon, G., et al. (2011). Release of exosomes from differentiated neurons and its regulation by synaptic glutamatergic activity. *Mol. Cell. Neurosci.* 46, 409–18. doi:10.1016/j.mcn.2010.11.004.

Lai, C. P.-K., and Breakefield, X. O. (2012). Role of Exosomes/Microvesicles in the Nervous System and Use in Emerging Therapies. *Front. Physiol.* 3, 228.

doi:10.3389/fphys.2012.00228.

Lavialle, F., Deshayes, S., Gonnet, F., Larquet, E., Kruglik, S. G., Boisset, N., et al. (2009). Nanovesicles released by Dictyostelium cells: A potential carrier for drug delivery. *Int. J. Pharm.* 380, 206–215. doi:10.1016/j.ijpharm.2009.06.039.

Lawson, C., Kovacs, D., Finding, E., Ulfelder, E., and Luis-Fuentes, V. (2017). Extracellular Vesicles: Evolutionarily Conserved Mediators of Intercellular Communication. *Yale J. Biol. Med.* 90, 481–491. Available at: http://www.ncbi.nlm.nih.gov/pubmed/28955186 [Accessed September 20, 2018].

Li, N., Zhang, Q., Gao, S., Song, Q., Huang, R., Wang, L., et al. (2013). Three-dimensional graphene foam as a biocompatible and conductive scaffold for neural stem cells. *Sci. Rep.* 3, 1604. doi:10.1038/srep01604.

Li, N., Zhang, X., Song, Q., Su, R., Zhang, Q., Kong, T., et al. (2011). The promotion of neurite sprouting and outgrowth of mouse hippocampal cells in culture by graphene substrates. *Biomaterials* 32, 9374–82. doi:10.1016/j.biomaterials.2011.08.065.

Liao, K.-H., Lin, Y.-S., Macosko, C. W., and Haynes, C. L. (2011). Cytotoxicity of Graphene Oxide and Graphene in Human Erythrocytes and Skin Fibroblasts. *ACS Appl. Mater. Interfaces* 3, 2607–2615. doi:10.1021/am200428v.

Liégeois, S., Benedetto, A., Garnier, J.-M., Schwab, Y., and Labouesse, M. (2006). The V0-ATPase mediates apical secretion of exosomes containing Hedgehog-related proteins in Caenorhabditis elegans. *J. Cell Biol.* 173, 949–61. doi:10.1083/jcb.200511072.

Linares, J., Matesanz, M. C., Vila, M., Feito, M. J., Gonçalves, G., Vallet-Regí, M., et al. (2014). Endocytic Mechanisms of Graphene Oxide Nanosheets in Osteoblasts, Hepatocytes and Macrophages. *ACS Appl. Mater. Interfaces* 6, 13697–13706. doi:10.1021/am5031598.

Lopez-Verrilli, M. A., and Court, F. A. (2012). Transfer of vesicles from schwann cells to axons: a novel mechanism of communication in the peripheral nervous system. *Front. Physiol.* 3, 205. doi:10.3389/fphys.2012.00205.

Lopez-Verrilli, M. A., and Court, F. A. (2013). Exosomes: mediators of communication in eukaryotes. *Biol. Res.* 46, 5–11. doi:10.4067/S0716-97602013000100001.

Lopez-Verrilli, M. A., Picou, F., and Court, F. A. (2013). Schwann cell-derived exosomes enhance axonal regeneration in the peripheral nervous system. *Glia* 61, 1795–806. doi:10.1002/glia.22558.

Lösche, W., Scholz, T., Temmler, U., Oberle, V., and Claus, R. A. (2004). Platelet-derived microvesicles transfer tissue factor to monocytes but not to neutrophils. *Platelets* 15, 109–15. doi:10.1080/09537100310001649885.

Lugli, G., Cohen, A. M., Bennett, D. A., Shah, R. C., Fields, C. J., Hernandez, A. G., et al. (2015). Plasma Exosomal miRNAs in Persons with and without Alzheimer Disease: Altered Expression and Prospects for Biomarkers. *PLoS One* 10, e0139233. doi:10.1371/journal.pone.0139233.

Maas, S. L. N., Breakefield, X. O., and Weaver, A. M. (2017). Extracellular Vesicles: Unique Intercellular Delivery Vehicles. *Trends Cell Biol.* 27, 172–188. doi:10.1016/j.tcb.2016.11.003.

Makridakis, M., and Vlahou, A. (2010). Secretome proteomics for discovery of cancer biomarkers. *J. Proteomics* 73, 2291–2305. doi:10.1016/j.jprot.2010.07.001.

Martín, C., Merino, S., González-Domínguez, J. M., Rauti, R., Ballerini, L., Prato, M., et al. (2017). Graphene Improves the Biocompatibility of Polyacrylamide Hydrogels: 3D Polymeric Scaffolds for Neuronal Growth. *Sci. Rep.* 7, 10942. doi:10.1038/s41598-017-11359-x.

Marzesco, A.-M., Janich, P., Wilsch-Bräuninger, M., Dubreuil, V., Langenfeld, K., Corbeil, D., et al. (2005). Release of extracellular membrane particles carrying the stem cell marker prominin-1 (CD133) from neural progenitors and other epithelial cells. *J. Cell Sci.* 118, 2849–58. doi:10.1242/jcs.02439.

Mateescu, B., Kowal, E. J. K., van Balkom, B. W. M., Bartel, S., Bhattacharyya, S. N., Buzás, E. I., et al. (2017). Obstacles and opportunities in the functional analysis of extracellular vesicle RNA – an ISEV position paper. *J. Extracell. Vesicles* 6, 1286095.

doi:10.1080/20013078.2017.1286095.

McKelvey, K. J., Powell, K. L., Ashton, A. W., Morris, J. M., and McCracken, S. A. (2015). Exosomes: Mechanisms of Uptake. *J. Circ. Biomarkers* 4, 7. doi:10.5772/61186.

Meldolesi, J. (2018). Exosomes and Ectosomes in Intercellular Communication. *Curr. Biol.* 28, R435–R444. doi:10.1016/J.CUB.2018.01.059.

Mendoza-Naranjo, A., Bouma, G., Pereda, C., Ramírez, M., Webb, K. F., Tittarelli, A., et al. (2011). Functional gap junctions accumulate at the immunological synapse and contribute to T cell activation. *J. Immunol.* 187, 3121–32. doi:10.4049/jimmunol.1100378.

Minciacchi, V. R., Freeman, M. R., and Di Vizio, D. (2015). Extracellular vesicles in cancer: exosomes, microvesicles and the emerging role of large oncosomes. *Semin. Cell Dev. Biol.* 40, 41–51. doi:10.1016/j.semcdb.2015.02.010.

Morris, C. E., and Homann, U. (2001). Cell surface area regulation and membrane tension. *J. Membr. Biol.* 179, 79–102. Available at: http://www.ncbi.nlm.nih.gov/pubmed/11220366 [Accessed July 19, 2018].

Mu, Q., Su, G., Li, L., Gilbertson, B. O., Yu, L. H., Zhang, Q., et al. (2012). Size-Dependent Cell Uptake of Protein-Coated Graphene Oxide Nanosheets. *ACS Appl. Mater. Interfaces* 4, 2259–2266. doi:10.1021/am300253c.

Mulcahy, L. A., Pink, R. C., and Carter, D. R. F. (2014). Routes and mechanisms of extracellular vesicle uptake. *J. Extracell. Vesicles* 3, 24641. doi:10.3402/jev.v3.24641.

Muralidharan-Chari, V., Clancy, J., Plou, C., Romao, M., Chavrier, P., Raposo, G., et al. (2009). ARF6-regulated shedding of tumor cell-derived plasma membrane microvesicles. *Curr. Biol.* 19, 1875–85. doi:10.1016/j.cub.2009.09.059.

Nimmerjahn, A., Kirchhoff, F., and Helmchen, F. (2005). Resting Microglial Cells Are Highly Dynamic Surveillants of Brain Parenchyma in Vivo. *Science (80-.).* 308, 1314–1318. doi:10.1126/science.1110647.

Novoselov, K. S., Geim, A. K., Morozov, S. V, Jiang, D., Zhang, Y., Dubonos, S. V, et al. (2004). Electric field effect in atomically thin carbon films. *Science* 306, 666–9. doi:10.1126/science.1102896.

Palmieri, V., Lucchetti, D., Gatto, I., Maiorana, A., Marcantoni, M., Maulucci, G., et al. (2014). Dynamic light scattering for the characterization and counting of extracellular vesicles: a powerful noninvasive tool. *J. Nanoparticle Res.* 16, 2583. doi:10.1007/s11051-014-2583-z.

Pampaloni, N. P., Lottner, M., Giugliano, M., Matruglio, A., D'Amico, F., Prato, M., et al. (2018). Single-layer graphene modulates neuronal communication and augments membrane ion currents. *Nat. Nanotechnol.,* 1. doi:10.1038/s41565-018-0163-6.

Pant, S., Hilton, H., and Burczynski, M. E. (2012). The multifaceted exosome: biogenesis, role in normal and aberrant cellular function, and frontiers for pharmacological and biomarker opportunities. *Biochem. Pharmacol.* 83, 1484–94. doi:10.1016/j.bcp.2011.12.037.

Parisse, P., Rago, I., Ulloa Severino, L., Perissinotto, F., Ambrosetti, E., Paoletti, P., et al. (2017). Atomic force microscopy analysis of extracellular vesicles. *Eur. Biophys. J.* 46, 813–820. doi:10.1007/s00249-017-1252-4.

Pellerin, L., Bouzier-Sore, A.-K., Aubert, A., Serres, S., Merle, M., Costalat, R., et al. (2007). Activity-dependent regulation of energy metabolism by astrocytes: an update. *Glia* 55, 1251–62. doi:10.1002/glia.20528.

Perez-Hernandez, D., Gutiérrez-Vázquez, C., Jorge, I., López-Martín, S., Ursa, A., Sánchez-Madrid, F., et al. (2013). The intracellular interactome of tetraspanin-enriched microdomains reveals their function as sorting machineries toward exosomes. *J. Biol. Chem.* 288, 11649–61. doi:10.1074/jbc.M112.445304.

Pilzer, D., Gasser, O., Moskovich, O., Schifferli, J. A., and Fishelson, Z. (2005). Emission of membrane vesicles: roles in complement resistance, immunity and cancer. *Springer Semin. Immunopathol.* 27, 375–87. doi:10.1007/s00281-005-0004-1.

Pizzirani, C., Ferrari, D., Chiozzi, P., Adinolfi, E., Sandonà, D., Savaglio, E., et al. (2007).

Stimulation of P2 receptors causes release of IL-1beta-loaded microvesicles from human dendritic cells. *Blood* 109, 3856–64. doi:10.1182/blood-2005-06-031377.

Pospichalova, V., Svoboda, J., Dave, Z., Kotrbova, A., Kaiser, K., Klemova, D., et al. (2015). Simplified protocol for flow cytometry analysis of fluorescently labeled exosomes and microvesicles using dedicated flow cytometer. *J. Extracell. vesicles* 4, 25530. Available at: http://www.ncbi.nlm.nih.gov/pubmed/25833224 [Accessed August 30, 2018].

Proia, P., Schiera, G., Mineo, M., Ingrassia, A. M. R., Santoro, G., Savettieri, G., et al. (2008). Astrocytes shed extracellular vesicles that contain fibroblast growth factor-2 and vascular endothelial growth factor. *Int. J. Mol. Med.* 21, 63–7. Available at: http://www.ncbi.nlm.nih.gov/pubmed/18097617 [Accessed June 12, 2018].

Rajendran, L., Honsho, M., Zahn, T. R., Keller, P., Geiger, K. D., Verkade, P., et al. (2006). Alzheimer's disease beta-amyloid peptides are released in association with exosomes. *Proc. Natl. Acad. Sci.* 103, 11172–11177. doi:10.1073/pnas.0603838103.

Raposo, G., Nijman, H. W., Stoorvogel, W., Liejendekker, R., Harding, C. V, Melief, C. J., et al. (1996). B lymphocytes secrete antigen-presenting vesicles. *J. Exp. Med.* 183, 1161–72. Available at: http://www.ncbi.nlm.nih.gov/pubmed/8642258 [Accessed June 10, 2018].

Raposo, G., and Stoorvogel, W. (2013). Extracellular vesicles: exosomes, microvesicles, and friends. *J. Cell Biol.* 200, 373–83. doi:10.1083/jcb.201211138.

Rauti, R., Lozano, N., León, V., Scaini, D., Musto, M., Rago, I., et al. (2016a). Graphene Oxide Nanosheets Reshape Synaptic Function in Cultured Brain Networks. *ACS Nano* 10, 4459–71. doi:10.1021/acsnano.6b00130.

Record, M., Subra, C., Silvente-Poirot, S., and Poirot, M. (2011). Exosomes as intercellular signalosomes and pharmacological effectors. *Biochem. Pharmacol.* 81, 1171–82. doi:10.1016/j.bcp.2011.02.011.

Regente, M., Pinedo, M., Elizalde, M., and de la Canal, L. (2012). Apoplastic exosome-like vesicles: a new way of protein secretion in plants? *Plant Signal. Behav.* 7, 544–6.

doi:10.4161/psb.19675.

Regev-Rudzki, N., Wilson, D. W., Carvalho, T. G., Sisquella, X., Coleman, B. M., Rug, M., et al. (2013). Cell-Cell Communication between Malaria-Infected Red Blood Cells via Exosome-like Vesicles. *Cell* 153, 1120–1133. doi:10.1016/J.CELL.2013.04.029.

Rhoads, R. E. (1999). Signal transduction pathways that regulate eukaryotic protein synthesis. *J. Biol. Chem.* 274, 30337–40. doi:10.1074/JBC.274.43.30337.

Rodrigues, M. L., Nosanchuk, J. D., Schrank, A., Vainstein, M. H., Casadevall, A., and Nimrichter, L. (2011). Vesicular transport systems in fungi. *Future Microbiol.* 6, 1371–1381. doi:10.2217/fmb.11.112.

Ronquist, G., Brody, I., Gottfries, A., and Stegmayr, B. (2009). An Mg2+ and Ca2+-Stimulated Adenosine Triphosphatase in Human Prostatic Fluid: Part I. *Andrologia* 10, 261–272. doi:10.1111/j.1439-0272.1978.tb03030.x.

Rowitch, D. H., and Kriegstein, A. R. (2010). Developmental genetics of vertebrate glial–cell specification. *Nature* 468, 214–222. doi:10.1038/nature09611.

Rufino-Ramos, D., Albuquerque, P. R., Carmona, V., Perfeito, R., Nobre, R. J., and Pereira de Almeida, L. (2017). Extracellular vesicles: Novel promising delivery systems for therapy of brain diseases. *J. Control. Release* 262, 247–258. doi:10.1016/j.jconrel.2017.07.001.

Salzer, J. L. (2015). Schwann cell myelination. *Cold Spring Harb. Perspect. Biol.* 7, a020529. doi:10.1101/cshperspect.a020529.

Saraiva, C., Praça, C., Ferreira, R., Santos, T., Ferreira, L., and Bernardino, L. (2016). Nanoparticle-mediated brain drug delivery: Overcoming blood–brain barrier to treat neurodegenerative diseases. *J. Control. Release* 235, 34–47. doi:10.1016/J.JCONREL.2016.05.044.

Satta, N., Toti, F., Feugeas, O., Bohbot, A., Dachary-Prigent, J., Eschwège, V., et al. (1994). Monocyte vesiculation is a possible mechanism for dissemination of membrane-associated procoagulant activities and adhesion molecules after stimulation

by lipopolysaccharide. *J. Immunol.* 153, 3245–55. Available at: http://www.ncbi.nlm.nih.gov/pubmed/7522256 [Accessed June 12, 2018].

Sbai, O., Ould-Yahoui, A., Ferhat, L., Gueye, Y., Bernard, A., Charrat, E., et al. (2010). Differential vesicular distribution and trafficking of MMP-2, MMP-9, and their inhibitors in astrocytes. *Glia* 58, 344–66. doi:10.1002/glia.20927.

Schafer, D. P., and Stevens, B. (2015). Microglia Function in Central Nervous System Development and Plasticity. *Cold Spring Harb. Perspect. Biol.* 7, a020545. doi:10.1101/cshperspect.a020545.

Schiera, G., Proia, P., Alberti, C., Mineo, M., Savettieri, G., and Di Liegro, I. (2007). Neurons produce FGF2 and VEGF and secrete them at least in part by shedding extracellular vesicles. *J. Cell. Mol. Med.* 11, 1384–1394. doi:10.1111/j.1582-4934.2007.00100.x.

Schuldiner, O., and Yaron, A. (2015). Mechanisms of developmental neurite pruning. *Cell. Mol. Life Sci.* 72, 101–19. doi:10.1007/s00018-014-1729-6.

Sharma, S., Rasool, H. I., Palanisamy, V., Mathisen, C., Schmidt, M., Wong, D. T., et al. (2010). Structural-Mechanical Characterization of Nanoparticle Exosomes in Human Saliva, Using Correlative AFM, FESEM, and Force Spectroscopy. *ACS Nano* 4, 1921–1926. doi:10.1021/nn901824n.

Shifrin, D. A., Beckler, M. D., Coffey, R. J., and Tyska, M. J. (2013). Extracellular vesicles: communication, coercion, and conditioning. *Mol. Biol. Cell* 24, 1253–1259. doi:10.1091/mbc.e12-08-0572.

Simeoli, R., Montague, K., Jones, H. R., Castaldi, L., Chambers, D., Kelleher, J. H., et al. (2017). Exosomal cargo including microRNA regulates sensory neuron to macrophage communication after nerve trauma. *Nat. Commun.* 8, 1778. doi:10.1038/s41467-017-01841-5.

Simons, M., and Raposo, G. (2009). Exosomes – vesicular carriers for intercellular communication. *Curr. Opin. Cell Biol.* 21, 575–581. doi:10.1016/j.ceb.2009.03.007.

Sims, P. J., Faioni, E. M., Wiedmer, T., and Shattil, S. J. (1988). Complement proteins

C5b-9 cause release of membrane vesicles from the platelet surface that are enriched in the membrane receptor for coagulation factor Va and express prothrombinase activity. *J. Biol. Chem.* 263, 18205–12. Available at: http://www.ncbi.nlm.nih.gov/pubmed/2848029 [Accessed June 12, 2018].

Skog, J., Würdinger, T., van Rijn, S., Meijer, D. H., Gainche, L., Sena-Esteves, M., et al. (2008). Glioblastoma microvesicles transport RNA and proteins that promote tumour growth and provide diagnostic biomarkers. *Nat. Cell Biol.* 10, 1470–6. doi:10.1038/ncb1800.

Snaidero, N., and Simons, M. (2014). Myelination at a glance. *J. Cell Sci.* 127, 2999–3004. doi:10.1242/jcs.151043.

Somjen, G. G. (1988). Nervenkitt: Notes on the history of the concept of neuroglia. *Glia* 1, 2–9. doi:10.1002/glia.440010103.

Soo, C. Y., Song, Y., Zheng, Y., Campbell, E. C., Riches, A. C., Gunn-Moore, F., et al. (2012). Nanoparticle tracking analysis monitors microvesicle and exosome secretion from immune cells. *Immunology* 136, 192–7. doi:10.1111/j.1365-2567.2012.03569.x.

Sreeprasad, T. S., Maliyekkal, S. M., Lisha, K. P., and Pradeep, T. (2011). Reduced graphene oxide-metal/metal oxide composites: facile synthesis and application in water purification. *J. Hazard. Mater.* 186, 921–31. doi:10.1016/j.jhazmat.2010.11.100.

Stoner, S. A., Duggan, E., Condello, D., Guerrero, A., Turk, J. R., Narayanan, P. K., et al. (2016). High sensitivity flow cytometry of membrane vesicles. *Cytom. Part A* 89, 196–206. doi:10.1002/cyto.a.22787.

Supronowicz, P. R., Ajayan, P. M., Ullmann, K. R., Arulanandam, B. P., Metzger, D. W., and Bizios, R. (2002). Novel current-conducting composite substrates for exposing osteoblasts to alternating current stimulation. *J. Biomed. Mater. Res.* 59, 499–506. Available at: http://www.ncbi.nlm.nih.gov/pubmed/11774308 [Accessed June 12, 2018].

Taylor, A. R., Robinson, M. B., Gifondorwa, D. J., Tytell, M., and Milligan, C. E. (2007).

Regulation of heat shock protein 70 release in astrocytes: Role of signaling kinases. *Dev. Neurobiol.* 67, 1815–1829. doi:10.1002/dneu.20559.

Théry, C., Ostrowski, M., and Segura, E. (2009). Membrane vesicles as conveyors of immune responses. *Nat. Rev. Immunol.* 9, 581–593. doi:10.1038/nri2567.

Tricarico, C., Clancy, J., and D'Souza-Schorey, C. (2017). Biology and biogenesis of shed microvesicles. *Small GTPases* 8, 220–232. doi:10.1080/21541248.2016.1215283.

Ulloa Severino, F. P., Ban, J., Song, Q., Tang, M., Bianconi, G., Cheng, G., et al. (2016). The role of dimensionality in neuronal network dynamics. *Sci. Rep.* 6, 29640. doi:10.1038/srep29640.

Urbanelli, L., Magini, A., Buratta, S., Brozzi, A., Sagini, K., Polchi, A., et al. (2013). Signaling pathways in exosomes biogenesis, secretion and fate. *Genes (Basel).* 4, 152–70. doi:10.3390/genes4020152.

Usmani, S., Aurand, E. R., Medelin, M., Fabbro, A., Scaini, D., Laishram, J., et al. (2016). 3D meshes of carbon nanotubes guide functional reconnection of segregated spinal explants. *Sci. Adv.* 2, e1600087. doi:10.1126/sciadv.1600087.

Valiunas, V., Polosina, Y. Y., Miller, H., Potapova, I. A., Valiuniene, L., Doronin, S., et al. (2005). Connexin-specific cell-to-cell transfer of short interfering RNA by gap junctions. *J. Physiol.* 568, 459–68. doi:10.1113/jphysiol.2005.090985.

van der Pol, E., Hoekstra, A. G., Sturk, A., Otto, C., van Leeuwen, T. G., and Nieuwland, R. (2010). Optical and non-optical methods for detection and characterization of microparticles and exosomes. *J. Thromb. Haemost.* 8, 2596–607. doi:10.1111/j.1538-7836.2010.04074.x.

van der Vos, K. E., Balaj, L., Skog, J., and Breakefield, X. O. (2011). Brain tumor microvesicles: insights into intercellular communication in the nervous system. *Cell. Mol. Neurobiol.* 31, 949–59. doi:10.1007/s10571-011-9697-y.

van Niel, G., D'Angelo, G., and Raposo, G. (2018). Shedding light on the cell biology of extracellular vesicles. *Nat. Rev. Mol. Cell Biol.* 19, 213–228. doi:10.1038/nrm.2017.125.

Verderio, C., Muzio, L., Turola, E., Bergami, A., Novellino, L., Ruffini, F., et al. (2012). Myeloid microvesicles are a marker and therapeutic target for neuroinflammation. *Ann. Neurol.* 72, 610–624. doi:10.1002/ana.23627.

Vincent, M., de Lázaro, I., and Kostarelos, K. (2017). Graphene materials as 2D non-viral gene transfer vector platforms. *Gene Ther.* 24, 123–132. doi:10.1038/gt.2016.79.

Wang, G., Dinkins, M., He, Q., Zhu, G., Poirier, C., Campbell, A., et al. (2012). Astrocytes Secrete Exosomes Enriched with Proapoptotic Ceramide and Prostate Apoptosis Response 4 (PAR-4). *J. Biol. Chem.* 287, 21384–21395. doi:10.1074/jbc.M112.340513.

Wang, S., Ang, P. K., Wang, Z., Tang, A. L. L., Thong, J. T. L., and Loh, K. P. (2010). High mobility, printable, and solution-processed graphene electronics. *Nano Lett.* 10, 92–8. doi:10.1021/nl9028736.

Wang, S., Cesca, F., Loers, G., Schweizer, M., Buck, F., Benfenati, F., et al. (2011). Synapsin I Is an Oligomannose-Carrying Glycoprotein, Acts As an Oligomannose-Binding Lectin, and Promotes Neurite Outgrowth and Neuronal Survival When Released via Glia-Derived Exosomes. *J. Neurosci.* 31, 7275–7290. doi:10.1523/JNEUROSCI.6476-10.2011.

Whitesides, G. M. (2003). The “right” size in nanobiotechnology. *Nat. Biotechnol.* 21, 1161–1165. doi:10.1038/nbt872.

Wilson, H. L., Francis, S. E., Dower, S. K., and Crossman, D. C. (2004). Secretion of intracellular IL-1 receptor antagonist (type 1) is dependent on P2X7 receptor activation. *J. Immunol.* 173, 1202–8. Available at: http://www.ncbi.nlm.nih.gov/pubmed/15240711 [Accessed June 12, 2018].

Witwer, K. W., Buzás, E. I., Bemis, L. T., Bora, A., Lässer, C., Lötvall, J., et al. (2013). Standardization of sample collection, isolation and analysis methods in extracellular vesicle research. *J. Extracell. Vesicles* 2, 20360. doi:10.3402/jev.v2i0.20360.

Wolf, P. (1967). The nature and significance of platelet products in human plasma. *Br. J. Haematol.* 13, 269–88. Available at: http://www.ncbi.nlm.nih.gov/pubmed/6025241

[Accessed June 10, 2018].

Wong, I. Y., Bhatia, S. N., and Toner, M. (2013). Nanotechnology: emerging tools for biology and medicine. *Genes Dev.* 27, 2397–408. doi:10.1101/gad.226837.113.

Wu, Y., Deng, W., Klinke, D. J., and II (2015). Exosomes: improved methods to characterize their morphology, RNA content, and surface protein biomarkers. *Analyst* 140, 6631–42. doi:10.1039/c5an00688k.

Yáñez-Mó, M., Siljander, P. R.-M., Andreu, Z., Zavec, A. B., Borràs, F. E., Buzas, E. I., et al. (2015). Biological properties of extracellular vesicles and their physiological functions. *J. Extracell. vesicles* 4, 27066. doi:10.3402/JEV.V4.27066.

Yoon, Y. J., Kim, O. Y., and Gho, Y. S. (2014). Extracellular vesicles as emerging intercellular communicasomes. *BMB Rep.* 47, 531–9. doi:10.5483/BMBREP.2014.47.10.164.

Yuana, Y., Koning, R. I., Kuil, M. E., Rensen, P. C. N., Koster, A. J., Bertina, R. M., et al. (2013). Cryo-electron microscopy of extracellular vesicles in fresh plasma. *J. Extracell. vesicles* 2. doi:10.3402/jev.v2i0.21494.

Zhang, B., Wei, P., Zhou, Z., and Wei, T. (2016). Interactions of graphene with mammalian cells: Molecular mechanisms and biomedical insights. *Adv. Drug Deliv. Rev.* 105, 145–162. doi:10.1016/j.addr.2016.08.009.

Zhou, H., Zhao, K., Li, W., Yang, N., Liu, Y., Chen, C., et al. (2012). The interactions between pristine graphene and macrophages and the production of cytokines/chemokines via TLR- and NF-κB-related signaling pathways. *Biomaterials* 33, 6933–6942. doi:10.1016/J.BIOMATERIALS.2012.06.064.